ANALYSIS, DESIGN, AND FABRICATION OF AN ELECTRIC INDUCTION MICROMOTOR FOR A MICRO GAS-TURBINE GENERATOR

by

Steven F. Nagle

B.S., Pennsylvania State University, 1994
M.S., Pennsylvania State University, 1995

Submitted to the Department of
Electrical Engineering and Computer Science
in partial fulfillment of the requirements
for the degree of

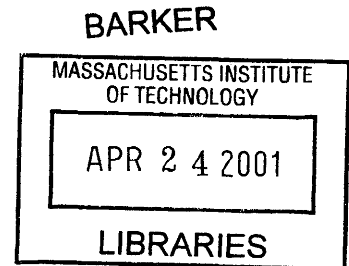

BARKER
MASSACHUSETTS INSTITUTE OF TECHNOLOGY
APR 2 4 2001
LIBRARIES

DOCTOR OF PHILOSOPHY

at the

MASSACHUSETTS INSTITUTE OF TECHNOLOGY

October 2000
[February 2001]

© MASSACHUSETTS INSTITUTE OF TECHNOLOGY, 2000
All Rights Reserved

Signature of Author ______________________________
Department of Electrical Engineering and Computer Science
26 October, 2000

Certified by ______________________________
Jeffrey H. Lang
Professor of Electrical Engineering
Associate Director, Laboratory of Electromagnetic and Electronic Systems
Thesis Supervisor

Accepted by ______________________________
Arthur C. Smith
Chairman, Department Committee on Graduate Students

Analysis, Design, and Fabrication of an Electric Induction Micromotor for a Micro Gas-Turbine Generator

by

Steven F. Nagle

Abstract

This thesis presents the analysis, design, fabrication, and testing of the first axial-gap electric induction micromotor, and the first controlled measurement of electric micromotor torque using integrated mechanical springs. Electric induction micromotors offer several advantages over electric variable capacitance micromotors and magnetic micromotors: neither rotor position nor speed need be known to achieve good performance; perfect sinusoids can be used for actuation to eliminate switching losses without loss of motor performance. In addition, the motor is fabricated from IC-compatible materials.

The tethered motor is a metrology device. To eliminate bearings and all friction forces, the rotor is attached to fixed supports by single-crystal silicon tethers that are calibrated after fabrication. The tethers are relatively compliant in the azimuthal plane, but stiff axially. This enables accurate measurement of in-plane displacements, free from losses, while preventing out-of-plane displacements that would alter the gap.

Ideally, the micromotor is fabricated from two fusion-bonded wafers in a process of 189 steps using 13 masks. Process complication comes from several sources. First, the stator structure uses a damascene insulator process to provide very thick passivation. Second, the rotor charge relaxation time constant is adjusted using a moderately Boron-doped polysilicon conductor. Third, tethers are defined by a through-wafer etch to be 385 μm tall and only 8 μm wide. Finally, the stator and rotor wafer are to be fusion bonded at the wafer level, although this was not carried out for the tested motor; it was assembled by hand with epoxy.

Torque is measured as high as 0.220 μN-m with 90 V square-wave actuation. Torque is shown to be consistent with models and the torque curves are shown to shift with rotor conductivity as expected with reference to a magnetic induction machine. The measurements are consistent with a gap of 12 μm, which is shown to be a result of the hand-assembly process. Bonding would yield a gap of 3 μm, making torque of 3 μN-m possible at the same voltage.

Thesis Supervisor: Dr. Jeffrey H. Lang
Professor of Electrical Engineering and Computer Science
Associate Director, Laboratory for Electromagnetic and Electronic Systems

ACKNOWLEDGEMENTS

I have the most gratitude for my advisor Jeffrey Lang, who has been a constant source of information, and whose availability at strange hours of the day has been an enormous help, especially during the last two months of my insane choice to work while finishing my thesis. Jeff's enthusiasm and support has also been greatly appreciated during the difficult portions of the last five years.

I also thank Stephen Senturia for many sessions that were extremely helpful in further developing good thought processes and experimental habits, and Marty Schmidt for his expertise in microfabrication. Thanks also to Alan Epstein for leading and finding funding for this project.

And of course, this thesis would simply not have been possible without the very generous support of equipment from Steven B. Leeb. I resign myself to owing him for the rest of my earthly life.

Many thanks to all of the other students who have helped me during my time at MIT, as well as the other numerous friends I have met while at MIT. You know who you are. I probably learned the most from these folks, and most of it had nothing to do with engineering. I would especially like to thank my first officemate Deron Jackson, who not only listened to me complain about everything you can imagine, but also taught me almost everything I know (but never really wanted to know) about DOS and Windows-based computers, and helped enormously in learning more about electronics and many other engineering topics. Deron is one of the best engineers I know. Next I'd like to thank Tim Denison who also taught me a lot about electronics and is also one of the best engineers I know. And with the very able help of John Rodriguez and Joshua Phinney, Tim made the final months of experimentation much more enjoyable.

I would also like to thank all of the folks on the MIT microengine project and in MTL. In particular, innumerable thanks to Arturo Ayon for his insight into all aspects of microfabrication and design. Also, thank you to Luc Fréchette, who is always up for a healthy scientific discussion, and who helped with the fabrication of the stator described in this thesis. Many thanks to Carol Livermore for her help fabricating tethered rotors and rotor conductor test structures. Thanks as well to Reza Ghodssi, Xin Zhang, MTL engineers Dan Adams, Joe Dimaria, Wayne Price, Bernard Alamariu, Paul Tierney, Kurt Broderick, John Mathias and Joe Walsh, all for their help with the fabrication. Thanks also to Debroah Hodges-Pabon, affectionately known as Debb with two b's, for much laughter and support, and to Pat Burkhart for motivating the troops in MTL. Many thanks also to Stephen Umans and Paul Warren for help with electronics and test setups.

Big thanks to everyone in my family for providing constant support, while never trying to rush me through this. Finally, I want to share my deep appreciation for Shereen Khatapoush. She has been a constant source of love and support during my most difficult times at MIT, and I will be forever grateful for her presence in my life.

This work was supported by the Army Research Office (DAAH04-95-1-0093) under Dr. Richard Paur, and by DARPA (DAAG55-98-1-0365, DABT63-C-0004) under Dr. R. Nowarck and Dr. J. McMichaels, respectively. The author was also partially supported by a National Science Foundation Graduate Fellowship for two years of this work.

Table of Contents

TABLE OF CONTENTS 7

LIST OF FIGURES 11

LIST OF TABLES 15

CHAPTER 1 INTRODUCTION 17

1.1 Electric Micromachines 18
1.2 Electric Induction Machines 21
1.3 Thesis Motivation: The MIT Micro Gas-Turbine Generator 22
1.4 Thesis Overview 23

CHAPTER 2 MODELING 25

2.1 Distributed Rotor Model 26
2.1.1 The 2D Single-Harmonic Model 28
Potential Field Solutions in the Rotor Half-Space 29
Rotor Charge Conservation 31
Analysis of the Rotor Potential Solution 32
2.1.2 Forces of Electromagnetic Origin 34
Fields and Forces from the 2D Single-Harmonic Model 34
2.1.3 The 3D Single-Harmonic Model 37
Coordinate Transformation 37
Transformed Solutions 39
Force and Torque from the 3D Single-Harmonic Model 40
2.1.4 The 3D Multiple-Harmonic Model 41
Fourier Decomposition of the Stator Potential Wave 43
Fourier Recombination of Single-Harmonic Solutions 45
2.2 An Equivalent-Circuit Motor Model 46
2.3 An Equivalent-Circuit Stator and Drive Model 50
2.3.1 Parasitics in the Power Electronic Drive 50
2.3.2 Parasitics in an Electric Induction Machine 51
2.3.3 Modeling of the Parasitics 52
2.3.4 The Pi-model and the T-model Equivalent Circuits 53
2.3.5 Equivalent-Circuit Element Definitions 56

First-Level Interconnects 56
The Second-Level Interconnect 59
2.4 Summary 61

CHAPTER 3 ANALYSIS AND TETHERED MOTOR DESIGN 63
Chapter Overview 63
3.1 Design Constraints 64
3.1.1 Design Inheritance 64
3.1.2 Micro-Fabrication Constraints 64
3.2 Micromotor Design 65
3.2.1 Micromotor Baseline Design Description 66
3.2.2 Micromotor Performance Trends 68
A Micromotor Performance Metric: Electromechanical Torque 69
Motor Performance Trends 69
3.2.3 Rotor Conductor Performance Trends 70
Underlying Physical Phenomena 74
3.2.4 Rotor Insulator Performance Trend 76
Underlying Physical Phenomena 77
3.2.5 Periodicity Performance Trend 78
Underlying Physical Phenomena 80
3.2.6 Higher Harmonics 81
3.3 Stator Design and Optimization 84
Optimization Procedure 85
3.3.1 Stator Optimization Results 87
Polysilicon Stator Optimization 87
Metallized Stator Optimizations 89
3.4 Tethered Rotor Design 92
3.4.1 Rotor Conductor Development 92
Experiment Design and Procedure 94
Results 96
Conclusions 101
3.4.2 Tether Design 101
3.5 Tethered Motor Design Summary 105

CHAPTER 4 TETHERED MICROMOTOR FABRICATION 107
4.1 Introduction 107
4.2 Process Flow Summaries 111
4.2.1 Ideal Stator Process Flows 111
4.2.2 Ideal Rotor Process Flow 112
4.2.3 Actual Process Flows 114
4.3 Unit Process Development 117
4.3.1 Thick Buried Oxide on Silicon (TBOS) 117
4.3.2 Wafer Bonding 118
4.3.3 Rotor Conductor Test Structure Fabrication 120
Fabrication Process Flow 121
4.3.4 Deep High-Aspect Ratio Tether Etch Development 122
The Etch Development Mask Feature Matrix 122
Carrier Wafer Effects 123

Recipe Development 125
4.4 Tethered Motor Die-Level Assembly 129
4.5 Packaging 131

CHAPTER 5 TETHERED MOTOR EXPERIMENTS 133
5.1 Test Rig Description 133
5.1.1 Electronics 133
5.1.2 Test Jig 135
5.1.3 The Computer Microvision System 136
5.2 Data Collection 139
5.2.1 Increase in the Air Gap Due to Epoxy 141
5.2.2 Maintenance of Elevated Machine Temperature 142
5.2.3 Confirmation of Zero Air Gap Change versus Temperature 144
5.2.4 Motion Measurement and Error Sources 146
5.3 Data Analysis 148
5.3.1 A Duffing Oscillator 148
5.3.2 Curve Fit to Find Stiffness and Torque 150
5.4 Summary and Conclusions 154

CHAPTER 6 CONCLUDING REMARKS 157
6.1 Summary 157
6.2 Conclusions 158
Technical Points 160
6.3 Recommendations for Future Work 162

APPENDIX A CONSEQUENCES OF THE INTER-ELECTRODE GAP 165

APPENDIX B THE MICROMOTOR-COMPRESSOR 167

APPENDIX C ADDITIONAL UNIT PROCESS DEVELOPMENT 169
C.1 Accelerated Development Approach 169
C.2 Stator Unit Process Development 170
C.2.1 Silicon Pit Etches 170
Issues with Intermediary Etches 170
C.2.2 Electrode Etch 172
C.2.3 TEOS versus Silane-Based Oxide 172
C.2.4 Alignment Issues 173

APPENDIX D DETAILED PROCESS FLOW DESCRIPTIONS 175
D.1 Complete Tethered Motor Stator Flow 175
D.2 Complete Tethered Rotor Flow 184
D.3 Complete Rotor Conductor Test Structure Flow 193

APPENDIX E FABRICATION RECIPES 197
E.1 Deposition Recipes 197
E.1.1 Electron Beam Aluminum Deposition 197
E.2 Lithography Recipes 198
E.2.1 Thin Resist: OCG825 20 cs 1.1 μm 198
E.2.2 Intermediary Resist: OCG825 35 cs 2.1 μm 198
E.2.3 Thick Resist: AZ P4620 8-9 μm 199
E.2.4 Image Reversal Resist: AZ 5214 1 μm 199
E.3 Etch Recipes 200
E.3.1 Anisotropic Intermediary Silicon Etch 200
E.3.2 Anisotropic Polysilicon Etch 200
E.3.3 Anisotropic Intermediary Oxide Etch 200
E.3.4 Isotropic Intermediary Silicon Etch: sts1 recipe SF6_5 201
E.3.5 Isotropic Polysilicon Etch 201
E.3.6 Deep Silicon Etches 201
MIT37 201
MIT59 202
MIT69 202
TM01 203
TM02 203
TM03 204
TM04 204
TM05 205

APPENDIX F MEASURED DATA 207
F.1 Experiment Set 1 208
F.2 Experiment Set 2 211
F.3 Experiment Set 3 216

BIBLIOGRAPHY 223

List of Figures

Figure 2.1: An illustration of a micro-scale electric induction machine showing (a) an assembled device, (b) the stator electrodes, and (c) the rotor disk, inverted to show the rotor conductor. Material thicknesses are not to scale, the actual device would have many more stator electrodes than shown, and topographical details are omitted. 26

Figure 2.2: Illustration of a 2D single-harmonic model for the electric induction machine. The ratio labeling each of the six regions is the charge relaxation time for that region. The picture is inverted in comparison to Figure 2.1(a). 27

Figure 2.3: Illustration of the electric field in the air gap of the electric induction micromachine. Ideally, the electrodes would be made very small and large in number with independent potentials to describe a smoothly varying potential wave. The actual machine is also poly-phase. 33

Figure 2.4: Cross-section of the closed surface surrounding the rotor of the 2D single-harmonic model over which the electromagnetic stress tensor is evaluated to find the force on a single wavelength unit cell of the rotor. 35

Figure 2.5: The process of mapping the 2D single-harmonic model to a 3D single-harmonic model: (a) a summary of the 2D model, (b) the 3D single-harmonic stator potential wave, (c) depiction of the mapping process, (d) the coordinate and other maps. 38

Figure 2.6: Two spatial wavelengths of the stator potential at an instant in time, at a particular radius. Here the potential across each inter-electrode gap is assumed to be the average of the electrode potentials on either side of the gap. 42

Figure 2.7: This picture shows the manner by which the 3D multiple-harmonic model uses the harmonic content of the discretely sampled stator wave to find the total electric potential, fields, torque, mechanical power and pull-in force as sums of 3D single-harmonic models that were transformed from 2D single-harmonic models. 44

Figure 2.8: The magnitude of the complex-valued potential harmonics which make up the wave in Figure 2.6 given a 300 V amplitude. The ordinate shows the index of each harmonic as the harmonic periodicity m_n divided by the fundamental periodicity m. 45

Figure 2.9: Cross section of the rotor half-space with overlaid lumped-parameter circuit elements for only the rotor half-space. 47

Figure 2.10: Equivalent lumped-parameter rotor circuit model with elements defined. 48

Figure 2.11: The complete lumped-parameter equivalent-circuit stator and rotor models, coupled with a circuit model to represent the series resonant power electronics. 50

Figure 2.12: Top view, simplified schematic of the power distribution for one phase of the stator and the associated lumped-parameter equivalent circuit model. 52

Figure 2.13: Two candidate circuits to model interconnect power dissipation and capacitive loading of the drive electronics: (a) the Π-model and (b) the T-model. 54
Figure 2.14: Capacitive coupling of the ring interconnect of one phase to the electrodes of each remaining phase. For clarity, the capacitance between electrodes is not drawn. 60
Figure 3.1: Micromotor output torque, power and pull-in force from the 3D simple-harmonic model
versus rotor speed. Motor design parameters are as specified in Table 3.1. 70
Figure 3.2: Torque versus rotor speed for various rotor conductor resistivities. Other model parameters are found in Table 3.1. 71
Figure 3.3: Torque versus rotor speed for various stator excitation frequencies. Other model parameters are found in Table 3.1. 72
Figure 3.4: Starting torque versus rotor conductor sheet resistance, and operating speed versus rotor conductor sheet resistance with the estimated load. 73
Figure 3.5: Term 1 from Equation 3.1 plotted as function of the rotor tip speed for a thin ring section of the rotor conductor located at $r = {}^{5r_o}/_6$. Other model parameters are found in Table 3.1. 75
Figure 3.6: Peak mechanical power plotted as a function of rotor insulator thickness, for several values of m. Other model parameters are found in Table 3.1..................................77
Figure 3.7: Term 2 times Term 3 of Equation 3.1 plotted as a function of the rotor insulator thickness Δ_{ri} and periodicity m. Other model parameters are found in Table 3.1. 79
Figure 3.8: Electromechanical torque, pull-in force, and resulting power versus rotor tip speed. Other model parameters are found in Table 3.1 and Table 3.2. 82
Figure 3.9: Peak electromechanical torque versus the rotor insulator thickness. Other model parameters are found in Table 3.1 and Table 3.2. 83
Figure 3.10: Major electric induction machine design aspects and their place in the context of system optimizations. 85
Figure 3.11: Maximum efficiencies, using polysilicon stator wiring, corresponding to combinations of stator lead and ring interconnect widths. See Figure 4.3 for an illustration of these components. 86
Figure 3.12: Predictions, using polysilicon stator conductors, of power out P_{out} and total efficiency of power conversion for operating speeds of the micromotor-compressor.... 86
Figure 3.13: Predictions of power source requirements and current ratings for all expected operating speeds of the micromotor-compressor. The source power calculation includes only real, non-reactive power...88
Figure 3.14: Electrical energy conversion efficiency for various stator electrical lead and interconnect combinations, plus the major sources of power loss in the electronics and stator. Table 3.5 contains the list of material combinations. 91
Figure 3.15: Breakdown of power losses during electrical energy conversion, shown in comparison to the power P_{in} drawn from the DC power source and the power P_{out} supplied to the compressor subsystem. Molybdenum gives results equivalent to those of Tungsten. 92
Figure 3.16: The rotor conductor test structure...93
Figure 3.17: An example of raw data from the rotor conductor development experiment, with a fit to the raw data. 96
Figure 3.18: Coarse-grain polysilicon rotor conductor resistivity for Trials A and C, averaged for all measurements of like devices. 98

Figure 3.19: Fine-grain polysilicon rotor conductor resistivity from Trials B and D, averaged for all measurements of like devices 98
Figure 3.20: Coarse-grain polysilicon rotor conductor resistivity for Trial E, averaged for all measured devices. Plot courtesy of Dr. Carol Livermore. 100
Figure 3.21: Fine-grain polysilicon rotor conductor resistivity for Trial F, averaged for all measured devices. Plot courtesy of Dr. Carol Livermore. 100
Figure 3.22: Predicted torque and pull-in force for the tethered motor. 104
Figure 3.23: Predicted deflections of the tethered rotor. 104
Figure 4.1: Simplified process flow representation for the tethered motor. Thicknesses have been exaggerated for clarity and only 3 ring interconnects are shown. See Figure 4.3 also.. 108
Figure 4.2: Illustration of the tethered motor with insets highlighting the tethers. 109
Figure 4.3: Cross-sectional and "unfolded" views for the two wafers of the tethered motor. To return to the device form, the wafer halves would be folded out of the page along the dashed line. The cross-section is not to scale and three ring interconnects are drawn instead of the full six. 110
Figure 4.4: Representative pictures of a wafer from rotor lot tmrot1 115
Figure 4.5: Representative pictures of a wafer from stator lot mcstat1. 116
Figure 4.6: Summarized process flow for the rotor conductor test structure. This structure is also fabricated in parallel with device wafers to serve as a process monitor. 121
Figure 4.7: Method for attaching a carrier wafer to a device wafer. 123
Figure 4.8: The footing effect in the context of the tether etch. 124
Figure 4.9: Initial results of the tether etch development using a standard recipe, MIT59: a) sample etched halfway; b) sample fully etched. 125
Figure 4.10: From a wafer etched with modified MIT59: 80 sccm passivation; TM04 in Section E.3.6. Grass formation from excessive passivation is visible in the bottom of the trench at the left. 126
Figure 4.11: From a wafer etched with modified MIT59: 60 sccm passivation and 10 W electrode power; TM03 in Section E.3.6. Note that the sidewall etch cut through the tether at its midpoint 127
Figure 4.12: Result from a development wafer for the chosen tether etch recipe, TM02 in Section E.3.6. 128
Figure 4.13: The first tethered electric induction motor, device TMA. This figure shows the first method of die-level assembly using metallic epoxy and crude alignment 130
Figure 4.14: Assembled and packaged tethered motor TMB. Scale is in inches. This figure shows the method of die-level assembly using non-metallic epoxy and precise alignment. The rotor of this motor became dislodged and is shown overturned at the upper right of the chip 131
Figure 5.1: Schematic of the power electronic drive based on the PA85 op-amp 134
Figure 5.2: Illustrative description of the tethered motor test rig and photo of the actual rig. Electronics, signal generators, computer and PIFOC controller are not labeled or are not shown in this figure 137
Figure 5.3: Two examples of data acquisition showing the process used to capture images of rotor deflection. In this case the number of sampling intervals is only 8 per period. The LED is on and the camera shutter is open during the entire sampling interval. The vertical axes are not to scale. 138

Figure 5.4: Illustration showing the differential slope of the stator plane and rotor plane: (a) shows a top view of the tilt measurement points, and (b) shows the associated variation of the air gap..141
Figure 5.5: Cross section of the device mount. Note that since a thick layer of oxide covers the stator die, it is substantially curved. Thus the point of contact between the two die is unclear. 142
Figure 5.6: A plot of rotor perimeter tangential displacement versus reversal frequency, as measured by the microvision system. X_1 is the fundamental fourier harmonic of the linear displacement in a direction tangential to the perimeter of the rotor................146
Figure 5.7: Fitted linear and cubic stiffnesses for experiment set 1. 151
Figure 5.8: Fitted linear stiffnesses for experiment sets 2 and 3. The cubic stiffness is the same as in experiment set 1. Note the increase in stiffness as the tethered motor temperature decreases from 90 °C in experiment set 2, to 41 °C in experiment set 3. ... 151
Figure 5.9: Plot of measured torque versus stator voltage, for stator excitation frequency equal to 300 kHz. Predicted torque is fit by the method of least squares. The fit assumes that Phase C does not contribute to torque. 152
Figure 5.10: Plots of measured torque versus stator excitation frequency, for two rotor temperatures, with predicted torque curves fit by the method of least-squares. The fit to Set 2 assumes that Phase C does not contribute to the torque..............................152
Figure 5.11: Variation in rotor conductor resistivity with rotor temperature, reduced from the torque measurements of experiment sets 2 and 3. See [29] for the origin of the resistivity equation...156
Figure A.1: Normalized maximum electromechanical torque plotted as a function of the stator electrode duty ratio D. The duty ratio is the ratio between the area of the electrodes and the area of the inter-electrode insulating gaps. Each curve is for a different assumed potential function across the inter-electrode insulating gap. 165
Figure C.1: (a) Silicon pillars that can remain after an intermediary etch. (b) Pits that remain when recipe is adjusted to decrease incidence of pillars. 171

List of Tables

Table 1.1: List of existing micro-scale electric machines. 18

Table 2.1: Lumped-parameter equivalent circuit elements in Figure 2.11. 58

Table 3.1: Parameters in the baseline electric induction micromotor design. These apply to both the micromotor-compressor and the tethered motor. 67

Table 3.2: Stator electrode geometry parameters. These apply to both the micromotor-compressor and the tethered motor. 81

Table 3.3: Additional stator geometry parameters. These apply to both the micromotor-compressor and the tethered motor. 87

Table 3.4: Resultant specifications for power electronic components. These results are typical of the circuit model simulations. 88

Table 3.5: Material combinations yielding the data shown in Figure 3.14. 90

Table 3.6: Optimized stator wiring designs. 91

Table 3.7: Summary of rotor conductor experimental trials. 95

Table 3.8: Tether design parameters. These are specific to the tethered rotor. 103

Table 3.9: Complete tethered motor design parameters, summarized for easier reference. 106

Table 4.1: Naming key and brief history for assembled tethered motors. 129

Table 5.1: Summary of as-fabricated condition of micromotor TMA. 140

Table 5.2: Data collection experiment parameters, grouped into three sets. The torque curves for each set are plotted in Section 5.3.2. 145

Chapter 1

Introduction

Miniaturization is the goal of nearly every leading-edge high-technology effort in the electronics, telecommunications, and biotechnology industries today. Over the past 30 years, small appliances have been developed for use in nearly every aspect of daily life, and the continuation of this trend towards the micro-scale will most likely continue well into the future. Undeniably, the most advanced miniaturization effort is that in the electronics industry. Today, tens of millions of transistors can be fabricated in the area previously required for a single integrated circuit (IC) that was composed of only a few transistors. So it is not surprising that beginning over 20 years ago the techniques of the IC industry have been applied toward the fabrication of mechanical devices of only tens of microns in size [62]. Being primarily electrically stimulated, such a device is now commonly referred to as a microelectromechanical system, or a MEMS device for short. Today it is common to find devices which integrate both MEMS devices and ICs on the same chip, though it is not always beneficial and usually not necessary to do this.

The miniaturization trend is now being extended beyond the device or appliance itself, to the power source. Recently, a research and development effort began at MIT to produce a micro-scale gas-turbine generator capable of producing tens of watts of electrical power [19]. Fundamental scaling laws suggest that the benefits of macro-scale turbomachinery may be preserved as the components are miniaturized, and to accomplish this at least three micro-scale technologies must be developed: rotating machinery, combustors, and high-temperature materials [18]. An overview of the effort is provided below in Section 1.3. The on-going project continues to move the technology closer to successfully enabling miniaturized power sources, which will allow high-power MEMS devices to sense and act upon their environment completely removed from any macro-scale system. For example, the high power promised by the microgenerator could be used to power a future generation of miniature communication components, allowing MEMS devices to send and receive information over great distances.

To accomplish the goals of the microgenerator, suitable micro-scale electric machine technology must also be developed. The device must be able to convert the high chemical energy density

of currently available fuels first to mechanical energy and then to electrical energy. If designed appropriately, the electric machine could also act as a starter for the gas-turbine in the microgenerator.

Suitable electric machine topologies have been explored in the literature, but no currently available device appears to enable the desired amount of energy conversion within the envisioned microengine topology. In fact, very few micro-scale electric machines have been successfully applied to practical problems. For reasons that will be described below, an electric induction machine topology seems most appropriate for integration in the micro gas-turbine generator. Many components of the gas-turbine will be under development for some time, so to provide a near-term goal the electric machine in this thesis will be designed to drive a micro-scale compressor, much as it would when functioning as a starter motor. In addition, to enable accurate torque measurement, the rotor will be suspended on mechanical springs, or tethers. Constrained motoring operation will then be explored experimentally using this so-called tethered motor. In doing so, this thesis presents the analysis, design, fabrication, and testing of the first electric induction micromotor.

1.1 Electric Micromachines

The electric induction machine is one of many micro-scale electric machine types that have been explored since the first operable electric micromotors were fabricated by Trimmer and Jebens [71] and Tai and Muller [66, 67] in 1989. Since then a wealth of literature has been generated on various types of electric micromachines, and well over 300 publications can be found on the theory and fabrication of the machine types marked by an × in Table 1.1.

Using the literature and the eventual goal of integration with a gas-turbine as guides, several factors lead to the electric induction machine as the most appropriate choice for the micro gas-turbine generator, through a process of elimination. First, all magnetic machine types are ruled out on the basis of poor material compatibility with IC processing methods and incompatibility with the temperatures of the micro gas-turbine generator. Second, any machine type that requires contact to

Table 1.1: List of existing micro-scale electric machines.

Electric		Magnetic	
variable capacitance	×	variable reluctance	×
electric induction	×	magnetic induction	
permanent electret	×	permanent magnet	×
corona discharge	×	—	
dielectric hysteresis		magnetic hysteresis	
elastodynamic	×	elastodynamic	×

the rotor is not considered because the microengine will necessarily operate at speeds on the order of one million revolutions per minute [23]. For this reason and others, elastodynamic machines are also unacceptable in the microengine. These include general ultrasonic [53, 53], piezoelectric ultrasonic [54], vibromotors [34], and scratch-drive machines using either electric or magnetic actuation [63]. At high speed and high temperature, rotor contact would lead to unacceptable wear and accelerated device failure. Third, there are very few IC-compatible materials that exhibit dielectric hysteresis. Fourth, a corona discharge motor would be an unwise choice in the microengine environment because that environment will contain fuel vapors. Fifth, permanent electrets are not particularly stable and furthermore do not seem to be capable of high performance when compared to other machine types [43], so they are also excluded. This leaves induction machines and variable capacitance machines as the only two candidates. As discussed below, it is felt that the induction machine is a much better choice.

It is important to note that in the future, magnetic materials may offer the greatest advantage in micro-scale machines, as they do today in macro-scale machines, but existing magnetic micromachines are relatively primitive compared to their electric counterparts [1, 6, 24, 33]. Macro-scale magnetic machines have a very clear advantage over macro-scale electric machines on the basis of sustainable energy densities. It has been theorized that an electric field strength of approximately 3×10^8 V/m is required for an electric machine to come close to the energy density of a similar magnetic machine operating at maximum magnetic field strength [4, 8], which is limited by saturation of the magnetic materials in the machine. In a practical macro-scale electric machine, this is not possible because the electric field strength is limited by breakdown to approximately 10^6 V/m, reducing the energy density by a factor of 10^4 compared to the magnetic machine. However, various electric micromotor experiments have confirmed that the fields in micron-sized gaps can reach the required field strength of 3×10^8 V/m, thus electric micromachines have dominated the MEMS field.

However, there are two additional reasons that magnetic machines were not chosen for the microengine application. First, Bollee has pointed out that as a magnetic machine is scaled down, it loses its ability to adequately dissipate the heat generated in its windings, so the power output of the machine must be decreased to compensate [8]. When the scaling law is worked out in terms of a common length scale and heat dissipation is assumed to be proportional to the exposed area of the windings, the electric machine has the advantage. Second, magnetic materials are currently integrated into micro-scale devices either by hand-assembly or electroplating of the magnetic material [15, 33], and neither of these is an attractive option. The micromotor developed in this thesis is to be batch fabricated along with the rest of the components in the microengine, from IC-compatible materials, so hand assembly is not acceptable or needed. Furthermore, to integrate several levels of fluid passages on-chip, the microengine will be comprised of several fusion bonded wafers [36, 35].

Current electroplating techniques applied to the production of micro-scale magnetic materials are not compatible with the high-temperature steps required to produce these bonds [33]. For these reasons, all magnetic machines are ruled out for the microengine application until suitable materials and processes are developed. An effort to do so is actually now underway as part of the microengine project at MIT and the Georgia Institute of Technology.

The only remaining micromachine choices, as outlined above, are variable capacitance and electric induction. Of these, the variable capacitance machine is the most mature. This type of motor has been fabricated both as a salient-pole top or side-drive micromotor [48, 67, 69, 39], and as a harmonic or wobble motor [71, 72, 17, 28]. The salient pole micromotor uses the change in capacitance that occurs as conducting salient-pole surfaces on the rotor slide parallel to those on the stator, each separated by a small gap. When a stator electrode is excited, a force is generated that tends to increase the total capacitance by increasing the overlapping area. Thus a multitude of azimuthally distributed salient surfaces can be sequentially excited to keep the rotor in continuous rotation in the manner of a stepper motor.

Similarly, the wobble motor uses the change in capacitance that occurs as the its rotor rotates within its stator. Here the motion also progresses in steps, and two types exist. In both types, stator electrodes are excited sequentially in an azimuthal direction. Again, as a stator electrode is charged, a force is exerted on the rotor that tends to increase the total capacitance, this time by decreasing the gap between the rotor and stator. In the first and most common type, the rotor outer surface is in contact with the inside surface of the stator. One surface is coated with an insulating material of very small thickness, so very large voltages and small gaps can be used, leading to large torque. Here the rotor rolls along the inner wall of the stator, following the excitation of the stator electrodes, which are oriented axially. Rotor rotation occurs in a direction opposing the rotation of the stator excitation. In a less common type, the rotor is restrained by a center pin-bearing and rotates in the same direction as the stator excitation. Here the insulation between rotor and stator is either a gas or a liquid, so in general the electrode voltages are smaller to avoid breakdown, and the torque is smaller.

Both variable-capacitance machine types seem to be poor choices for the micro gas-turbine generator because of several inherent characteristics. Although the wobble motors have obtained the highest reported torque output of any micromotor, the rotor is required to be in contact with either the stator inner surface or a pin bearing. Thus they must be excluded based on the excessive wear that would occur at high speed. Furthermore, these motors are generally not fabricated with IC-compatible processes because in order to develop high torque, they must be very long, on the order of several millimeters. A conductor of such dimensions can be obtained using a LIGA or similar electroplating process, but is difficult to obtain by any other method.

Likewise, as for the less-common type of wobble motor, salient-pole VC micromotors also employ pin bearings and bushings to maintain clearances, so they might be excluded because of rotor contact as well; however, gas bearings could serve the same purpose. Out of the various forms of salient-pole VC micromotors that have been fabricated, the axial-gap machine is most compatible with the proposed planar layout of the microengine. Still, like all VC micromotors, an axial-gap salient-pole micromotor is synchronous, requiring rotor position information for good performance, and requiring hard switching which leads to power loss in the drive electronics. Torque decreases rapidly if the excitation of a stator pole does not occur with perfect timing as the rotor pole moves past [32]. While speed information can be obtained in the microengine [36, 35], accurate position information is much more difficult. Conversely, the electric induction motor is excited most readily with perfect sinusoids, which can be generated using a series resonant power electronic topology that naturally incorporates soft switching, and position information is not required for good performance because the machine is asynchronous. In addition, it can be fabricated with IC-compatible materials, and the rotor need not make contact with the stator if gas bearings are employed. Thus the electric induction machine is chosen for the micro gas-turbine generator application.

1.2 Electric Induction Machines

The first electric induction motor was fabricated over 100 years ago by Arno [2]. Bollee [8] believed that this motor exploited a dielectric hysteresis effect in the glass and ebony rotors that Arno used. Since that time, very little research has been conducted, as several authors have noted [4, 5, 31, 8]. Indeed, a search of the literature for both micro-scale and macro-scale electric machines, combined, returned less than 10 citations. The modern form of the electric induction machine, which employs free surface charge, was first fabricated 30 years ago, and measurements of the staring torque were made as a function of excitation frequency [8, 14]. Building upon these results, other authors fabricated similar electric induction motors [31, 51, 52], and some investigated non-ideal effects inherent to the electric machine [31, 10]. The governing equations were explored early on by [32, 73] and more recently by [5, 11, 52]. This thesis will add a new perspective and new insight into the theory of electric induction machines like that of Bollee, as well as present measurements on a microfabricated version of the machine.

There are several types of electric machine linked to induction-like phenomena. Two types function solely through the polarization of perfectly insulating rotor material, perhaps like the motor of Arno, using either the dielectric hysteresis or dielectrophoresis effect. This thesis considers a third type, the free-surface-charge electric induction machine, which functions through the Lorentz force on free surface charges, as in the motor of Bollee. This machine operates by inducing a free charge distribution on the surface of a nearly-insulating rotor and then dragging this charge across

the rotor surface to produce a torque. This rotor charge can be induced by a potential wave made to travel along the stator on the surface of a multitude of stator electrodes. Equivalently, the stator can be said to carry a travelling wave of charge. The stator and rotor charge waves travel at the same speed, but the rotor surface moves at a different speed. Thus the electric induction machine is an asynchronous machine. Since the rotor surface is not perfectly conducting, charge relaxation combines with charge convection to result in a phase lag between the stator charges and the rotor charges. As a result, a net torque is applied to the rotor surface. The electric induction machine performs best when the charge relaxation time constant of the rotor and the speed of the rotor are matched. Here the torque is maximized; at rotor speeds greater or lower, the torque decreases. However, adequate torque is generated over a broad range of relative speed and neither rotor speed nor position information is needed for good performance.

An electric induction motor, employing free surface charge conduction, has never been reported in the literature. This thesis represents the first known successful attempt to fabricate and test this type of micromotor.

1.3 Thesis Motivation: The MIT Micro Gas-Turbine Generator

The micro gas-turbine generator, or microgenerator, will be a complex piece of equipment; therefore its deeply multi-disciplinary development is been divided into smaller segments, which come in the form of separate development devices. For all devices, materials characterization is an ongoing effort [12, 13, 40]. The first development device is a micro bearing rig [35, 36, 57, 60]. These bearings are essential to the gas-turbine, and their development once contained a great amount of uncertainty. Many questions regarding the bearings and general microfabrication design have been answered through experiments on the microbearing rig, and the microbearing rig has also helped to verify the design of the turbine. A second development device, a microcombustor [46, 47], contained no moving parts. It confirmed the feasibility of sustainable micro-scale combustion. A third device builds on the results of the micro-bearing rig. This device, a so-called micromotor-compressor [21] incorporates bearings designed according to data from the micro bearing rig, provides a test bed for the compressor of the micro gas-turbine generator, and provides a near-term design goal for the electric induction micromotor of this thesis. The fourth device is the tethered motor [55] that enables closed-loop development of a motoring version of the starter/generator electric induction micromachine. The tethered motor consists of the electric induction micromachine and a metrology structure to measure motoring performance. This thesis describes the development of the tethered motor, as laid out in the next section. A fifth device under development, a turbine-generator, will specifically concentrate on the development of the generator. This device will build on experience

from all previous development devices except the microcombustor. Finally, lessons learned from all development devices will be combined to build the microgenerator itself.

1.4 Thesis Overview

This thesis details the analysis, design, fabrication, and testing of a tethered electric induction micromotor. Chapter 2 provides an analysis of the electromechanical behavior of a generalized electric induction machine. This analysis is first derived by solving for the potential and fields in the machine. The field analysis is then used to develop an equivalent circuit model of the rotor and air gap of the machine. Finally, an equivalent circuit model is derived to capture non-ideal effects in the stator wiring of the machine and to be connected to a model of the power electronics for simulation of the system.

Chapter 3 uses the models to design an electric induction machine within the framework of a micromotor-compressor. Section 3.2 considers the rotor and air-gap in detail first. Much of the geometry and material choices are dictated by the motor-compressor application. Other design parameters are chosen based on physical limitations. Essentially, only the following three aspects of the machine are variable to reach design goals: the rotor conductor sheet resistance, the rotor insulator thickness, and the stator periodicity. Performance trends related to each of these are discussed in detail, and the reasons behind their baseline values are described. Section 3.3 describes two optimizations of the stator wiring that connects the electrodes to the drive electronics. The first optimization is done within a constraint on stator construction materials; i.e., heavily-doped polysilicon is used for the stator wiring. The second optimization considers many different materials, and shows the benefits of performance gained by using a low-resistivity material such as a metal or metal silicide for the stator wiring. Finally, Section 3.4 details the development of the rotor conductor and describes the tether design. Section 3.4.1 is particularly important as it presents the details of experiments that have been conducted to design a rotor conductor with the resistivity specified by design goals in Section 3.2.3.

Next, Chapter 4 describes the fabrication of the tethered electric induction motor. Section 4.2 outlines the total fabrication process flow, and Section 4.3 describes four unit processes that are especially critical to the fabrication of a micromotor within the design specifications of Chapter 3. The chapter also describes the deviation of the actual motor build from the ideal case.

Chapter 5 recounts measurements made on the tethered electric induction motor. The chapter first describes the drive electronics and measurement set-up in detail. Next, the method of data collection is described, measurements of torque produced by the tethered electric induction motor are presented and discussed, and the effects of a changing rotor conductor sheet resistance are shown. Chapter 5 also draws conclusions from the data. Finally, Chapter 6 summarizes the thesis, presents

broad detailed conclusions based on the results of micromotor testing, and outlines recommendations for future work.

Chapter 2

Modeling

This chapter develops several analytical models for the planar, axial gap electric induction machine illustrated in Figure 2.1. Two distinct model types are developed: distributed electromechanical models and equivalent-circuit models. The distributed models use Maxwell's Equations to describe the electromagnetic fields throughout the machine, while the equivalent-circuit models average the fields over space and replace the distributed model with representative networks of circuit elements.

The distributed electromechanical models are developed first then used as the basis for developing the equivalent-circuit models. A distributed-field model is developed in Section 2.1 to describe both the air gap and the rotor. It begins as a rectilinear model constructed from Maxwell's Equations with simplifying assumptions to provide a basic description of an ideal rectilinear electric induction machine. Then, on this foundation, more detailed models are constructed to describe the disk-shaped machine of this thesis. Finally, the distributed rotor and air-gap model is simplified and condensed into an equivalent-circuit rotor and air-gap model in Section 2.2.

A model for the stator is developed in Section 2.3. Since this model is primarily needed to describe the parasitic capacitances and resistances of the interconnections between the electrodes and the package leads, it also takes the form of an equivalent-circuit. It is combined with the equivalent-circuit rotor model, and with similarly condensed circuit models of the packaging and the power electronics. The resulting circuit is then analyzed as a complete network model of the electric induction machine and its environment.

Each model is used to answer specific questions about an electric induction machine. Distributed models are used primarily to generate design rules for the overall size of various machine components. This is because they directly describe the fields which actually exist within the machine. Thus they provide a direct link between the extent and strength of the fields in the air gap and rotor, and power produced by the machine. Their only input is the desired azimuthal stator potential distribution.

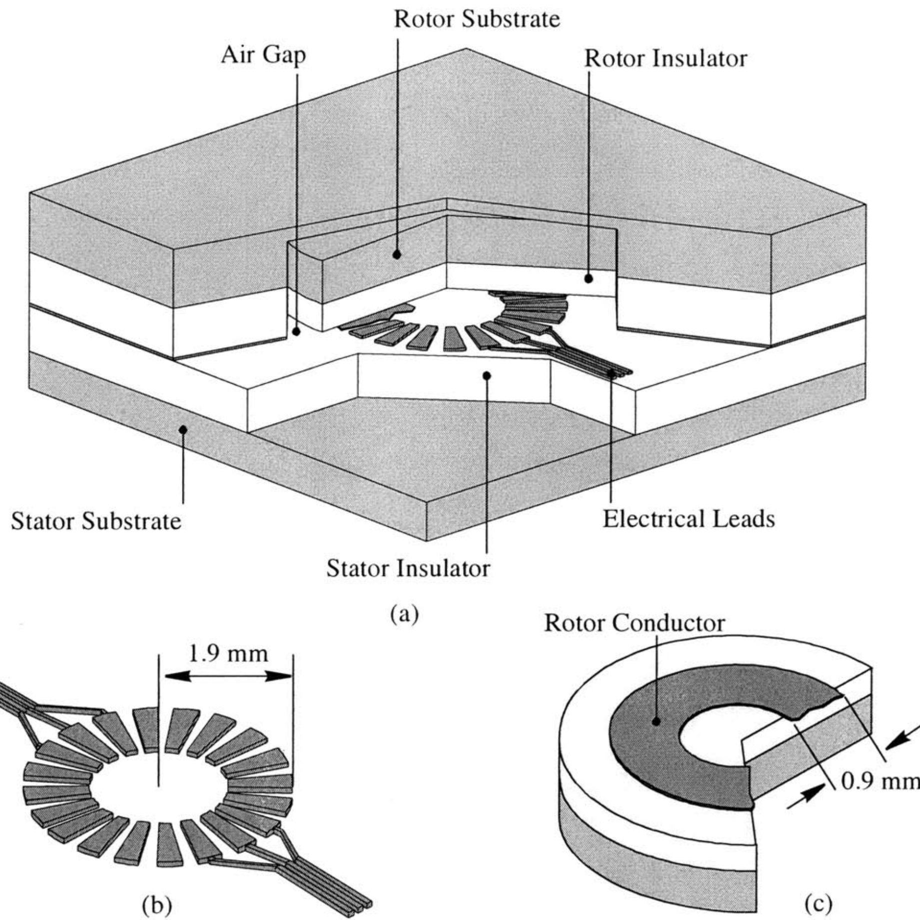

Figure 2.1: An illustration of a micro-scale electric induction machine showing (a) an assembled device, (b) the stator electrodes, and (c) the rotor disk, inverted to show the rotor conductor. Material thicknesses are not to scale, the actual device would have many more stator electrodes than shown, and topographical details are omitted.

The distributed model is linked directly to particular geometric regions of the machine. The distributed models are used to optimize the rotor conductivity, the rotor insulator thickness, the number of electrodes, and the air gap length for best performance. In contrast, the circuit models are approximations of geometry and field extent. They are used to optimize over total system efficiency by optimizing the design of stator interconnections such that the desired stator potential distribution will be delivered to the electrodes while dissipating as little energy as possible. They are also used to determine current and voltage ratings for the power electronics, and to answer any other questions regarding the electrical system as a whole.

2.1 Distributed Rotor Model

Distributed electromechanical models of the air gap and rotor are developed here in several stages with reference to Figure 2.2. The upper structure of the stator is excluded for reasons to be

described in Section 2.1.1. A multi-stage approach is taken to allow a fuller description of the modeling process. In the first stage, a two-dimensional rectilinear single-harmonic model is developed. In the second stage, the single-harmonic rectilinear model is warped into an approximation of three dimensions to produce a single-harmonic annular model. This model supports fast analyses to enable broad parametric studies. Finally, in the third stage, an orthogonal set of the previous models are combined to form a single model of the air gap and rotor. This model properly describes the effects of non-ideal design due to fabrication constraints, and non-ideal fabrication within those constraints.

As a way of introducing the electric induction machine and to provide a framework within which to discuss the machine, four of its most descriptive characteristics are highlighted with the help of Figure 2.1. First, the figure shows insulating layers that serve to separate the active portions of the machine from relatively highly conductive structural material. These are generally referred to as passivation layers. Second, the figure shows the location and extent of the rotor conductor. This thin film is analogous to rotor windings in a magnetic induction machine, and its exact conductivity has a large impact on machine performance. Third, the figure shows that the rotor is a disk; it is unavoidably three-dimensional (3D) and this must be taken into consideration. Finally, the figure

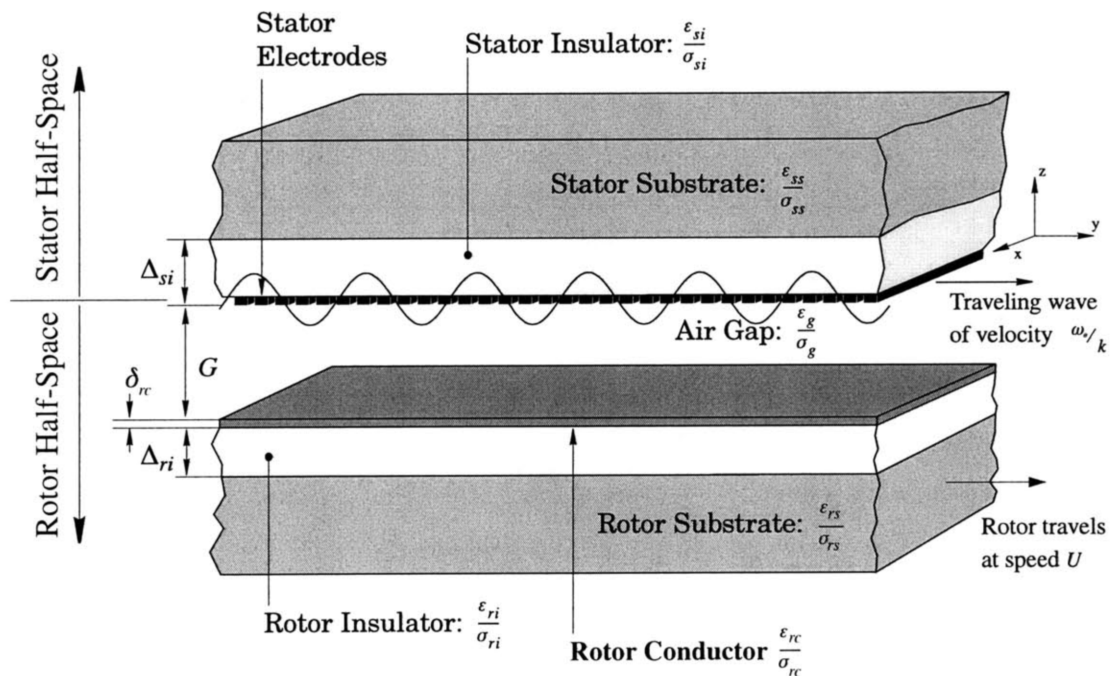

Figure 2.2: Illustration of a 2D single-harmonic model for the electric induction machine. The ratio labeling each of the six regions is the charge relaxation time for that region. The picture is inverted in comparison to Figure 2.1(a).

highlights the fact that there are only a finite number of stator electrodes with a small number of connections to off-chip electronics. Thus choices of stator excitation are constrained by geometry.

2.1.1 The 2D Single-Harmonic Model

The use of a cylindrically-symmetric 3D model of the electric induction machine is more computationally intense than desired for the purposed of design. As a building block for a simple and fast model that will approximate the full 3D solution, a simple 2D model based in the cartesian coordinate system is developed in this section. Instead of a disk that rotates past the stator, the 2D single-harmonic model describes a semi-infinite rotor half-space that moves linearly past a semi-infinite stator half-space, as depicted in Figure 2.2. Use of this model is like considering only a very small region of a very large disk-shaped machine in which the x-coordinate points in the radial direction while the y-coordinate would follow the azimuthal direction. Given the size of the electric induction machine to be analyzed here, this is not a bad approximation. However, there are limits to this approximation, and these are quantified in Section 2.1.3.

The 2D single-harmonic model assumes that only a single-harmonic traveling-wave of potential is applied across the stator surface. Such a potential wave would theoretically be possible with an infinite set of independently controlled electrodes, having infinitely small spaces between them. Unfortunately, fabrication constraints limit the minimum electrode width as well as the space between them, in turn limiting their total number. Additionally, electronic control becomes much more difficult as the number of independent electrodes is increased. Thus, the actual potential distribution is piece-wise continuous, i.e., the potential is constant across the surface of one electrode, and then varies across the insulating space between electrodes, to reach the potential of the next electrode. This thesis will assume an average potential function between the electrodes. Appendix A describes the consequences of several different potential functions across the inter-electrode gap. Finally, the 3D multiple-harmonic model provides a more accurate picture by superposing multiple potential harmonics in order to describe the finite and isolated nature of practical electrodes.

The electric induction machine is parsed into two half-spaces as shown in Figure 2.2. Each half-space encompasses several material layers, and the fields in each layer are found using the boundary conditions at the interfaces between them. In total, the induction micromachine as a stack of six independent layers with common interface potentials. Using the assumption of no free volume charge, Laplace's equation can be solved for each of the six layers with free-charge conservation boundary conditions at material interfaces and potential boundary conditions on outer surfaces.

The rotor half-space and the stator half-space can be analyzed independently because the electrode potential divides these regions and is externally enforced. The stator half-space consists of a complex structure of wiring between the electrodes and the stator substrate, and the parasitic capaci-

tances and resistances inherent to this wiring dominate the electrical description. These parasitics are very important in a system-level description of the machine, but if the stator wiring is designed properly the electrode surface will provide a stiff potential boundary condition that uncouples the rotor and stator half-spaces. For this reason, a discussion of stator half-space modeling is delayed until Section 2.3, and rotor potentials are assumed to be unaffected by any potentials in the stator half-space.

Potential Field Solutions in the Rotor Half-Space

This section describes the use of Maxwell's Equations to develop the distributed-field models used in this thesis. It is useful now to state a few definitions that will be used in the following solutions. First, for the purposes of this thesis, the electric fields are assumed to be quasi-static [75]. Second, no free volume charge exists within the electric induction machine. Third, it is assumed that the stator electrodes impose a traveling wave of electric potential having the form

$$\Phi(x, y, z = 0, t) = \Re\left\{\hat{V}_s e^{(ky - \omega_e t)}\right\} \tag{2.1}$$

over their surface adjoining the air gap. Here $\hat{V}_s$ is the complex potential amplitude of the traveling wave on the stator, ω_e is its temporal excitation frequency and k is its wavenumber, or spatial frequency. Fourth, the phase velocity of the stator potential wave is in the y-coordinate direction with magnitude ω_e/k. Lastly, although this thesis will work primarily with complex quantities for convenience, at times real quantities are necessary; so for brevity, the notation

$$X(x, y, z, t) = \Re\left\{\hat{X}(x, y, z, t)\right\} \tag{2.2}$$

is defined for use throughout this chapter.

Since free volume charge is assumed to be non-existent, Laplace's equation may be solved for the electric potential within the electric induction machine. Laplace's equation for the complex electric potential $\hat{\phi}(x, y, z, t)$ in cartesian coordinates takes the form

$$\frac{\partial^2\hat{\phi}}{\partial x^2} + \frac{\partial^2\hat{\phi}}{\partial y^2} + \frac{\partial^2\hat{\phi}}{\partial z^2} = 0. \tag{2.3}$$

The solution to this equation in the air gap of the 2D single-harmonic model with z = 0 at the electrode surface can be written as

$$\hat{\phi}_g(x, y, z, t) = \frac{\hat{V}_s \sinh[k(z+G)] - \hat{\Phi}_{ri}\sinh(kz)}{\sinh(kG)} e^{j(ky - \omega_e t)} \qquad 2.4$$

where the term $\hat{V}_s$ is the complex amplitude of the potential wave on the stator electrode surfaces. This applied potential induces a potential wave on the rotor conductor having the complex amplitude $\hat{\Phi}_{ri}$. Similarly, the solution in the rotor insulator is

$$\hat{\phi}_{ri}(x, y, z, t) = \frac{\hat{\Phi}_{ri}\sinh[k(z+G+\Delta_{ri})] - \hat{\Phi}_{rs}\sinh[k(z+G)]}{\sinh(k\Delta_{ri})} e^{j(ky - \omega_e t)} \qquad 2.5$$

where $\hat{\Phi}_{rs}$ is the induced potential amplitude at the interface of the rotor insulator and the rotor substrate. The parameters G and Δ_{ri} refer to the air gap thickness and rotor insulator thickness, respectively, as shown in Figure 2.2.

The potentials given above include a major simplification that should be clarified. In arriving at Equation 2.5, the rotor conductor has been treated as a sheet of zero thickness. This means that the potential at the interface of the air gap and rotor conductor is assumed to be exactly the same as the potential at the interface between the rotor conductor and the rotor insulator. This assumption is valid as long as the rotor conductor thickness δ_{rc} in Figure 2.2 is much less than one spatial wavelength $2\pi/k$ of the potential wave on the rotor. When exploring various designs, this simplification must be kept in mind as k can change greatly.

The analysis is further simplified by treating the rotor substrate as a perfect conductor. This is an appropriate assumption since the silicon substrate is highly conductive, but it reflects a non-ideal situation. A very conductive rotor substrate and a thin rotor insulator create a very large capacitance in parallel with the rotor conductance that leads to an unrecoverable loss of machine performance. The rotor insulator is made as large as possible to reduce the size of the capacitance, but fabrication constraints both limit the thickness of the rotor insulator and demand that silicon be used for the rotor substrate. A quartz substrate would be ideal, but deep fluidic channels would need to be cut into the quartz to make it viable in the microengines for which the electric induction machine is intended. Thus, the choice is silicon, which is several orders of magnitude more conductive than the rotor conductor, and the perfectly conducting substrate assumption is valid.

As a result of the assumption of infinite rotor substrate conductivity, the electric potential is uniform within the rotor substrate. In addition, since the stator excitation averages to zero in time and space, the value of the rotor substrate potential becomes

$$\hat{\Phi}_{rs} = 0.$$

Thus, Equation 2.5 is simplified, and the two potentials from Equations 2.4 and 2.5 become

$$\hat{\phi}_g(x, y, z, t) = \frac{\hat{V}_s \sinh[k(z+G)] - \hat{\Phi}_{ri} \sinh(kz)}{\sinh(kG)} e^{j(ky - \omega_e t)} \quad 2.4$$

$$\hat{\phi}_{ri}(x, y, z, y) = \frac{\hat{\Phi}_{ri} \sinh[k(z+G+\Delta_{ri})]}{\sinh(k\Delta_{ri})} e^{j(ky - \omega_e t)} \quad 2.6$$

Rotor Charge Conservation

It is now possible to substitute the solutions for electric potential into an expression for charge conservation and find all relevant electromagnetic quantities in the rotor half-space. The electric field is simply the negative gradient of the scalar potentials that have been formulated above, and the materials used to construct the electric induction micromachine are linear and isotropic, so

$$\hat{D} = \varepsilon \hat{E} = -\varepsilon \nabla \hat{\phi} . \quad 2.7$$

Next, by expressing the free surface charge density as

$$\hat{\rho} = \hat{z} \bullet (\hat{D}_g - \hat{D}_{ri}) , \quad 2.8$$

it is straight-forward to apply charge conservation at the interface of the air gap and rotor insulator; recall that the rotor conductor is of insignificant thickness.

Charge conservation at the rotor conductor is expressed as

$$\left(\frac{\partial}{\partial t} + U\frac{\partial}{\partial y}\right) \hat{\rho}_{rc} + \frac{\partial}{\partial y} \sigma_{rcs} \hat{E}_{riy} + \sigma_{ri} \frac{\partial \hat{\phi}_{ri}}{\partial z}\bigg|_{z=-G^-} = 0 . \quad 2.9$$

where $\hat{\rho}_{rc}$ is the amplitude of the traveling wave of free surface charge on the rotor, and $\sigma_{rcs} = \delta_{rc}$-$\sigma_{rc}$ and σ_{ri} are the rotor sheet conductivity and rotor insulator conductivity, respectively. The first term in Equation 2.9 accounts for charge convection, the second term accounts for lateral conduction through the rotor conductor, and the last term accounts for charge conduction through the volume of the rotor insulator.

Substitution of the potential solutions into Equation 2.9 via Equations 2.8 and 2.7, with rearrangement of terms leads to

$$\frac{1}{\omega}\left[k\sigma_{rcs}+\sigma_{ri}\frac{\cosh(k\Delta_{ri})}{\sinh(k\Delta_{ri})}\right]\hat{\Phi}_{ri} = \tag{2.10}$$

$$\frac{[\omega-kU]}{\omega}\left\{\frac{\varepsilon_g}{\sinh(kG)}\hat{V}_s-\left[\varepsilon_g\frac{\cosh(kG)}{\sinh(kG)}+\varepsilon_{ri}\frac{\cosh(k\Delta_{ri})}{\sinh(k\Delta_{ri})}\right]\hat{\Phi}_{ri}\right\}.$$

This equation may be solved for the rotor potential $\hat{\Phi}_{ri}$ and simplified to yield

$$\hat{\Phi}_{ri} = \beta\cdot\frac{j\tau_R\omega S}{1+j\tau_R\omega S}\cdot\hat{V}_s = \beta\left[j-\Gamma\right]\cdot\frac{\Gamma}{1+\Gamma^2}\cdot\hat{V}_s, \tag{2.11}$$

where

$$S\equiv\frac{\omega_e-kU}{\omega_e}, \tag{2.12}$$

$$\tau_R\equiv\frac{\varepsilon_{eff}}{\sigma_{eff}} = \varepsilon_{eff}\rho_{eff}, \tag{2.13}$$

$$\varepsilon_{eff} = \varepsilon_g\frac{\cosh(kG)}{\sinh(kG)}+\varepsilon_{ri}\frac{\cosh(k\Delta_{ri})}{\sinh(k\Delta_{ri})}, \tag{2.14}$$

and

$$\sigma_{eff} = k\sigma_{rcs}+\sigma_{ri}\frac{\cosh(k\Delta_{ri})}{\sinh(k\Delta_{ri})}. \tag{2.15}$$

Analysis of the Rotor Potential Solution

The parameters in Equation 2.11 have been grouped into definitions that are inspired by physical phenomena. First, τ_R is the equivalent charge relaxation time of the entire rotor half-space shown in Figure 2.2, and ε_{eff} and σ_{eff} are the effective conductivity and the effective permittivity, respectively, of that half-space. Recall that ω_e is simply the electrical excitation frequency. Second, the slip S in Equation 2.11 is a normalized measure of the relative speed by which the rotor potential and free charge waves "slip" through the rotor. In other words, the slip is the phase velocity of these waves relative to the rotor, expressed as a fraction of their phase velocity.

Slip is most descriptive when compared to the time relaxation constant of the rotor. In addition to the fact that positive slip indicates motoring operation for positive rotor velocities, and negative

slip indicates generating operation, there is a torque-optimizing value for the magnitude of the slip. First, slip time is defined here as

$$\tau_S \equiv \frac{1}{\omega_e S}. \tag{2.16}$$

This is the time it takes for the induced rotor surface potential wave to travel $1/2\pi$ of one wavelength through the rotor, parallel to the rotor velocity. The ratio of the slip time, a mechanical measure, and the rotor charge relaxation time, an electrical measure, will be called the rotor time ratio and is defined as

$$\Gamma \equiv \frac{\tau_R}{\tau_S} = \tau_R \omega_e S. \tag{2.17}$$

It will be seen in Section 2.1.2 and Section 3.2.3 that torque from an electric induction machine, all other parameters held constant, is maximized when the absolute value of rotor time ratio is unity. This is true during both generating operation and motoring operation. Thus consideration of the rotor time ratio is at the heart of any electric induction machine design process.

The remaining term in Equation 2.11

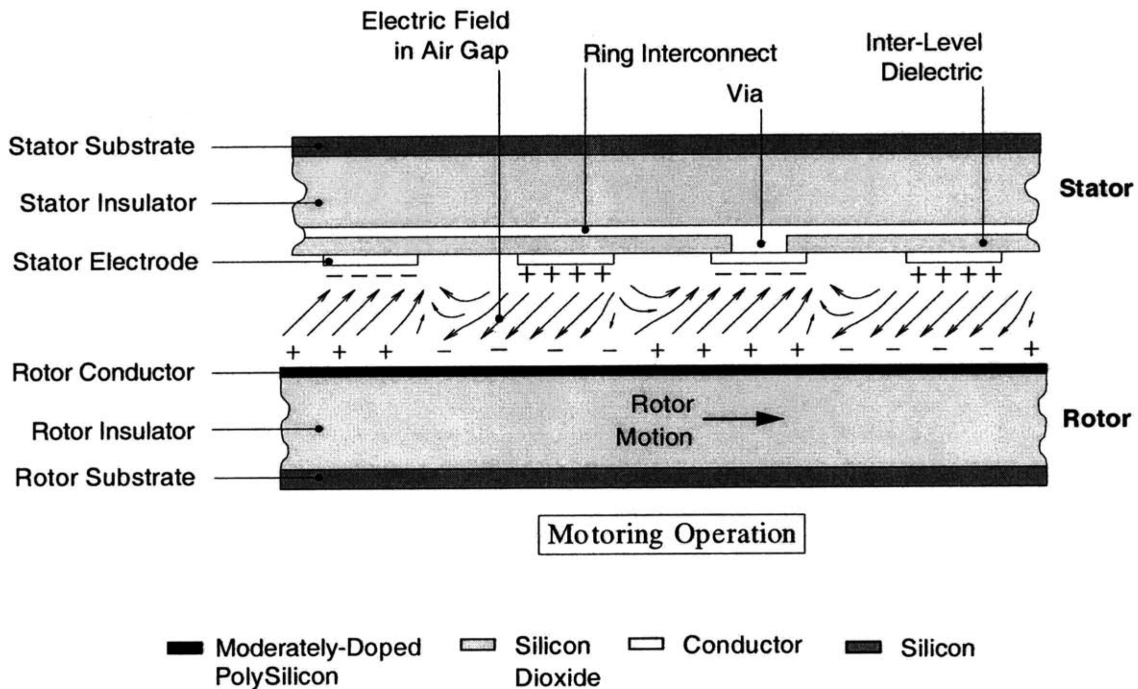

Figure 2.3: Illustration of the electric field in the air gap of the electric induction micromachine. Ideally, the electrodes would be made very small and large in number with independent potentials to describe a smoothly varying potential wave. The actual machine is also poly-phase.

$$\beta = \frac{\frac{\varepsilon_g}{\sinh(kG)}}{\varepsilon_{eff}} \quad 2.18$$

captures the limiting effects of shunting capacitance that exists in parallel with the rotor conductance. With the help of a lumped-parameter equivalent circuit model to be derived later in this chapter, Chapter 3 will show that this term describes a capacitance divider between the gap capacitance and the capacitance of the rotor. The various ways in which this term affects performance though machine torque will be described in detail.

This section has analyzed the electric potential and free charge in the rotor and air gap of a rectilinear electric induction machine, and has interpreted the potential to guide a designer toward a powerful and efficient machine. Section Section 2.1.3 will show that the resulting 2D potentials can be transformed into a 3D model that is adequate for most design purposes, including those of this thesis. First, the next section will show how the potentials are used to derive the performance metrics of torque and pull-in force.

2.1.2 Forces of Electromagnetic Origin

This section uses the electromagnetic stress tensor [75] to determine the electromagnetic forces that act on the surface of the rotor through the charges that reside there. Chapter 3 will show that the magnitudes of these forces are strongly related to the induced rotor surface potential as defined above and have particularly noteworthy dependencies on the rotor time ratio Γ and on β.

Fields and Forces from the 2D Single-Harmonic Model

Expressions for the electric fields in the air gap and in the rotor insulator may be obtained from the potentials and used to determine the force on the rotor. The force on any body due to electromagnetic fields is conveniently expressed using the electromagnetic stress tensor. The electromagnetic stress tensor is defined in terms of the electric fields and the permittivity of the material surrounding the body as

$$T_{mn} = \varepsilon E_m E_n - \frac{\varepsilon}{2}\delta_{mn}\sum_k E_k E_k \quad 2.19$$

where m and n each refer to the coordinate x, y or z, and k is indexed over all coordinates. To find the force per unit area acting on the rotor, the stress tensor must be integrated over a closed surface that includes that area and surrounds the rotor. A 2D cross-section of this closed surface, surrounding a single-wavelength section of the 2D rotor, is shown in Figure 2.4. The corresponding integral may be divided into six pieces, one for each face of S, to simplify the analysis. The contributions from

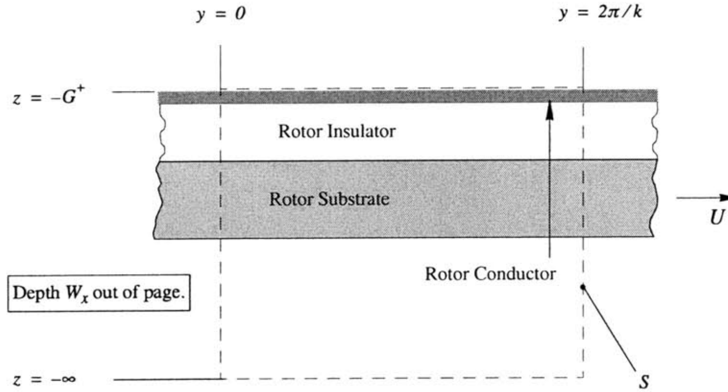

Figure 2.4: Cross-section of the closed surface surrounding the rotor of the 2D single-harmonic model over which the electromagnetic stress tensor is evaluated to find the force on a single wavelength unit cell of the rotor.

the two faces at $x = 0$ and $x = W_x$ cancel because the fields do not depend on x and the normals to these faces are oppositely directed. Similarly, the contributions from the two faces at $y = 0$ and $y = {}^{2\pi}/_{k}$ cancel because the fields are periodic in ${}^{2\pi}/_{k}$ and the normals to these faces are again oppositely directed. This is the reason for choosing a volume of length ${}^{2\pi}/_{k}$ to obtain average forces. Finally, integration over the face at $z = -\infty$ yields zero contribution since all fields decay to zero as $z \to -\infty$. In fact, for this type of machine fields below Δ_{ri} vanish as described in electromagnetic analysis of Section 2.1.1. The only remaining surface over which a net integration contribution is obtained is the face at $z = -G^+$. When this final piece of the integral is evaluated, it is found that the total force on the single wavelength section of the rotor has only the two components

$$F_y = \int_0^{\frac{2\pi}{k}} \int_0^{W_x} \varepsilon_g \left[E_y E_z \right] \Big|_{z = -G^+} dy dx \qquad 2.20$$

and

$$F_z = \int_0^{\frac{2\pi}{k}} \int_0^{W_x} \frac{\varepsilon_g}{2} \left[E_z E_z - E_y E_y \right] \Big|_{z = -G^+} dy dx . \qquad 2.21$$

Note that the stress tensor is a real quantity, and that the electric fields in Equations 2.20 and 2.21 are real quantities. Since the analysis to this point has been carried out in complex space, the fields obtained from the potential descriptions in Equations 2.4 and 2.6 must be converted from complex space to real space. Thus, for example,

$$E_y E_z = \Re\left\{\tilde{E}_y e^{j(ky - \omega t)}\right\}\Re\left\{\tilde{E}_z e^{j(ky - \omega t)}\right\} \tag{2.22}$$

in which the definitions

$$\tilde{E}_y = \frac{\hat{E}_y}{e^{j(ky - \omega t)}} \quad \text{and} \quad \tilde{E}_x = \frac{\hat{E}_x}{e^{j(ky - \omega t)}} \tag{2.23}$$

have been made to make the following integrals less cumbersome. Since $\tilde{E}_y$ and $\tilde{E}_z$ have no y-coordinate or time dependence, through purely algebraic manipulation Equations 2.20 and 2.21 become

$$F_y = \int_0^{\frac{2\pi}{k}} \int_0^{W_x} \frac{\varepsilon_g}{2}\Re\left\{\tilde{E}_y^* \tilde{E}_z\right\}\Bigg|_{z = -G^+} dy dx \tag{2.24}$$

$$F_z = \int_0^{\frac{2\pi}{k}} \int_0^{W_x} \frac{\varepsilon_g}{4}\Re\left\{\tilde{E}_z^* \tilde{E}_z - \tilde{E}_y^* \tilde{E}_y\right\}\Bigg|_{z = -G^+} dy dx \tag{2.25}$$

$$. \tag{2.26}$$

Further, since $\tilde{E}_y$ and $\tilde{E}_z$ are independent of the x-coordinate, the y-coordinate and time, the space and time averaged forces per unit area are defined as

$$f_y = \frac{F_y}{\left(\int_0^{\frac{2\pi}{k}} \int_0^{W_x} dy dx\right)} = \frac{\varepsilon_g}{2}\Re\left\{\tilde{E}_y^* \tilde{E}_z\right\}\Bigg|_{z = -G^+} \tag{2.27}$$

and similarly

$$f_z = \frac{\varepsilon_g}{4}\left[\Re\left\{\tilde{E}_z^* \tilde{E}_z\right\} - \Re\left\{\tilde{E}_y^* \tilde{E}_y\right\}\right]\Bigg|_{z = -G^+} . \tag{2.28}$$

Finally, inserting the potentials of Equations 2.4 and 2.6, the average force densities from the 2D single-harmonic model are summarized as the tangential force per unit area

$$f_y = \frac{\beta \varepsilon_g k^2 |\hat{V}_s|^2}{2\sinh(kG)} \cdot \frac{\Gamma}{1 + \Gamma^2} . \tag{2.29}$$

and the normal force per unit area

$$f_z = \varepsilon_g \left[\frac{k|\hat{V}_s|}{2\sinh(kG)} \right]^2 \cdot \frac{1 + \Gamma^2 \left[\beta^2 - 2\beta\cosh(kG) + 1 \right]}{1 + \Gamma^2} . \qquad 2.30$$

2.1.3 The 3D Single-Harmonic Model

Since this thesis discusses the development of disk-shaped rotating machines, a 3D model will yield a more accurate description of their electromechanics. This section will describe a practical, computationally-fast 3D model.

A fully 3D model, for example one derived in a cylindrical coordinate system, is more computationally expensive than needed in this thesis. The solutions to Laplace's equation in cylindrical coordinates involve integral equations of high-order Bessel functions. In fact, their order matches the number of pole pairs around the stator annulus. Preliminary designs suggest that this number is near 100. The use of high order Bessel functions of this order is extremely time-consuming. Reliable computation and integration may be out of reach without massively parallel computation capabilities [76]. Fortunately, the estimated additional accuracy provided by that solution is not necessary for the purposes of this thesis.

Below, a simple coordinate transformation is used to create a practical 3D model from the 2D rectilinear model described in Section 2.1.1. In effect, this coordinate transformation warps a rectangular strip of the rectilinear electric induction machine such that it closes on itself to form an annulus as suggested in Figure 2.5. The target coordinate system is cylindrical, but since the 2D cartesian solution is used as a starting point there are no Bessel functions involved. The accuracy of the process illustrated in Figure 2.5(c) depends on the degree of curvature needed. A quantitative metric is included to gauge this accuracy.

Coordinate Transformation

Quantitative bounds on the cylindrical coordinate space follow from a mathematical treatment of the mapping process. To begin, recall that the 2D cartesian solution to Laplace's equation is of the form

$$\hat{\phi} \propto e^{\pm jky} e^{\pm kz} \qquad 2.31$$

since sinh and cosh are composed of sums of exponentials. To apply a solution of this form to a cylindrical geometry, it is necessary only to take advantage of the coordinate map shown in the left column of Figure 2.5(d). The solution in cylindrical coordinates is then approximated by

$$\hat{\phi}^* \propto e^{\pm jm\theta} e^{\pm \frac{m}{r} z}. \quad 2.32$$

Within this section only, the superscript * denotes any potential approximation resulting from the mapping. The new parameter m is the number of pole pairs, or angular wavenumber. It is the number of whole wavelengths described by the potential wave around the stator annulus. For example, m is 15 for the wave pictured in Figure 2.5(b). To be consistent with previous work on electric induction machines, m will henceforth be referred to as the *periodicity* of the machine. The same periodicity is characteristic of all fields in any one electric induction machine.

Equation 2.32 will be an appropriate approximation only within a certain range of the cylindrical coordinates r, θ, z. To define this range, $\hat{\phi}^*$ is inserted into the cylindrical coordinate form of Laplace's equation

$$\frac{1}{r}\frac{\partial}{\partial r}\left(r\frac{\partial}{\partial r}\hat{\phi}\right) + \frac{1}{r^2}\frac{\partial^2}{\partial \theta^2}\hat{\phi} + \frac{\partial^2}{\partial z^2}\hat{\phi} = 0 \quad 2.33$$

leading to

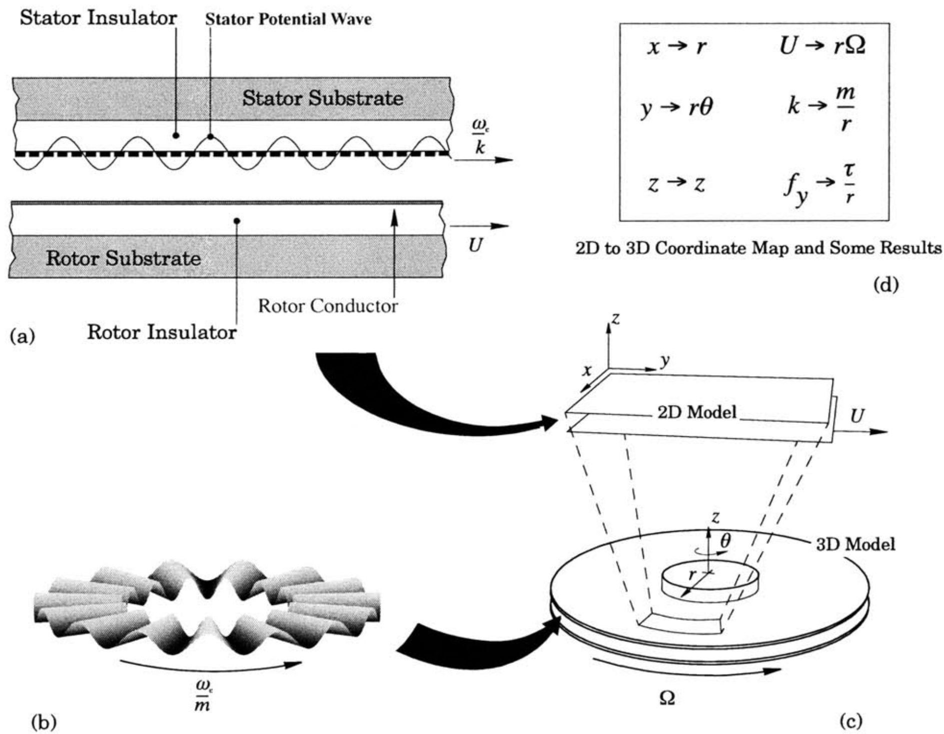

Figure 2.5: The process of mapping the 2D single-harmonic model to a 3D single-harmonic model: (a) a summary of the 2D model, (b) the 3D single-harmonic stator potential wave, (c) depiction of the mapping process, (d) the coordinate and other maps.

$$\frac{1}{r}\frac{\partial}{\partial r}\left(r\frac{\partial}{\partial r}\hat{\phi}^*\right) - \frac{m^2}{r^2}\hat{\phi}^* + \frac{m^2}{r^2}\hat{\phi}^* = 0 \quad 2.34$$

The derivatives with respect to θ and z cancel right away. However, expansion of the first term yields

$$\frac{1}{r}\frac{\partial}{\partial r}\left(r\frac{\partial}{\partial r}\hat{\phi}^*\right) = \frac{mz}{r^3}\hat{\phi}^* + \frac{m^2z^2}{r^4}\hat{\phi}^* \quad 2.35$$

This term cannot be zero for all non-trivial physically significant values of m, z, and r. And since it also depends on the sign of the z coordinate, this term must be insignificant compared to the second and third term if the dominant balance of those two terms is to be preserved, which must happen for the coordinate system approximation to be valid. Therefore in order for a model that is based on the approximation underlying Equation 2.33 to be accurate, energy stored in the fields must be significant only in regions that satisfy

$$\frac{mz}{r^3}, \frac{m^2z^2}{r^4} \ll \frac{m^2}{r^2}, \quad 2.36$$

leading to the two conditions

$$\begin{bmatrix} z \ll mr \\ z \ll r \end{bmatrix}. \quad 2.37$$

Since m will not be less than unity, the second condition is most demanding. This is easily satisfied by all preliminary designs, which have minimum radii on the order of a millimeter and fields that vanish within 100 μm in the z–coordinate direction, even when those fields are not limited by the relatively conductive substrate layers. Thus, from here on $\hat{\phi}$ will be taken to mean $\hat{\phi}^*$, dropping the superscript * for notational simplicity.

Transformed Solutions

For future reference, the transformed electric potential solutions are summarized below. These describe the potentials in what is henceforth referred to as the 3D single-harmonic model. The electric potentials expressed by Equations 2.4 and 2.6 become, approximately,

$$\hat{\phi}_g(x, y, z, t) = \frac{\hat{V}_s \sinh\left[\frac{m}{r}(z+G)\right] - \hat{\Phi}_{ri}\sinh\left(\frac{m}{r}z\right)}{\sinh\left(\frac{m}{r}G\right)} e^{j(m\theta - \omega_e t)} \quad 2.38$$

and

$$\hat{\phi}_{ri}(x, y, z, y) = \frac{\hat{\Phi}_{ri}\sinh\left[\frac{m}{r}(z + G + \Delta_{ri})\right]}{\sinh\left(\frac{m}{r}\Delta_{ri}\right)} e^{j(m\theta - \omega_e t)}. \quad 2.39$$

In a similar fashion, the expression for the rotor potential $\hat{\Phi}_{ri}$ must also be modified to

$$\hat{\Phi}_{ri} = \beta(r) \cdot \frac{j\Gamma(r)}{1 + j\Gamma(r)} \cdot \hat{V}_s = \beta(r)\left[j - \Gamma(r)\right] \cdot \frac{\Gamma(r)}{1 + \Gamma^2(r)} \cdot \hat{V}_s \quad 2.40$$

in which

$$\Gamma \equiv \frac{\tau_R(r)}{\tau_S} = \tau_R(r)\omega_e S, \quad 2.41$$

$$\beta(r) = \frac{\varepsilon_g(r)}{\varepsilon_{eff}(r)\sinh\left(\frac{m}{r}G\right)}, \quad 2.42$$

$$S = \frac{\omega_e - m\Omega}{\omega_e}, \quad 2.43$$

and Ω is the rotor rotational speed. Notice that the relaxation time is now dependent on the radius as

$$\tau_R(r) \equiv \frac{\varepsilon_{eff}(r)}{\sigma_{eff}(r)} = \frac{\varepsilon_g \frac{\cosh\left(\frac{m}{r}G\right)}{\sinh\left(\frac{m}{r}G\right)} + \varepsilon_{ri} \frac{\cosh\left(\frac{m}{r}\Delta_{ri}\right)}{\sinh\left(\frac{m}{r}\Delta_{ri}\right)}}{\frac{m}{r}\sigma_{rcs} + \sigma_{ri} \frac{\cosh\left(\frac{m}{r}\Delta_{ri}\right)}{\sinh\left(\frac{m}{r}\Delta_{ri}\right)}}. \quad 2.44$$

Force and Torque from the 3D Single-Harmonic Model

Force expressions for the 3D single-harmonic model are nearly identical to those from the 2D single-harmonic model. Nevertheless, for reference these expressions are included below. The force density in the azimuthal direction is

$$f_\theta = \frac{\beta(r)\varepsilon_g m^2 |\hat{V}_s|^2}{2r^2 \sinh\left(\frac{m}{r}G\right)} \cdot \frac{\Gamma(r)}{1 + \Gamma(r)^2} \quad 2.45$$

and that in the axial direction is

$$f_z = \varepsilon_g \left[\frac{m|\hat{V}_s|}{2r\sinh(kG)} \right]^2 \cdot \frac{1 + \Gamma^2(r)\left[\beta^2(r) - 2\beta(r)\cosh(kG) + 1 \right]}{1 + \Gamma(r)^2} \quad 2.46$$

Torque is then obtained by integrating the product of the azimuthal force density f_θ at the rotor conductor with a lever arm that extends from the center of rotation to the differential area, over the surface of the rotor conductor. This results in

$$\tau = \varepsilon_g \pi |\hat{V}_s|^2 \int_{r_i}^{r_o} \left\{ \frac{\Gamma(r)}{1 + \Gamma(r)^2} \cdot \beta(r) \cdot \frac{m^2}{\sinh\left(\frac{m}{r}G\right)} \right\} dr \,. \quad 2.47$$

Likewise, total pull-in force F_{pi} is defined as

$$F_{pi} = \varepsilon_g \pi \frac{|\hat{V}_s|^2}{2} \cdot \int_{r_i}^{r_o} \left\{ \frac{1 + \Gamma^2(r)\left[\beta^2(r) - 2\beta(r)\cosh(kG) + 1 \right]}{1 + \Gamma(r)^2} \cdot \frac{m^2}{r\sinh^2\left(\frac{m}{r}G\right)} \right\} dr \,. \quad 2.48$$

Following this, the mechanical shaft power supplied by the machine to a load, such as the compressor in a microengine during start-up, is

$$P_m = \Omega\tau = \varepsilon_g \pi \Omega |\hat{V}_s|^2 \int_{r_i}^{r_o} \left\{ \frac{\Gamma(r)}{1 + \Gamma(r)^2} \cdot \beta(r) \cdot \frac{m^2}{\sinh\left(\frac{m}{r}G\right)} \right\} dr \quad 2.49$$

2.1.4 The 3D Multiple-Harmonic Model

In practice, a perfect sinusoid cannot be excited around the stator annulus, thus the 3D single-harmonic model must be modified to account for this. A practical electric induction machine will have a small number of electrodes for each spatial wavelength of the stator potential wave, thus the wave will look more like a staircase function than a sine wave. This will create higher spatial harmonics which may be important [31]. The 3D multiple-harmonic model uses Fourier decomposition of the actual wave and superposition of the higher harmonic solutions to generate a model which more accurately predicts the performance of an electric induction machine.

The single-harmonic models obtain their name from the fact that the potential wave excited on the stator is spatially sinusoidal in shape. The excitation of such a wave would require an infinite number of electrodes, including an infinite number of connections to those electrodes. However, an infinite number of electrodes is obviously impractical, and it is shown in Section 3.2.1 that even an aggressive design of the stator and its electronics will not approach the excitation of a perfect sine wave. The number of electrodes will be less than ten per wavelength, in fact preliminary designs call for only 2, 3 or 6 electrodes per wavelength.

Because of the small number of electrodes per wavelength, the actual potential wave is nearly step-wise discontinuous around the stator annulus. With a finite number of electrodes that have insulating space between them, the potential is constant across the surface of each electrode and follows a smoothly varying function across the insulating space between one electrode and the next. As an example, Figure 2.6 shows how the cycle generally describes a discretely sampled sine function. On each of the electrodes the potential oscillates sinusoidally in time with neighboring electrodes being out of phase by a balanced amount, so on average the wave in Figure 2.6 will move around the annulus, though its exact shape will vary somewhat as it moves.

The number of electrodes per wavelength is defined here as the number of phases N_p of the machine. Since the periodicity m gives the number of wavelengths enforced around the entire circumference of the stator, the total number of electrodes is given by

$$N_e = N_p m . \qquad 2.50$$

In order to better model the actual stator potential wave described above, the 3D multiple-harmonic model exploits the linear nature of Laplace's equation and uses Fourier superposition to sum the results of several 3D single-harmonic model solutions, each of which are characterized by a dif-

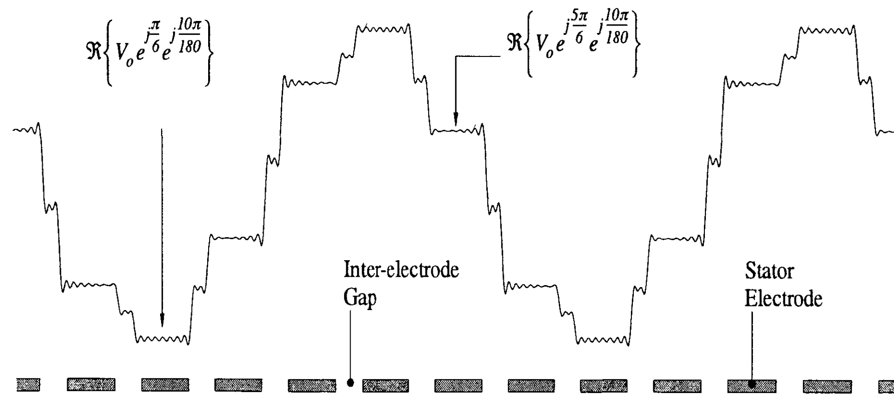

Figure 2.6: Two spatial wavelengths of the stator potential at an instant in time, at a particular radius. Here the potential across each inter-electrode gap is assumed to be the average of the electrode potentials on either side of the gap.

ferent spatial frequency. The step-wise discontinuous wave can be perfectly described by an infinite sum of forward- and backward-travelling harmonics. However, due to the nature of induction machine electromechanics, most harmonics contribute very little to the total torque near the synchronous speed of the fundamental. Thus very good results can be obtained using one single-harmonic model based on only the fundamental spatial harmonic. However, to accurately model a general situation that may include various numbers and shapes of electrodes per wavelength, various electrode thicknesses, or to include the effects of different potential functions between the electrodes, all harmonics should be considered.

Fourier Decomposition of the Stator Potential Wave

The 3D multiple-harmonic model uses Fourier decomposition and recombination to account for the discretely varying nature of the stator wave, like the one exemplified in Figure 2.6, that is enforced on the stator by a finite number of stator electrodes, like those illustrated in Figure 2.1. The assumed step-wise discontinuous stator potential function is first decomposed into its spatial harmonics. Each harmonic is characterized by a period, amplitude, and a phase. A limited number N_f of the Fourier harmonics are then summed at each point in space to yield the approximate stator wave shown in Figure 2.6. The Fourier weights are complex numbers because they contain temporal information, the temporal phase shift between neighboring electrodes, as well as spatial information. The figure plots the real part of the wave at an instant in time.

For a time-varying solution, even in steady state, it is a complicated and time-consuming operation to fully describe the spatial variation of the potential across the inter-electrode insulator. The potential across the inter-electrode insulator will assume a function which depends greatly on the thickness of the electrodes, the condition of the insulator surface, as well as the potentials of nearby materials. For electrodes which are thicker than the width of the inter-electrode insulator when the insulator is clean and smooth, this function will be very nearly linear since the electrode side-walls form a parallel-plate capacitor. The function will be similar for very thin electrodes with a dirty or moist insulator in between them. The insulator forms a resistor between the electrodes, and in general this situation should be avoided since the resistance cannot be easily included in the distributed models like those above. However, the situation could arise if the stator insulator becomes contaminated with adsorbed combustion products, dust particles or moisture.

If the surface is clean and the electrodes are thin compared to the inter-electrode gap, the potential function across the inter-electrode insulator will be difficult to describe for most states of machine operation. Specifically, if neighboring electrodes are further apart than they are thick, the function will begin at the potential of one electrode and then follow a hyperbolic sine to the average potential of the two neighboring electrodes at the middle of the inter-electrode insulator. Nearing the next electrode, the function will then follow another hyperbolic sine shape to the potential of that

electrode and extent of the hyperbolic sine shape depends upon the thickness of the electrode to first order. If the inter-electrode insulator is several times wider than the electrodes are thick, then it will be easier to neglect the extent of the hyperbolic function and the potential across the insulator can be approximated as the average of the two neighboring electrodes.

As a further complication, if there is a ground plane or some other fixed potential region in the vicinity of the electrodes, the potential function across the inter-electrode insulator could be pulled down toward that fixed potential, near the middle of the insulator. To compare three possible situations, the two extremes and a more likely case, the effects on maximum torque of three different potential functions across the inter-electrode insulator—a linear potential, a zero potential, and an average potential—are described in Appendix A. The appendix shows that the best case, in terms of torque output, is the linear case, and that the zero-potential case would be severely limiting. Throughout this thesis, the average potential will be assumed.

An example of this wave is shown in Figure 2.6, plotting the real part of the potential at a time of $\omega_e t = {}^{10\pi}/_{180}$. In the simulations, the potential is described as a complex number to account for the 60° temporal phase shift between neighboring electrodes.

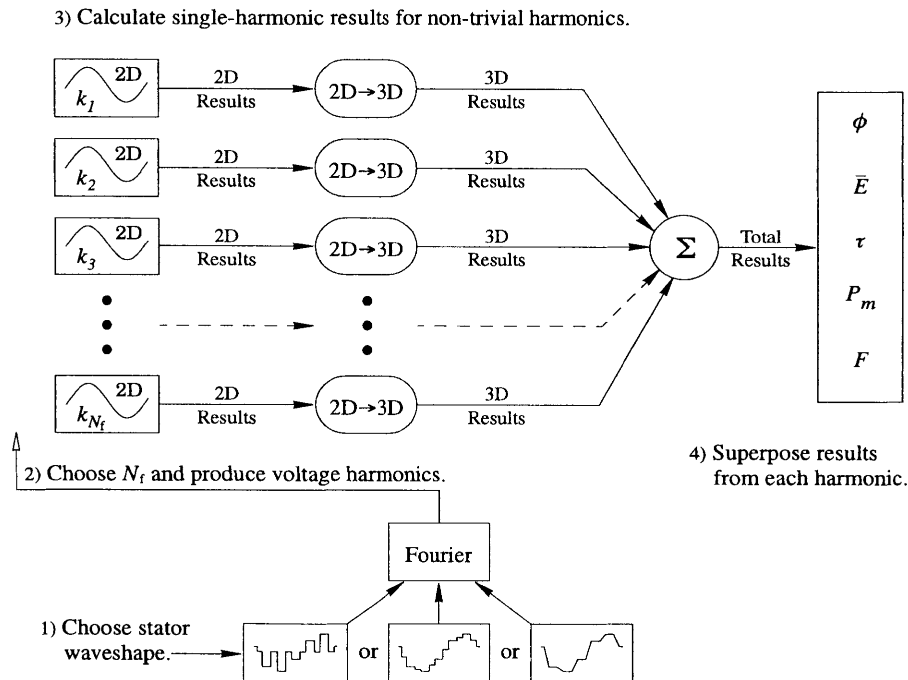

Figure 2.7: This picture shows the manner by which the 3D multiple-harmonic model uses the harmonic content of the discretely sampled stator wave to find the total electric potential, fields, torque, mechanical power and pull-in force as sums of 3D single-harmonic models that were transformed from 2D single-harmonic models.

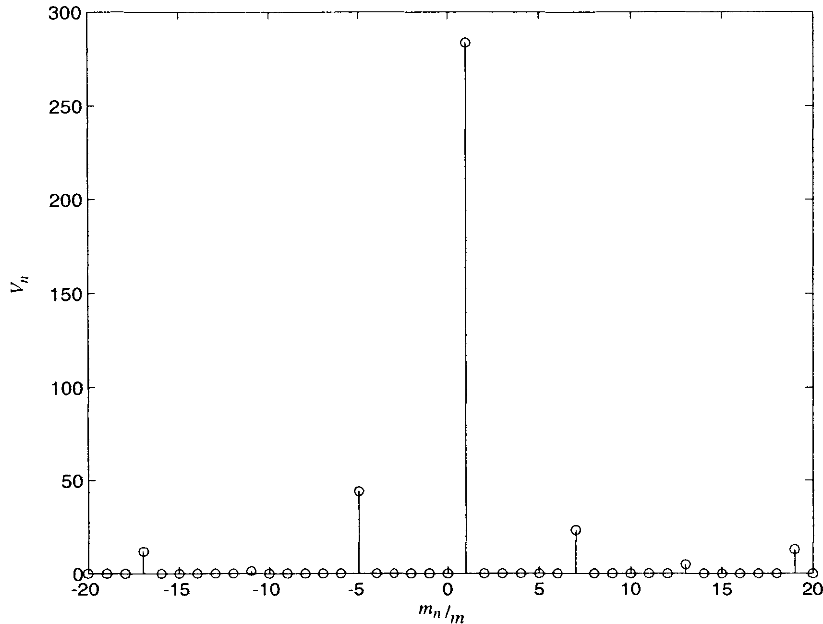

Figure 2.8: The magnitude of the complex-valued potential harmonics which make up the wave in Figure 2.6 given a 300 V amplitude. The ordinate shows the index of each harmonic as the harmonic periodicity m_n divided by the fundamental periodicity m.

Fourier Recombination of Single-Harmonic Solutions

Since Laplace's equation is a linear partial differential equation, each harmonic of the stator potential wave produces a linearly independent electrical response. These responses may be superposed to find the total electric potential, field and charge within the machine due to the total stator potential wave. Further, since the torque produced by the machine is an integrated product of electric field and charge, both of which are assembled from orthogonal Fourier components, the torque from the individual Fourier components may also be superposed to find the total torque. The process is described schematically in Figure 2.7.

First the stator potential wave is decomposed into an appropriate number of Fourier harmonics. Then, for each non-zero harmonic, a 2D single-harmonic electric potential and field solution is transformed to a 3D single-harmonic solution as described in Section 2.1.3 to determine the transformed electric potential and fields. Finally, to yield a 3D multiple-harmonic model, the contributions from each harmonic are summed to yield the total electric potential and electric field. Since torque, pull-in force, and power involve integrations of the electric field solutions throughout the volume of the device, these are also computed individually for each harmonic. The results are again summed, yielding the total torque, pull-in force and power

Fortunately, only a small amount of the total harmonic content need be included in the 3D multiple-harmonic model. Under the condition of maximized torque, only the fundamental harmonic contributes significantly to the sum. Figure 2.8 plots example potential harmonic magnitudes. Note that the magnitudes of the higher and lower harmonics are small fractions of the fundamental harmonic magnitude. Torque and power are proportional to the square of the stator potential, so the contribution from these harmonics is an even smaller fraction of the torque and power from the fundamental. Relative to the single-harmonic models, the 3D multiple-harmonic model is time-consuming to compute, thus it is often useful to take advantage of the dominance of the fundamental and explore the design space using results of a 3D single-harmonic analysis with only the fundamental harmonic of the stator potential wave.

Although torque scales with the square of the fundamental potential magnitude, an increase in the fundamental is not necessarily beneficial from a system point of view. For example, one way of increasing the magnitude of the fundamental is to increase the number of phases, thus providing a better approximation of the sine wave intended to be enforced around the stator. But design studies in Chapter 3 will show that due to space constraints that limit the total number of electrodes, this would require a decrease in the periodicity. Section 2.1.4 above also shows this. This decrease in periodicity reduces torque significantly. Chapter 3 will also show that increasing the complexity of inter-phase connections would cause more ohmic losses and decrease the system efficiency. These two points show that, depending on whether the performance metric is torque and power or system efficiency, the design choices will be different.

2.2 An Equivalent-Circuit Motor Model

To determine the terminal characteristics of the electric induction machine, an equivalent-circuit rotor model is most appropriate. For system design, it is generally not necessary to know the potential distribution at every point as described in the last section. Terminal characteristics are much more relevant, which are represented by an equivalent-circuit model of the rotor and air gap developed here. This equivalent-circuit rotor model will later be combined with an equivalent-circuit model of the stator and with a circuit model of the power electronics to produce a system-level model of the micromachine and its drive. To a good approximation, torque, power, efficiency and terminal behavior can all be described by such an equivalent-circuit model, suitably distilled from the 2D single-harmonic model of the rotor and air gap. This is because of the dominance of the fundamental harmonic observed in Figure 2.8.

There are at least two possible equivalent-circuit model representations of the rotor. One consists of a simple network of capacitors and resistors that represent different portions of the rotor half-space. The other consists of an admittance element that performs a similar function but is not

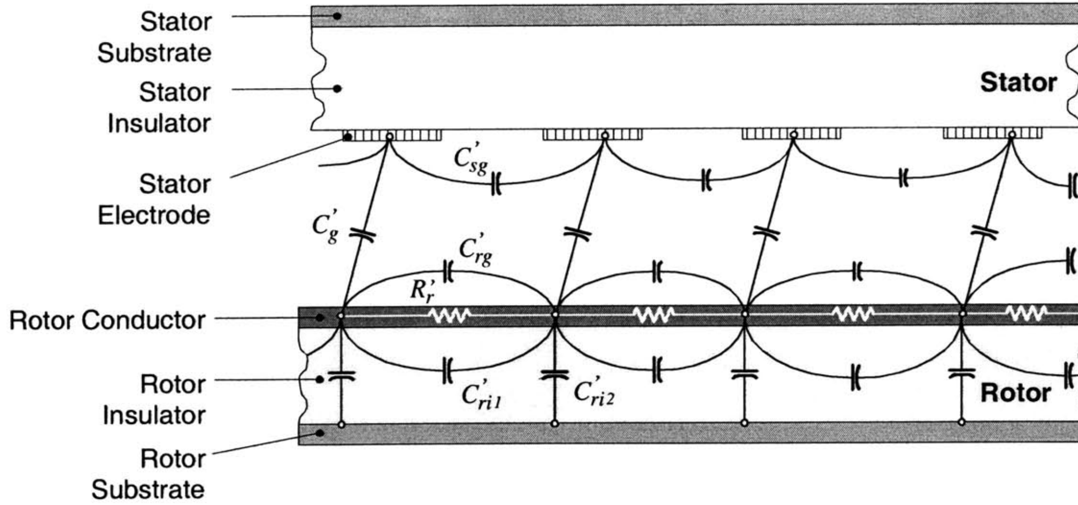

Figure 2.9: Cross section of the rotor half-space with overlaid lumped-parameter circuit elements for only the rotor half-space.

limited by containing only resistors and capacitors, instead it contains a general transfer function between terminal voltage and terminal current.

If only precise terminal characteristics are desired, the admittance element provides the most direct description of the rotor. It uses a transfer function that must be calculated numerically to determine the unknown current flowing into the positive terminal of the element, for a single phase of the micromachine, from the known voltage across the device terminals. The current is found in terms of the terminal voltage of the induction machine by using Gauss' law to integrate the stator surface charge over the width of one electrode, thus accounting for the charge flow into only one phase of the device. For simplicity, the inter-electrode gap is decreased to zero in this model. Furthermore, the charge summation includes only the fundamental of the stator charge wave. The transfer function representing the admittance of one phase of the micromachine is then obtained by taking the time derivative of the charge integral and dividing by the fundamental stator potential harmonic. The second dimension of the integral, the radius, must be integrated numerically to allow for the parameter dependencies on radius, yielding the admittance expression for a single phase of the electrostatic induction micromachine

$$\hat{Y}_T = 2mj\omega_e \varepsilon_g \int_{r_i}^{r_o} W_1(r) \frac{\left[\cosh\left(\frac{m}{r}G\right) \sinh\left(\frac{m}{r}G\right) - \beta(r) \frac{j\Gamma(r)}{1 + j\Gamma(r)} \right]}{\left[\sinh\left(\frac{m}{r}G\right) \right]^2} dr \,. \qquad 2.51$$

For zero inter-electrode gap, the factor $W_1(r)$ simplifies to

$$W_1^o = \frac{N_p}{\pi}\left[\sin\left(\frac{\pi}{N_p}\right)\right]^2. \qquad 2.52$$

It accounts for the width of the electrodes and results from the azimuthal integration of charge over one electrode and the fourier weighting of the fundamental stator potential harmonic.

Because of the admittance must be calculated numerically, an admittance element cannot readily be used in circuit analysis packages such as PSPICE, although it is not impossible to do so. Nevertheless, it can be easily analyzed by a more versatile mathematical analysis package such as MatLab™. In fact, most analyses conducted in this thesis are carried out in MatLab.

As an alternative to the admittance element, an equivalent-circuit model can be more intuitive visually and also very useful in developing external drive circuitry. A series equivalent is useful for initial sizing of drive inductors in resonant drive schemes, while individual element values are useful in setting initial targets for parasitic capacitances and resistances.

As an aid to visualizing the form of the equivalent-circuit model, the rotor half-space (see Figure 2.2) is divided into sub-regions based on the fundamental sine-wave potential distribution on the stator and redrawn in Figure 2.9. Equivalent capacitances and resistances, denoted with primes, can be defined for each wavelength-wide sub-region around the micromachine annulus. Noting that all of the sub-regions are arranged in parallel by definition, they can be combined to form the circuit model shown in Figure 2.10. The values of each element in this circuit are then derived by fitting the terminal admittance of the circuit

$$\hat{Y}_T = j\omega_e C_g \frac{1 + j\omega_e SR_r C_r}{1 + j\omega_e SR_r C_r + j\omega_e SR_r C_g} + j\omega_e C_{sg} \qquad 2.53$$

to the terminal admittance of Equation 2.51 when simplifying assumptions are made. Namely, the electrodes are approximated as rectangles of length $L_e = r_o - r_i$ with properties sampled at a reference radius of $r_c = {}^{5r_o}/_6$ — the centroidal location of the torque density since f_y varies only slightly over

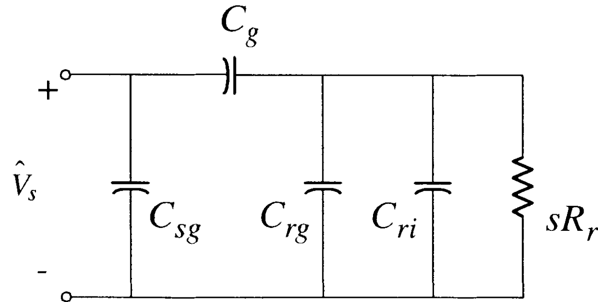

Figure 2.10: Equivalent lumped-parameter rotor circuit model with elements defined.

the rotor surface — and all curved parentheses indicate functional dependencies. Thus, the integral in Equation 2.51 is evaluated to yield

$$\hat{Y}_T = \frac{2j\omega_e W_1(r_c) m\varepsilon_g L_e}{\left[\sinh\left(\frac{m}{r_c}G\right) \right]^2} \cdot \left[\cosh\left(\frac{m}{r_c}G\right) \sinh\left(\frac{m}{r_c}G\right) - \beta(r_c)\frac{j\Gamma(r_c)}{1+j\Gamma(r_c)} \right] \quad . \qquad 2.54$$

This expression is then matched to Equation 2.53, yielding the values of the equivalent-circuit elements

$$C_g = 2W_1(r_c)L_e m \frac{\varepsilon_g}{\sinh\left(\frac{m}{r_c}G\right)} \qquad 2.55$$

$$C_{sg} = 2W_1(r_c)L_e m \frac{\varepsilon_g\left[\cosh\left(\frac{m}{r_c}G\right) - 1 \right]}{\cosh\left(\frac{m}{r_c}G\right) \sinh\left(\frac{m}{r_c}G\right)} \qquad 2.56$$

$$C_r = C_{rg} + C_{ri} = 2W_1(r_c)L_e m \cdot \qquad 2.57$$

$$\left[\varepsilon_g \frac{\left[\cosh\left(\frac{m}{r_c}G\right) - 1 \right]}{\sinh\left(\frac{m}{r_c}G\right)} + \varepsilon_{ri} \frac{\cosh\left(\frac{m}{r_c}\Delta_{ri}\right)}{\sinh\left(\frac{m}{r_c}\Delta_{ri}\right)} \right]$$

$$R_r = \frac{1}{2W_1(r_c)L_e \frac{m^2}{r_c}\sigma_{rcs}} , \qquad 2.58$$

where σ_{rcs} is the sheet conductivity — bulk conductivity times thickness — of the rotor conductor.

The equivalent-circuit model of Figure 2.9 and Figure 2.10 can easily be analyzed as part of a larger circuit using software packages such as PSPICE, or it can be analyzed manually using a program like Matlab™, or within C or FORTRAN code. It is worth noting that, as expected, the form of this circuit is the dual of the much-used equivalent-circuit description for magnetic induction machines [75]. Both rotor models developed above are used, each were appropriate, in Chapter 3 to

analyze and design the electric induction micromachine. They are combined with a circuit-level model of the stator half-space, which is described below.

2.3 An Equivalent-Circuit Stator and Drive Model

Parasitic capacitance and resistance related to the stator structure can significantly decrease the total electrical efficiency of the micromachine and drive electronics. Parasitic capacitive coupling between the stator interconnects and other conductors in the stator causes increased losses due to the finite conductivity of the stator interconnects and due to the conduction and magnetic losses in the inductors of the power electronics. The primary goal of the equivalent-circuit stator model is to describe the parasitic capacitances and resistances, predict losses in the micromachine and in the drive electronics, and enable a design optimization that maximizes the efficiency of the micromachine-drive system. This is accomplished by compacting the distributed parasitic capacitances and resistances of one phase of the electric induction machine into an equivalent circuit, combining this with the equivalent-circuit rotor model, and coupling these with an equivalent circuit of the drive electronics.

2.3.1 Parasitics in the Power Electronic Drive

In order to properly place the discussions of the equivalent-circuit models for the rotor and stator, a model of the power electronic drive is described now, rather than at the end of this section. From left to right, the first two boxes in Figure 2.11 provide a basic model of the series resonant drive electronics. The model describes the major sources of power loss in the electronics: the power dissi-

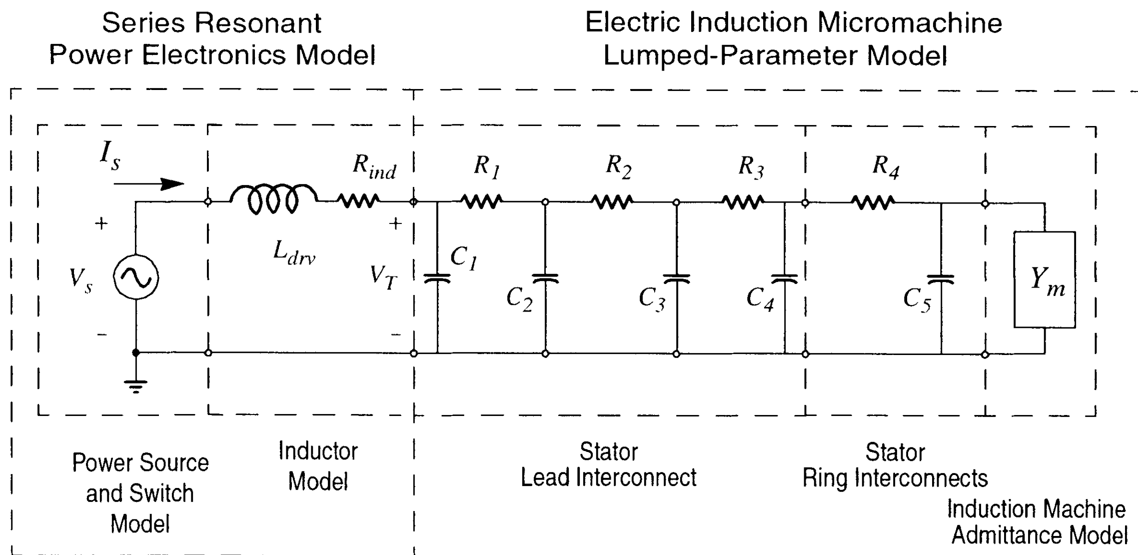

Figure 2.11: The complete lumped-parameter equivalent-circuit stator and rotor models, coupled with a circuit model to represent the series resonant power electronics.

pation in the inductor windings and core. When operating properly, and at the resonant frequency of the total circuit, a series resonant drive is quite well modeled with the AC voltage source shown in the first dashed box and the inductor and resistor shown in the second dashed box in Figure 2.11. The resistor accounts for inductor losses, which can be computed from the inductor quality factor Q_{ind} using the relation

$$R_{ind} = \frac{\omega L_{drv}}{Q_{ind}}. \qquad 2.59$$

The quality factor has been experimentally measured at target voltages for several optimized candidate inductor designs, and those results are used in the analyses and optimizations in Chapter 3.†

2.3.2 Parasitics in an Electric Induction Machine

Parasitics are well modeled by the elements of Figure 2.11, and they come from several sources. The reasons for the exact form of the stator equivalent circuit are described in more detail below. Both parasitic resistance and parasitic capacitance are associated with the stator interconnects. Resistance arises because conductors always have some resistance, however small, and parasitic capacitance arises because the passivation thickness is finite. Capacitive coupling exists between the interconnects and the relatively conducting substrates, as well as between second level interconnects and the electrodes of other phases that are not at the same voltage. The first parasitic capacitances are proportional to the total plan-view areas of corresponding interconnect sections. The latter are proportional to only the intersection of the first and second-level interconnects, but the gap between these two levels is small, making this capacitance dominant in general.

The reactive current drawn by all parasitic capacitances, plus the current delivered to the micromachine, passes through the inductor in the power electronics and through the most of the interconnects. From this viewpoint, it is desirable to narrow the interconnects to reduce the reactive currents and the associated losses. However, the parasitic resistance of each section of the interconnects is inversely proportional to its width, and from this viewpoint it is desirable to widen the interconnect to reduce losses. Thus, there exists a trade-off which must be balanced when designing the stator interconnects to minimize losses. Chapter 3 describes an optimization that minimizes this total power loss using the models developed here and in Section 2.2. The remainder of this section will describe the process used to construct that model.

†. Inductor Q measurements were performed by Dr. Stephen D. Umans using specialized high-frequency magnetic cores.

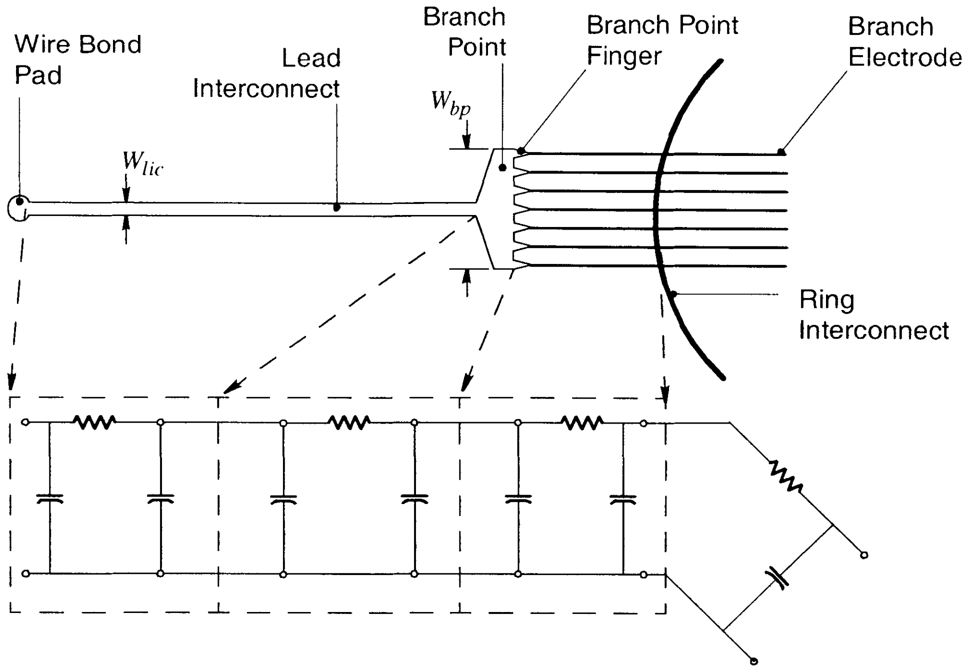

Figure 2.12: Top view, simplified schematic of the power distribution for one phase of the stator and the associated lumped-parameter equivalent circuit model.

2.3.3 Modeling of the Parasitics

The distributed parasitic capacitance and resistance throughout the stator interconnect structure can be lumped into the small set of representative elements shown in Figure 2.12. This figure depicts the origin of the stator equivalent-circuit elements used in Figure 2.11 in more detail, comparing them to a cross section of the interconnects of the stator in order to describe their origin. For the expressions for capacitance and resistance that follow, geometric parameters can be found on this figure and on Figure 2.2, with values listed in Table 3.9.

Note that a major simplification is used to calculate all parasitic capacitances: contributions due to fringing fields are assumed to be negligible. This simplification is warranted because the fringing contribution is small compared to the parallel plate contributions. The preliminary designs call for interconnects which are around ten times as wide as the thickness of the insulation layers between conductors.

As an example, the wire bond pad lies on the same level as the electrodes, so the associated parasitic capacitance is defined as

$$C_{wbp} = \left[\frac{\varepsilon_{si}}{\Delta_{si} + \delta_{ILD} + \delta_{ric}}\right]\pi r_{bp}^2 \quad , \qquad 2.60$$

where Δ_{si} is the stator insulator thickness defined in Figure 2.2, r_{bp} = 250 μm is the pad radius, and G is the air gap length. Also, δ_{ILD} is the thickness of the inter-level dielectric that isolates the electrodes from the phase interconnects, and δ_{ric} is the thickness of the phase interconnects, both shown in Figure 2.3. Chapter 3 describes the design of the device in much more detail, so these thicknesses have more meaning with reference to that chapter. The bond pad essentially contributes no parasitic resistance since it is much wider than any other part of the interconnects, and is current-fed at its center from a large gold-wire ball bond, which spreads the current out before it continues through the remainder of the first-level interconnects.

2.3.4 The Pi-model and the T-model Equivalent Circuits

The lead interconnect is a long thin conductor, a strip-line, separated from the stator substrate, which is a fairly good ground plane. Thus parasitic displacement current from the lead interconnect to the stator substrate is distributed along its length. The sum total of this displacement current is defined as I_d. The lead interconnect is also loaded at its end by the current supplied to the machine I_L. The primary goal of the equivalent circuit model is to adequately account for power dissipation in the conductors of the stator wiring, like the lead interconnect, but an accurate calculation is complicated by the fact that the line-to-ground voltage decreases from one end of the interconnect to the other, meaning that the current flow to the parasitic capacitance is not evenly distributed along the interconnect — it is not linear — and thus not easy to represent mathematically.

However, if the voltage drop along the length of the lead interconnect is neglected, it is straightforward to derive a circuit model that adequately accounts for the power dissipation in the interconnect. To load the power electronics properly, the equivalent circuit model must have the same total capacitance as the strip-line when looking in from the terminals of the equivalent circuit. And to properly account for the power dissipation attributable to the machine load current, the circuit model must include the total resistance of the strip line. The two simplest circuits that accomplish this are the Pi-model and the T-model in Figure 2.13. The power dissipated in the strip-line is first calculated using a simplification, and the result is compared to the power dissipation of the Pi- and T-models. Then the best topology is chosen for use in the equivalent circuit model in Figure 2.11.

First, the power dissipation in the strip-line is calculated. The voltage drop along a long thin conductor is assumed to be small, so that the displacement current is linearly distributed along it length. Thus, when end-loaded, the power dissipation in the strip-line is

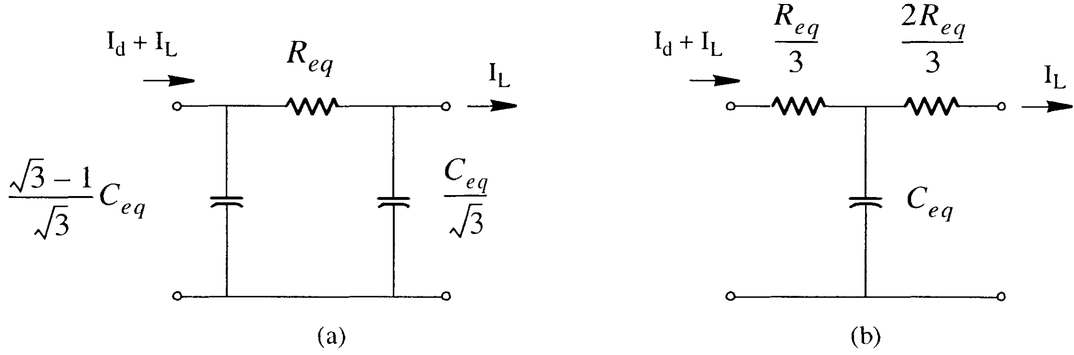

Figure 2.13: Two candidate circuits to model interconnect power dissipation and capacitive loading of the drive electronics: (a) the Π-model and (b) the T-model.

$$
\begin{aligned}
P_{sl} &= \bar{R}\int_{-L}^{0}\left[I_d\left(-\frac{x}{L}\right) + I_L \right]^2 dx \\
&= \bar{R}\left\{ \frac{I_d x^3}{L^2 3} - \frac{I_d I_L}{L}x^2 + I_L^2 x \right\}\Bigg|_{-L}^{0} \\
&= R_{eq}\left\{ \frac{1}{3}I_d^2 + I_d I_L + I_L^2 \right\} .
\end{aligned}
\qquad 2.61
$$

The equivalent resistance $R_{eq} = \bar{R}L$ is simply the total lumped DC resistance of the conductor.

Next, the strip-line power dissipation is compared to that of two candidate lumped-element configurations shown in Figure 2.13. Similarly, C_{eq} is the DC equivalent capacitance for the entire strip-line. The power dissipation in these circuit models is

$$
P_T = R_{eq}\left[\frac{1}{3}I_d^2 + \frac{2}{3}I_d I_L + I_L^2 \right], \qquad 2.62
$$

and

$$
P_\Pi = R_{eq}\left[\frac{1}{3}I_d^2 + \frac{2}{\sqrt{3}}I_d I_L + I_L^2 \right] . \qquad 2.63
$$

The best circuit is chosen by inserting the extremes of the end-loading and comparing the power dissipated in each topology to the approximate result of Equation 2.61 for the strip-line.

Equations 2.61 through 2.63 show that the mismatch between each model and the strip-line simplification is worsened by either a large displacement current or a large load current, and that the worst mismatch occurs when the two currents are equal. Thus if $I_d = I_L$

$$P_T = \frac{6}{3} R_{eq} I^2 \qquad 2.64$$

and

$$P_\Pi = \left[\frac{4 + 2\sqrt{3}}{3}\right] R_{eq} I^2 , \qquad 2.65$$

while in this case the power dissipation in the strip-line reduces to

$$P_{sl} = \frac{7}{3} R_{eq} I^2 . \qquad 2.66$$

So, in the worst case scenario the T-model rather greatly underestimates the power dissipation of the strip-line by 14%, while the Π-model overestimates the dissipation by 6%. To provide a conservative estimate of power dissipation, all circuit models of primarily end-loaded strip-lines in this thesis use the Π-model.

The third dashed box in Figure 2.11 encloses three Π-models which have been pieced together to describe power dissipation in the first-level interconnects. These include the lead interconnect, the branch point hub and fingers, and the outer segments of the electrodes connected to the branch point fingers, as shown in Figure 2.12.

On the other hand, the second level interconnects, the ring interconnects, are modeled with a T-model. In this case the machine load is evenly distributed, by the many stator electrodes, along the length of the strip-line. The power dissipation, under the same assumption of negligible voltage drop along the length, is calculated as

$$\begin{aligned} P_{sl} &= \bar{R} \int_{-L}^{0} [I_d + I_L]^2 \left(-\frac{x}{L}\right)^2 dx \\ &= \bar{R}\left[I_d^2 + 2 I_d I_L + I_L^2 \right]\left[\frac{x^3}{3L^2} \right]\Bigg|_{-L}^{0} \\ &= \frac{R_{eq}}{3}\left[I_d^2 + 2 I_d I_L + I_L^2 \right] . \end{aligned} \qquad 2.67$$

For the case in which $I_d = I_L = I$, the power dissipation in a strip-line that is loaded evenly along its length reduces to

$$P_{sl} = \frac{4}{3} R_{eq} I^2 . \qquad 2.68$$

Now, the circuit models must still be end loaded with the current I_L, so the expressions of Equations 2.64 and 2.65 are still valid. But in this case, of the two choices, the T-model would provide the closest match on the basis of power dissipation. However, a perfect match is obtained if the second resistance is removed, leaving only the $\frac{1}{3}R_{eq}$ element. This is allowable since all load current does not flow through the entire length of the ring interconnect, so the second resistor is dropped and the modified form is used in the circuit model, as shown in Figure 2.11.

In the equivalent-circuit model, the Π-models are joined by simply adding the capacitance at the interface between each model pair. The first Π-model describes the bond pad and interconnect between the pad and the branch point, the lead interconnect, while the second describes the branch point root and the branch point hub. The last Π-model describes the branch point fingers and the outer segments of the seven electrodes which carry all current flowing into the phase. The values for each of the circuit elements in the combined model are given in Table 2.1 in terms of several constitutive resistances and capacitances that will now be defined.

2.3.5 Equivalent-Circuit Element Definitions

First-Level Interconnects

All constitutive parasitic resistance and capacitance elements are defined as DC equivalents in a manner that is consistent with the strip-line power dissipation model developed above. The first level interconnects are composed of the bond pad, the lead interconnects, the branch point and the branch point electrodes, as illustrated in Figure 2.12. The bond pad is easily accounted for as a single parallel capacitance, but for the rest of the package interconnects, calculation of equivalent circuit elements is slightly more involved.

Note that the parasitic coupling in the stator is not always limited to that between the interconnects and the stator substrate as in the case of the bond pad capacitance. Since the electric induction micromachine is fabricated from a two-wafer stack, there is parasitic capacitive coupling not only from the first-level interconnects to the stator substrate, but also to the rotor substrate. For example, the lead interconnects lie on the stator insulator, but they are covered by the rotor wafer. Thus the rotor substrate is isolated from them only through the series combination of the capacitance across the air gap length and the capacitance across the rotor insulator. Thus, it is useful to define an effective permittivity to gap ratio for the stator-rotor combination

$$\frac{\varepsilon_{s\text{-}r}}{\Delta_{s\text{-}r}} = \left[\frac{\varepsilon_{si}}{\Delta_{si} + \delta_{ILD} + \delta_{pic}} + \frac{\varepsilon_g \varepsilon_{ri}}{\varepsilon_g \Delta_{ri} + \varepsilon_{ri} G}\right]. \qquad 2.69$$

Then, the lead interconnect capacitance is expressed as

$$C_{lic} = \frac{\varepsilon_{s\text{-}r}}{\Delta_{s\text{-}r}} L_{lic} W_{lic}, \qquad 2.70$$

where L_{lic} and W_{lic} are the length and width of the lead interconnect strip-line as shown in Figure 2.12. The branch point root — matching the width of the lead interconnect to that of the branch point hub — and branch point hub are also covered by the rotor substrate, so their capacitances are defined as, respectively,

$$C_{bpr} = \frac{\varepsilon_{s\text{-}r}}{\Delta_{s\text{-}r}} L_{bpr}\left[\frac{W_{bp} + W_{lic}}{2}\right], \qquad 2.71$$

and

$$C_{bph} = \frac{\varepsilon_{s\text{-}r}}{\Delta_{s\text{-}r}} L_{bph} W_{bp}, \qquad 2.72$$

in which L_{bpr} is the length of the root segment of the branch point, L_{bph} is the length of the hub segment, and W_{bp} is the total width of the branch point. Similarly, the branch finger and outer-half electrode capacitances are

$$C_{bpf} = \frac{\varepsilon_{s\text{-}r}}{\Delta_{s\text{-}r}}\left[\frac{\frac{W_{bp}}{2N_{bpf}} + W_{eo}}{2}\right] \qquad 2.73$$

and

$$C_{eo} = \frac{\varepsilon_{s\text{-}r}}{\Delta_{s\text{-}r}} \frac{L_e}{2}\left[\frac{3W_{eo} + W_{ei}}{4}\right], \qquad 2.74$$

where N_{bpf} is the number of branch point fingers, and hence branch point electrodes, used to distribute current through vias to the ring interconnect. In addition, L_e is the length of an electrode, W_{eo} is the width of an electrode at the outer radius of the stator r_o, and W_{ei} is the width at the inner radius r_i.

The derivations of DC equivalent resistances for the lead interconnect and branch point are also straightforward. Consider a thin cross-sectional element of width dx on a plane that is perpendicular to the direction of current flow. This element defines a resistance per unit length which can be integrated along a section of the interconnect, yielding the total DC resistance of that section. In other

words, given that the width W_{sxn} of the section can vary along its length, but its thickness δ_{sxn} and resistivity ρ_{sxn} do not, the DC equivalent resistance is well-approximated as

$$R_{eq} = \int_0^{L_{sxn}} \frac{\rho_{sxn}}{\delta_{sxn} W_{sxn}(x)} dx. \quad 2.75$$

It then follows that the resistance of the lead interconnect is

$$R_{lic} = \frac{\rho_{hdp} L_{lic}}{\delta_{l1} W_{lic}}, \quad 2.76$$

where ρ_{hdp} is the resistance of heavily phosphorous-doped polysilicon. Likewise, the resistance of the branch point root is

Table 2.1: Lumped-parameter equivalent circuit elements in Figure 2.11.

Circuit Element	Constitutive Parameters
C_1	$C_{wbp} + \frac{\sqrt{3}-1}{\sqrt{3}} C_{lic}$
R_1	R_{lic}
C_2	$\frac{C_{lic}}{\sqrt{3}} + \frac{\sqrt{3}-1}{\sqrt{3}} \left[C_{bpr} + C_{bph} \right]$
R_2	$R_{bpr} + R_{bph}$
C_3	$\frac{C_{bpr} + C_{bph}}{\sqrt{3}} + \frac{\sqrt{3}-1}{\sqrt{3}} N_{bpf} \left[C_{bpf} + C_{eo} \right]$
R_3	$\frac{R_{eo} + R_{bpf}}{N_{bpf}}$
C_4	$\frac{N_{bpf} \left[C_{bpf} + C_{eo} \right]}{\sqrt{3}}$
R_4	$\frac{R_{ric}}{12}$
C_5	C_{ric}

$$R_{bpr} = \frac{\rho_{hdp} L_{lic}}{\delta_{l1} [W_{bp} - W_{lic}]} \ln\left(\frac{W_{bh}}{W_{lic}}\right) \quad ; \qquad 2.77$$

the resistance of the branch point hub is

$$R_{bph} = \frac{\rho_{hdp} L_{lic}}{\delta_{l1} W_{bph}} ; \qquad 2.78$$

the resistance of the branch point fingers is

$$R_{bpf} = \frac{\rho_{hdp} L_{bpf}}{\delta_{l1} \left[\frac{W_{bp}}{2N_{bpf}} - W_{eo} \right]} \ln\left(\frac{W_{bp}}{2N_{bpf} W_{eo}}\right) \quad ; \qquad 2.79$$

and the resistance of the outer half of an electrode is

$$R_{eo} = \frac{\rho_{hdp} L_{bpf}}{\delta_{l1} [W_{eo} - W_{ei}]} \ln\left(\frac{2W_{eo}}{W_{ei} + W_{eo}}\right) . \qquad 2.80$$

The Second-Level Interconnect

The final equivalent capacitances and resistances in the model are associated with the ring interconnect. For the purposes of this model, the center of the ring interconnect is assumed to be located at the center of the total radial extent of the micromachine active area, i.e., at the center of the length of the electrodes. To calculate the equivalent resistance, note that all current for one phase flows through N_{bpf} vias at the branch point, at which point half will flow around the ring clockwise and half will flow counter-clockwise. In this case, since the ring width W_{ric} is much smaller than the average radius of the micromachine, the total resistance is

$$R_{ric} = \frac{\rho_{hdp} \pi (r_o - r_i)}{\delta_{ric} W_{ric}} . \qquad 2.81$$

However, because the current splits, the ring interconnect appears as two segments of half the circumference, carrying half the current. This means the equivalent resistance will be the total resistance divided by four, since half of that resistance is effectively in parallel with the other half. An additional division by three is provided by the modified form of the T-model, as described at the end of Section 2.3.4, resulting in a total division of R_{eq} by 12, as shown in Table 2.1.

The ring interconnect capacitance must be calculated according to the same current division as noted above, but parallel capacitance adds so the ring interconnect capacitance is simply the sum total of all capacitances distributed around the ring. However, the calculation of the total involves an important subtlety. The ring interconnect capacitance includes both coupling to the grounded stator substrate as well as coupling to the electrodes of the other $N_p - 1$ phases. First, the coupling

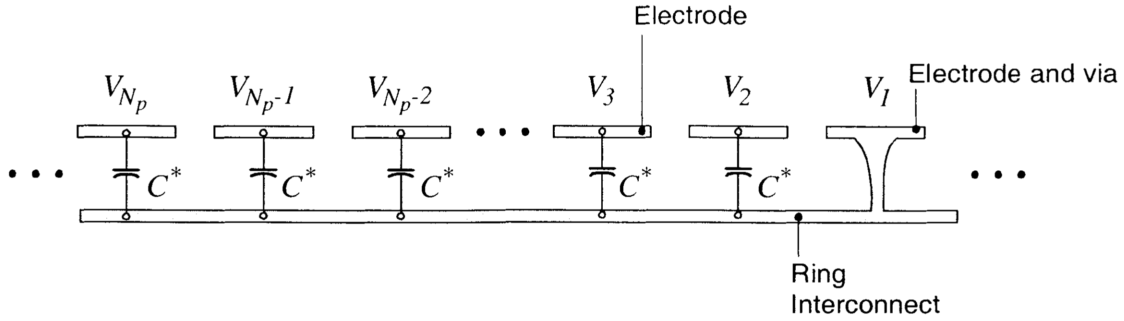

Figure 2.14: Capacitive coupling of the ring interconnect of one phase to the electrodes of each remaining phase. For clarity, the capacitance between electrodes is not drawn.

of one entire ring interconnect to the substrate ground plane is represented in the model by the capacitance

$$C_{ricg} = \frac{\varepsilon_{si}}{\Delta_{si}}\pi(r_{rico}^2 - r_{rici}^2), \tag{2.82}$$

where r_{rico} and r_{rici} are the outer and inner radii of the ring interconnects, equal to the mean motor radius r_{ric} plus and minus one half W_{ric}, respectively.

Second, the capacitances in the circuit model are specified between the interconnects and the ground plane, but the electrodes of the other phases carry a time-varying voltage that must be taken into account when computing the effective capacitance of a ring interconnect to ground for inclusion in the model. Figure 2.14 shows a cross section, over the length of one wavelength, along the circumference of one ring interconnect. Thus, m of these unit cells placed end to end makes up a complete ring interconnect for one phase. The calculation of the equivalent capacitance for use in the circuit model, expressed as a line to ground capacitance, begins by recalling that capacitance is the ratio of charge stored to the voltage across the capacitance, or

$$C = \frac{\hat{Q}}{\hat{V}} \quad , \tag{2.83}$$

where $\hat{V}$ is the voltage across the capacitance C. So the total equivalent capacitance between the ring interconnect of one phase and the electrodes of the other phases is found by summing all ring-to-electrode stored charge Q_{eq}. For example, Phase 1

$$\hat{Q}_{eq} = \sum_{n=2}^{N_p} \hat{q}_n = \sum_{n=2}^{N_p} C^*[\hat{V}_1 - \hat{V}_n] \ . \tag{2.84}$$

where C^* is the capacitance between the ring interconnect and one electrode of another phase if that electrode were at ground, modeled as a parallel plate capacitor. The charge $\hat{q}_n$ is that stored by each of the constitutive capacitances. Equation 2.84 is then related to the line to ground voltage, which is $\hat{V}_s$ as defined in Section 2.1.1. Expressing the balanced phase to phase voltages as

$$\hat{V}_n = \hat{V}_s e^{j\left(\omega t - (n-1)\frac{2\pi}{N_p}\right)} \tag{2.85}$$

and inserting them into Eq 2.84, C^* is factored out, the total capacitance is converted from ring-to-electrode capacitance and expressed as ring-to-ground capacitance, resulting in

$$\begin{aligned} C_{eq} &= C^*\left[[N_p - 1] - \sum_{n=2}^{N_p} \cos\left([n-1]\frac{2\pi}{N_p}\right) \right] \\ &= N_p C^* \end{aligned} \tag{2.86}$$

Thus, the total equivalent ring-to-ground capacitance between the ring interconnect and the electrodes of other phases is

$$C_{rice} = N_p \frac{\varepsilon_{si}}{\Delta_{si}} W_e W_{ric} . \tag{2.87}$$

Finally, the total ring interconnect capacitance also includes the coupling between neighboring electrodes, across the inter-electrode gap. Although this gap can be quite large compared to the thickness of the electrodes in many viable designs, a parallel-plate equivalent again provides a useful representation of the coupling. In other words, the more relevant that the inter-electrode coupling becomes, compared to other capacitances in the circuit, the more negligible the fringing becomes compared to the total inter-electrode capacitance. Thus, the inter-electrode capacitance is expressed as

$$C_{ee} = \frac{\varepsilon_g}{G_{ee}} L_e \delta_{lic} , \tag{2.88}$$

and the total ring interconnect parasitic capacitance is

$$C_{ric} = C_{ricg} + C_{rice} + C_{ee} . \tag{2.89}$$

2.4 Summary

This chapter has described all models used in this thesis for analysis and design of the electric induction machine. In the first half of the chapter, models which capture the distributed nature of

the electromagnetic fields extending from the stator electrodes into the rotor were developed. A relatively general geometry was chosen, along with general material types, and it was noted that the solution assumes that there is no bulk free charge in the system at rest. Laplace's equation was solved to arrive at a model that describes the distributed fields in the induction machine. The model began as a 2D representation of the electric induction machine and was next developed into a 3D representation to account for the actual 3D nature of the design. The distributed-field models were developed to enable a detailed understanding of the magnitude and extent of the driving electromagnetic fields, and thus to enable a detailed design of the majority of the machine structure.

The second half of this chapter dealt with equivalent-circuit models that describe the terminal behavior of the electric induction machine. These lumped-parameter models are useful for coupling to lumped-parameter models of external power electronics. Section 2.2 showed that it is straightforward to represent the terminal behavior of an ideally-driven induction machine with an admittance function that represents the air gap and rotor, and accounts for the 3D nature of the machine, but this must be calculated numerically and does not add to an understanding of the internal field structure and electromechanics. On the other hand, an equivalent circuit model of the air gap and rotor can be useful to properly gauge the size of internal machine capacitance for comparison to parasitic capacitance from the stator wiring. It is also very useful in understanding the relation between performance and geometry, as will be seen in Chapter 3. An equivalent circuit model of the parasitic capacitances and resistances in the stator was also developed. The model was developed so that power dissipation would be well-represented but equivalent impedance would not necessarily be accurate.

Chapter 3

Analysis and Tethered Motor Design

The tethered motor is designed to be a metrology device that permits accurate torque measurement. To this end, the tethered motor essentially consists of two components: an electric induction micromotor and the tethers which serve as the torque transducer. This chapter describes the design of both the electric induction motor and its tethers.

Nearly any micromotor design could be investigated with the tethered motor concept, so this chapter focuses on the micromotor-compressor introduced in Chapter 1, briefly described in Appendix B, and described in detail in [21]. Every aspect of the electric induction micromotor is designed with this application in mind.

The models developed in Chapter 2 are used to predict the operating characteristics of the micromotor and adjustments are made toward satisfaction of design goals for the micromotor-compressor [21]. Fabrication constraints also play a pivotal role in the design process; in fact, these constraints firmly dictate many aspects of the design. Additionally, torque transducing tethers must be found and incorporated such that the operation of the electric induction micromotor is predictable.

Chapter Overview

First, Section 3.1 summarizes the overall design constraints. Next, Section 3.2 describes the design of the induction micromotor. In this section, the focus is on the core of the micromotor, the air gap and the rotor, assuming that an idealized potential wave is properly excited by the electrodes. Then Section 3.3 describes an optimization of the stator interconnections to efficiently deliver the proper micromotor excitation voltage to the stator electrodes. Optimization is especially important when designing for high system efficiency since considerable power can be lost within the stator wiring. Also, recall from Chapter 2 that excessive reactive current in parasitic capacitance causes excessive loss in the power electronics. Next, Section 3.4 describes the complete design of the tethered rotor. Its first part, Section 3.4.1, describes the design of the rotor conductor, the most essential component of an electric induction micromotor. Section 3.4.2 designs the tethers: high aspect ratio single-crys-

tal silicon beams intended to be a linear transducer from torque to deflection. Finally, Section 3.5 briefly summarizes the tethered motor and this chapter.

3.1 Design Constraints

The desired performance of an electric induction micromotor cannot be realized without either careful consideration of fabrication constraints early in the design process or many fabrication iterations. Micro-fabrication constraints can be severe, and are costly. So it is much more desirable to recognize constraints early in the design phase, rather than in fabrication. This section summarizes constraints that arise from existing components of the micromotor-compressor, and introduces some of the major fabrication constraints inherent to the electric induction micromotor.

3.1.1 Design Inheritance

The micromotor inherited many aspects of its design from the overall micro gas-turbine generator design that preceded it. The first device that was fabricated based on the gas turbine design was a microbearing rig [36, 35, 60, 57], and it consisted essentially of the gas-turbine structural design, minus the combustion chamber and the electric induction machine considered in this thesis. From that bearing rig the micromotor-compressor inherited its structural design so that lessons learned from bearing rig fabrication and testing would be directly applicable. Since the electric induction micromotor in the tethered motor is intended to be the same as that in the micromotor-compressor, it shares the same structural boundaries. These shared boundaries dictate a planar, axial-gap micromotor topology and constrain the inner and outer radii to those listed in Table 3.1.

3.1.2 Micro-Fabrication Constraints

Many fabrication constraints are apparent in the inherited geometry that is illustrated in Figure 2.1, and some factors are especially pertinent to induction micromotor performance. Due to the limitations of microfabrication techniques, only shapes constructed from stacked 2-dimensional projections can be incorporated into the micromotor design. In addition, the thickness of each projection is limited by the maximum possible reactive ion etch depths. Inductively-coupled plasma etchers have improved to the point where 500 μm etches are common, but the aspect ratio of etch trenches is still limited to 50:1 for etch trenches wider than 10 μm. Aspect ratio is defined in several ways, but in general a high-aspect-ratio etch trench would have side walls that are nearly vertical, while a high aspect ratio feature left behind by the etch would be tall and narrow. It so happens that a deep and wide trench is easier to fabricate so that two trenches can be etched next to each other to define an extremely thin vertical wall, but the results are unpredictable. Therefore, in general, a limited aspect ratio means that deep straight walls are challenging and the geometry of any micro-scale device is constrained.

The electric induction micromotor is especially limited by fabrication constraints. In order to remain compatible with the process flows into which the micromotor will eventually be incorporated, materials choices are limited to only those that are CMOS compatible and will withstand 1100 °C temperature cycles. Within the Microsystem Technology Laboratories (MTL) at MIT these include only silicon, polysilicon, silicon dioxide, silicon nitride, and variants of these materials. These material choices, in turn, constrain film thicknesses due to residual stress concerns and, for the most part, define their electrical properties. This chapter shows that these constraints limit the design of the electric induction micromotor.

It is extremely beneficial to anticipate the fabrication process flow during all stages of the design of a micro-fabricated device. While it is true that the designer of a macro-fabricated device must also consider the limits of fabrication, the micro-fabrication toolset is much smaller, material selection much more limited, and iterations much more costly. Several important aspects of the design for the baseline electric induction micromotor, the stator wiring and mechanical springs of the tethered rotor, require dedicated fabrication development efforts. All fabrication efforts are detailed in Chapter 4, but the design process description here will necessarily include a great deal of fabrication discussion.

3.2 Micromotor Design

This section describes the analysis and design of the core of the electric induction micromotor. In other words, the focus is on those portions of the electric induction micromotor that most directly influence high torque delivery to the rotating components of the micromotor-compressor. This section does not discuss the fluid mechanics within the rotating machinery of the micromotor-compressor. A coupled analysis is summarized in [21] using the electromechanical models developed in Chapter 2 in tandem with fluid models.

In addition, this thesis excludes detailed consideration of losses due to fluid viscosity or friction. Although there will be significant losses due to fluid viscosity or rubbing friction in the small clearances between moving parts in turbomachinery, this thesis ignores the influence of such losses to simplify the design process. It could be argued that the losses of viscous drag in a small gap should always be included in motor performance characterization studies, because the electric induction micromotor does require a small gap to generate high torque. However, the micromotor does not require the high rotor speed which leads to high windage losses. For example, this micromotor would be very useful as a high torque slow-moving stepper motor. The effects of rubbing friction are neglected because air bearings are included in the design of the micromotor-compressor to avoid contact between the rotor and the rest of the structure, while in the tethered motor these losses are absent. The tethered motor is designed to avoid all windage and friction losses. Windage torque is

only mentioned to explain the concept of operating speed† through load lines calculated by assuming simple Couette flow between the rotor and stator, with no load from the compressor since the windage effects will dominate in the first micromotor-compressor. High performance is defined simply as the creation of high electromechanical torque.

This section focuses only on the electromechanical energy conversion process and the ways in which it can be improved. To that end, its primary purpose is to describe several important electric induction micromotor performance trends in the subsections that follow. First a baseline design is defined, carefully considering the design constraints of the micromotor-compressor. Then three particularly important micromotor parameters are systematically varied, and the resulting performance trends are analyzed based on underlying physical phenomena. The second purpose of this section is to describe the effect of higher harmonics that can result from poor stator excitation and from the finite number of electrodes in a practical design. This topic is covered in Section 3.2.6.

3.2.1 Micromotor Baseline Design Description

The baseline electric induction micromotor design described in this section is the culmination of many preliminary micromotor designs. Much of the geometry is inherited and fixed, or dictated by fabrication constraints, and the remaining design is constrained by physical limitations. Nonetheless, there is considerable latitude for device design, and this section outlines the baseline starting point of that exploration.

Table 3.1 lists the parameters for the baseline electric induction micromotor design. The following list briefly outlines the factors that led to the baseline micromotor design.

1. **Rated Stator Voltage.** This is defined to be 300 V based on the breakdown strength of gases. In the absence of field emission or field enhancement, a clean gas of any kind will withstand a voltage of at least 300 V, even for small electrode separation because of rarefaction in the space between the electrodes [58, 45].
2. **Stator Periodicity.** The models in Chapter 2 show that for an electric induction machine, higher periodicity yields higher torque to first order. The maximum attainable periodicity for a fixed geometry is determined by fabrication constraints on the minimum line-width at the inner radius of the stator electrodes, in combination with the maximum number of stator phases desired. Section 3.2.6 will show that the limits of fabrication are reached before second-order effects result in a decrease in torque with periodicity. Thus, given the motor inner radius, the baseline value is the maximum value allowed by fabrication constraints.
3. **Stator Excitation Frequency.** Induction motors are most efficient if the rotor speed is close the synchronous speed, where the rotor travels at the same speed as the potential wave on the stator. However, as the design is changed to move the operating point away from synchro-

†. Operating speed is defined as the speed at which electromechanical torque is balanced by the sum of all load torque.

Table 3.1: Parameters in the baseline electric induction micromotor design. These apply to both the micromotor-compressor and the tethered motor.

Parameter	Value in Baseline Design	Symbol
Stator rated voltage	300 V	V_s
Stator periodicity	131	m
Stator-rotor air gap length	3 μm	G
Stator Excitation Frequency	2.6 MHz	f_e
Air gap permittivity	ε_o	ε_g
Air gap resistivity	∞	—
Rotor insulator thickness	10 μm	Δ_{ri}
Rotor insulator (SiO_2) permittivity	$3.9\varepsilon_o$	ε_{ri}
Rotor insulator (SiO_2) resistivity	1.0×10^{14} Ω-cm	ρ_{ri}
Rotor conductor sheet resistivity	200 MΩ	ρ_{rcs}
Rotor conductor thickness	0.5 μm	δ_{rc}
Rotor disk radius	2.0 mm	r_d
Micromotor inner radius	1.0 mm	r_i
Micromotor outer radius	1.9 mm	r_o

nous, the tolerance to fabrication errors can be increased. The percentage difference between operating and synchronous speeds is essentially the amount of power dissipated in the rotor, and for a research device 25% seems tolerable. For the micromotor-compressor the target operating speed is 1,000,000 rpm. With the baseline periodicity of 131, the excitation frequency is targeted at 2.6 MHz, corresponding to a synchronous speed that is 33% higher than the operating speed, making the rotor efficiency about 75%.

4. **Stator-Rotor Air Gap Length.** The minimum value of the air gap length is constrained by the breakdown strength of air, in combination with the rated stator voltage. According to Equation 2.11, the worst case situation is a stalled rotor when the potential difference across the gap is twice the magnitude of the stator potential wave. Conversely, at synchronous operation the rotor potential is zero by Equation 2.11 so that a potential difference across the air gap is only the magnitude of the stator potential wave. At speeds between stall and synchronous speed, the potential difference can be even less. Previous experimental evidence suggests a maximum safe field strength on the order of 100 MV/m [4, 48, 67], suggesting a safe air gap length of 6 μm due to the fact that the gap potential difference is twice the stator voltage magnitude when the rotor is stalled. However, because of the large torque returns realized by a smaller air gap, a more aggressive baseline air gap of 3 μm is chosen.
5. **Stator Air Gap Permittivity.** It so happens that in the context of the micromotor-compressor, the permittivity of the "air gap" cannot easily differ from the permittivity of free space. The gap must be filled with a low viscosity fluid to avoid excess viscous friction losses, but this fluid must also have a very low conductivity to avoid conduction losses from the electrodes. At this point the fluid of choice is dry bleed air from the compressor, which has a permittivity close to free space and a conductivity of near zero if it is clean. Most non-conductive gases have a permittivity very similar to air.
6. **Rotor Insulator Conductivity and Permittivity.** The rotor insulator must be an insulating

material with a low conductivity that can be deposited as a thick film and is compatible with a CMOS process. Thus a good choice is silicon dioxide, which has an extremely low conductivity as shown in Table 3.1. This choice also determines the rotor insulator permittivity. Although not discussed, the models of Chapter 2 shows that a low rotor insulator relative permittivity yields a higher torque and that of SiO_2 is one of the lowest available at 3.9. For comparison, the second most widely used CMOS-compatible dielectric, silicon nitride, has a relative permittivity of 7.5, and, its thickness is severely limited due to residual stresses from required thermal cycles in the rest of the micromotor-compressor process flow. Therefore SiO_2 is the best available choice.

7. **Rotor Insulator Thickness.** This value comes from current fabrication limits on the maximum reliable thickness of a deposited silicon dioxide film. The oxide film is deposited with a high throughput Novellus Concept-One PECVD deposition system, so its thickness is much larger than that possible through thermal growth. However, the micromotor-compressor requires several high-temperature fusion bond anneal steps, and these lead to high residual stresses in the deposited oxide films. If the film is too thick it will crack due to the mismatch of thermal expansion coefficients between the film and the substrate. Prescribed anneal temperatures and the resulting high residual stresses limit a reliable oxide thickness to the baseline value listed, in the experience of the micro gas-turbine generator project. Section 3.2.4 will show the performance trend resulting from a variation of the rotor insulator thickness.
8. **Rotor Conductor.** The sheet resistance of the rotor conductor is chosen to produce a particular functional dependence of torque on rotor speed and stator excitation frequency, and the performance trends as a result of rotor sheet resistance variation are described in Section 3.2.3. The film thickness is chosen primarily because of the existence of a well-characterized precess in the Microsystem Technology Laboratories at MIT. Note that this thickness is much smaller than the intended stator potential fundamental spatial wavelength, so the rotor conductor can be treated as a sheet as described in Chapter 2. Section 3.4.1 describes experiments that were conducted to develop the rotor conductor and tailor its resistivity through ion implantation.
9. **Rotor Geometry.** The radius of the rotor disk is inherited from the micromotor-compressor as described in Section 3.1.1. The outer radius of the micromotor was chosen to generally coincide with the size of the rotor disk, but minus an area needed for a fluid seal [21]. The inner radius of the micromotor is chosen based on two requirements. First, there must be enough room for thrust bearings. Second, due to limits on the smallest possible width of patterned lines during photolithography, a smaller radius leads to fewer electrodes. Section 3.2.5 shows that this leads to lower micromotor torque by requiring a reduction in periodicity.

3.2.2 Micromotor Performance Trends

Using the baseline design, the remainder of Section 3.2 analyzes this design in detail and considers ways in which it could be improved if fabrication constraints could be relaxed. Thus this section serves three purposes. First, it defines the meaning of micromotor performance in this thesis. Sec-

ond, it introduces the concept of operating speed in the presence of a load. Finally, it introduces three major performance trends whose physical origins are described in the sections that follow.

A Micromotor Performance Metric: Electromechanical Torque

Electromechanical torque, from Equation 2.48, is used as the primary metric of micromotor performance. The torque equation is repeated below with 3 terms numbered for later reference. This equation defines the classic bell-shaped curve of torque versus rotor speed, as shown in Figure 3.1.

$$\tau = \varepsilon_g \pi |\hat{V}_s|^2 \int_{R_i}^{R_o} \left\{ \underbrace{\frac{\Gamma(r)}{1+\Gamma(r)^2}}_{①} \cdot \underbrace{\beta_i(r)}_{②} \cdot \underbrace{\frac{m^2}{\sinh\left(\frac{m}{r}G\right)}}_{③} \right\} dr \qquad 3.1$$

It is fortunate that the torque is described by this simple integral. The grouping of its constitutive parameters lends itself elegantly to the purposes of the next three sections. Furthermore, for properly excited electrodes, only a single stator-potential spatial harmonic at the fundamental spatial frequency f_e need be considered in the design space exploration. Thus Equation 3.1 is adequate for nearly all design purposes, when the voltage $|\hat{V}_s|$ is properly defined as discussed in Section 2.1.4 and Section 3.2.6. Focusing attention on only one harmonic also aids greatly in describing the underlying physics. Until the discussion of spatial harmonics in Section 3.2.6, it is assumed that electrodes are fabricated and excited to produce a perfect sinusoidal travelling potential wave on the stator.

Figure 3.1 presents the most basic view of the design space, showing torque and power delivered by the micromotor, plus the rotor-stator pull-in force, versus rotor speed. Since this thesis considers only perfect insulators in the air gap, a large pull-in force is generated for the same reason a large torque is generated: the image charges on the rotor are attracted to the enforced charges on the stator. Unfortunately, the normal forces are much greater than the tangential forces, and the pull-in force is a major design consideration. The micromotor-compressor deals with this by incorporating stiff thrust bearings while the tethered motor uses stiff mechanical springs, described in Section 3.4.2.

Motor Performance Trends

Using the baseline design as a staring point, the next three sections highlight the behavior of the electric induction micromotor as a function of the rotor conductor sheet resistance ρ_{rcs}, the rotor insulator thickness Δ_{ri}, and the stator periodicity m, respectively. These parameters are chosen for design studies primarily because they greatly affect the performance of the micromotor, but also

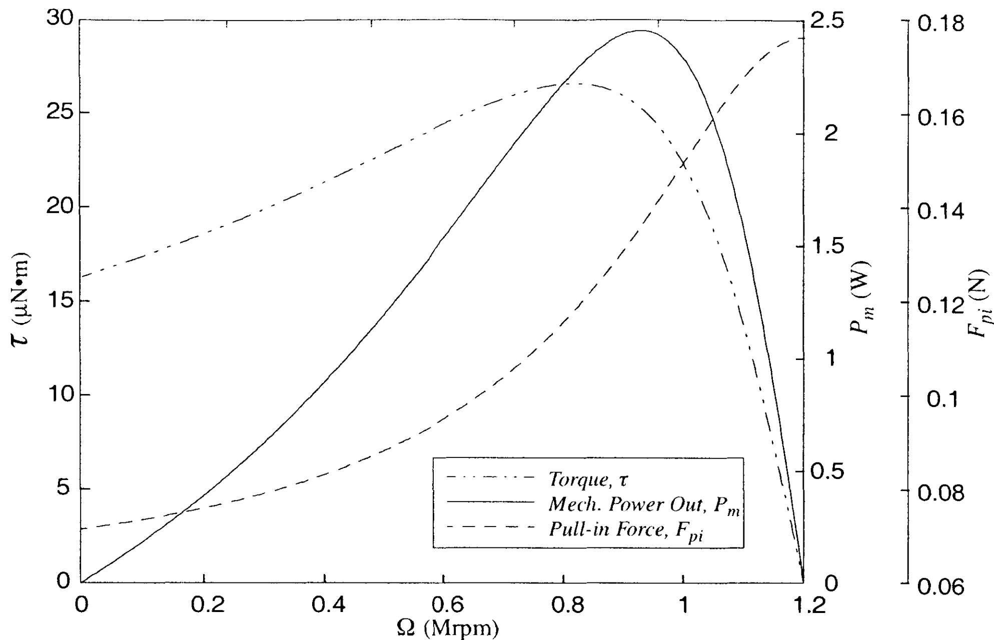

Figure 3.1: Micromotor output torque, power and pull-in force from the 3D simple-harmonic model versus rotor speed. Motor design parameters are as specified in Table 3.1.

because they can be controlled through fabrication. Unlike most of the parameters in the baseline design, they are not extremely constrained by design inheritance or physical limitations, but they are constrained by fabrication. The periodicity and the rotor insulator thickness are both greatly constrained by fabrication limitations, and the value of the rotor conductor sheet resistance is uncertain because of fabrication complexity.

3.2.3 Rotor Conductor Performance Trends

Motor-compressor operating curves are greatly affected by deviations of rotor conductor sheet resistance from the baseline value. The micromotor-compressor is intended to be excited by a fixed-frequency power electronic drive because, in general, highly efficient power electronics are either limited to relatively low voltages with a broad frequency range in the hundreds of kHz, or they are limited to a single frequency if they posses high voltage capability. High voltage and high frequency are both greatly desired in the motor-compressor application: Micromotor torque increases with the square of the voltage, and motor-compressor output power increases approximately linearly with drive frequency. In general electronics capable of operation near the baseline frequency of almost 3 MHz tend to exhibit high losses at high-voltage. One topology that limits these losses is a resonant design, which has no ohmic losses if constructed using a perfect inductor and a perfect capacitor. However, efficient operation is possible only within a very limited bandwidth. Thus,

because operating speed is directly related to the resulting limited bandwidth stator excitation frequency, it is important to design for a fixed operating speed.

However, since the rotor conductor is constructed of moderately doped polysilicon, its resistivity cannot be tightly controlled [29] and the effect of variations in rotor conductor sheet resistance on operating curves must be explored. Sheet resistance has been demonstrated to vary by at least one order of magnitude in comparison to what had been intended. Such changes profoundly affect the shape of the torque curve, greatly affecting operating speed and starting torque as shown in Figure 3.2.

The figure overlays micromotor torque curves for several different sheet resistances on an estimated load torque curve. Looking at the baseline curve, the figure shows that although the operating speed is unlikely to equal the speed of maximum torque, the rotor is certain to spin up to the baseline operating speed. The figure also shows that lower sheet resistance will give a lower operating speed.

Conversely, an unfortunate situation would arise if a much higher sheet resistance results from the fabrication. For example, for the estimated load torque line, the torque curve corresponding to a rotor sheet resistance of 600 MΩ is balanced at three speeds, but only Points A and C are stable

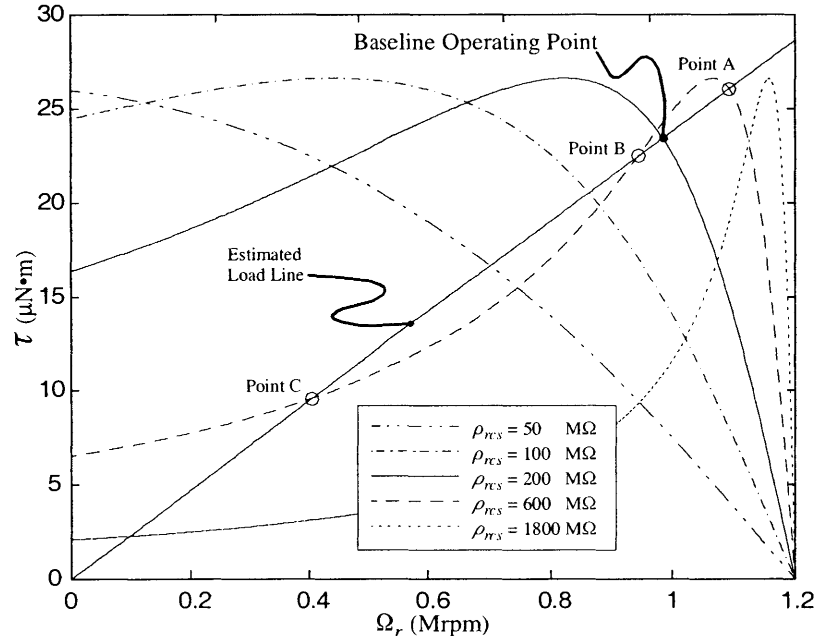

Figure 3.2: Torque versus rotor speed for various rotor conductor resistivities. Other model parameters are found in Table 3.1.

[75]. This sheet resistance could be detrimental to micromotor-compressor performance because the rotor would not accelerate to Point A. Instead, operating speed would be limited to Point C. Thus, for a fixed frequency drive, a rotor conductor sheet resistance just three times higher than the baseline value could destroy micromotor-compressor performance. Skipping ahead, Figure 3.4 summarizes the dependence of operating speed on rotor sheet resistance, for fixed-frequency stator excitation.

On the other hand, if the stator excitation frequency can be smoothly altered, while powering the micromotor-compressor, it would be possible to compensate for an unexpected rotor sheet resistance. In the ideal case, any frequency would be possible, and desired motor performance could be obtained given any as-fabricated rotor sheet resistance. Figure 3.3 shows the case in which the rotor sheet resistance is nearly an order of magnitude higher than desired, for several stator excitation frequencies. This range of stator frequencies is possible at the rated stator voltage. Such variability might be obtained by using a specially designed variable capacitor as part of the resonant power electronics topology. The figure shows that if the excitation frequency could be decreased to 1 MHz, and then slowly increased to 2.08 MHz, the operating speed could slowly be brought up to the baseline operating speed of just under 1 Mrpm, Point A in Figure 3.3. Figure 3.2 shows that without a variable-frequency power electronic drive, a sheet resistance 3× the baseline value would result in

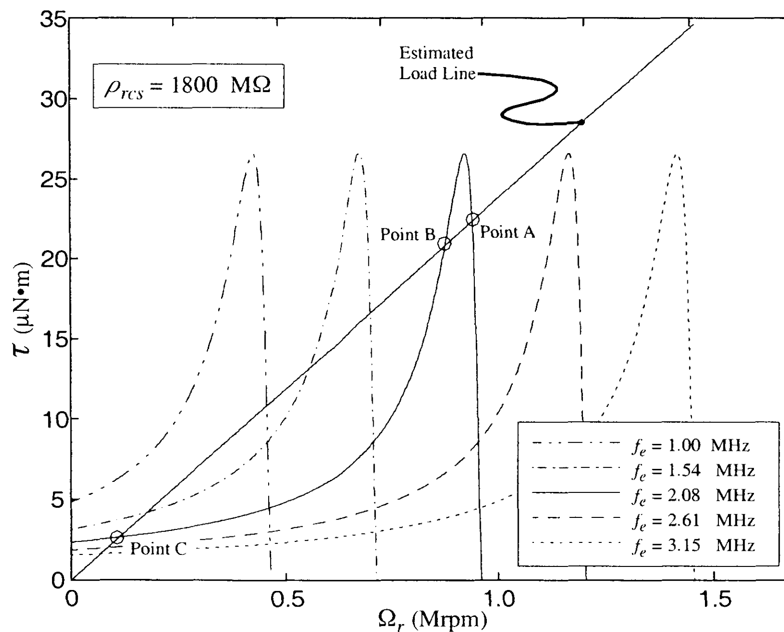

Figure 3.3: Torque versus rotor speed for various stator excitation frequencies. Other model parameters are found in Table 3.1.

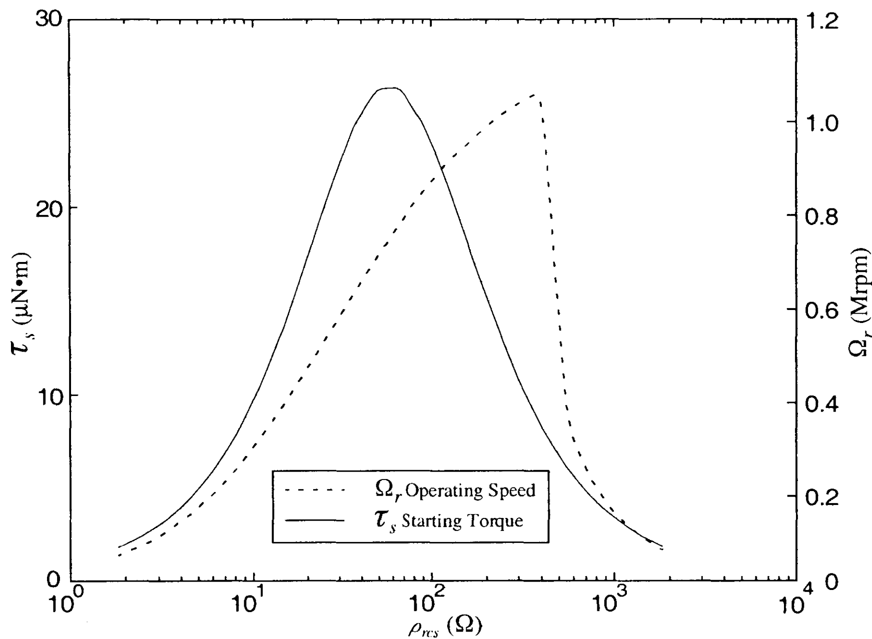

Figure 3.4: Starting torque versus rotor conductor sheet resistance, and operating speed versus rotor conductor sheet resistance with the estimated load.

an operating speed of less than half the intended operating speed, severely limiting the device. A sheet resistance 9x the baseline value would effectively ruin the device. Thus variable high-frequency high-voltage drive would increase the micromotor yield from a fabrication run.

Starting torque is also a strong function of rotor resistance. Figure 3.4 shows the trend of starting torque versus order-of-magnitude changes in rotor sheet resistance. In general, it is desirable to have high starting torque because the hydrostatic thrust bearings of the micromotor-compressor may function improperly. A future design calls for more compact hydrodynamic thrust bearings so a source of pressurized gas is not required. Whereas the hydrostatic thrust bearings are pressurized with gas from an external source, hydrodynamic thrust bearing would have to pressure themselves, using the speed of the rotor and spiral-grooves on the rotor to pump gas into the thrust bearings [27].

The baseline value of the rotor conductor sheet resistance is essentially a trade-off between two design goals. On one hand, high starting torque is desirable to overcome inertia and static friction forces in a micromotor started from rest. Figure 3.4 shows that this would call for a slightly lower rotor resistance. On the other hand, the figure also shows that a lower sheet resistance will result in a slower operating speed with a fixed-frequency drive, so there is a compromise value.

In addition, the baseline sheet resistance is set as a way of reducing risk. The goal of this thesis is to design a micromotor that produces fair performance in the presence of many uncertainties, such

as those of the rotor sheet resistance and the load. Thus the baseline design of $\rho_{rcs} = 200\ \mathrm{M\Omega}$ results in a fairly broad torque curve to allow a broader range of operating point. At the same time, the design is predicted to produce a reasonably large starting torque in the event that the bearings fail to levitate the rotor.

Underlying Physical Phenomena

The shape of the torque speed curve is a direct result of the competition between charge relaxation through the rotor and charge convection by the rotor. The parameter Γ is the ratio between the charge relaxation time and the time required for the rotor to move a distance $\lambda/2\pi$ relative to the traveling stator charge waveform, where λ is the wavelength of the charge distribution on the stator. Thus it is not surprising that torque is maximized through Term 1 when these two time scales are equal, i.e., when $\Gamma = 1$ as shown in Figure 3.5. The same parameter has been found in solutions for other electric induction micromotor geometries [49,75], but little has been written about its significance. The parameter Γ appears to be related to the electric Reynolds number R_e introduced by Stuetzer [65] for electrohydrodynamics and applied to other charge relaxation problems by Woodson and Melcher [75], but the intent is usually to increase the electric Reynolds number to increase the induced potentials. In fact the two numbers represent similar physics, but it appears that for a periodic excitation the Reynolds number must be bounded since the convection length scale is bounded. The fact that the optimum value here occurs at the value of 1 seems to be merely an artifact of its definition for this particular type of periodic induction machine. More could be learned from a deeper investigation of the parameter, but this is beyond the scope of this thesis.

The definition of Γ presented here is very useful for developing intuition in the design and operation of the electric induction micromotor, by providing a method of explanation for the shape of the torque curve. During this discussion the effective permittivity ε_{eff} and effective resistivity ρ_{eff} are fixed. At synchronous speed, the stator charge distribution travels at exactly the same speed as the rotor and the slip time is zero because

$$\tau_s = \omega_e S = (2\pi f_e - m\Omega_r), \qquad 3.2$$

where Ω_r is the rotor speed. Thus there is plenty of time for the charges induced on the surface of the rotor to move directly under the charges on the stator. At the same time, these charges shield the rest of the rotor from the fields in the air gap and the potential in the rotor is zero, as shown by Equation 2.11 for $\Gamma = 0$. Since the stator charge distribution lies directly over the image charges on the rotor, there is no tangential field, the rotor charges feel no force parallel to the rotor, and there is no torque. Interestingly, the same result is obtained by modeling the entire rotor as a perfect conductor [75].

As the rotor slows from synchronous, or the stator wave speed increases, the charges on the rotor have less time to relax through the rotor and, in the frame of the stator wave, convection pushes their steady state position slightly downstream relative to the stator charge distribution. Because of this lag, a tangential electric field develops and toque increases until it reaches a maximum at $\Gamma = 1$.

As the rotor speed is decreased further, or the stator wave speed is increased further, convection begins to dominate and the charges have less and less time to develop in the first place. As a result, the torque falls off as the relative speed between the stator wave and the rotor is increased. In the limit of an infinite Γ, the rotor could be replaced with a perfectly insulating rotor to yield the same result.

The same torque curve shape can be produced with rotor sheet resistance as the abscissa. During this discussion the excitation frequency f_e and slip S are fixed. Setting the rotor effective resistance equal to zero also sets the charge relaxation time to zero by the definition

$$\tau_R = \varepsilon_{eff} \rho_{eff} . \tag{3.3}$$

Thus the charges induced on the rotor surface can immediately rearrange themselves by conduction, fields are again excluded from the rotor making its potential zero, and torque is again zero due to the lack of a tangential electric field. As the resistivity is increased, the charges on the rotor can no

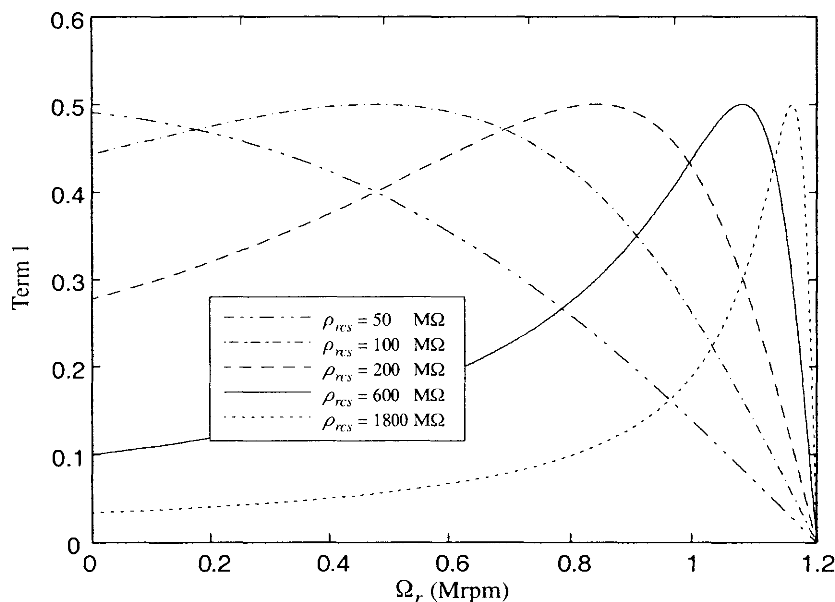

Figure 3.5: Term 1 from Equation 3.1 plotted as function of the rotor tip speed for a thin ring section of the rotor conductor located at $r = {}^{5r_o}/_6$. Other model parameters are found in Table 3.1.

longer conduct through the rotor as easily, so they lag their images on the stator and a tangential electric field develops, giving rise to torque. Again, the torque peaks when the charge relaxation time is equal to the slip time. As the resistivity is increased further, the charges continue to lose their ability to keep up with the stator charges in steady state, they loose the ability to develop, and torque gradually falls off to zero.

Note that the same argument could be made, hypothetically, by considering a change in the effective permittivity. However, it is easier to modify the conductivity of a solid material than it is to modify the permittivity. In addition, the torque is affected by changes in permittivity through other, much stronger interactions that are described below.

3.2.4 Rotor Insulator Performance Trend

Rotor insulator thickness is also set during fabrication, but the effects of non-optimum as-fabricated insulator thickness cannot be remedied by a shift in electrical excitation frequency as in the case of non-optimum rotor resistance or permittivity. This section describes the increase in performance possible via an increase in the rotor insulator thickness, while pointing out some design compromises that lead to the baseline value.

Figure 3.6 shows that a thicker insulator is desirable, but the benefits are limited. In short the trend is the result of the relatively high-conductivity substrate being brought into close proximity with the air gap. Recall from Chapter 2 that the substrate conductivity was assumed to be infinite. Alternate models that accurately account for the finite substrate conductivity show the same trends. Those models also show that as the conductivity of the substrate decreases, the torque generally increases. The perfect-conductivity models are retained because they are applicable to silicon substrates and physical phenomena are much more readily represented mathematically. Thus Figure 3.6 is a proper guide for coming to a compromise on an acceptable rotor insulator thickness.

There are several fabrication issues which lead to an upper bound on Δ_{ri}. The most important of these issues is the residual stress in deposited thick films which have been exposed to high temperatures. Silicon dioxide has been chosen as the rotor insulator in large part because it is the only insulator that can be deposited as a very thick film. To date, oxide films have been deposited in thicknesses up to 40 µm at MIT using a Novellus Concept-One™ Plasma-Enhanced Chemical Vapor Deposition system. After a high-temperature anneal, required for fusion bonding, the larger thickness films were found to have cracked. At the time of this research, the largest reliable thickness is the 10 µm specified in the baseline design, although recent work by the materials group of the MIT microengine project may lead to an increase for future devices. That work suggests possible thicknesses up to 20 µm, which would increase the maximum torque by 17%. However, the significant post-anneal residual stress causes the wafer to deform, making processing difficult because

many machines rely on vacuum to hold wafers in place. Wafer deformation also complicates wafer bonding because of the surface adhesion required to counteract the stress of deformation. Poor boding would result in a non-uniform or ill-defined air gap, leading to unpredictable micromotor performance. Thus, although torque could be increased, a greater oxide thicknesses is probably impractical. Alternate materials are needed, perhaps in the form of insulating substrates such as quartz or sapphire, although the high permittivity of sapphire could reduce torque significantly.

Underlying Physical Phenomena

The functional dependence of torque on rotor insulator thickness is the result of a capacitance voltage divider within this machine topology. The equivalent circuit in Figure 2.10 shows this voltage divider and captures the exact transfer function. To show this, note that the transfer function between $\hat{V}_2$ and $\hat{V}_1$ in the fields models is provided by Equation 2.11, where $\hat{V}_1 = \hat{V}_s$ and $\hat{V}_2 = \hat{\Phi}_{ri}$:

$$\hat{\Phi}_{ri} = \beta \cdot \frac{j\Gamma}{1+j\Gamma} \cdot \hat{V}. \qquad 3.4$$

Similarly, the transfer function from the equivalent circuit is computed as

$$\hat{V}_2 = \beta_{ec} \cdot \frac{j\Gamma}{1+j\Gamma} \cdot \hat{V}_1, \qquad 3.5$$

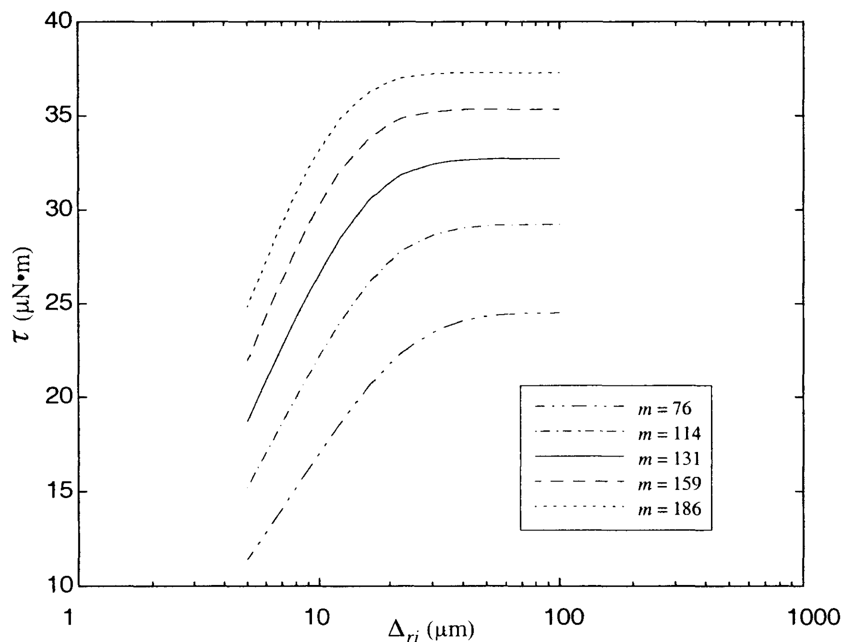

Figure 3.6: Peak mechanical power plotted as a function of rotor insulator thickness, for several values of m. Other model parameters are found in Table 3.1.

where Γ is defined as in the fields model. By substituting the definitions for the capacitances in the equivalent circuit, it can be shown that

$$\beta_{ec} = \frac{C_g}{C_g + C_r} = \frac{C_g}{C_g + C_{rg} + C_{ri}} = \beta. \qquad 3.6$$

Now the circuit model can be used to explain the trend of torque versus Δ_{ri}. Note that the relation for C_r, Equation 2.57, can be parsed into two parallel capacitors: C_{rg} and C_{ri}. One capacitor is primarily dependent only on kG and the other only on $k\Delta_{ri}$. Thus, as Δ_{ri} is increased the effective bulk capacitance of the rotor C_{ri} is increased, more of the current across the gap is shunted through the rotor capacitance making the power dissipated in the resistor R_r drop, and thus making the torque drop. Conversely, as the rotor capacitance decreases, the rotor voltage increases and approaches a limit, which approaches unity as both rotor permittivity and kG become very small. In this ideal case C_{sg}, C_{rg}, and C_{ri} vanish and the micromotor relaxation time is defined entirely by C_g and R_r. Thus, for best performance one would decrease the air gap G or increase the inner and outer radii.

Finally, it is important to note that the comparison to the circuit model is simple in part because the rotor substrate has been modeled as a perfect conductor. Other substrates could exhibit a higher resistance, like the rotor conductor. In that case, referring again to Figure 2.10, there would be two voltage dividers and thus two terms like Term 2. In this case, the machine would exhibit two charge relaxation times: one related to the rotor conductor and one related to the slightly conducting substrate. The models generated in Chapter 2 would require modification to predict machine performance.

3.2.5 Periodicity Performance Trend

Periodicity m is constrained by the techniques of microfabrication. Its value is based on the inherited geometry, the resolution of available lithography tools, and the upper frequency limit of the drive electronics. As with the insulator thickness, the baseline value is the maximum value allowed by the constraints. In this case, it is the constraints of photolithography that dominate.

Returning to Equation 3.1, Term 3 suggests that torque increases linearly with periodicity to first order, but then falls off exponentially. However, Figure 3.6 shows a linear dependence on periodicity with only slightly diminishing returns as periodicity is increased. In actuality, all three terms highlighted in Equation 3.1 are functions of periodicity, but maximum torque is plotted in Figure 3.6 so Term 1 is optimized to 1/2 in that figure. Regardless, it is shown below that the decrease in peak torque seen in Figure 3.6 is entirely attributable to a phenomenon described by Term 2.

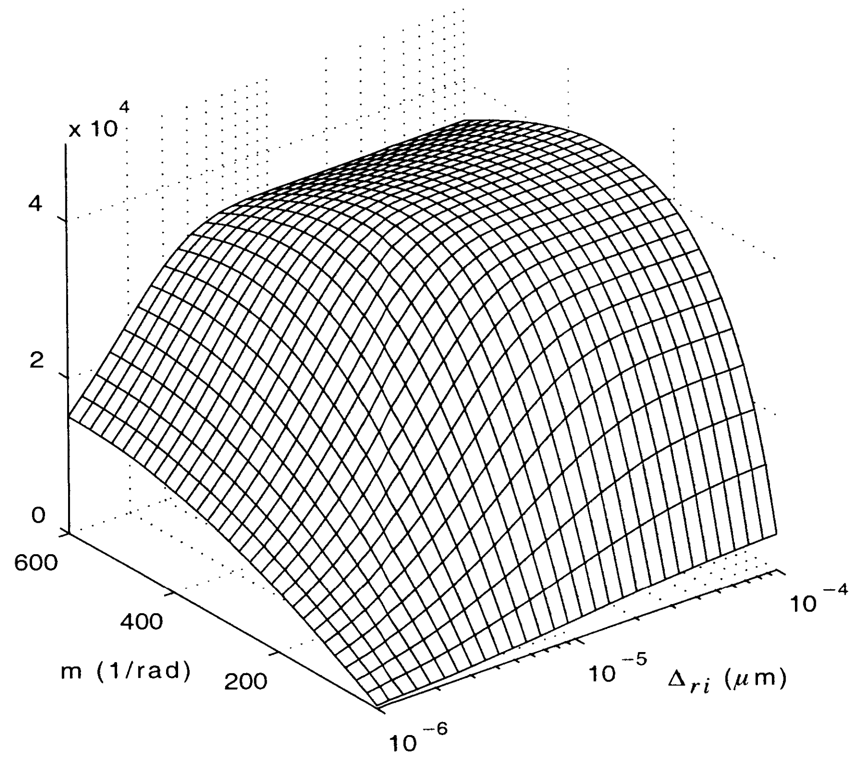

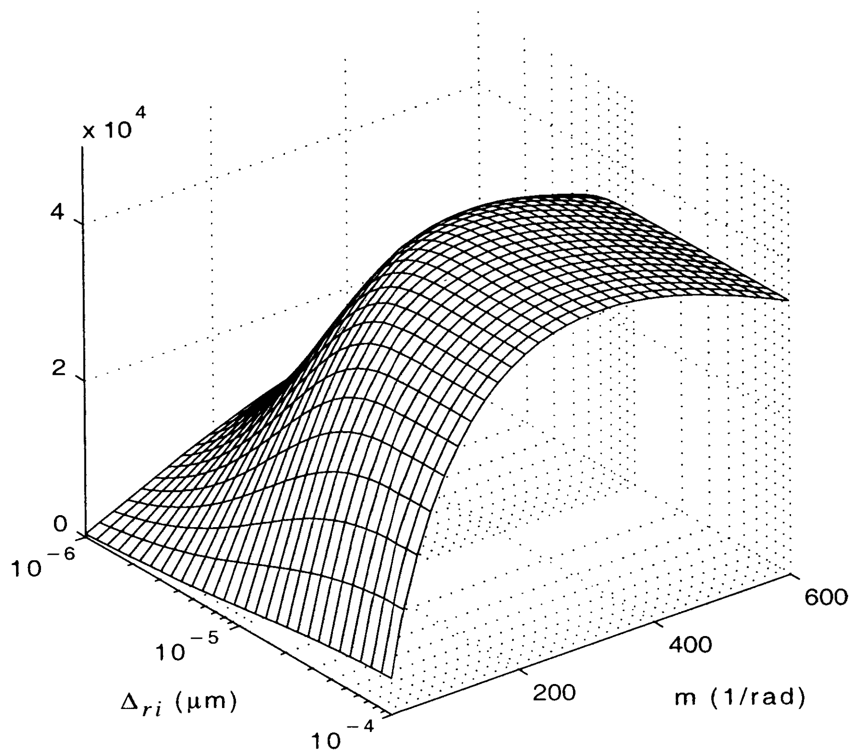

Figure 3.7: Term 2 times Term 3 of Equation 3.1 plotted as a function of the rotor insulator thickness Δ_{ri} and periodicity m. Other model parameters are found in Table 3.1.

Increases in maximum torque by increasing periodicity carry a cost when the overall electrical sub-system is considered. As the periodicity is increased, the electrical frequency must be increased to maintain the same synchronous speed. Losses in the electronics generally scale linearly with frequency.

Underlying Physical Phenomena

Periodicity effects can be found in both Term 2 and Term 3 as shown in Figure 3.7, but the phenomena at work are very different. For the baseline design, the largest of the two trends embodied in Term 3 is somewhat of an artifact of terminology. The torque predicted in Equation 3.1 is proportional to the magnitude of the shearing force per unit area calculated in Equations 2.20 and 2.27. That force is actually a Lorentz force due to the charges on the rotor surface being acted upon by the tangential electric field at the surface of the rotor. In order to see why the total force, and hence the torque, increases linearly with periodicity, consider a hypothetical case in which charge relaxation and charge convection can be held in balance, the rotor permittivity is very small, and $^{mG}/_{r}$ is small so that $\sinh(^{mG}/_{r})$ is well approximated by its argument. Through these requirements, Term 1 is fixed, Term 2 is maximized at 1, and

$$\text{Term 3} \cong \frac{mr}{G}. \qquad 3.7$$

Thus, all else held constant, the torque increases linearly with periodicity m. In the hypothetical case, the magnitude and relative phase of both the charge density and electric field distributions remain fixed as their spatial wavelength is decreased with increasing periodicity. Thus the average shearing force *per wavelength* is unchanged. Since the force density is inversely proportional to the wavelength as described in Section 2.1.2, the spatial rate of energy conversion increases with periodicity m, so for a constant motor size the torque increases. In other words, the total torque increases linearly with periodicity only in the way it is counted.

Next, Term 3 shows the effect of field decay across the air gap. In its exact form, with one factor of periodicity factored out, Term 3 is proportional to C_g, thus it is proportional to the electric field in the air gap. Mathematically, the complete Term 3 is found to be approximately linear until kG reaches about 0.75, corresponding to a periodicity increase to $m = 200$ or an air gap increase to 4.5 μm. As either the periodicity m or the air gap length G are increased further, the electric field lines emanating from one pole on the stator increasingly find their image charges on an opposing pole on the stator, rather than on the rotor. This effect is represented by a decrease in the gap capacitance C_g and an increase in the stator fringing capacitance C_{sg}. Note, at the same time, the rotor fringing capacitance C_{rg} also increases. In fact both C_{sg} and C_{rg} are very small in the baseline design, and the non-linearity of Term 3 is found to have only a second order effect on torque.

Table 3.2: Stator electrode geometry parameters. These apply to both the micromotor-compressor and the tethered motor.

Parameter	Value in Baseline Design	Symbol
Number of phases	6	N_p
Number of electrodes	786	N_e
Stator electrode thickness	1.0 μm	δ_e
Stator electrode inner width	4.0 μm	W_{ei}
Stator electrode outer width	11.2 μm	W_{eo}
Inter-electrode air gap	4.0 μm	G_{ee}

Finally, the primary reason that torque rolls off as shown in Figure 3.7 is found again through Term 2, i.e., β. Although the effect is more complicated in this case, it can still be attributed to the large rotor bulk shunting capacitance. The effect is more complicated because the effective length-scales through the micromotor are changed, rather than the individual thickness of the rotor insulator or the length of the air gap. It occurs because the field penetration depth, the depth where the field still has appreciable energy, is inversely related to the periodicity. Thus as the penetration depth decreases, the effective capacitor plates in the air gap appear to become further apart. Since an increase in air gap decreases torque, this effective increase in the air gap also decreases torque. Note that initially the decrease in penetration depth helps because the rotor shunting capacitance is effectively reduced. However, as the figure shows, the effective increase in gap eventually dominates and the torque rolls off.

3.2.6 Higher Harmonics

In general, higher spatial and temporal harmonics must be included in electric induction machine models for accurate torque prediction. Higher temporal harmonics can be beneficial because they add to the torque, but higher spatial harmonics will decrease performance [4, 31]. For the micromotor in this thesis, the power electronic drive is designed to produce a purely sinusoidal voltage so that there are no higher temporal harmonics of importance. Also, the stator electrodes are designed to greatly reduce the higher harmonics.

Recall that in the first 5 subsections of Section 3.2, it was assumed that enough stator electrodes were present to define a perfect sine wave of potential in space on the stator. This is actually untrue; it would be impractical to pattern and interconnect enough electrodes to do this. In fact, there are only six electrodes for each spatial wavelength of the stator potential. This and other additional stator geometry parameters needed for the multiple-harmonic model are listed in Table 3.2. With reference to Section 2.1.4, in the baseline design six electrodes per wavelength is enough to make most

higher spatial harmonics insignificant in the motor-compressor. Thus, the performance trends explored in the previous subsections are generally unchanged in form. The micromotor torque is simply scaled according to the weight of the fundamental spatial potential harmonic shown in Figure 2.8. This is untrue only for the trend in periodicity because the weight of the fundamental is a strong function of the periodicity. It is also important to note that higher harmonics may be important if some stator electrodes are improperly connected, or if some electrodes become damaged.

For the baseline design, the only effect of the 3D multiple-harmonic model is to provide the proper weighting of the fundamental stator spatial potential harmonic. Still, the results from the 3D multiple-harmonic model are the fourier superpositions of the results of several single-harmonic models, corresponding to each of the higher harmonics. As an example, the 3D multiple-harmonic model is used to produce the torque curve in Figure 3.8, which also includes the pull-in force and power output.

In addition, Figure 3.9 provides a direct comparison between results from the ideal single-harmonic and the multiple-harmonic models. The curves for each model show peak torque versus rotor insulator thickness since an increase in this thickness is probably the most near-term method of increasing torque. The plot shows the substantial difference between the ideal and the practical.

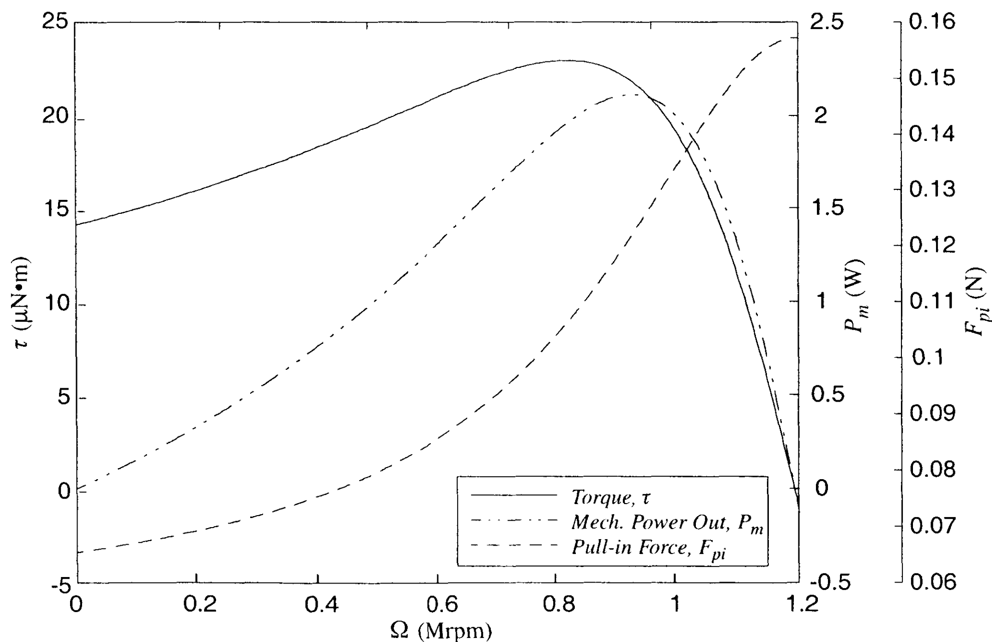

Figure 3.8: Electromechanical torque, pull-in force, and resulting power versus rotor tip speed. Other model parameters are found in Table 3.1 and Table 3.2.

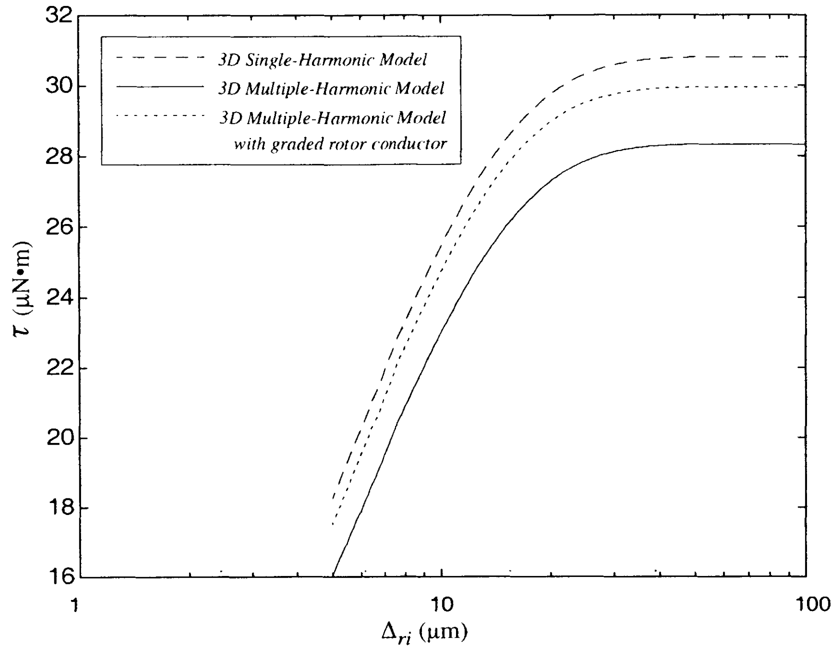

Figure 3.9: Peak electromechanical torque versus the rotor insulator thickness. Other model parameters are found in Table 3.1 and Table 3.2.

The figure also shows torque gains predicted with a specially modified rotor. There is at least one additional way of increasing the torque output in the baseline design. If the rotor conductor is fabricated so that the sheet resistance varies radially across the rotor conductor, in other words having a graded sheet resistance, then the balance between charge relaxation and charge convection can be obtained across the micromotor annulus. Recall that in the baseline design, the charge relaxation time is a function of radius. Mathematically, if the arguments of the sinh and cosh terms in Equation 2.44 are small, the rotor insulator is ideally insulating, and the rotor sheet resistance varies according to radius as

$$\rho_{rcs} = \frac{1}{r^2}\left[\frac{\tau^*_{eff}}{\left(\frac{\varepsilon_g}{m^2 G} + \frac{\varepsilon_{ri}}{m^2 \Delta_{ri}}\right)}\right], \qquad 3.8$$

where τ^*_{eff} is found approximately by solving the equation

$$\Omega_p = \frac{\omega_e}{m} - \frac{1}{m\tau^*_{eff}} \qquad 3.9$$

using a value of Ω_p either found from simulations or specified by a design constraint, then for a single rotor speed, the torque would be maximized at all radii. This generates the condition in which Term 1 in Equation 3.1 is optimized to 1/2 at every radius, a condition reflected in the curve plotted in Figure 3.9. Thus, if the rotor in the baseline design were modified to include a graded sheet resistance, a 16% increase in torque would be realized.

To produce the graded conductivity, either the rotor conductor thickness or its resistivity must be fabricated to have the functional dependence prescribed by Equation 3.8. This could require between 5 and 10 extra lithography steps and either extra etch steps or extra ion implants. For the purposes of this thesis the added fabrication complexity is unwarranted, but the method would be effective toward increasing torque, especially for micromotors of greater radial extent. Thus, perhaps a graded-resistance rotor could be used as a way of regaining the torque lost due to the small number of electrodes.

3.3 Stator Design and Optimization

Although the electrical efficiency of any electric induction machine can be improved using the methods of this section, the discussion is again focused on the micromotor-compressor application. Two broad optimization efforts have been conducted in the course of micromotor-compressor development, one is explained here and the other is the subject of another thesis [21].

The micromotor-compressor can be described in terms of two subsystems: the electromechanical subsystem comprising the power electronics and electric induction micromotor, and the compressor subsystem, as shown in Figure 3.10. The power electronics provide electrical excitation to the electric induction micromotor under the supervision of a controller that is not shown. The micromotor in turn converts this excitation to mechanical power to drive the compressor subsystem.

The first bubble of Figure 3.10 encloses the major design aspects that were varied in [21]. The goal of that optimization was to maximize the difference between the electromechanical output power of the micromotor and the power lost to the fluid in the air gap and bearings of the micromotor. The major results of that optimization are not reflected in the baseline design; they suggested a major change in geometry that would have made it difficult to use data on bearing behavior gathered using a micro-bearing rig [36] with the geometry reflected in the baseline design described in this chapter.

The beginning of this chapter deals entirely with this energy conversion process, while the optimization effort described here focuses on details of the stator wiring and power electronics, highlighted in the second bubble of Figure 3.10, to maximize the efficiency of the electromechanical subsystem. The term stator wiring refers to the lead interconnects, the vias, and the ring intercon-

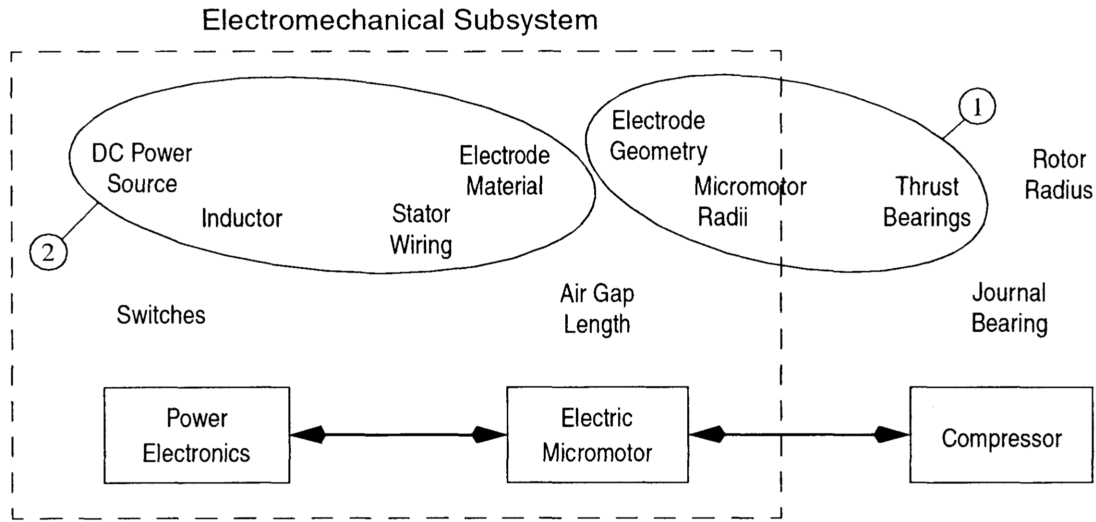

Figure 3.10: Major electric induction machine design aspects and their place in the context of system optimizations.

nects as defined in Section 2.3.3. To produce a model for use in the optimization, the single-phase equivalent circuit model for the electric induction micromotor, developed in Section 2.3 is combined with a model for one phase of the series resonant power electronics. When operating at resonance, these power electronics may be represented by the AC source and inductor shown in Figure 2.11. The model neglects losses in the switches that are used to implement the series resonant electronics.

Optimization Procedure

Together, the two models are used to predict the performance of the micromotor and to predict the losses in the stator wiring and drive inductor. This information enables the stator wiring, the drive voltage source, and the inductor to be optimized. It also allows recommendations for stator wiring materials beyond the current choice of heavily n-doped polysilicon. These results are combined to provide a full optimization of the micromotor stator, within the limits of the equivalent circuit model.

The optimization approach is straightforward using the equivalent circuit model in Figure 2.11. See Chapter 2 for a description of the parasitics which are being minimized. Four steps are taken for various combinations of stator lead interconnect widths, ring interconnect widths, and conductor materials. First, an initial geometry is chosen and the parasitic resistances and capacitances are computed. Second, the inductor is chosen to resonate with the rest of the equivalent circuit at the baseline excitation frequency of 2.6 MHz. Third, the source voltage in the power electronics is sized as a function of micromotor speed to provide the desired excitation voltage of 300 V peak at the branch point to the stator electrodes. This step takes into account the voltage drop across the

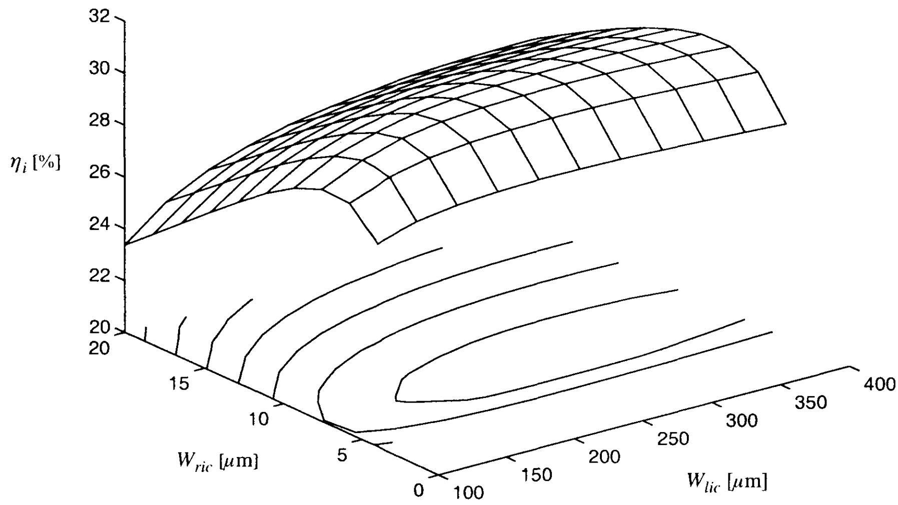

Figure 3.11: Maximum efficiencies, using polysilicon stator wiring, corresponding to combinations of stator lead and ring interconnect widths. See Figure 4.3 for an illustration of these components.

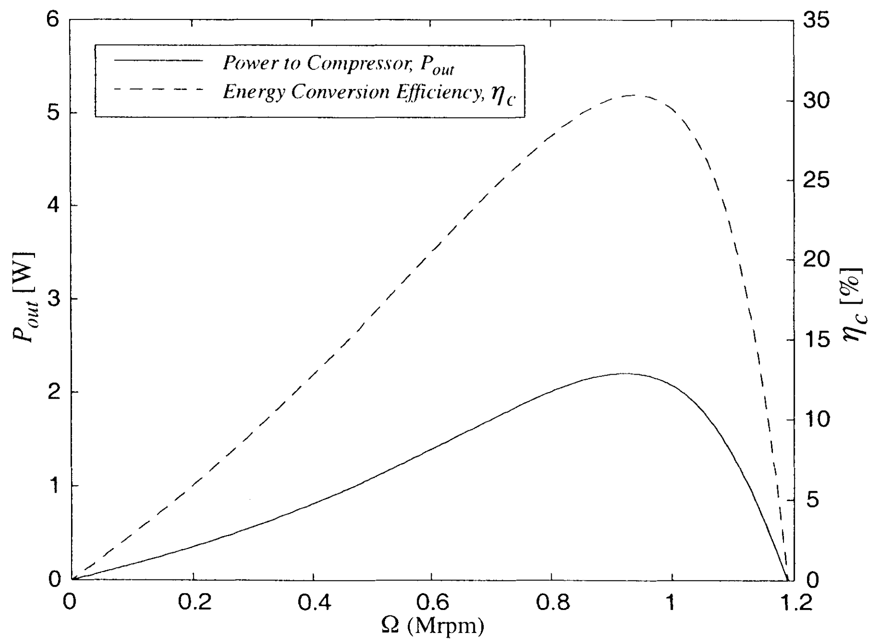

Figure 3.12: Predictions, using polysilicon stator conductors, of power out P_{out} and total efficiency of power conversion for operating speeds of the micromotor-compressor.

Table 3.3: Additional stator geometry parameters. These apply to both the micromotor-compressor and the tethered motor.

Parameter	Value in Baseline Design	Symbol
Stator insulator thickness	10 μm	Δ_{si}
Stator insulator (SiO_2) permittivity	$3.9\varepsilon_o$	ε_{si}
Stator lead interconnect thickness	1.0 μm	δ_{lic}
Stator lead interconnect width	200 μm	W_{lic}
Stator lead interconnect length	3.6 mm	L_{lic}
Stator ring interconnect thickness	1.0 μm	δ_{ric}
Stator ring interconnect width	8 μm	W_{ric}
Number of branch point fingers	7	N_{bpf}
Width of branch point	545 μm	W_{bp}
Stator ring interconnect mean radius	1.5 mm	r_{ric}
Inter-Level Dielectric thickness	1.0 μm	δ_{ILD}

lead interconnect resistance, but neglects that across the ring interconnects since the latter is actually distributed around the segmented annulus of the stator electrodes. Fourth, the power output from the micromotor, and the conduction losses within the inductor and the stator wiring, electrodes, and vias are calculated and summed, all as functions of micromotor speed. Finally, new stator wiring widths are chosen and the process is repeated over a matrix of lead interconnect and ring interconnect widths. The stator design that yields the highest peak efficiency over the speed range of the micromotor is chosen as the optimum design for that material. Efficiency is defined as the ratio of power output to the compressor, to power lost in the power electronics and stator wiring. Simultaneously, the optimization routine specifies the source voltage and inductor in the power electronics, and predicts the currents through all sections of the power electronics and stator wiring, all for the speed of maximum efficiency. The results of two optimizations are reported below, one for polysilicon stator wiring and one that also chooses the optimum wiring material.

3.3.1 Stator Optimization Results

Polysilicon Stator Optimization

The first design optimization concentrates on the use of heavily-doped polysilicon stator wiring since this is the material used in the first tethered motor and micromotor-compressor. The peak efficiency of the micromotor, over all speeds, as a function of the lead and ring interconnect widths is shown in Figure 3.11. Note that the peak efficiency from each of the power-speed curves that lead to these numbers, one of which is shown in Figure 3.12, occurs at different but very nearly equal

Table 3.4: Resultant specifications for power electronic components. These results are typical of the circuit model simulations.

Power Electronic Specification	Symbol	Polysilicon Design	Tungsten Design
Power Source Voltage	V_s	26 V	18 V
Inductor Size	L_{drv}	199 μH	235 μH
Current Rating (rms equivalent)	$I_{s\text{-}rms}$	65 mA	55 mA
Stator Terminal voltage	V_T	301 V	300 V
Terminal frequency	f_e	2.6 MHz	2.6 MHz
Assumed Inductor Q	Q_{Ind}	60	60

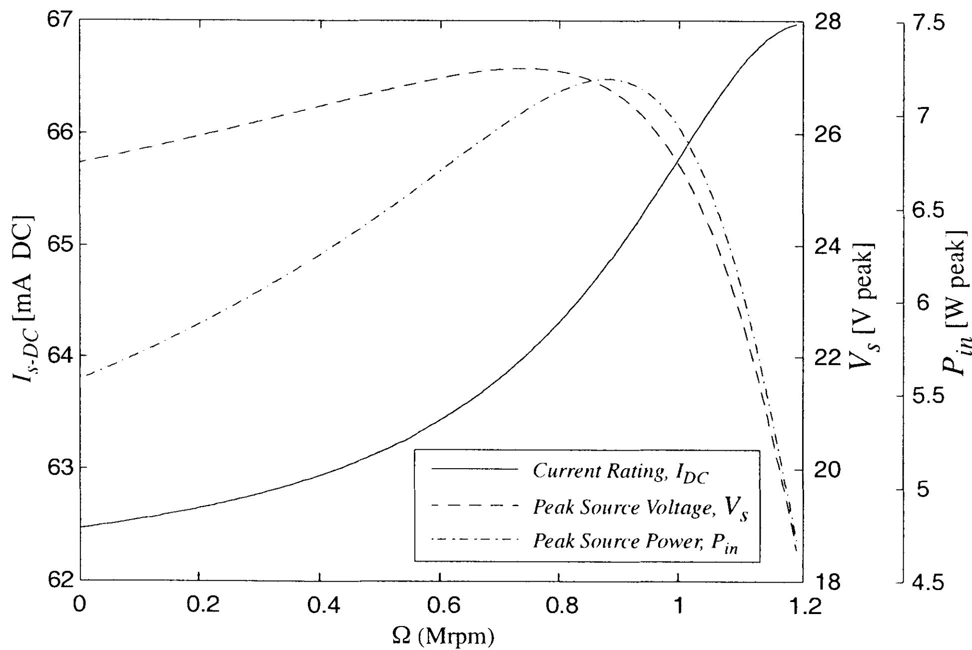

Figure 3.13: Predictions of power source requirements and current ratings for all expected operating speeds of the micromotor-compressor. The source power calculation includes only real, non-reactive power.

micromotor speeds for different wiring width combinations. This result is the basis for the stator wiring design given in Table 3.3 and used to produce the mask set summarized in Figure 4.3.

Three additional performance metrics are plotted in Figure 3.13. As mentioned above, the stator wiring optimization also specifies recommendations for these parameters, and they are listed in Table 3.4 for two different stator designs: the optimized polysilicon design and a tungsten design described next. The table provides a complete set of specifications for the power electronics for driving a micromotor-compressor. This model has also been used to provide specifications for power electronics needed to drive the tethered motor, which must operate at a variety of frequencies, making the power electronics much more difficult to build. This is a worthwhile endeavor, since these electronics could also be used to explore the operating space of the micromotor-compressor more fully and to compensate for as-fabricated differences in the rotor sheet-resistance as described in Section 3.2.3.

Metallized Stator Optimizations

In addition to heavily-doped polysilicon, many other conductors could be used for the stator wiring. It was selected for the initial micromotor because it is most readily integrated into the rest of the micromotor-compressor fabrication process flow, but the predicted energy conversion efficiency of only 30% motivated a search for a better conductor material. Here the initial field of candidates was large and included both metals and metal silicides.

However, major fabrication constraints quickly limited the field of conductors. First, high temperatures such as those encountered during fusion bonding were shown to cause undesirable agglomeration and/or oxidation of some of the candidates. Second, etch processes for some of the candidates were readily available. Third, deposition of some of the candidates was considered to be problematic. Fourth, the Microsystem Technology Laboratories at MIT prohibited fabrication with some candidate materials due to contamination concerns. Finally, there were material interaction concerns such as reaction and diffusion to be accommodated. After taking these concerns into consideration, the initially broad field was narrowed to those material combinations shown in Table 3.5.

Following the same iterative process described above for the polysilicon stator wiring, the stator is optimized again for each material combination in Table 3.5. Figure 3.14 shows the peak efficiencies from these optimizations. From the figure it can be seen that the efficiency generally increases as materials with higher conductivity are used, as expected. The best efficiency is obtained with stator wiring fabricated entirely of tungsten, and the geometry recommendations for tungsten stator wiring and polysilicon stator wiring are compared in Table 3.6.

Concerns over the possibly high residual stress in the metal films lead to a conductor thickness that is only one tenth that of the polysilicon wiring. There are also special considerations for some

Table 3.5: Material combinations yielding the data shown in Figure 3.14.

Material Combination	Ring Interconnect	Lead Interconnect
1	Polysilicon	Polysilicon
2	Polysilicon	CoSi
3	Polysilicon	WSi
4	CoSi	Polysilicon
5	Polysilicon	Co
6	Polysilicon	W
7	CoSi	CoSi
8	WSi	Polysilicon
9	CoSi	WSi
10	CoSi	Co
11	WSi	CoSi
12	CoSi	W
13	Co	Polysilicon
14	WSi	WSi
15	WSi	Co
16	Co	CoSi
17	WSi	W
18	W	Polysilicon
19	Co	WSi
20	Co	Co
21	W	CoSi
22	Co	W
23	W	WSi
24	W	Co
25	W	W

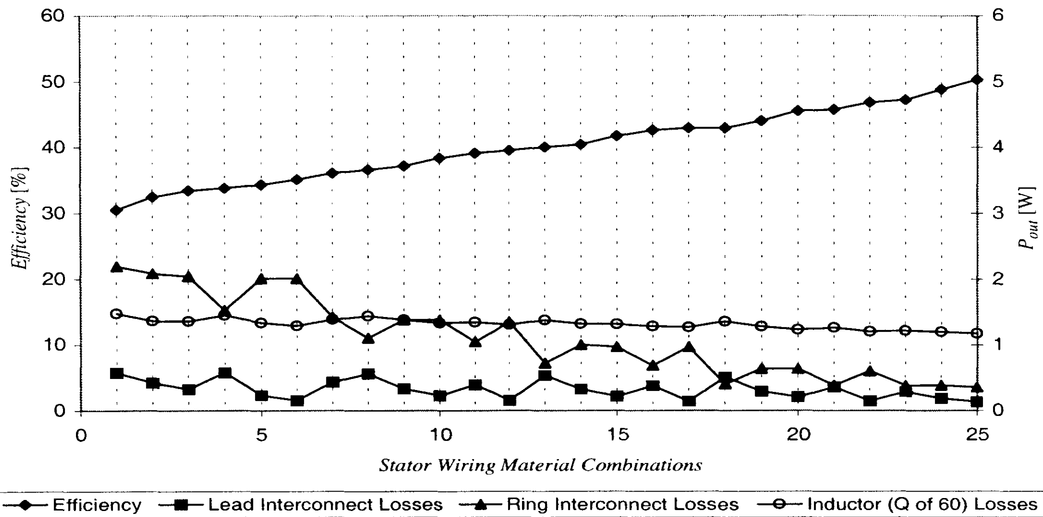

Figure 3.14: Electrical energy conversion efficiency for various stator electrical lead and interconnect combinations, plus the major sources of power loss in the electronics and stator. Table 3.5 contains the list of material combinations.

materials. For example, tungsten would need a cover-layer to provide a barrier against oxidation. Tungsten oxides are volatile at rather low temperatures, causing rapid material erosion during any temperature cycle above 500 °C. Even higher temperatures are required for fusion bonding. If larger thicknesses become possible, the peak efficiency can easily approach 60%. In this case the stator wiring will have negligible losses, 10% of the input power will be lost in the rotor conductor and 30% will be lost in the inductor. This optimization exposes the impact of inductor operation at high frequencies; the inductor Q is a decreasing function of frequency. When the wiring conductivity is maximized by using a material like Tungsten so that the width can be decreased and parasitic capacitance nearly eliminated, extremely good inductors still dissipate a large amount of power. This is because the inductors must still carry the power output load of the micromotor. The inductor quality factors listed in Table 3.4, which are very good for high voltage operation, have become possible only after a substantial optimization effort as part of the MIT microengine project.

Table 3.6: Optimized stator wiring designs.

Design Parameter	Symbol	Polysilicon Design	Tungsten Design
Lead interconnect width	w_{lic}	200 μm	85 μm
Ring interconnect width	w_{ric}	8 μm	5 μm
Lead and ring interconnect thicknesses	δ_{lic}, δ_{ric}	1 μm	0.1 μm

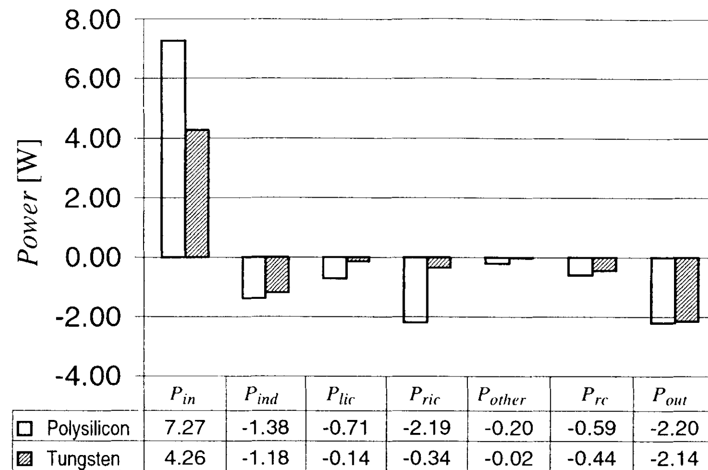

	P_{in}	P_{ind}	P_{lic}	P_{ric}	P_{other}	P_{rc}	P_{out}
Polysilicon	7.27	-1.38	-0.71	-2.19	-0.20	-0.59	-2.20
Tungsten	4.26	-1.18	-0.14	-0.34	-0.02	-0.44	-2.14

Figure 3.15: Breakdown of power losses during electrical energy conversion, shown in comparison to the power P_{in} drawn from the DC power source and the power P_{out} supplied to the compressor subsystem. Molybdenum gives results equivalent to those of Tungsten.

Power losses in the inductor and elsewhere within the electromechanical subsystem are compared to the input and output powers, and to each other, via the bar chart in Figure 3.15 for the optimized polysilicon and tungsten designs. The difference in the output power of the two designs arises only because the speed at which maximum efficiency occurs shifts slightly with respect to the rotor speed at which maximum power occurs for better conductors. The losses reported in the chart include those in the inductor P_{ind}, in the lead interconnects P_{lic}, in the ring interconnects P_{ric}, elsewhere in the wiring P_{other}, and in the rotor conductor P_{rc}. The large difference in stator wiring losses between the two designs may or may not be important for the micromotor-compressor application, but since minimization is the goal, a smaller power source will most likely always be preferred. Therefore, if possible, all future designs should incorporate metallized stator wiring where possible.

3.4 Tethered Rotor Design

3.4.1 Rotor Conductor Development

The rotor conductor required more development than any other part of the electric induction micromotor. Doped polysilicon was chosen because it is CMOS compatible and its resistivity can be drastically modified. The resistivity of polysilicon can be divided into three regions: lightly doped, moderately doped, and heavily doped [29]. For lightly doped polysilicon, conduction is dominated by thermionic emission over depletion regions at the grain boundaries. The lightly doped region is separated from the moderately doped region by the critical doping value. This is the dopant concentration at which all grain boundary traps are filled with carriers from the substitutional dopant atoms.

Beyond this concentration the free carrier concentration within the grain rapidly increases, thus rapidly decreasing the resistivity as the heavily-doped regime is approached. The barrier height also decreases with increasing doping beyond the critical doping, but thermionic emission plays a limiting role in the moderately doped region. Moderately doped polysilicon is extremely sensitive to the dopant concentration. Polysilicon is considered to be heavily doped for doping approximately an order of magnitude greater than the critical doping. In this region the barrier height and width have decreased significantly and free carriers nearly saturate the interior of the grain, therefore the resistivity is low and relatively insensitive to dopant concentration.

The baseline design called for a resistivity that was predicted to be within the moderately doped region. This is because the thickness was chosen to be 5000 Å so that it could be very well controlled with the available equipment. Doping beyond the critical value was preferred, however, because here the resistivity is primarily dependent on the implant dose and less dependent on the grain boundary structure. It was thought that the latter would be more difficult to control repeatable. Similarly, after several experimental iterations, Boron implantation was chosen over Phosphorus because Boron dopants do not segregate to the grain boundaries where they would be electrically inactive. The experimental results of this section confirm that the Boron dosage needed to reach the baseline resistivity lies just beyond the critical doping level.

The resistivity is measured using the structure shown in Figure 3.16, which is in part designed to emulate the structure of the electric induction micromotor, thereby permitting the use of the same

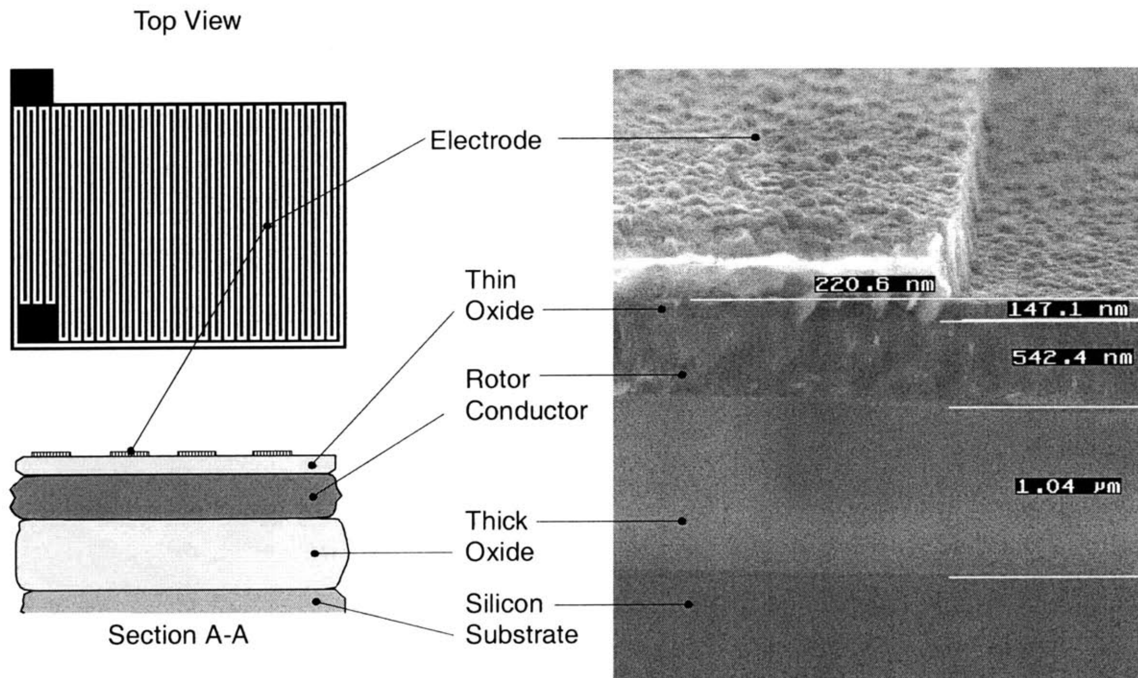

Figure 3.16: The rotor conductor test structure.

models developed in Chapter 2 to predict the impedance between the two terminals. The fabrication of these structures is outlined in Section 4.3.3 and described in detail in Section D.3. Most importantly, however, the structure makes a non-contact resistivity measurement possible. For lightly and moderately doped polysilicon, a substantial portion of the free carriers from dopant atoms become trapped in the grain boundaries, but may open states exist. In a contact measurement such as the four-point probe method, the electrodes inject carriers into the polysilicon that can fill some of the remaining charge traps in the grain boundaries. In this case, very little voltage is required to maintain the grain boundaries in this low-resistance, neutral state [29, p 241]. Thus the material appears more conductive to the observer. This phenomenon occurs for both n-type and p-type polysilicon, and a non-contact method avoids the issue.

Experiment Design and Procedure

The goals of the experiment were four-fold. First, the range of the dopant implant dose was modified through the initial experiments to find the a roll-off in at the critical dopant concentration — all implants in these trials were conducted with the same ion energy. Second, the batch-to-batch consistency of the out-sourced ion implant was verified. Third, the effect of Chemical Mechanical Planarization (CMP) of the PECVD oxide before polysilicon deposition was investigated. Fourth, the use of fine-grain polysilicon as a rotor conductor material was investigated.

In the course of the experiment 14 trials were completed, but only the last 6 provided reliable data. The first three trials attempted to measure the resistivity of polysilicon implanted with phosphorous since it was unknown at the time that phosphorous segregates to the grain boundaries, where it is unable to contribute to conduction [29]. The remaining experimental trials all used boron as the dopant species; boron does not segregate to the grain boundaries. The next five trials were used to refine the process and resolve various equipment issues. Results from these trials were significant with regard to the first goal above because they directed the experimental effort toward the final range of implant dose used in the remaining trials, but the results were too insignificant to warrant discussion here.

The final six trials produced the major results of the experiment. These consisted of three trials to measure the resistivity of lightly doped coarse-grain polysilicon deposited at 625 °C, and three trials to measure the resistivity of fine-grain polysilicon deposited at 585 °C. Due to the high sensitivity of resistivity to dopant concentration in the moderately doped region and the fact that the ion doses are much smaller than the average implant request, it was necessary to verify the implant vendor's ability to provide a consistent result in satisfaction of the second goal of the experiment. Therefore the wafer lot was submitted in three separate batches and the vendor was asked only to calibrate the ion beam to a specific beam current of 14.8 μA in order to be consistent with previous

trials. The implant batch is noted for each trial summarized Table 3.7. Doses range between 10^{12} and 10^{13}, while the implant energy is fixed at 180 keV.

The third goal exists because CMP could affect the surface roughness, changing the polysilicon as-deposited grain structure, and possibly changing the rotor conductor resistivity. Although the ideal process flow does not include CMP, the rotor lot used in devices that are tested in this thesis included a CMP step before rotor conductor deposition, so this goal is directly relevant to the results of this thesis.

Coarse-grain polysilicon is the primary form of polysilicon used for the experiments, but fine-grain polysilicon is also considered to satisfy the final goal of this experiment. Coarse-grain polysilicon has fewer grain boundaries and therefore fewer grain boundary charge traps. This allows the charge traps to be filled at a lower implant dose compared to fine-grain polysilicon, thus extending the moderately doped regime and possibly allowing greater control of the resistivity. However, grain growth during the high-temperature anneals that are required for fusion bonding in the micro-motor-compressor may be unpredictable. In all of the accepted conduction models for polysilicon, resistivity is a strong function of the grain size [29]. Grain size is a function of many variables, most notably the roughness of the deposition surface, the dopant concentration, and the length and temperature of thermal cycles in back-end processing. Thus it will be a challenge to the development of a rotor conductor to produce a predictable resistivity. Grain size and growth in doped fine-grain polysilicon may be less sensitivity to process variables, so three trials using fine-grain polysilicon are included to characterize and compare fine-grain polysilicon to course-grain polysilicon for use as a rotor conductor.

Table 3.7: Summary of rotor conductor experimental trials.

Trial	Number of Wafers	Polysilicon Type	Implant Batch	CMP of PECVD Oxide
A	5	Coarse-grain	1	Yes
B	5	Fine-grain	1	Yes
C	5	Coarse-grain	2	Yes
D	5	Fine-grain	2	Yes
E	7	Coarse-grain	3	No
F	7	Fine-grain	3	No

Results

Testing and analysis of completed devices is organized into several wafer fabrication trials and three strategies of testing the wafers in each trial. Each trial contained several wafers, one for each ion implant dose in that trial. Each wafer contained sixty 10×10 mm groups of four different device designs. The four designs formed a matrix of two coverage areas and two electrode line widths and are thus referred to as L1, L2, S1, and S2 on the plots in this section. The sixty die explored wafer-scale variation, arranged as an 8×8 matrix with the corners removed. After fabrication, a micro-probe stand was used to connect individual devices, chosen according to one of the test strategies, to an HP4194A impedance and phase analyzer which measured the total impedance and phase angle of the current with respect to the applied voltage as a function of frequency across the two terminals of the device. A Lab View front-end controlled the analyzer and stored the data in tabular form.

Figure 3.17 shows typical the raw data, with raw impedance magnitude converted to an effective capacitance by inverting it and dividing by the angular frequency. A model much like that described in Section 2.1.1 was then used to fit calculated impedance and phase angle to the measured values. In contrast to the models used in the rest of this chapter, this model allowed the rotor conductor to have any thickness, and allowed the rotor substrate to be a poor conductor. This allowed very accurate prediction of the current flow through the rotor conductor test structure which was then used to predict the impedance. The fit was obtained in two steps. First the permittivity of the oxide layers were adjusted to align the low-frequency capacitances, the layer thicknesses are known. Then the resistivity in the model was adjusted so that the calculated phase angle peak aligns

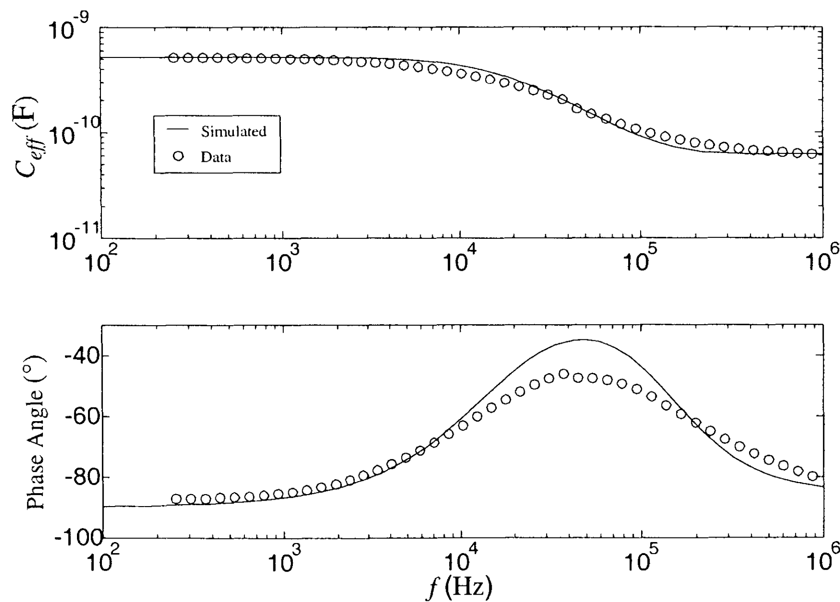

Figure 3.17: An example of raw data from the rotor conductor development experiment, with a fit to the raw data.

with the measured peak. The permittivity of deposited films in the equipment used in this experiment was shown to vary slightly from run to run. The matching procedure provided an indirect but accurate measurement of the polysilicon resistivity.

As mentioned above, three testing strategies were used to illuminate the most significant experimental results. The three testing strategies included: a 5-point measurement, a measurement of uniformity across the center of the wafer, and a detailed wafer-level uniformity measurement on two particular wafers. Each strategy used a different set of test structure designs.

Wafers from Trials A, B, C, and D were measured using the first strategy. All four device designs were used at each of five points on each wafer: the center, right, left, bottom and top. These measurements revealed the uniformity of the implant vendor's process, compared coarse-grain polysilicon to fine-grain polysilicon, and provided information on wafer-level uniformity.

For each type of polysilicon, the measurements from this strategy are grouped according to implant dose and measurement structure design, and then averaged within each group to produce Figure 3.18 and Figure 3.19. Although averaging across the two wafer batches obscures this, the data shows that one can expect the implant dose to differ by as much as 85% for low doses and as little as 5% for moderate and higher doses, from one implant run to the next.

In addition, a comparison of Figure 3.18 and Figure 3.19 suggests that fine-grain polysilicon may be a better alternative for the rotor conductor because the measured resistivity is very near the targeted baseline resistivity of $1{\times}10^4$ Ω-cm for the chosen range of implant dose. A detailed analysis of the data also shows that for doses between $5{\times}10^{12}$ to $7{\times}10^{12}$ cm^{-2}, the rotor conductor resistivity can be predicted anywhere on the wafer to within 20% for either type of polysilicon. The 5-point measurement thus provides a broad view of the ability to control resistivity across the surface of the wafer.

It should be noted that for some implant doses, the prediction capabilities can be much worse. For example, according to the data, at $3{\times}10^{12}$ cm^{-2} the uncertainty in predicted rotor conductivity can be as far off as 85% for coarse-grain polysilicon and 128% for fine-grain polysilicon. Regardless, the data clearly shows the roll-off of resistivity when the dose is increased, increasing the dopant concentration beyond the critical concentration. In addition, a comparison of Figure 3.19 to Figure 3.18 shows that fine-grain polysilicon requires more dopant to fill up the greater grain boundary area in that case, as expected.

The second testing strategy concentrated on the center of the wafer where an actual device wafer generally has the highest probability of yielding a functional device. In other words, this strategy yielded more specific information for the most useful part of the wafer. Two devices in the center four groups were measured on the wafers from Trials E and F.

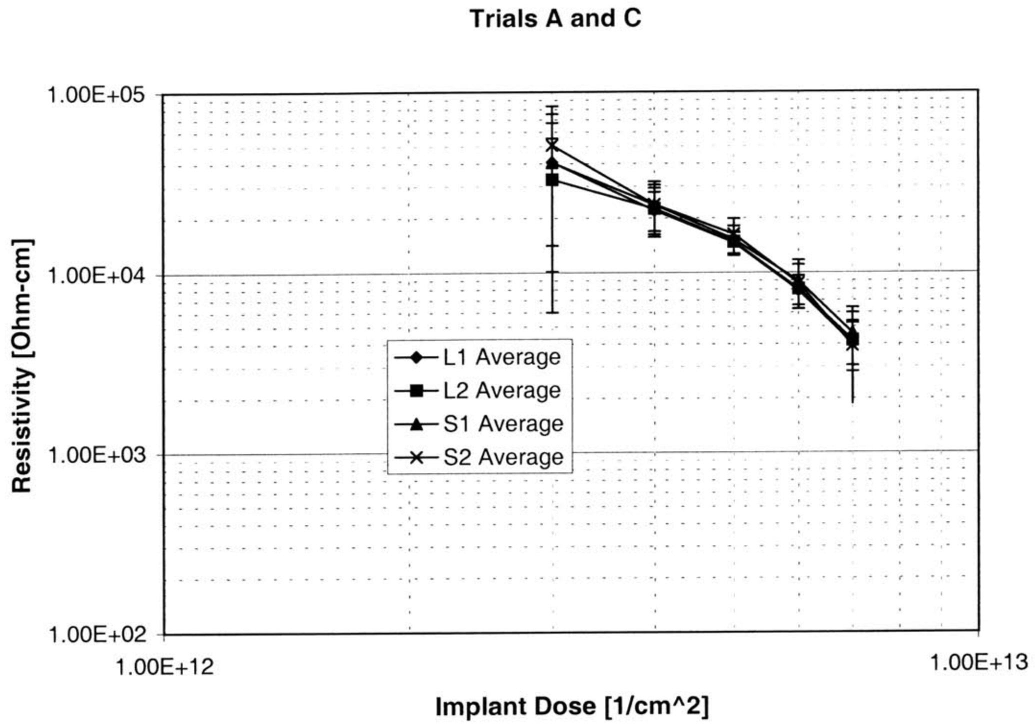

Figure 3.18: Coarse-grain polysilicon rotor conductor resistivity for Trials A and C, averaged for all measurements of like devices.

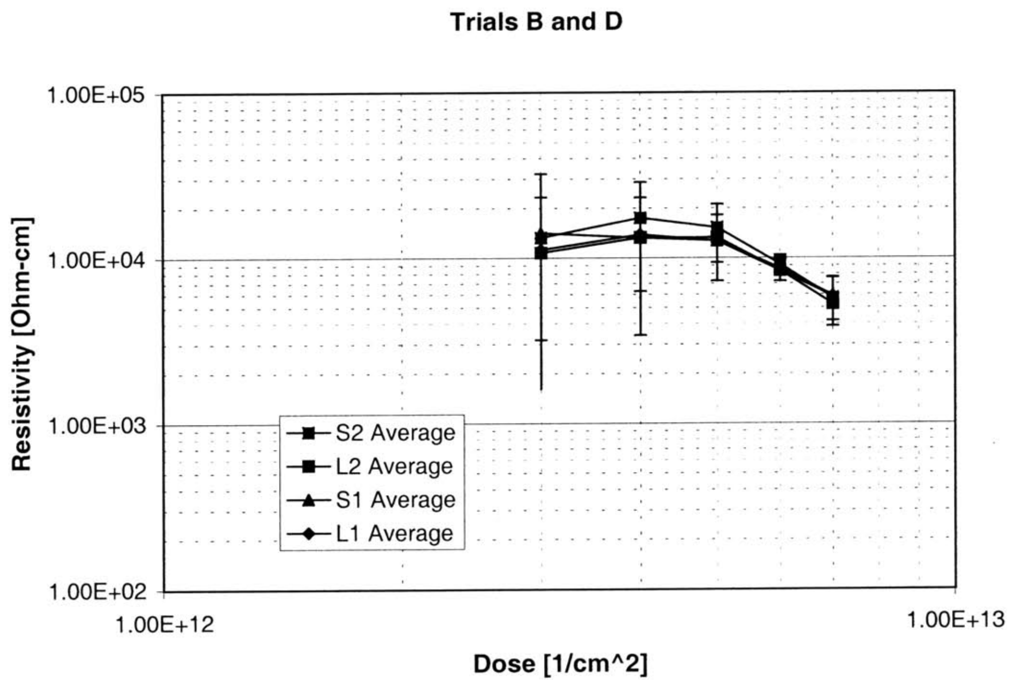

Figure 3.19: Fine-grain polysilicon rotor conductor resistivity from Trials B and D, averaged for all measurements of like devices.

Figure 3.20 plots the resistivity of 625 °C polysilicon at the center of the wafers from Trial E vs. implant dose. As the doping decreases from its maximum of 1×10^{13}, the resistivity increases to the target value of 10^4 Ω-cm at an implant dose of 4×10^{12} cm^{-2}, but note that the resistivity measured here is a factor of 3 lower than that from Trials A and C. This could be due to the CMP done on the thick oxide of these wafers. These trials show another interesting effect that was also found through some of the trials that are excluded from this discussion. As doping decreases further, the resistivity reaches of maximum but then declines for lower dose. According to the literature, the resistivity should level-off at around 10^6 Ω-cm for lightly doped polysilicon. However, the literature primarily considers light and moderate doping mainly with Phosphorus; studies on lightly Boron-doped polysilicon could not be found in the literature. For Phosphorus-doped polysilicon, grain growth is limited in undoped or lightly-doped polysilicon compared to moderately-doped or heavily-doped polysilicon. Conversely, the data here suggests that grain growth is actually retarded in moderately Boron-doped polysilicon. Further investigation is needed on this subject, but is not included in this thesis.

Figure 3.21 shows the measured resistivity of the 585 °C polysilicon wafers of Trial F. The basic trends are similar, but the maximum resistivity is higher and is attained at higher doping. Each of these are consistent with the fine grain structure of 585 °C polysilicon, compared to that of coarse-grain 625 °C polysilicon since the grains are smaller and there are more grain boundaries, and hence more grain boundary traps to fill to reach the critical doping concentration.

In the last test strategy, one device per group on one wafer from each of Trials E and F was used to measure the conductivity over the entire wafer. This strategy yielded more detailed wafer-level uniformity information than the 5-point measurement of the first strategy. Although the standard deviation was found to be quite modest, as shown in Figure 3.20 and Figure 3.21, the third test strategy revealed that the resistivity can be significantly higher on one side of the wafer than on the other. The measurements were made on one wafer from Trial E that was implanted with a dose of 3×10^{12} cm^{-2} and one wafer from Trial F that was implanted with a dose of 5×10^{12} cm^{-2}. These wafers were chosen because the measured resistivities were close to the value targeted in the baseline design. From the 585 °C polysilicon wafer, the mean resistivity was 23.4 ± 8 kΩ-cm, with a standard deviation of 34%. However, the minimum and maximum measured values differed by a factor of 3.4. From the 625 °C polysilicon wafer, the mean resistivity was 10.2 ± 5.1 kΩ-cm with a standard deviation of 50%. Here the minimum and maximum measured resistivities differ by a factor of 6.2. Layer thicknesses were carefully monitored during processing and were too uniform to account for the observed resistivity variation. In addition, the polysilicon grain size is expected to be uniform across the wafer surface, but this is unconfirmed. For these reasons and because of the

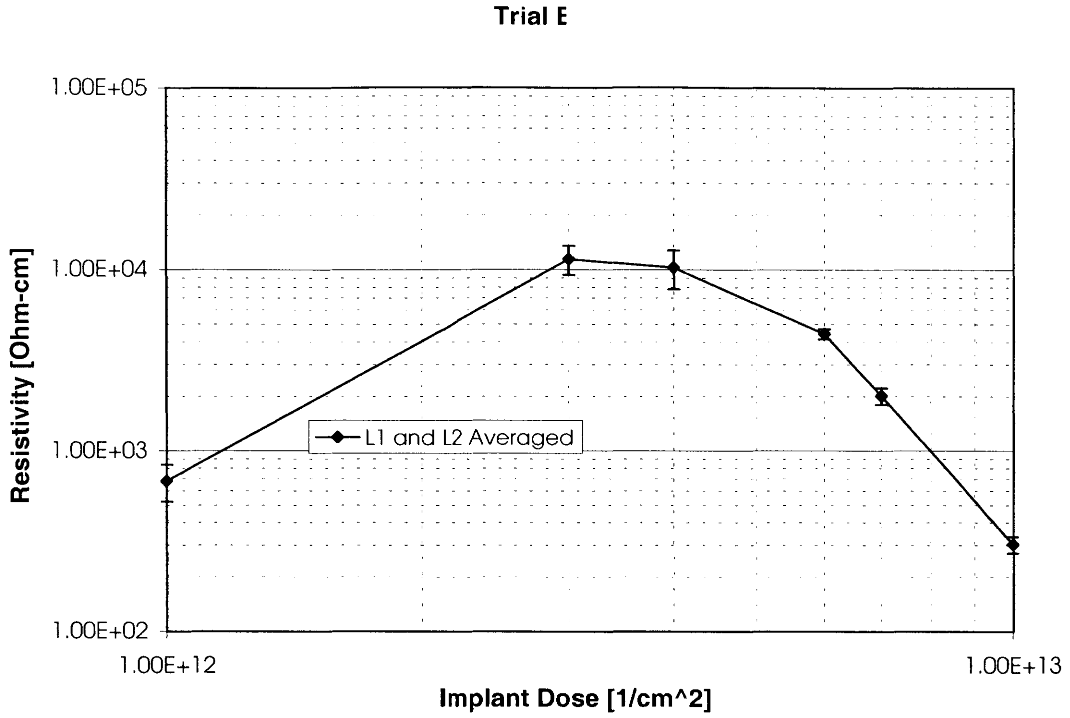

Figure 3.20: Coarse-grain polysilicon rotor conductor resistivity for Trial E, averaged for all measured devices. Plot courtesy of Dr. Carol Livermore.

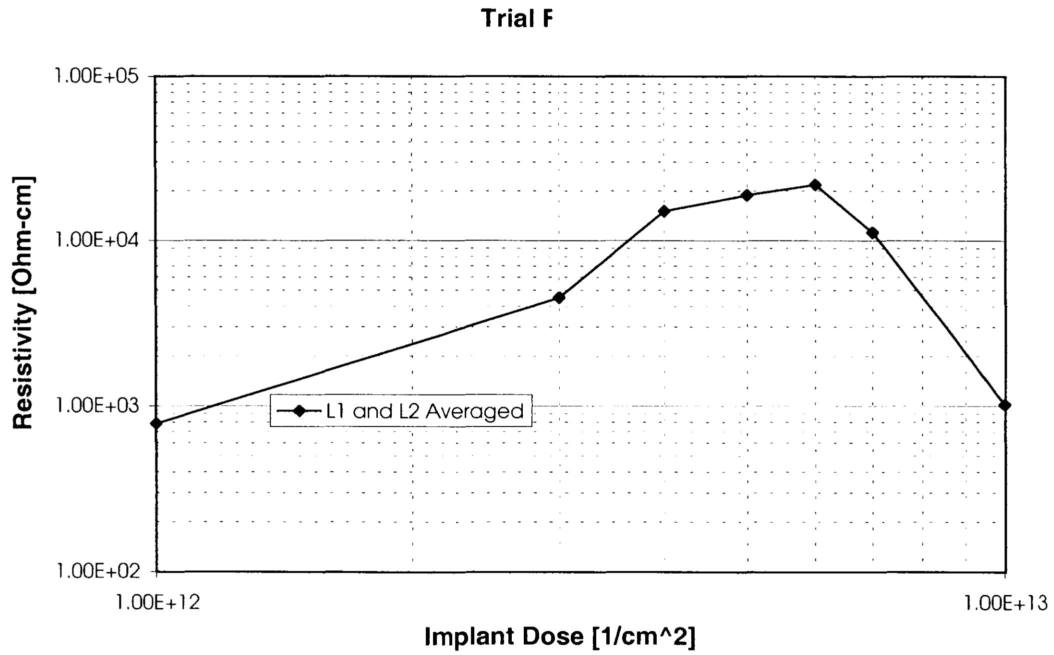

Figure 3.21: Fine-grain polysilicon rotor conductor resistivity for Trial F, averaged for all measured devices. Plot courtesy of Dr. Carol Livermore.

shape of the trend, the most likely cause of the variation is believed to be a non-uniform implant. It is conceivable that the beam current could change as it is rastered across the surface of the wafer.

Conclusions

There are many additional questions that could have be answered with several more experimental trials; but at this point it seemed that a process had been found to reliably produce a rotor conductor that would exhibit a suitably predictable resistivity across the center four die of the wafer. The results suggested that the desired resistivity of 10^4 Ω-cm could be obtained and that this resistivity could be predictably increased or decreased by a factor of two. The non-uniformity across a given wafer remained an issue of concern, but a functional device was still possible. Therefore 625 °C polysilicon was chosen and implanted with a dose of 5.5×10^{12} cm^{-2}, and the process was incorporated into the process flow of the tethered rotor.

Development of the rotor conductor process flow is described in detail in Section 4.3.3, but one outstanding issue should be discussed here. At present, there is a significant difference between the rotor conductor process flow when executed either within the tethered motor or micromotor-compressor fabrication, and when executed as part of test structure fabrication. In both the tethered motor and the micromotor-compressor flow, the last step of the rotor flow includes a high temperature anneal as part of a fusion bond. During this step, it is possible for implanted Boron ions to rapidly diffuse out of the polysilicon into the anneal furnace. As described in the process flow in Figure 4.6, the rotor conductor test structures incorporate an oxide layer during high temperature steps. This oxide covering prohibits the escape of Boron into the furnace; instead the Boron diffuses slowly into the oxide with some accumulation at the interface between the oxide and the polysilicon. Thus, it is possible that the rotor conductor in either the tethered motor or the micromotor-compressor will have a lower resistivity than that predicted by the test structures.

It was not mentioned above, but several wafers were included in the final trials of the rotor conductor development experiments to verify that dopant is lost from an exposed polysilicon surface, but only one wafer provided useful data because the other wafers were damaged by an equipment malfunction. This wafer showed a wide variation of resistivity across its surface, and the average resistivity was measured to be lower than in samples covered with oxide. Additional verification experiments were not conducted due to a lack of development time.

3.4.2 Tether Design

The tethered motor derives its name from the eight long, high aspect-ratio beams which tether the rotor to stationary supports and enable measurement of the torque supplied by the electric induction micromotor. The beams are designed to allow a large azimuthal deflection while being stiff enough to withstand the larger axial forces and maintain the air gap length. Thus the tethers must be very

tall, yet very thin. This high aspect-ratio demands the very challenging etch recipe described in detail in Section 4.3.4.

The experimental goal was to determine the as-fabricated stiffness of the tethers by exciting the first resonant mode of the azimuthal and axial directions. During normal operation of the tethered motor, both azimuthal and axial deflection would be measured. The measured azimuthal and axial stiffnesses could then be used to convert measured deflections into measurements of torque and pull-in force, respectively. With this method, torque and pull-in force can be measured as functions of frequency and voltage.

Nevertheless, it is important to estimate the expected deflections to guide the design of the tethered motor. To predict the response of the tethered motor, a mechanical model of the tethers is coupled to the distributed electromechanical models of Chapter 2. In actuality, the tethers are thin plates and the deflection of their ends is constrained to follow a circle with the radius of the tethered rotor. It is not the intent of this section to devise a rigorous mechanical model for this situation. The exact solution of this type of combined loading problem is beyond the scope of this thesis, and it appears that no solution is readily available in the literature [70]. Thus simple beam theory, that includes the constraints on deflection, is used to produce estimates of the predicted deflections.

For rotor deflection in the plane of the rotor, superposition is used to combine the effects of lateral forces at the ends of the tethers, bending moments at the ends of the tethers, and stretching of the tethers. This solution is accurate for small deflections and yields a reasonable result for larger deflections. For rotor deflection out of the plane, those that would decrease the air gap, simple beam theory is again utilized but this time the longitudinal stress is neglected because the deflections are much smaller. For small rotor deflections Θ_r and z_r, the model predicts the torques due to azimuthal and axial rotor deflections as

$$\tau_\theta = k_\theta \Theta_r + k_l \left(\sqrt{\left[L_T^2 - \left(2L_T r_T \left(1 - \frac{\pi^2}{8}\right) \Theta_r + \pi L_T r_T \Theta^2 + \frac{L_T r_T}{4} \Theta^3 \right) \right]} - L_T \right) \qquad 3.10$$

and

$$\tau_z = k_z z_r . \qquad 3.11$$

In these equations, the equivalent azimuthal bending stiffnesses is

$$k_\theta = \frac{12 N_T E_{Si} I_{az} r_T^2}{L_T^3} , \qquad 3.12$$

Table 3.8: Tether design parameters. These are specific to the tethered rotor.

Parameter	Value in Baseline Design	Symbol
Tether length	850 μm	L_T
Tether height	386.5 μm	h_T
Tether width	8.0 μm	w_T
Tether anchor point	2.1 mm	r_T
Number of tethers	8	N_T

the axial bending stiffness is

$$k_z = \frac{12 N_T E_{Si} I_{ax}}{L_T^3}, \qquad 3.13$$

and the non-linear longitudinal stretching stiffness is

$$k_l = \frac{N_T E_{Si} w_T h_T}{L_T} r_T \sin(\Theta_r). \qquad 3.14$$

Also, E_{si} is the elastic modulus of single crystal silicon, and the area moments of inertia are

$$I_{az} = \frac{w_T^3 h_T}{12}, \qquad 3.15$$

and

$$I_{ax} = \frac{w_T h_T^3}{12}. \qquad 3.16$$

All parameters in this mechanical model are listed in Table 3.8. Using those parameters, the linear stiffness terms are predicted to be

$$k_\theta = 19.3 \times 10^{-4} \text{ N-m/rad} \qquad 3.17$$

and

$$k_\theta = 102 \times 10^{4} \text{ N/m}. \qquad 3.18$$

When coupled with the predictions of torque in the electric induction micromotor, this model yields the approximate predicted deflection of the tethered rotor. Since beam theory underestimates the comparatively large stiffness of a plate with loading parallel to one of its edges while the other is clamped, use of this model overestimates the out-of-plane deflection of the rotor. Thus, the model

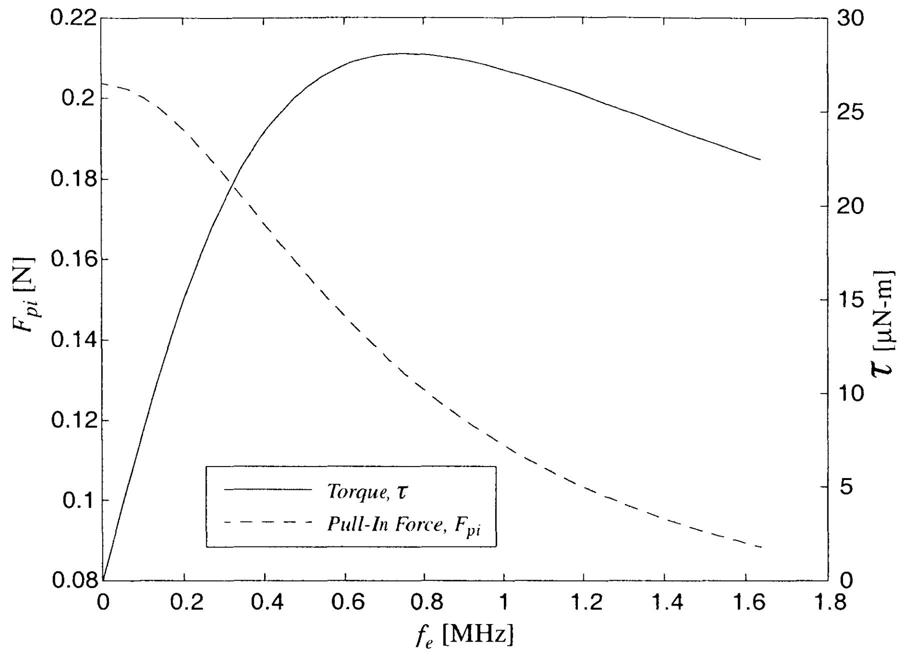

Figure 3.22: Predicted torque and pull-in force for the tethered motor.

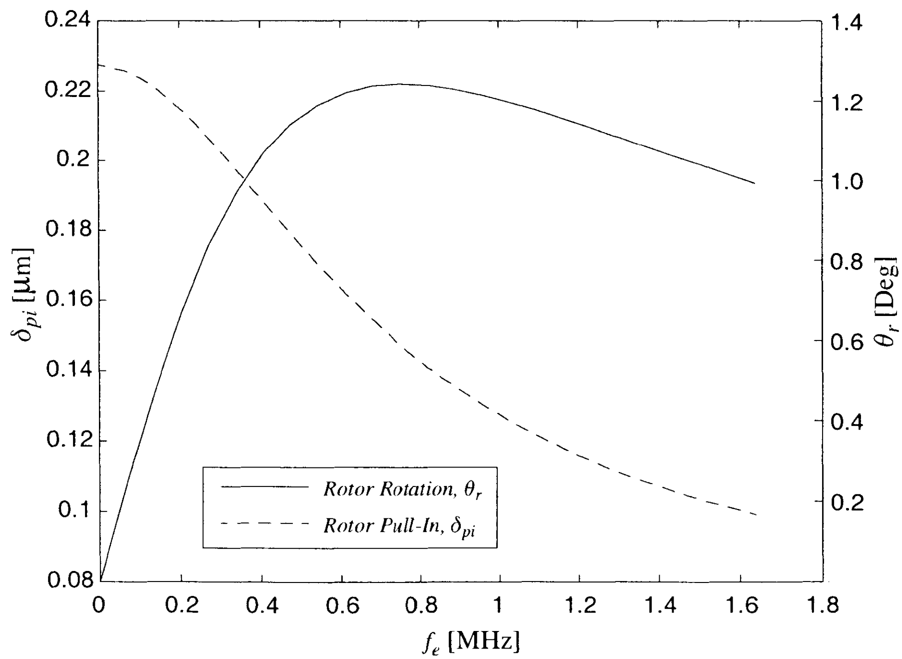

Figure 3.23: Predicted deflections of the tethered rotor.

provides a conservative estimate on the decrease in air gap length due to the pull-in force, while it gives a reasonable estimate of the in-plane motion resulting from micromotor torque.

Figure 3.22 and Figure 3.23 show the resulting predictions of torque, pull-in force and deflections as functions of stator excitation frequency given a 300 V excitation voltage and the tether design listed in Table 3.8. The coupled model is also used to generate tolerances on the tethers and other parts of the design that are to be maintained during fabrication. For example, if the excitation voltage remains set at 300 V, the as-fabricated air gap can be no smaller than 80% of its design value or the rotor will snap down immediately, contacting the stator and possibly ruining the device. In addition, these models suggest that if the tether width is reduced to 5 μm to gain more sensitivity to torque, then only a 10% reduction in air gap length is allowed before pull-in. If the air gap is improperly fabricated, the tethered motor cannot be operated at full voltage.

3.5 Tethered Motor Design Summary

In summary, the tethered motor is designed to investigate the electric induction micromotor design space, and is therefore primarily a metrology device. Thus, the tethered motor consists of two components: the electric induction micromotor designed above to drive the micromotor-compressor, and the tethers that serve as the mechanical transducer of torque to deflection. The models developed in Chapter 2 were used to predict the operating characteristics of the micromotor, and adjustments were made toward meeting the design goals as the underlying physics were explained to aid in future design processes. It was found that fabrication constraints play a pivotal role the design process, and these constraints dictate many aspects of micromotor geometry. The stator wiring of the micromotor was optimized to provide the best efficiency possible given the poor conductivity of the heavily-doped polysilicon, relative to other options that were also presented. The development of the very critical rotor conductor thin film was also described with comment on its physics and stability. Finally, a transduction method was found that is expected to interfere very little with the operation of the electric induction micromotor. As a result, a complete list of design specifications was generated for the tethered motor and is summarized in Table 3.9.

Table 3.9: Complete tethered motor design parameters, summarized for easier reference.

Parameter	Value in Baseline Design	Symbol
Stator rated voltage	300 V	$\hat{V}_s$
Stator periodicity	131	m
Stator-rotor air gap length	3 μm	G
Stator Excitation Frequency	2.6 MHz	f_e
Air gap permittivity	ε_o	ε_g
Air gap resistivity	∞	—
Rotor insulator thickness	10 μm	Δ_{ri}
Rotor insulator (SiO_2) permittivity	$3.9\varepsilon_o$	ε_{ri}
Rotor insulator (SiO_2) resistivity	1.0×10^{14} Ω-cm	ρ_{ri}
Rotor conductor sheet resistivity	200 MΩ	ρ_{rcs}
Rotor conductor thickness	0.5 μm	δ_{rc}
Rotor disk radius	2.0 mm	r_d
Micromotor inner radius	1.0 mm	r_i
Micromotor outer radius	1.9 mm	r_o
Number of phases	6	N_p
Number of electrodes	786	N_e
Stator electrode thickness	1.0 μm	δ_e
Stator electrode inner width	4.0 μm	W_{ei}
Stator electrode outer width	11.2 μm	W_{eo}
Inter-electrode air gap	4.0 μm	G_{ee}
Stator insulator thickness	10 μm	Δ_{si}
Stator insulator (SiO_2) permittivity	$3.9\varepsilon_o$	ε_{si}
Stator lead interconnect thickness	1.0 μm	δ_{lic}
Stator lead interconnect width	200 μm	W_{lic}
Stator lead interconnect length	3.6 mm	L_{lic}
Stator ring interconnect thickness	1.0 μm	δ_{ric}
Stator ring interconnect width	8 μm	W_{ric}
Number of branch point fingers	7	N_{bpf}
Width of branch point	545 μm	W_{bp}
Stator ring interconnect mean radius	1.5 mm	r_{ric}
Inter-Level Dielectric thickness	1.0 μm	δ_{ILD}
Tether length	850 μm	L_T
Tether height	386.5 μm	h_T
Tether width	8.0 μm	w_T
Tether anchor point	2.1 mm	r_T
Number of tethers	8	N_T

Chapter 4

Tethered Micromotor Fabrication

4.1 Introduction

Tethered motor fabrication is an intimate combination of surface micromachining and bulk micromachining. The device is built as an aligned two-wafer stack: a stator wafer and a rotor wafer. The fabrication process flows for both wafers are shown in Figure 4.1 with simplified views of the wafer cross-sections. Appendix D contains fully detailed process flows and cross-sections, with drawings of each mask pattern. A simplified illustration of the finished device is shown in Figure 4.2. In addition, Figure 4.3 overlays the mask patterns and summarizes the patterned features.

The stator was designed for use in either the tethered motor, or a micromotor-compressor. Thus, if necessary, the tethered motor stator wafer can be further processed for use in a micromotor-compressor device. The required extra steps can be found in [21]. Conversely, the process flow for the tethered rotor wafer is unique. This wafer can be used only for a tethered motor due to the incorporation of the deep high-aspect-ratio tethers necessary for torque measurement. In an ideal process flow, the stator and rotor wafers are ultimately fusion bonded to produce a set of tethered motor die ready for dicing, packaging, wire-bonding and testing. For reasons that will be described below, fusion bonds could not be attained and the tethered motors tested in this thesis were assembled at the die level.

This chapter describes the fabrication of the tethered motor. While the main purpose of this chapter is to provide a history of device fabrication, it also explains fabrication constraints that are inherent to the electric induction micromotor and either provides a solution to deal with those constraints, or suggests a solution. More fabrication development is necessary to build an electric induction micromotor using a fusion bond, and it is hoped that the information provided here will be used as a stepping stone toward that goal. More complete details, which would be helpful to fabricate another tethered motor or any electric induction micromotor, are provided in Appendix C in order to focus on key aspects of the process within this chapter. The chapter contains a summary of the total fabrication process flow, and then describes the key unit processes in detail.

Stator Wafer

1. Etch silicon pit; deposit thick oxide. Wet etch oxide where not over pit; deposit CMP stop oxide. Densify; CMP entire area. Etch-back.
2. Deposit LPCVD polysilicon, pattern and etch ring interconnect.
3. Deposit oxide inter-level dielectric; etch-back field level with pit oxide; CMP; pattern and etch vias.
4. Deposit LPCVD polysilicon. Deposit bonding oxide and CMP.
5. Wet etch to clear active area. Pattern and etch electrodes and lead interconnects.

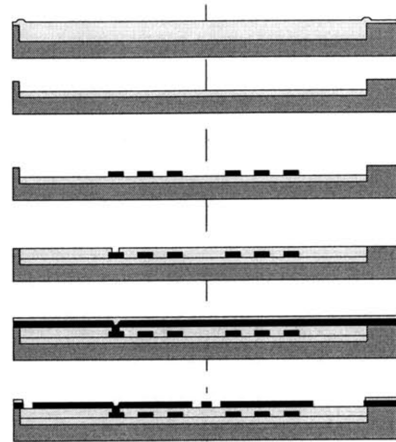

Tethered Rotor Wafer

1. *Top side (TS):* Etch ID marks and measurement patterns. Deposit tether etch mask oxide; densify.
2. *Bottom side (BS):* Etch silicon pit; deposit 90% of rotor isolation oxide; wet etch field oxide; densify. Deposit remaining rotor isolation oxide; densify. Possible CMP sequence.
3. *Both sides:* Deposit LPCVD polysilicon.
   BS: Deposit implant shield oxide; anneal. Implant with Boron ions, drive-in and anneal. Wet etch to remove implant shield. Pattern and etch rotor film.
4. *BS:* Pattern and wet etch remaining 10% field rotor isolation oxide.
5. *BS:* Attach carrier wafer.
   TS: Etch polysilicon layer; pattern and etch tether mask oxide.
6. *TS:* Deep RIE tethers and rotor disk; remove carrier wafer.

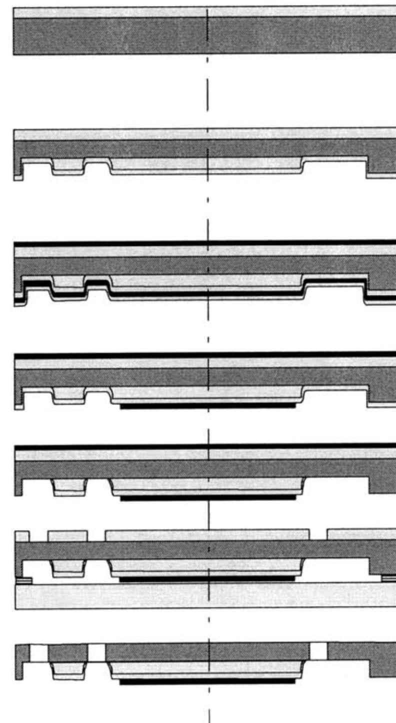

Silicon Polysilicon Oxide Resist

Figure 4.1: Simplified process flow representation for the tethered motor. Thicknesses have been exaggerated for clarity and only 3 ring interconnects are shown. See Figure 4.3 also.

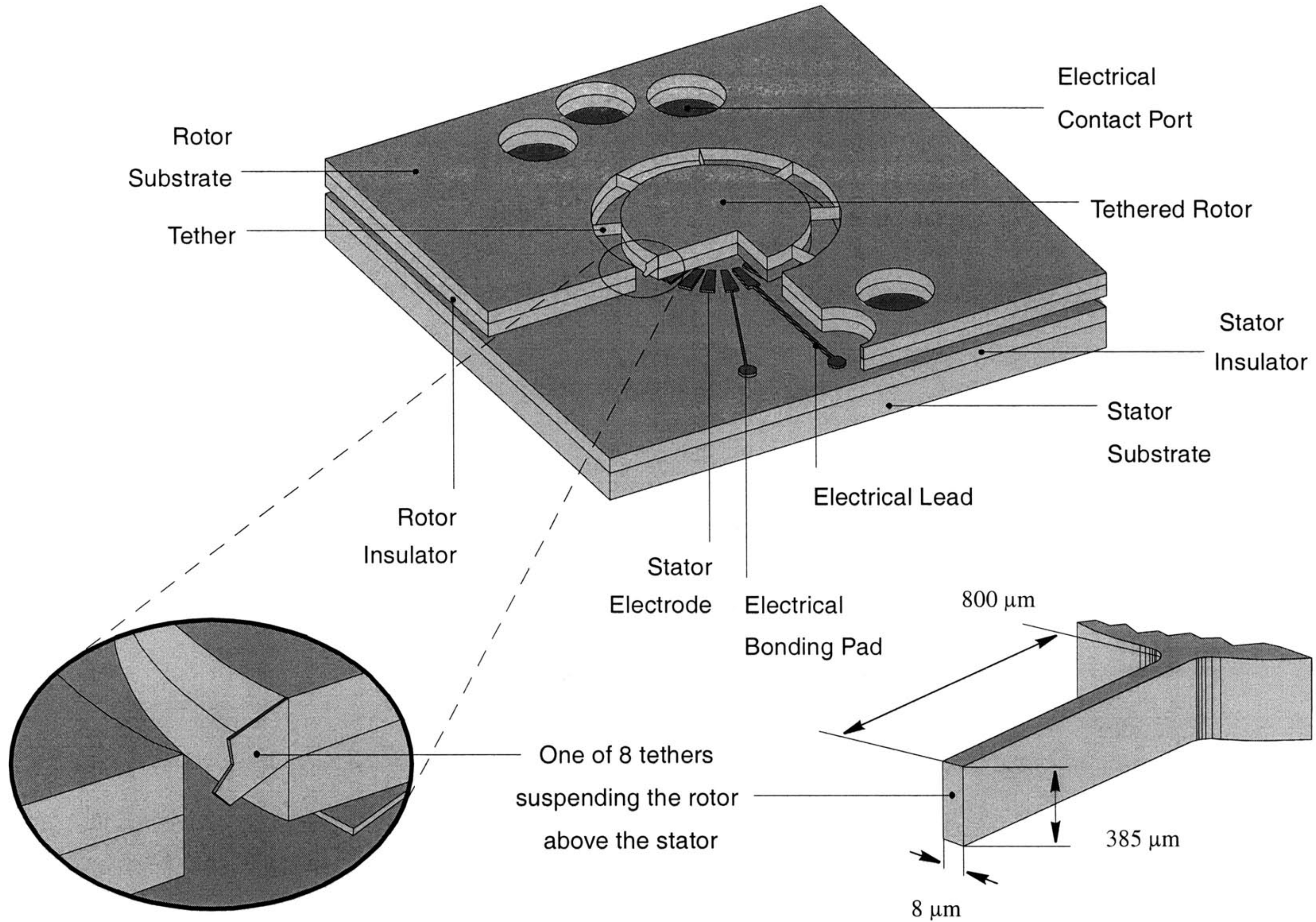

Figure 4.2: Illustration of the tethered motor with insets highlighting the tethers.

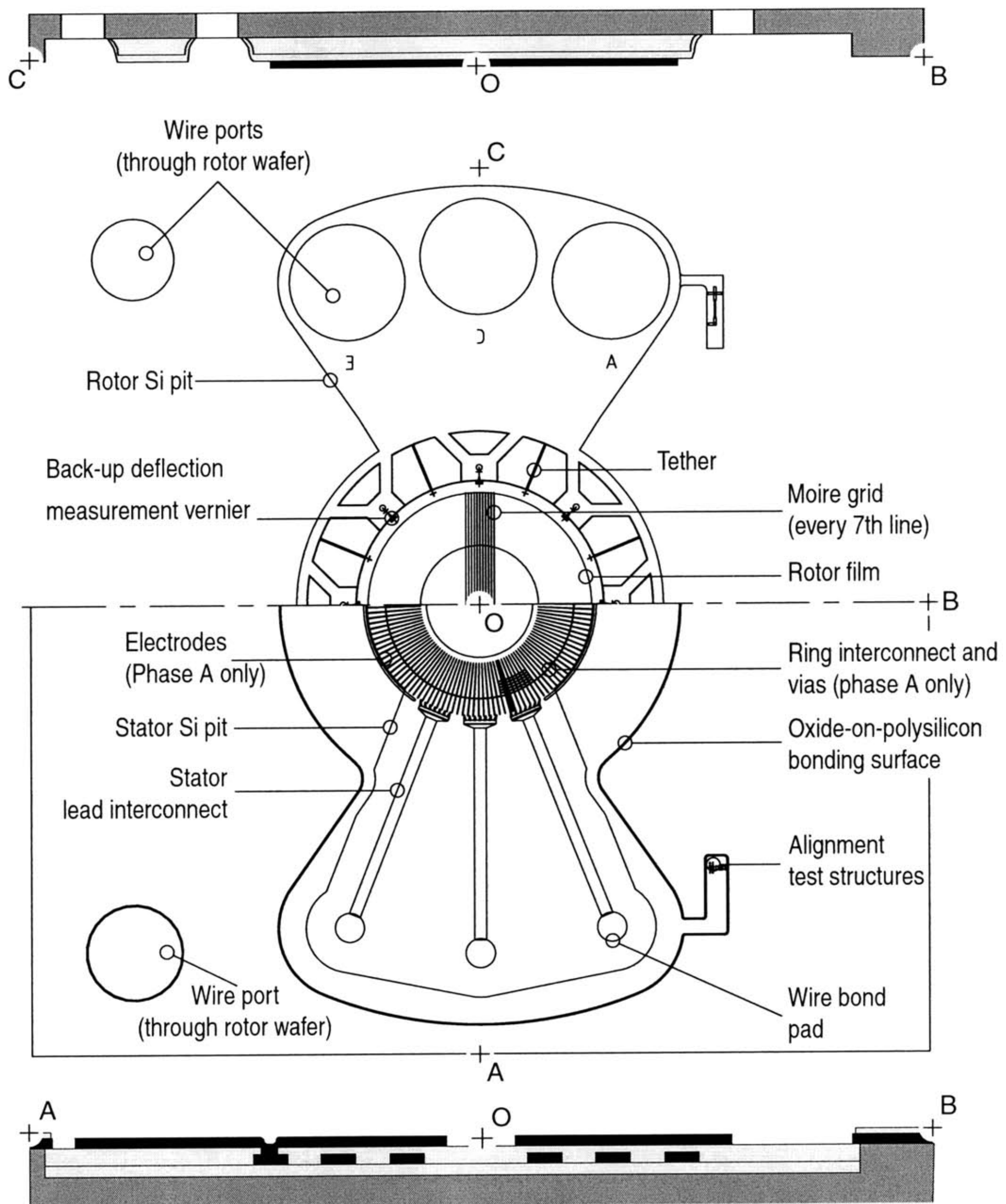

Figure 4.3: Cross-sectional and "unfolded" views for the two wafers of the tethered motor. To return to the device form, the wafer halves would be folded out of the page along the dashed line. The cross-section is not to scale and three ring interconnects are drawn instead of the full six.

4.2 Process Flow Summaries

The process flows for the stator and rotor are based on the designs described in Chapter 3 and involve several noteworthy fabrication challenges. Detailed process flow sheets are provided found in Appendix D. The process flows are summarized, followed in this chapter by detailed explanations of several unit processes. Together, the stator and rotor process flows involve over 180 steps, so there are many opportunities for defects to arise. In comparison, the first Intel Pentium™ processor involved around 200 steps, when steps are defined in a similar fashion. In this chapter, recipes are listed in Appendix E and referenced by their section number.

4.2.1 Ideal Stator Process Flows

The Stator Process Flow begins with a 450 μm double-side-polished wafer; includes two Chemical Mechanical Planarization (CMP) steps, two timed wet etches, and one timed dry etch. It also includes one particularly critical alignment near the tolerance of the contact alignment system. Of all steps in this process flow, Step 1 is the most aggressive. It begins with a 12 μm etch of the wide stator insulator pit using chlorine-based recipe E.3.1, the details of which are described in Appendix C. Next, the 12 μm stator insulator is deposited on the top surface of the stator wafer. The insulator was chosen to be silicon dioxide for reasons described in Chapter 3 and in particular a TEOS source was chosen for reasons described in Appendix C. All PECVD TEOS oxide depositions will be on only one side of the wafer unless otherwise noted. The oxide is not densified at this time. The insulator is first wet etched, using 7:1 Buffered Oxide Etch (BOE), from the entire field of the wafer, everywhere but in the 12 μm pit and a narrow lip, approximately 50 μm wide, surrounding the silicon pit. Next a 2 μm thick oxide CMP stop is deposited, again over the entire wafer surface, and the two films are densified at 1100 °C, for 1 hour, in either a Nitrogen or an Oxygen ambient. Finally, the wafer is planarized until the ridges are no more than 1000 Å high using CMP and the recipe described in Step 22 in Appendix D. Finally, a blanket wet etch is performed to remove any field oxide that remains after CMP and recess the stator insulator 2 μm into the silicon pit. The result of this step is referred to as recessed Thick Buried Oxide in Silicon (TBOS) and the motivation for its complexity is described in Section 4.3.1.

Step 2 defines the ring interconnects that define the six stator phases. In Step 4 each of these rings is contacted by the 131 electrodes of one phase, through vias defined in Step 3. Step 2 begins with the deposition of a 2000 Å etch-stop layer of silane-based PECVD silicon dioxide. Next 1 μm of LPCVD polysilicon is deposited at 625 °C. This coarse-grain polysilicon is heavily n-doped from a $POCL_3$ source at 925 °C and then anisotropically etched using the chlorine-based recipe E.3.2. More details are given in Appendix D.

Step 3 defines the inter-level dielectric (ILD) and vias that connect the electrodes of one phase to the ring interconnect for that phase. This step is similar to Step 1 in that ridges of oxide will be planarized, but it is less aggressive since these ridges are no more than 3 μm high, compared to 12 μm for the pit. First, 5 μm of PECVD TEOS oxide is deposited over the entire surface of the wafer and densified with the recipe in Step 1. Then the field region is wet etched 2 μm to bring it down to the level of the oxide over the pit region. Now the wafer is planarized, removing the ridges surrounding the silicon pit and the ridges over the interconnects, with the same CMP recipe used in Step 1, and then etched back to be level with the native silicon surface in the field. Next a 2000 Å TEOS-based PECVD silicon dioxide etch-stop layer is deposited, for use with the electrode etch of Step 4. Finally, vias that range in size from 2 μm square to 8 μm square are anisotropically etched through the ILD using CHF_3-based recipe E.3.3 described in Appendix E. The exact thickness of the ILD is not known at this point, so to ensure that the oxide is completely etched, precautions are taken. First the etch is stopped at an estimated 85% of the total etch depth and the remaining oxide films in the vias are visually characterized by the light interference in the films. Thus the initially uncolored vias now appear colored under the microscope. An estimate of the remaining oxide is made, and the etch is continued until it is believed that the vias are clear, at which point they are examined again. If there is no color in the smallest vias, then all vias are assumed to be clear, and to clear any residual oxide the wafer is etched an additional 10% of the total time to this point. However, if the vias still appear colored, the process is repeated. The vias must be completely clear of any oxide or the electrodes will not make proper electrical contact with the ring interconnects.

In Step 4 the electrodes and lead interconnects are deposited. First another 1 μm layer of LPCVD coarse-grain polysilicon is deposited, again at 625 °C. Then it is heavily n-doped from a $POCl_3$ source and the doped glass is removed.

Step 5 adds a thin layer of oxide intended to promote a fusion bond to the rotor wafer, and defines the electrodes. First a 2000 Å PECVD TEOS oxide layer is deposited. Then the oxide is polished using a short CMP recipe designed to give a surface that adhere well to another similarly prepared surface. The oxide is wet etched over the area over the silicon pit, defined as the active area of the stator. Finally, the lead interconnects and electrodes are patterned and etched as in Step 2.

4.2.2 Ideal Rotor Process Flow

The Rotor Process Flow involves processing on both sides of a 400 μm double-side-polished wafer. In Step 1, 2 μm deep features are first etched into the top-side of the wafer. These include identification codes and marks that could be used to measure rotor deflection. Then a 3 μm silane-based PECVD oxide layer is deposited and densified. This layer will be a hard mask for the tether etch at the end of the process flow.

Step 2 recesses the active surface of the tethered rotor and begins the definition of the air gap. On the bottom side, a 13.5 μm silicon pit is etched, again with the chlorine-based recipe E.3.1, using either an oxide hard mask or a soft mask of AZ-P4620 thick resist. Next a 9 μm oxide film is deposited and cleared from only the field of the wafer with a wet etch, after the tether mask is protected with a layer of resist. In this flow, the remaining oxide does not cover the walls of the silicon pit; it is contained entirely within the pit. Then the remaining 1 μm of the rotor insulator is deposited and the complete film is densified. Finally, a profilometer is used to measure the thickness of the rotor insulator, and, if necessary, a timed wet etch is used to define the air gap, since the thickness of the rotor conductor is well-controlled in the next step. While the field oxide will eventually be cleared, the thick insulation oxide will not be touched after this step in the ideal process.

Step 3 defines the rotor conductor. A detailed description of the fabrication development required for this very essential thin film is found in Section 3.4.1 and Section 4.3.3. First, a 0.5 μm coarse-grain LPCVD polysilicon layer is deposited at 625 °C, on both sides of the wafer. Next, a 2500 Å implant shield of silane-based PECVD oxide is deposited on the bottom-side and densified at 950 °C to limit grain growth in the polysilicon. The bottom-side is then implanted with a Boron dose of 5.5×10^{12} ions/cm^2 and the wafers are annealed at 1000 °C to drive in the dopant ions and repair crystal damage due to the ion bombardment. Next the implant shield is removed with a wet etch and the rotor conductor is patterned and isotropically etched using the SF_6-based recipe E.3.5.

Step 4 simply removes unneeded films. The oxide and rotor film are patterned and the field oxide removed with a wet etch in 7:1 BOE. Then the wafer is flipped over and the polysilicon is removed from the top side of the wafer.

Step 5 prepares the wafer for the tether etch. First, the tether etch hard-mask is patterned using 2 μm OCG 825 resist. Then the rotor wafer is attached to a quartz carrier wafer using a narrow ring of thick resist around the perimeter of the carrier wafer. This carrier wafer is necessary because the P5000 can damage the surface of a wafer either because of defects on the surface of the metal spatula used to move wafers or because there could be debris present on the wafer chuck in the etch chamber or both. Finally, the 3 μm thick silicon dioxide tether mask is etched in the P5000 using recipe E.3.3 and the same method as for the stator vias to detect etch completion. The carrier wafer is removed and all resist cleaned in a standard piranha solution. At this point some wafers also received a 2000 Å sliane-based PECVD oxide that was then polished to promote bonding to the stator wafer, see the section on wafer bonding below.

Step 6 is by far the most critical step of the tethered rotor process flow, it defines the deep high-aspect-ratio tethers. The development of the etch recipe is described in Section 4.3.4. First, a quartz carrier wafer is attached as in Step 5. Then the tethers are etched using the Bosch process in an inductively-coupled-plasma, deep-reactive-ion etcher from Surface Technology Systems (STS).

The tether pattern is etched until approximately 30 μm remain out of the total 386.5 μm. Then the quartz carrier wafer is replaced with a silicon carrier wafer and the etch is continued until it is complete. Section 4.3.4 explains the need for this last step, and gives other details about this very critical etch. Figure 4.4 shows pictures of a finished rotor.

4.2.3 Actual Process Flows

The stator and rotor wafers used to build the two devices that were tested in this thesis were not necessarily processed exactly as described above. Both devices used the same rotor process flow, which was only slightly different. In one device, the stator was essentially fabricated using the ideal process. For the device that yielded experimental results, the stator was very different. See Table 4.1 for a brief description of the assembled and tested devices.

The stator wafer for device TMA came from an early process development lot called mcstat1 used to develop the more straight-forward parts of the process. The wafers used for mcstat1 were single sided 525 μm thick and the process flow did not include TBOS, instead it used a 5 μm blanket coat of oxide for the stator insulator. In addition, the vias were wet etched because the etcher used in the anisotropic recipe had been inoperable for several weeks. Finally, the electrodes were etched with a different recipe that lead to very rough sidewalls. Since rough sidewalls could result in a much lower breakdown voltage between electrodes, recipe E.3.2 was developed. At the time the first rotor wafers were ready, wafers from mcstat1 were the only stator wafers available, so they were used with a rotor wafer that had broken, but was not destroyed, at the end of its fabrication. See Section 4.5 concerning the assembly of a motor using these wafers. Some SEM pictures of a wafer from lot mcstat1 are shown in Figure 4.5.

For the remaining devices, the stator came from the last lot processed, mcstat9, and the process flow differed from the ideal flow only by a metallization layer at the end of the lead interconnects so that gold wire bonding could be done at room temperature. After Step 5 in the stator process flow, the wafers then received a 1 μm Aluminum layer. This layer was formed using image-reversal resist in the lift-off process E.2.4. The Aluminum was deposited in a Temescal electron beam system.

Furthermore, for every rotor wafer used in this thesis, the process flow included a CMP step. For reasons that were never determined, pillars of silicon remained in the rotor insulator pit after the 13.5 μm etch of Step 1. Refer to the section of Appendix C entitled "Intermediary Etches" for a discussion of this problem. The pillars were planarized somewhat by the oxide depositions and their slight reflow during anneal, but the pillar height remained high enough in some cases to cross the air gap. Therefore a sequence of oxide deposition, timed field etch, CMP, and field oxide removal was added to the flow. There is little doubt that these extra steps increased the surface roughness, possibly affecting the grain size of the rotor conductor, thereby affecting the sheet resistance in an char-

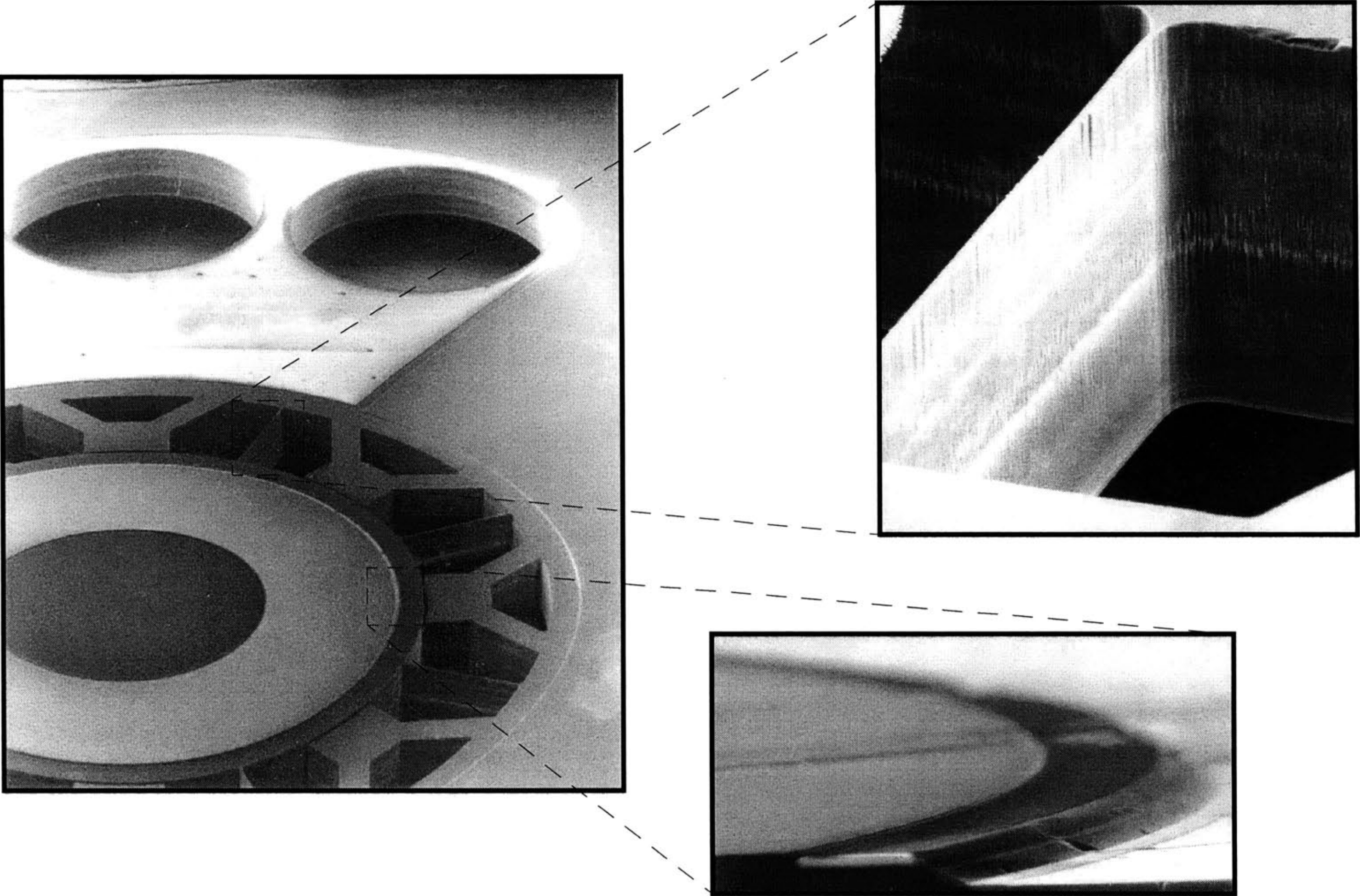

Figure 4.4: Representative pictures of a wafer from rotor lot tmrot1.

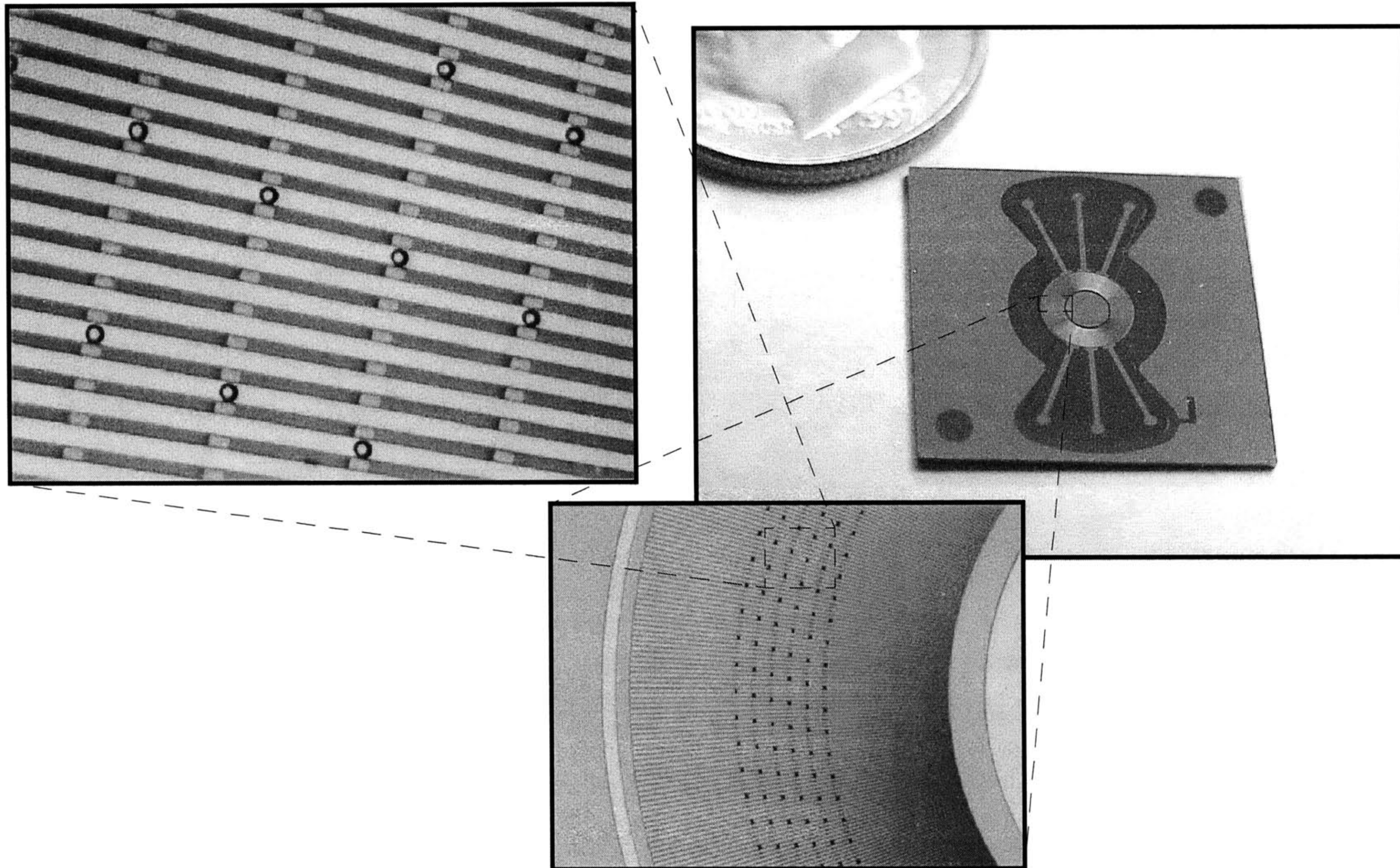

Figure 4.5: Representative pictures of a wafer from stator lot mcstat1.

acterized manner. In addition, although the wafers were water-cleaned in an Evergreen post-CMP cleaner, the brush on this cleaner was not functional and there may have been contamination from CMP. According to [30, 68], significant Potassium can remain after polishing with KOH-based slurries such as the Semisperse-25 solution used in this thesis. This contamination, combined with other cotaminants from the CMP pad, could also affect the sheet resistance of the rotor conductor. The experimental evidence in Section 3.4.1 does not show a difference due to CMP, nevertheless, the cleaning procedure of [30, 68] is recommended for any future micromotor builds.

Finally, in the ideal process flow, the stator and rotor wafers would be fusion bonded together and diced for packaging. Section 4.3.2 discusses possible reasons that bonding could not be achieved. The rest of Section 4.3 describes the details of especially involved unit process steps. Section 4.4 describes the process of assembling the tethered motor, and Section 4.5 describes packaging for test.

4.3 Unit Process Development

Several unit processes in the process flows described above were both very difficult to perfect and, at least in their intent, crucial to the successful fabrication of an electric induction micromotor. The TBOS, wafer bonding, rotor conductor and tether etch processes entailed especially large development efforts and were especially critical to the development of the tethered motor. TBOS process development involved an aggressive silicon etch process, thick oxide deposition and etch-back, and CMP. Wafer bonding developing did not actually lead to a robust process, but the development here lead to several recommendations toward successful bonding when the bonding surfaces cannot be well-protected before bonding is attempted. The rotor conductor development experiment sought to define polysilicon deposition and ion implant parameters to produce a thin film that would be compatible with a CMOS fabrication process — in order not to contaminate equipment — and have a predictable conductivity at room temperature. The experiment, described in Section 3.4.1, utilized a special test structure whose fabrication is described here. The actual rotor conductors were fabricated an a similar fashion. The goal of tether etch development was to define a recipe that would reliably produce mechanical springs approximately 8 μm wide and 400 μm tall from single crystal silicon. This etch was especially critical since it must be the last step of the rotor process flow.

4.3.1 Thick Buried Oxide on Silicon (TBOS)

By its nature, an electric induction micromotor requires thick insulating films, and the TBOS process to incorporate thick buried oxide in silicon makes this possible. As shown in Chapter 3, from an electromechanics viewpoint, it is undesirable for the stator electrodes and rotor conductor to operate in the vicinity of relatively better-conducting substrates. Yet, due to the construction of the turbomachinery in which the electric micromotor will eventually be housed, such operation is inevi-

table. The conducting stator substrate increases the parasitic stator capacitance, reduces overall machine efficiency and can make a power electronic drive more difficult to implement, as described in Section 3.3. Worse still, the large capacitance of the rotor insulator acts to short out the rotor conductor, thereby directly limiting machine performance as described in Section 3.2.2. Consequently, the process flows described above necessarily include very thick insulators, as thick as can be fabricated.

Thick oxide (around 10 μm and above) can be difficult to work with because of residual stress. Large film thickness lead to large residual stresses in films that are either deposited or annealed at high temperature. Residual film stress leads to large overall wafer bow which makes further processing difficult, for example, some machines cannot pick the wafer up. If very severe, wafer bow can also prohibit wafer bonding. Furthermore, as the film is made thicker and thicker, the wafer simply cannot bow enough relieve the stress, and the films crack. The micromotor is fabricated with a nominal insulator thickness of 10 μm because this thickness has been reliably achieved without subsequent cracking, but, due to the other reasons mentioned, wafer bow would remain a problem if not dealt with further.

The TBOS process is intended to reduce wafer bow while providing thick insulators where they are needed. It is well known that wafer bow is a function of the area over which the film is deposited [56]. By incorporating thick oxides only where they are needed, this area can be reduced substantially. For the electric induction micromotor described in this thesis, the area that requires a thick insulator is only 8.7% of the total wafer area.

Using the recessed TBOS process of the ideal stator process flow, it was possible to reduce the total wafer bow from 330 μm with a blanket 12 μm PECVD silane-based oxide film, to 60 μm. Measurements were made after 1100 °C anneals for both blanket oxide and TBOS. Note that the TBOS bow was measured on an actual stator wafer, so the effects of the other films are included. However, heavily phosphorous doped polysilicon that has been subjected to these temperatures is not expected to be in compressive stress [29, p 314]. Thus the polysilicon layers should not affect the bow; it should arise only as a result of the oxide films.

4.3.2 Wafer Bonding

Wafer bonding is required to reliably define the air gap in the electric induction micromotor. Without intimate contact around the perimeter of the stator pit, the air gap would certainly be increased non uniformly and unpredictably. It was known quite early in the development of the tethered motor that wafer bonding would be difficult given the nature of the process. The process includes several films that are to be subsequently removed from most of the wafer surface, surely leaving pieces behind, and PECVD films are known to be very rough as deposited [20]. In addition, it was

later realized that long exposure to buffered oxide etch (BOE) will roughen the surface of single crystal silicon enough to prevent wafer bonding [37]. In order to remove these films and repair surface damage, CMP development was an integral part of the process flow development. However, in the end it seemed that CMP was not enough. For many reasons, which are described in brief here, wafer bonding was never accomplished for the tethered motor.

Development of a wafer bonding protocol for the tethered motor progressed through many trials; only a few are reported here. In all cases the bonding step was preceded by an RCA clean of each wafer, after which the wafers were rinsed and stored in resistivity-monitored flowing DI water before spin-drying in nitrogen. In some cases, the RCA clean was preceded by a 3:1H_2SO_4:H_2O_2 mixture to strip resist. This may have affected results due to adsorbed sulfur [38].

It was immediately clear that as-deposited PECVD films were too rough for bonding. Thus a standard CMP recipe was used to polish the surface. This CMP process was found to promote wafer bonding and subsequently used to successfully bond a blanket coated PECVD oxide wafer to a prime silicon wafer. Then the same "soft polish" procedure was attempted on stator wafers from the actual process flow described above — not from the ideal process. These polished wafers would not bond to a prime silicon wafer either. Roughness data could not be used to explain this since the roughness of this stator wafer was very similar to that of the blanket coated wafer. Also, unpolished rotor wafers from the actual flow, with no bonding oxide, would not bond to prime silicon. Here, it was initially expected that the wafers would bond, since the original silicon surface was used as the bonding surface. It is believed that the lack of bonding was either related to poor surface quality due to roughening in the BOE solutions used to strip oxide layers [25] or related to observed bits of the oxide layers that remained on the bonding surface of the rotor wafer [42].

In an attempt to mend the surface of the remaining rotor wafers, a thin layer of PECVD silane-based oxide was added. This was then polished with a new CMP recipe developed to perform better than the previous recipe [16, 9, 25]. One of these rotor wafers was then successfully bonded to a prime silicon wafer. The wafer was then carefully and slowly, to avoid surface damage, separated with a razor blade. Separation was done under water, because this has been qualitatively shown to help break the bond and decrease surface damage. Finally, a stator wafer from the ideal process flow was polished with the new CMP recipe and a bond was attempted with one of the mended rotor wafers. The bond was not successful.

There are several possible reasons for unsuccessful bonding. The stator wafer from the ideal process flow used TEOS-based oxide for the bonding layer. Surface analysis showed that the TEOS surface exhibited a much greater roughness than the silane-based oxide layer used on the rotor wafers, although TEOS should be much more dense and smooth due to higher surface migration during the deposition reaction, which was done at the same temperature as the silane-based oxide

depositions [61, 41]. It is likely that contamination or mechanical problems in the CMP system were the cause of the high roughness since the system had exhibited substantial problems throughout this research and the stator wafer would not bond to a prime silicon wafer either.

Wafer surface quality and bond quality could be dramatically improved using a well-maintained CMP machine to execute a carefully developed polishing recipe. Gui et al [26] describe the various ways in which CMP is used to polish defects from thin films on the bonding surfaces, and includes many references to the work of others. Later research also describes a theory for wafer bonding that essentially reduces to one parameter, the surface adhesion parameter [25]. This theory was successfully tested on wafers having surfaces prepared in four different ways. The most relevant results showed that, if not done properly, CMP can actually decrease the likelihood of successful bonding. However, the combined research of [26] and [25] clearly shows that surface quality can be improved using a CMP recipe, or combination of recipes, developed in accordance with measurements of the surface roughness and the radius of the caps on the asperities of the roughness, along with knowledge of material-related parameters such as the Young's modulus and the specific surface energy of adhesion between the two surfaces. In this thesis, due to a lack of time, limited access to the atomic force microscope required to make the proper measurements, and very little control of the available CMP system, attempts to bond were set aside in favor of die-level assembly for the first tethered motors, as explained in Section 4.4.

4.3.3 Rotor Conductor Test Structure Fabrication

A specialized structure was necessary to properly characterize the resistivity of the rotor conductor; this section will describe the fabrication of that structure. The development of the experiment and its results were presented in Section 3.4.1. Recall from that section that the rotor conductor test structures consisted of two inter-digitated electrodes patterned on top of a thin layer of oxide, on top of a layer of lightly doped polysilicon, on top of a thick layer of oxide, on top of a relatively conducting silicon substrate.

This structure, shown in Figure 3.16, possesses a cross-section identical to that of the electric induction machine except that here a thin oxide spacer replaces the air gap because the process flow, summarized in Figure 4.6, is designed to be incorporated into the rotor wafer process flow with very little modification. The nature of the implant species and dose in Step 3 leads to different polysilicon resistivities and is varied for different lots of rotor conductor characterization wafers, as described in Section 3.4.1. The complete process flow and a drawing of the electrode mask can be found in Appendix D and Appendix F, respectively. A summary of the pertinent details is given here.

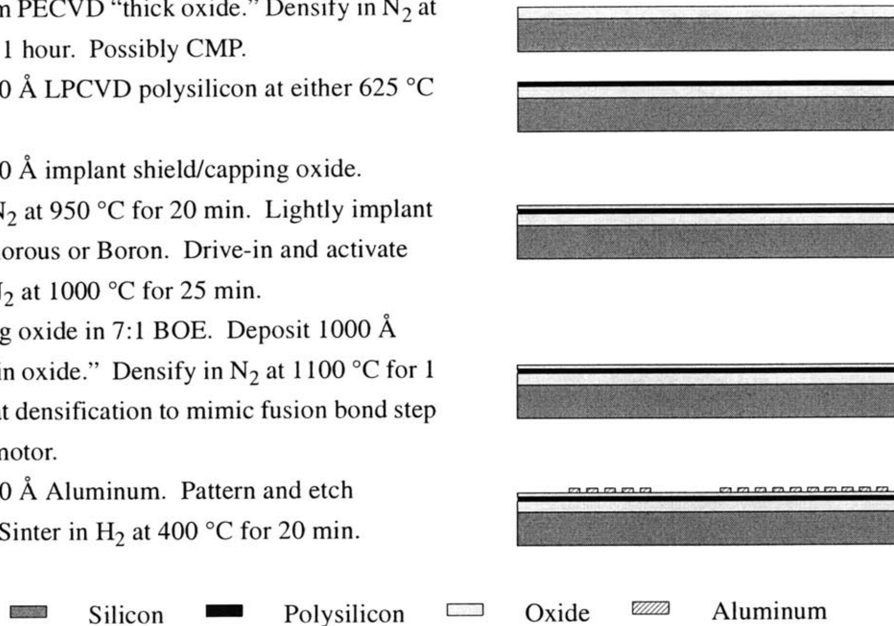

Figure 4.6: Summarized process flow for the rotor conductor test structure. This structure is also fabricated in parallel with device wafers to serve as a process monitor.

Fabrication Process Flow

First, in Step 1, the 1 μm thick oxide layer is deposited, densified and in some cases polished. This layer is PECVD oxide from a silane source and is densified at 1100 °C for 1 hour in a Nitrogen ambient. Polishing is included to account for the planarization step that is included in some rotor process flows. Step 2 adds the 5000 Å layer of polysilicon, deposited at either 625 °C or 585 °C. In Step 3, a 2500 Å PECVD silane-based oxide implant shield is deposited to minimize damage from ion bombardment and annealed at 950 °C for 25 min. Then the wafers are implanted according to the experimental results in Section 3.4.1, and are annealed at 1000 °C for 25 min so that the species can diffuse uniformly through the thickness of the thin film and crystal damage from the implant process is repaired. Next, in Step 4 the implant shield is removed and the 1000 Å oxide layer is deposited. This layer is also PECVD silane oxide and is densified at 1100 °C. During this time grain growth will occur to an extent that depends on the time at high temperature and the species that is implanted [29]. This step also mimics the fusion bond in the ideal tethered motor process flow. An extra fusion bond mimic is also included to verify previous results, which are not described in Section 3.4.1, that the resistivity of the polysilicon rotor conductor does not change after the first high temperature anneal.

Finally, in Step 5 the 5000 Å Aluminum electrode layer is deposited by electron beam evaporation, patterned and etched. The electrode arrays can cover as much as 16 mm^2, see Section 3.4.1, so

this step is somewhat difficult. For example, across the electrode area of one of the 10 μm devices, any defect larger than 10 μm can destroy an entire device by shorting two electrodes. Even in a Class 10 cleanroom, the lithography often has to be repeated several times. Once satisfactory lithography is accomplished, the electrodes are either dry etched using a chlorine chemistry or wet etched using the proprietary PANetch™ solution. Its composition is primarily 2:16:1:1 water:Phosperic Acid:Acetic-Acid:Nitric-Acid, hence the name. Finally, the Aluminum layer is sintered at 400 °C for 20 min in a Hydrogen forming gas.

4.3.4 Deep High-Aspect Ratio Tether Etch Development

High aspect-ratio tethers are essential for proper tethered motor operation. These tethers are mechanical springs which are compliant enough in the plane of the wafer to allow rotor rotation to be related to electromechanical torque, yet stiff enough out of the plane to maintain the air gap.

The tethers were etched in an Inductively Coupled Plasma (ICP), Reactive-Ion Etcher (RIE) made by Surface Technology Systems (STS). The target design of 8 μm in width by nearly 400 μm in height was aggressive, so a dedicated experiment was necessary to develop the etch recipe. Figure 4.3 shows that the tethers are bordered by large open areas, while the gap between the rotor and the measurement vernier structure is much smaller. So that all etched features would be the same width, and thus etch at the same rate, an outline trench of the same size as the small gap was used to cut-out the open areas. This etch was called a halo etch. The development of this etch began with a recipe that was previously developed for deep high-aspect-ratio etches [3]. However, this recipe was not intended for etches any deeper than 300 μm, so it had to be optimized to produce a higher anisotropy at the depth of the tethers.

The Etch Development Mask Feature Matrix

A matrix of feature sizes must be used to develop any deep etch with critical feature sizes because dimensions on the mask do not precisely transfer to etched features. The discrepancy is not entirely due to lithography, instead it is due to etch run-out. No etch is entirely anisotropic, so there will always be some dilation of trench width and shrinkage of features not etched. The total change in any feature is called the run-out; defined here as microns per 100 μm of etch depth. Run-out is sensitive to the trench width and depth, and the rate of run-out can vary substantially during a 400 μm etch. Recall from Section 3.1.2 that anisotropy is defined in terms of the angle of the sidewalls, 90 degrees to the wafer plane being perfectly anisotropic. As defined here, run-out is the difference between the mask feature and the narrowest point of the etched trench. Anisotropy is then superimposed over the run-out bias.

Since run-out and anisotropy had not been characterized for the tether etch trench width, depth and loading, each test wafer contained a 4×4 matrix of tether patterns, varying the tether width and

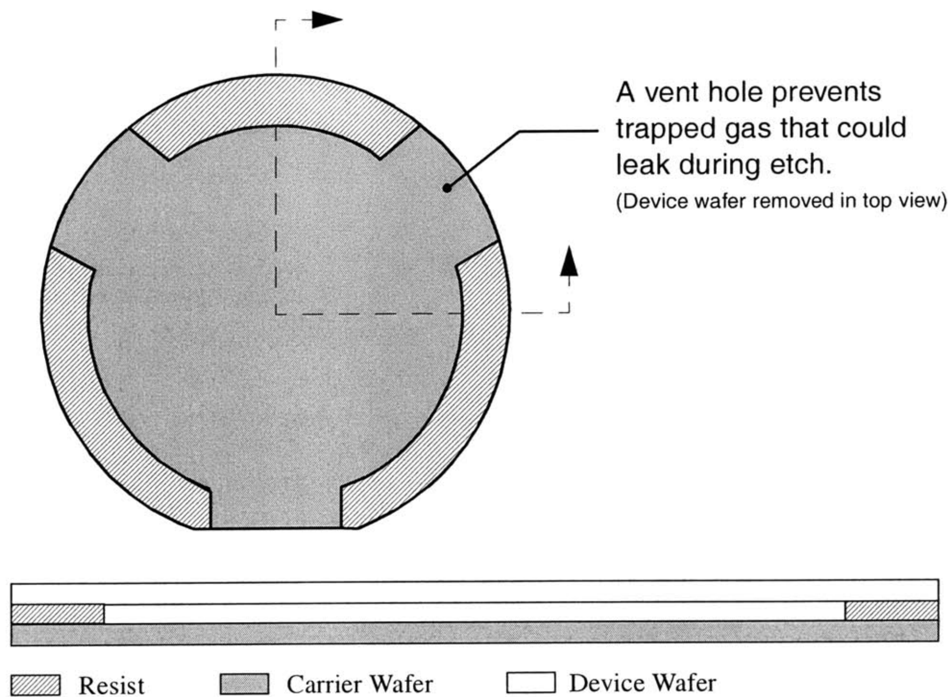

Figure 4.7: Method for attaching a carrier wafer to a device wafer.

halo trench width on the mask. After etching approximately 380 μm, the wafers were diced and the tether and halo widths were measured using a calibrated Scanning Electron Microscope (SEM). In general, the run-out was measured to be near the expected value of 1–2 μm per 100 μm, but each matrix position gave a unique result. The anisotropy could not be defined by a single angle, because the trenches were narrower near the mid-point. Rather, measurements were made at the top, mid-point, and bottom of the etched trenches, and etch development strove to decrease the difference in trench width as a function of depth. In the end, the mask tether and halo width combination that gave the most uniform tether width in the wafer, closest to the goal of 8 μm, was chosen for the rotor process flow. The remaining sections give a summary of the development process.

Carrier Wafer Effects

In the STS, a carrier wafer is necessary for any etch that will eventually break through the wafer. A carrier wafer is simply a wafer that carries the device wafer during the etch. For etches in this thesis, the device wafer is attached to the carrier wafer by a ring of thick resist, about 6 mm wide, applied just within the perimeter of the wafers, as shown in Figure 4.7. The carrier wafer is necessary for etches that break through the wafer because without it, Helium backside cooling-gas would leak into the chamber and choke the etch.

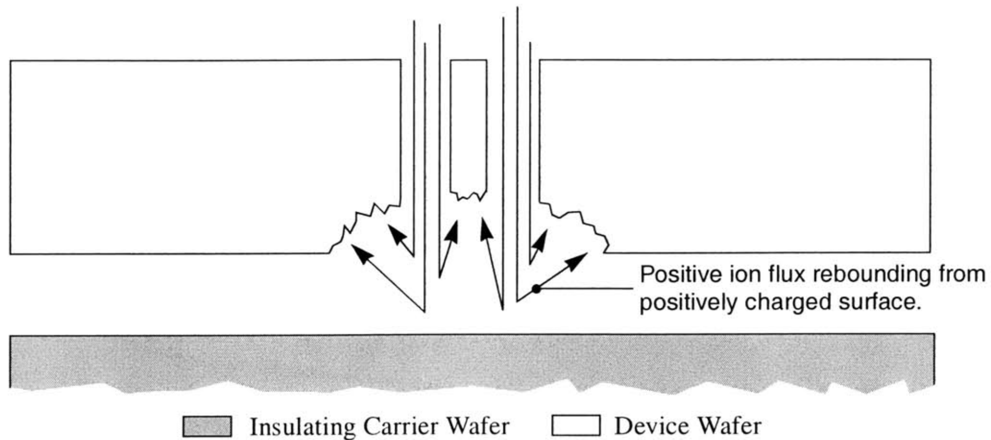

Figure 4.8: The footing effect in the context of the tether etch.

Based on comparisons between etches performed with and without a carrier wafer and between etches using different kinds of carrier wafers, the choice of carrier wafer will affect the character of a deep etch in the STS. In a typical etch, a wafer is cooled by heat transfer through Helium that flows between the wafer and the electrode, whose temperature is held at a fixed temperature with a cooling water loop. The wafer and electrode are also in electrical contact and their electric potential is measured relative to the plasma potential. Experience has shown that a quartz carrier wafer significantly decreases the ability to cool the carried wafer, and since quartz is an insulator it also slightly decreases the wafer potential relative to the plasma. Changes in both temperature and bias potential affect the etch. In general, a hotter wafer will give rise to a faster, less selective, and more isotropic etch, while a smaller potential difference will decrease the selectivity and etch rate. However compared with the use of a quartz carrier wafer, the use of a silicon carrier wafer has been shown to give rise to a more isotropic and re-entrant etch, even though the silicon wafer, with a high thermal conductivity, helps to cool the device wafer more than the quartz wafer. One explanation for this observation is that with the silicon wafer the bias potential will be higher, and since the trenches are very deep there is time for the positively-charge etch ions to be deflected through attraction to the sidewalls. As the etch depth is increased toward 400 μm, the etch becomes more re-entrant because of this effect, the tethers are pinched-off at their midpoint and destroyed. For this reason, a quartz carrier wafer is used during the majority of the tether etch.

A silicon carrier wafer is used, however, during the last 20-30 μm of the etch because of lateral silicon attack at the interface between the silicon and the silicon dioxide. This so-called footing effect arises when a reactive-ion etch reaches any insulating layer, as shown in Figure 4.8. The SF_6^+ and other positively charged ions bombard the insulating layer, some become immobilized there, and additional arriving ions are deflected. The insulating surface need only be close enough that the

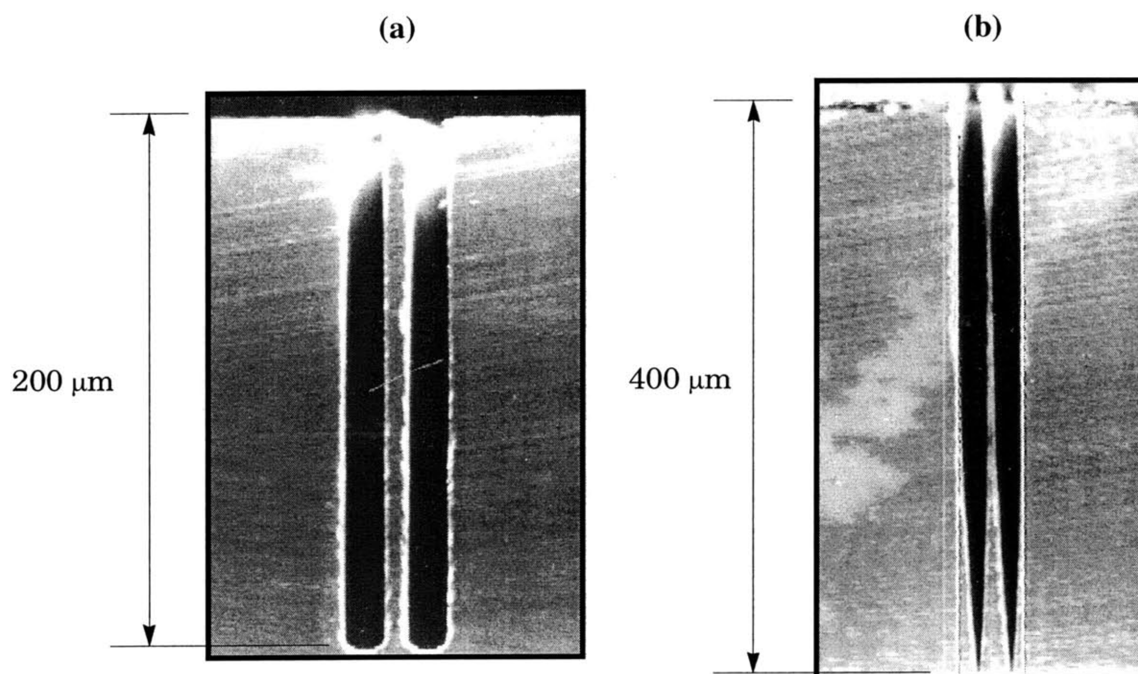

Figure 4.9: Initial results of the tether etch development using a standard recipe, MIT59: a) sample etched halfway; b) sample fully etched.

field due to the trapped charge can affect the trajectory of the arriving ions. The quartz carrier wafer behaves like a buried insulator, because the resist ring used to attach the wafer is only 8–10 μm thick. Also, Alumina fingers that hold the wafer in place on the electrode cause the wafer stack to bow up slightly, decreasing the gap between device wafer and carrier wafer.

If a quartz carrier wafer is used for the final portion of the etch, the bottom surface of the tethers will be critically damaged. Therefore the protocol for the tether etch calls for a quartz carrier wafer to be used for all but the last 20-30 μm of etch, after which a silicon carrier wafer is used. Because of the re-entrant nature of the etch with a silicon carrier wafer, the quartz wafer is used as long as possible. As the remaining silicon in the trench becomes thinner, damage becomes more likely during the release of the device wafer from the quartz carrier wafer.

Recipe Development

Recipe development began with a standard deep etch recipe — MIT59 in Appendix E. Two parameters in this recipe were systematically modified to produce a more anisotropic etch, these were the amount of C_4F_8 flowing during the passivation cycle, and the electrode power during the etch cycle. In each of these etches, the silicon handle wafer was not used because the etches were not carried to completion so that they would remain intact during cross-sectioning.

The STS achieves a deep etch by multiplexing between an etch cycle during which SF_6 flows through the chamber, and a passivation cycle during which C_4F_8 flows through the chamber. SF_6

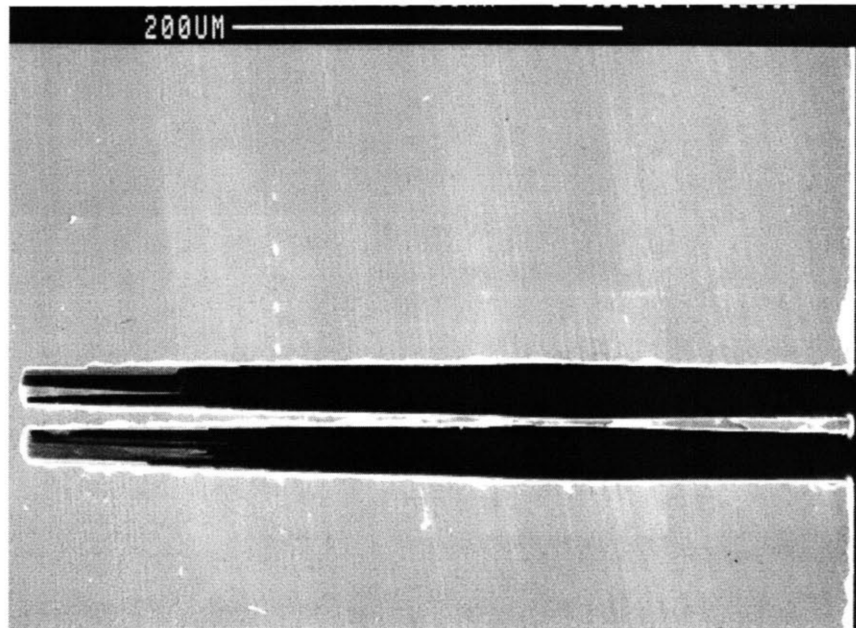

Figure 4.10: From a wafer etched with modified MIT59: 80 sccm passivation; TM04 in Section E.3.6. Grass formation from excessive passivation is visible in the bottom of the trench at the left.

isotropically etches any exposed silicon, while C_4F_8 forms a protective conformal polymer coating on all surfaces of the device wafer. Ion bombardment is directed perpendicular to the wafer surface during the etch cycle. This preferentially removes material on horizontal surfaces. Thus, on average the etch proceeds perpendicular to the surface of the wafer as shown in Figure 4.9(a), which was etched with recipe MIT59. This process technology is licensed to STS and other companies that produce ICP RIE etchers, such as Alcatel and Unaxis, from Robert Bosch GmbH, Stuttgart, Germany.

Notice the profound difference when the etch depth was doubled in Figure 4.9(b). This occurred for several reasons through a complex interaction of electrostatic attraction, ion mean free path, and ion and neutral flux into the trench [3]. The primary goal of the experiments described here was only to produce a working understanding of the processes that caused this difference. Thus limited modifications were made to recipe MIT59 until the problem was acceptably reduced. To begin, the passivation flow was increased to 60 sccm in an attempt to protect the sidewalls. This made it possible to etch a trench with an anisotropy like that of the trench in Figure 4.9(a), but at 400 μm deep. Higher passivation of 80 sccm was also attempted, but it was found that this much passivation lead to the formation of grass at the bottom of the trenches due to localized build-up of the polymer, as seen in Figure 4.10. In addition, the increased passivation did not lead to a further

increase in the anisotropy. Thus the passivation was held at 60 sccm, but the trenches were still dilated more than was acceptable.

As mentioned above, one reason for etch trench dilation could be the attraction of positively charged SF_6 ions toward the negatively biased walls of the trench. While it is true that the substrate bias pulls the ions out of the plasma glow and accelerates them across the dark space between the glow and the wafer surface, once they enter the etch trench the ions are accelerated toward one of the sidewalls as well. The ions move toward the wall to which they were closest when they entered the trench. The distance between the plasma and the device wafer surface is about 25 mm while half the trench width is approximately 10 μm. Combined with the fact that the maximum potential difference in the trench is much smaller than the bias of the wafer relative to the plasma, this means that the ion momentum is several orders of magnitude greater in the direction perpendicular to the device wafer. Thus, anisotropy suffers only slightly due to this effect, but increases with etch depth.

However, before the process was understood it was thought that a lower ion energy would decrease the attack of the sidewalls, because a lower ion energy would decrease the physical sputtering that aids the etch by breaking through the passivation layer, so the electrode power was decreased slightly. As shown in Figure 4.11, this made the situation much worse. Thus either the etch of the passivation is a chemical process as well, or the physical process is relatively indepen-

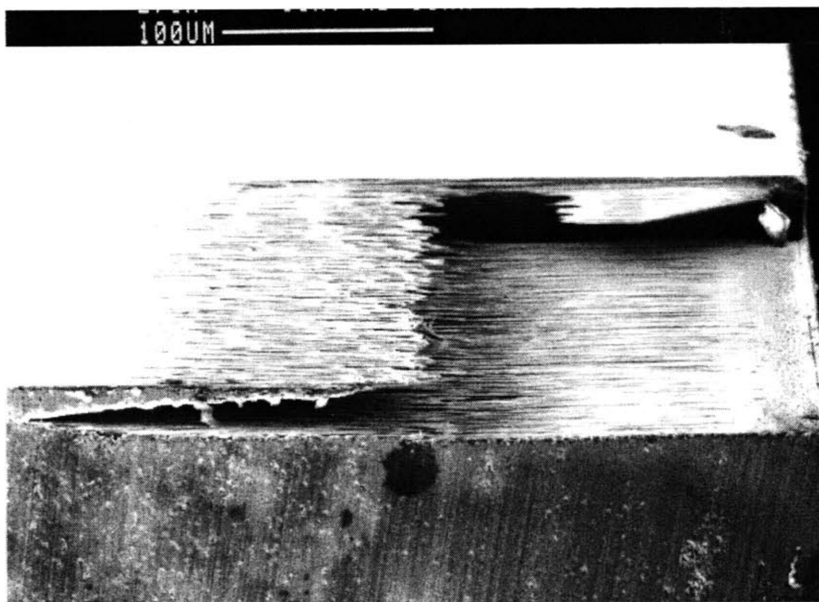

Figure 4.11: From a wafer etched with modified MIT59: 60 sccm passivation and 10 W electrode power; TM03 in Section E.3.6. Note that the sidewall etch cut through the tether at its midpoint.

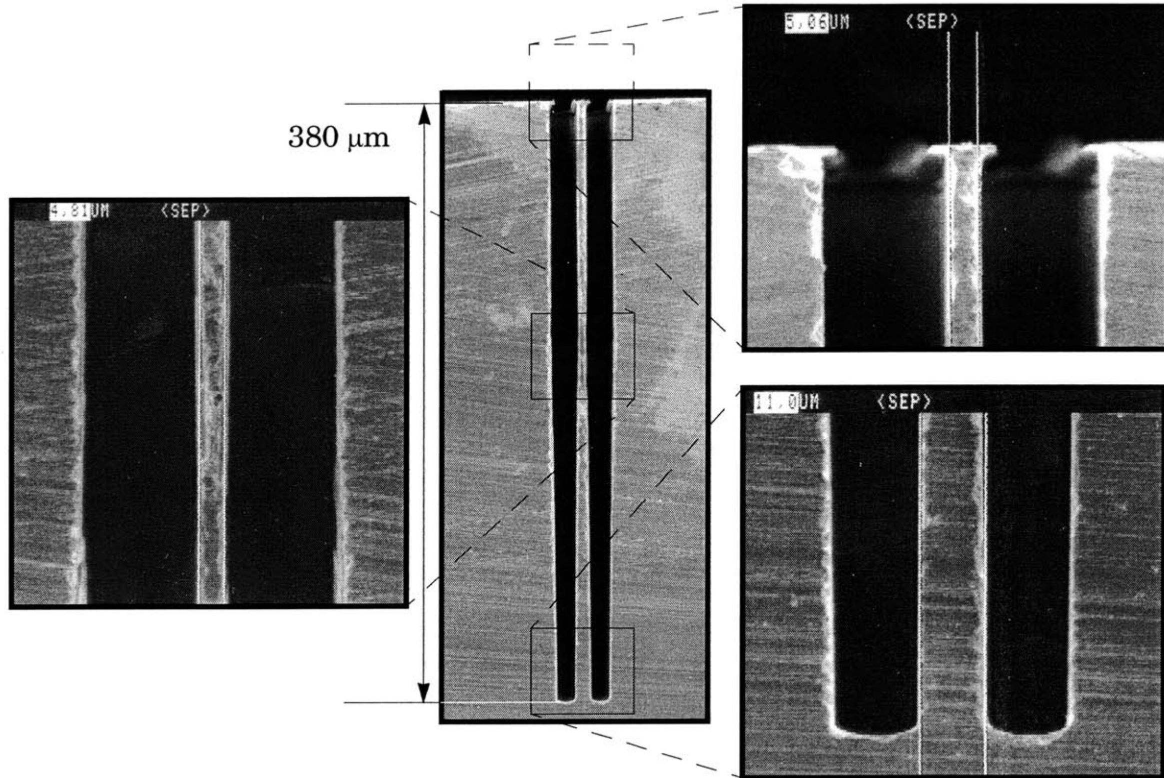

Figure 4.12: Result from a development wafer for the chosen tether etch recipe, TM02 in Section E.3.6.

dent of ion energy and very depend on ion flux. A lower electrode power would decrease the device wafer bias and allow the ions to be more effectively steered toward the trench walls. Therefore the anisotropy might increase with increasing electrode power, but this remains to be proven. It is important to remember that an increase in electrode power will most likely decrease the selectivity, so a thicker mask would be required.

In light of the etch results, the best etch conditions and the most suitable initial tether and halo widths were chosen to produce the etch shown in Figure 4.12. The initial features chosen were 13 μm tethers and 20 μm halos. Next the etch was tested on a mask containing only the chosen pattern, repeated once for each die of the rotor wafer layout. This etch used the full process — it included the silicon carrier wafer for the last 20-30 μm of the etch — and uncovered a positive effect. Apparently, the decreased loading increased the anisotropy, making the tethered width the same at top and bottom. In addition, the run-out was decreased, compared to the etch in Figure 4.12 and such that the top and bottom tether widths finished between 7 and 8 μm. Most likely, the middle of the tether is thinner than the top or bottom, but Chapter 5 will show that the tethers are fairly stiff and only the lumped stiffness is important.

It is important to note that this etch can be very dependent on the condition of the etcher. Out of 5 total device etches, then final 2 were conducted over a year after the first 3. These two etches

Table 4.1: **Naming key and brief history for assembled tethered motors.**

Device Name	Stator/Rotor Lot	Comments
TMA	mcstat1/tmrot1	Functional with 3 tethers. Phase C connected to ground because of metallic epoxy used during assemble.
TMB	mcstat9/tmrot1	Motor appeared to be functional, with all 8 tethers intact, but rotor fell out during handling.
TMC	mcstat9/tmrot1	All tethers intact, but stator die-level bow caused rotor-stator strike upon assembly.
TMD	mcstat9/tmrot1	Initially functional with 7 tethers. Limited data obtained because stator die-level bow caused rotor-stator strike.

yielded tethers that were 3 μm wide at top and bottom in one case and 5 μm in the other case. The first of these two etches yielded the 3 μm result, so the last etch was modified to have a delayed switch to the silicon carrier wafer. By waiting until the etch with a quartz carrier wafer had only 10-20 μm remaining, instead of the usual 20-30 μm, it was possible to limit the effect of the more re-entrant etch with the silicon carrier wafer, and etch tethers that were 5 μm thick.

4.4 Tethered Motor Die-Level Assembly

In the ideal process flow, tethered motors are assembled at the wafer level. A fusion bond is necessary to properly define the air gap. Only then will the air gap be defined by the union of the topography of the stator and rotor wafers in the silicon pits. The topography can be measured with a profilometer, relative to the bonding surfaces on each wafer. Since fusion bonding was not possible, another method of assembly was used.

All tethered motors assembled in this thesis were assembled by first dicing a stator wafer and a rotor wafer, then bonding the die with an epoxy adhesive either between the die or along the edge of the stack. Table 4.1 lists the 4 motors that were assembled on the die-level with a brief history. TMA is the most relevant since it was using this device that most data was collected. The planned packaging scheme required a gold wire bond to polysilicon at 350 °C, so this motor was assembled using H2OE metallic epoxy from Epoxy Technologies, which is rated for prolonged exposure up to 200 °C, but has been shown to withstand 350 ° long enough to wire bond. No epoxy was applied to the mating surfaces, the intent was to place three beads at three corners. However, the stator die was not completely flat due to stress-induced bow and the epoxy wicked into the space between it and

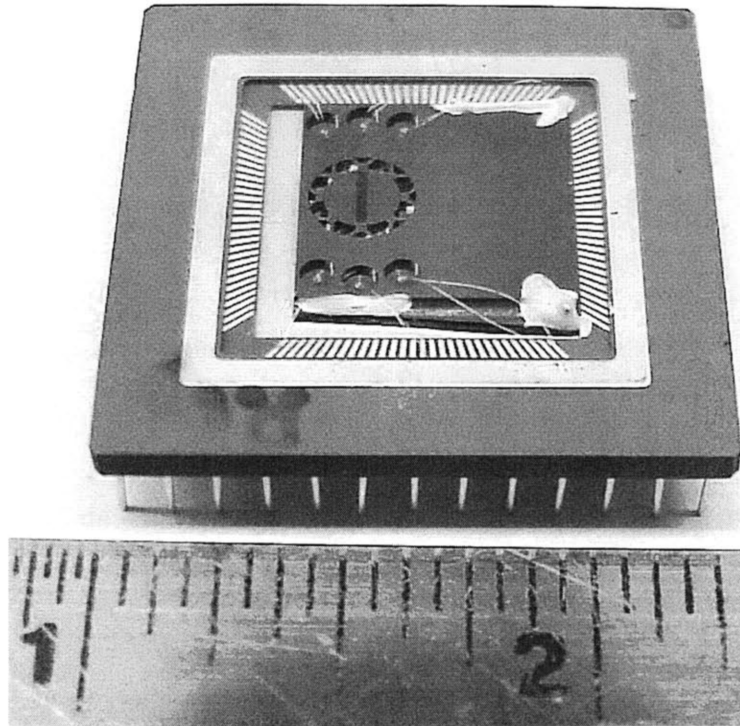

Figure 4.13: The first tethered electric induction motor, device TMA. This figure shows the first method of die-level assembly using metallic epoxy and crude alignment.

the rotor die. It was later discovered that this epoxy connected one phase of the motor to the substrate, nominally at ground. The adhesive also increased the air gap length significantly as described in Section 5.2.1, thus reducing output torque significantly. Nevertheless, it was possible to test the first device ever assembled, and these results are the only results presented in this thesis. The assembled device is shown in Figure 4.13, rotated 180° with respect to Figure 4.3.

For devices TMB, TMC, and TMD the lead interconnect wire-bond pads had a metal layer so that gold bonding could be accomplished at room temperature. Therefore a low-temperature non-metallic epoxy was used. Since both bonding surfaces on the motor die were covered with oxide, the separation between die could have been indirectly measured by directly measuring the capacitance between the two die. Hence, a non-metallic epoxy was essential, otherwise it would be extremely difficult, perhaps impossible, to measure the air gap accurately after assembly, without destroying the device.

These last three motors were assembled by placing the stator die on a flat surface in a cleanroom and placing the rotor die on top. A pair of micromanipulators was used to position the rotor directly over the stator electrodes by viewing through the large open spaces around the tethers and aligning stator features to rotor features. Alignment accuracy approached 10 μm as measured relative to features on the stator. Then the same micro-manipulators were used to clamp the rotor die and a bead

of Devcon 5-minute epoxy was placed along two edges of the die. This epoxy is quite viscous and did not wick between rotor and stator, so the air gap should have been very close to design.

However, here too the stator was not flat. The center of the stator die bulged up across the air gap and came into contact with the rotor, which was also bowed down due to the stress of the rotor insulator. This caused immediate rotor seizure in TMC and eventually lead to rotor seizure in TMD as well, though limited data was collected for TMD. The rotor of TMB did not strike, but its rotor became dislodged during handling.

Device TMB is shown in Figure 4.14 only to aid in the description of an assembled motor. The rotor shown in the upper-right and is turned over to show the rotor film. Also, the 5-minuted epoxy beads can be seen at the top and bottom edges of the die stack. The device is rotated 90° CCW with respect to the illustration of Figure 4.3.

4.5 Packaging

Packaging considerations for the tethered motor were in the foreground at all stages of fabrication planning and fabrication development. Fortunately, packages were available that could accommodate the size of the tethered motor chip, 15 mm square. Since it was desired to keep parasitic capac-

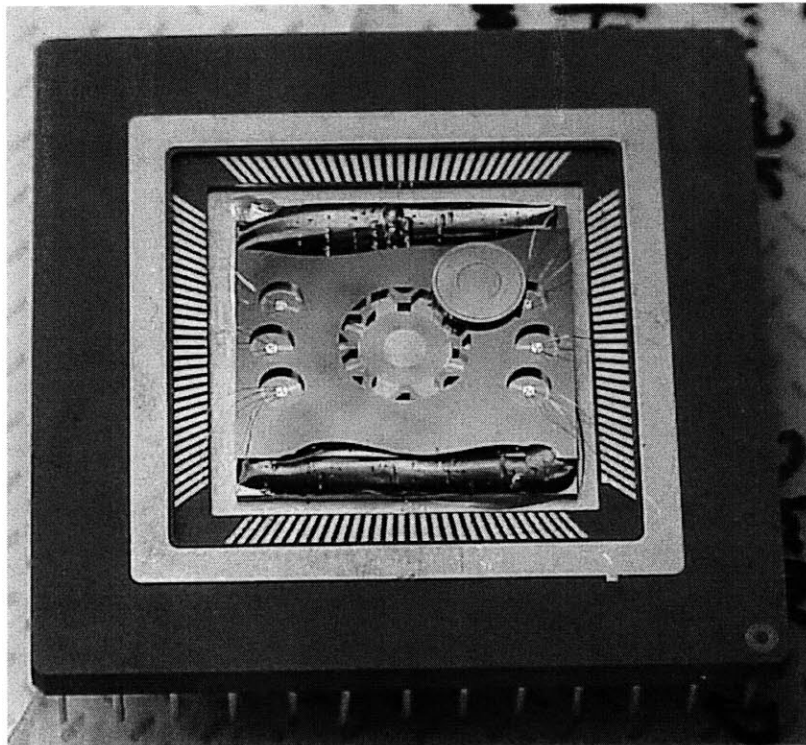

Figure 4.14: Assembled and packaged tethered motor TMB. Scale is in inches. This figure shows the method of die-level assembly using non-metallic epoxy and precise alignment. The rotor of this motor became dislodged and is shown overturned at the upper right of the chip.

itance and resistance to a minimum, ceramic PGA packages manufactured by Kyocera were chosen, although these packages have many more pin-outs than necessary for the tethered motor.

Assembled tethered motors were bonded to the packages using metallic epoxy to provide electrical contact to the stator substrate, the epoxy was cured at 120 °C for 15 minutes. Next the motor phases were electrically connected to the package using an ultrasonic gold-ball wire bonder. This was accomplished at room temperature for TMB, TMC, and TMD since they each had metal on the lead interconnect bond pads. Wire bonding of TMA required that the device be heated in situ to 350 °C so that the gold would adhere to the polysilicon. Wire-bonding directly to polysilicon is laborious; two hours were required successfully accomplish twenty-one total bonds, a redundancy of three for each phase contact plus three for the ground connection to stator and rotor substrates. TMA did not have metallized contacts because originally it was to be fusion bonded to a stator wafer.

Chapter 5

Tethered Motor Experiments

The primary goal of the tethered motor is to accurately measure the torque produced by the electric induction micromotor. To accomplish this goal, the tethered motor stator is excited to produce a square-wave of torque which vibrates the rotor on its tethers; the square-wave of torque is created by abruptly reversing the direction of the traveling stator potential wave. Using a highly accurate machine-vision system, the deflection of the rotor and tethers is measured as a function of the torque reversal frequency, producing a forced-motion response curve to which an equation of motion is fit. The fit yields tether stiffness and motor torque. The process is repeated for several stator travelling wave velocities and voltages, and at two temperatures to show the affect of a change in the rotor conductor sheet resistivity on torque.

Henceforth, the frequency at which the torque changes direction will be called the "reversal frequency," and the excitation frequency of individual phases will continue to be called the "stator excitation frequency." This is also the frequency at which the stator travelling potential wave moves the distance of one stator wavelength around the stator.

5.1 Test Rig Description

5.1.1 Electronics

The tethered motor is excited using electronics based on the PA85 high-speed high-voltage op-amp from Apex Microtechnology. A schematic of the power electronics is shown in Figure 5.1. Using the PA85 op-amps, a six-amplifier circuit is constructed to produce six square-waves that are each phase-shifted 60° from their neighbors. The six-phase control circuit that produces these 60° delays also includes two Maxim 4547 bidirectional RF/video switches, which each contain two single-pole double-throw switches to reverse the firing order of the op-amps when given a 5 V stimulus. This 5 V stimulus is what reverses the direction of the stator potential wave propagation and thus changes the sign of the tethered motor torque. For both forward and reverse potential wave travel, the logic-level signals of the six-phase clock are first fed through three LM319 dual high-speed comparators that boost the six logic-level signals to ±15 V and pass them to the input of the PA85 amplifiers.

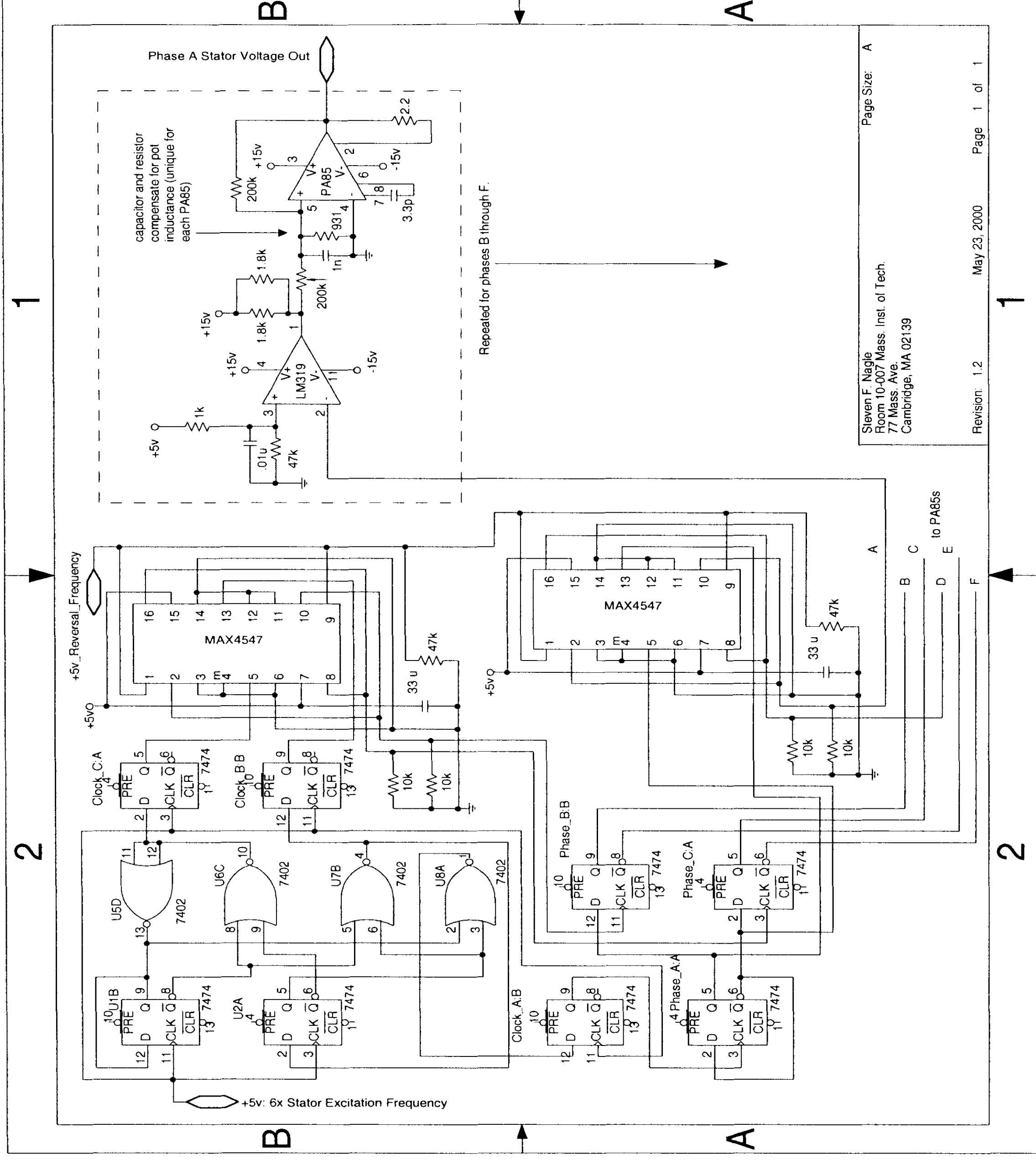

Figure 5.1: Schematic of the power electronic drive based on the PA85 op-amp.

The op-amps are connected to form inverting amplifiers and are powered by ±130 V, although they are capable of operation up to ±225 V. To obtain variable gain, potentiometers are used for the input resistors; variable gain is used to adjust the output voltage. Because the potentiometers add feed-forward inductance, compensation is required to stabilize the amplifier. On the other hand, if the potentiometer is used as the feedback resistor, the inductance is in the feedback loop and produces a zero, thus slowing the response of the amplifier in a manner that can not be compensated. By adjusting the feed-forward potentiometers, the square-wave output voltages of the op-amp electronics can be adjusted from 0 to ±110 V.

The op-amp electronics are relatively simple in construction, but extra time harmonics produced by the square-wave excitation complicate data analysis. Resonant electronics that produce nearly perfect sinusoids have been fabricated by MIT Lincoln Laboratories[†] to drive the electric induction motor, and they are capable of producing voltages at the design goal of 300 V. Unfortunately, the resonant electronics are designed for operation at frequencies near 3 MHz, and it is difficult to decrease this resonant frequency. As a result, they are not useful for the tethered motor because it requires stator excitation at a variable frequency, between 100 kHz and 700 kHz. Also, as fabricated, the six-phase clock in the resonant electronics is not capable of reversing the firing order of the phases and reverse the tethered motor torque. Therefore, the op-amp electronics, producing square-wave output voltages, are used to obtain all torque measurements reported in this thesis. The op-amps are capable of driving more than enough current to compensate for all parasitic capacitances between the op-amp output and the stator electrodes.

5.1.2 Test Jig

The power electronics output must make good electrical contact with the motor, but it is also desirable to have easy removal of the motor from the test jig for storage between experiments. Therefore, the packaged motor is held by a zero-insertion-force (ZIF) socket that is soldered to a custom PC board. The PC board runs balanced leads from the ZIF socket to pins where equal lengths of RG-174 coaxial cable connect each of the 6 motor phases to the outputs of the op-amp electronics. As described in Chapter 3 and Chapter 4, 6 pin leads on the PGA package are wire bonded to the wire bond pads on the 6 lead interconnects. Thus each cable is connected to one phase of the motor, or 131 electrodes, through the vias and ring interconnects. The RG-174 and PC board leads both add additional parasitic capacitance that is proportional to their lengths, so the respective lengths of each of these are made equal across all 6 phases. Added capacitance includes the capacitance of the coaxial cable, the ZIF socket and PGA package, and the stator wiring and all of this can be placed in parallel with the first capacitance in Figure 2.11[‡]. Finally, the stator and rotor substrates are

---

†. Many thanks to Dr. David Otten for the circuit design and to Dr. Stephen Umans for all of the arrangements for fabrication at Lincoln Labs.

grounded by being bonded with conductive epoxy to the conducting plane of the PGA package, and then wire-bonded to pins in the package that are connected to earth ground through the PC board.

5.1.3 The Computer Microvision System

Motion measurements are made using a computer microvision system developed at MIT by Professor Dennis Freeman, his students, and his staff [22]. The microvision system essentially consists of a microscope and a fast image acquisition and analysis system, which itself is made up of a high speed camera and a high speed frame grabber managed by a PC running the Linux operating system. The microscope used here is a ZEISS Axiotech Vario with optics modified as described below; it is shown in Figure 5.2. The microscope is mounted on a standard vibration isolation table.

A Polytec piezoelectric focus control actuator, a PIFOC, is inserted between the microscope turret and a standard ZEISS long working distance 20× objective. Normally, the microvision system uses the PIFOC to precisely measure vertical deflections. However, for all measurements in this thesis, vertical deflection due to the pull-in force are not large enough to be measured. Attempts to measure the vertical deflection for the largest stator voltage applied in the experiments of this chapter failed to show vertical deflection larger than the noise floor of the microvision system, which is shown below to be 20 nm. Therefore, the vertical deflections are negligible and do not affect torque. The models predict this negligible deflection for the stator voltages used in the measurements of this chapter. However, the actuator is used to measure thermal expansion of the motor and test jig, as described in Section 5.2.

When using a CCD camera, the best images are produced with a collimated source of light, so the standard ZEISS halogen source is replaced by a super-bright green LED. The diffuser is removed from the light path and the LED is centered using a Bertrand lens telescope inserted in the eyepiece socket to obtain the brightest, most direct rays of light through the microscope. A custom controller turns this LED on and off to strobe the motion of the rotor. The motion itself is generated by a 5 V square-wave stimulus that is produced by the same controller. This stimulus provides the reversal frequency in the op-amp electronics and thereby produces the square-wave of torque. At the same time, the controller also signals the CCD camera, a Pulnix Megaplus digital camera, to open its shutter and the frame grabber to capture an image and store it in the PC RAM. All three signals are synchronized by the controller. The signals are repeated to record the average rotor position for several intervals in the period of the rotor motion, as described schematically in Figure 5.3 and below.

---

‡. Note that when using the op-amp electronics, the AC voltage source in the equivalent circuit of Figure 2.11 is replaced with a square-wave source, and the inductor is removed. Linearity can be exploited to return to a simple sine-wave analysis for each individual excitation harmonic, and the results may be summed for total loss calculations if they are desired.

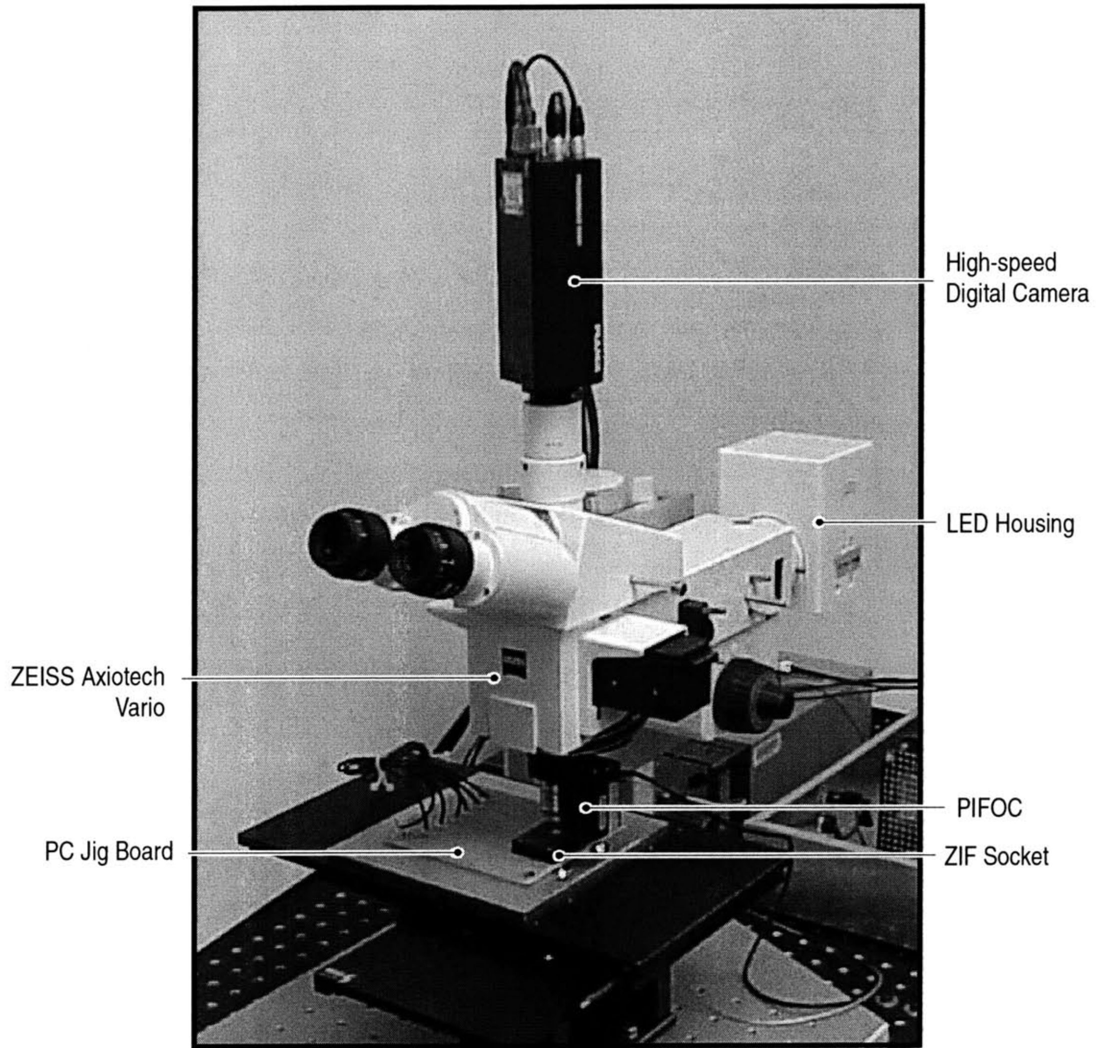

Figure 5.2: Illustrative description of the tethered motor test rig and photo of the actual rig. Electronics, signal generators, computer and PIFOC controller are not labeled or are not shown in this figure.

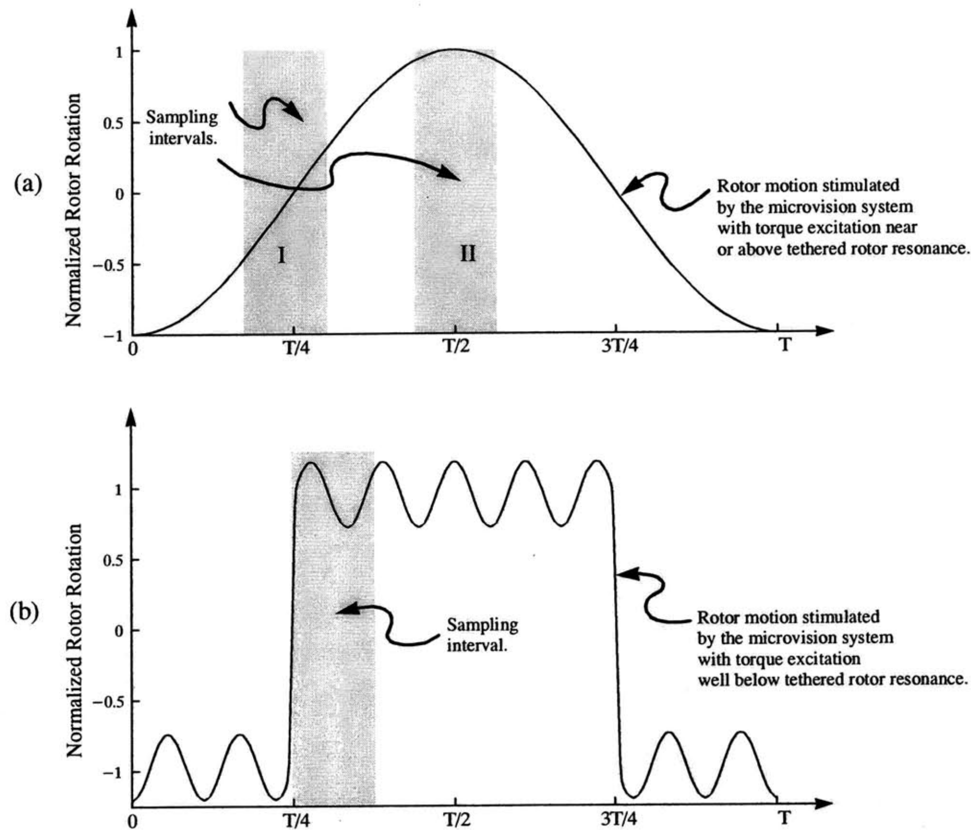

Figure 5.3: Two examples of data acquisition showing the process used to capture images of rotor deflection. In this case the number of sampling intervals is only 8 per period. The LED is on and the camera shutter is open during the entire sampling interval. The vertical axes are not to scale.

After an image is collected for each interval in a period and at each reversal frequency in the sweep, the images are transferred to the hard disk for analysis. Finally, at the heart of the microvision system, specialized software algorithms compare sequential images to determine the amount of rotor motion. With proper vibration and optical isolation, this microvision system is capable of measuring 1 nm of motion in the focal plane and 10 nm of motion perpendicular to the focal plane. The exact sequence used for data collection in this thesis is described in detail in the following section.

At each reversal frequency, the sampling interval steps along the period of the motion, thus recording an average rotor position for each sampling interval in the period. The camera is recording an image during the entire time that its shutter is open. Thus if significant motion occurs while the shutter is open, the images will be blurry and the motion detection algorithms will give erroneous answers. Figure 5.3 is used to illustrate this problem. Figure 5.3(a) shows motion typical of frequencies near and above the natural frequency of the tethered rotor. In sample interval I, much more motion occurs while the shutter is open compared to sample interval II. Because very little motion

occurs during interval II, it will yield a better snapshot of the motion. It is easy to see that, regardless of the speed of the motion, as the number of intervals is increased and their width is decreased, the snapshot becomes is less blurred and the motion error is decreased. Naturally, for very fast motion, many sample intervals are required.

Figure 5.3 also illustrates another reason to increase the number of sample intervals. Figure 5.3(b) shows motion typical of reversal frequencies well below the natural frequency of the tethers. Here a lightly-damped oscillatory response is superimposed on a square-wave of motion. In fact, the motion in Figure 5.3(b) is similar to that produced by the tethered motor at frequencies lower than resonance. A problem arises because the microvision system is only asked to report the magnitude of the first harmonic of the motion, and this magnitude is then related to the first harmonic of the tethered motor torque in Section 5.3. Thus when measuring motion like that in Figure 5.3(b) with only 8 sample intervals, only one of which is shown in the figure, the microvision system will report an erroneous rotor rotation. First, the measured rotation will be an average over the time of the sample, and the image will be blurry as for sample interval I of Figure 5.3(a). In this case, the averaging will underestimate the size of the fundamental while the blur will give random error. More importantly, for any motion containing high frequency components, the higher frequency motion will be aliased down to the fundamental if a low sampling rate is used. This leads to an over-estimate of the fundamental. For these reasons, discussed further in Section 5.2.4, the number of sampling points is 24 or 30 in the rotor rotation measurement experiments reported below.

5.2 Data Collection

Motion is measured in 15 separate experiments to determine the function of torque versus two independent variables: stator excitation frequency and stator voltage. All measurements are made on micromotor TMA, which is summarized in Table 5.1. First, experiments are conducted at three different stator voltages $|\hat{V}_s|$, for a constant stator excitation frequency f_e. Second, two sets of measurements are made as a function of the stator excitation frequency, the primary independent variable, which is varied between 100 kHz and 700 kHz for a constant stator voltage within the first two experiment sets. Table 5.2 lists the parameters of each motion measurement experiment and groups them into three sets. Each experiment is analyzed in Section 5.3, and each set is used to produce a plot of torque versus stator voltage or stator excitation frequency. Finally, micromotor TMA has the inadvertent ability to heat its silicon structure, so this feature is used to provide a semi-quantitative measurement of rotor sheet resistance versus the temperature of the structure.

Table 5.1: Summary of as-fabricated condition of micromotor TMA.

General notes on the device		
Tethers	Only 3 tethers remain but they are nearly evenly distributed around the rotor. Two are 45° apart, the other is 180° from the bisector of this 45° angle.	
Electrodes	Phase C is connected to ground through a 1.2 kΩ resistance and does not contribute to torque. If voltage is applied to this phase, the entire micromotor can be heated to about 90 °C. Since the rotor sheet resistance is a function of temperature as described in Section 3.4.1, the torque curve can be shifted to produce the effects described in Section 3.2.3.	
Assembly	This motor was assembled with a metallic high-temperature epoxy. The epoxy was applied only the edges of the stator-rotor stack, but a small amount seeped between the two die. This had been expected to result in expansion of the air gap as the device is heated, but no such expansion could be measured. The epoxy that seeped in is assumed to be the cause of the "shorted" Phase C.	
As-fabricated geometry parameters For all parameters not listed, the design goal is reflected in the device. For reference, see Table 3.9.		
G	—	Stator-rotor air gap length is determined in Section 5.3.2.
ρ_{rcs}	—	Rotor conductor sheet resistivity is determined in Section 5.3.2.
Δ_{si}	10.1 μm	Rotor insulator thickness
δ_{rf}	0.510 μm	Rotor conductor thickness
M_r	13.1 mg	Rotor mass averaged from several samples
r_m	2.04 mm	Radius at which tangential rotor motion is measured
r_i	1.00 mm	Inner radius of rotor conductor.
r_o	1.90 mm	Outer radius of rotor conductor. This and the inner radius define the active area of the machine. Utilization of the total active area requires a perfectly functioning stator, among other requirements.
δ_e	1.17 μm	Stator electrode thickness
W_{ei}	3.7 μm	Stator electrode inner width
W_{eo}	11.0 μm	Stator electrode outer width
G_{ee}	4.3 μm	Inter-electrode air gap
Δ_{si}	4.88 μm	Stator insulator thickness
δ_{lic}	1.17 μm	Stator lead interconnect thickness
δ_{ric}	0.990 μm	Stator ring interconnect thickness
W_{ric}	6.5 μm	Stator ring interconnect width
δ_{ILD}	1.40 μm	Inter-Level Dielectric thickness
w_T	7.0 μm	Tether width
N_T	3	Number of tethers

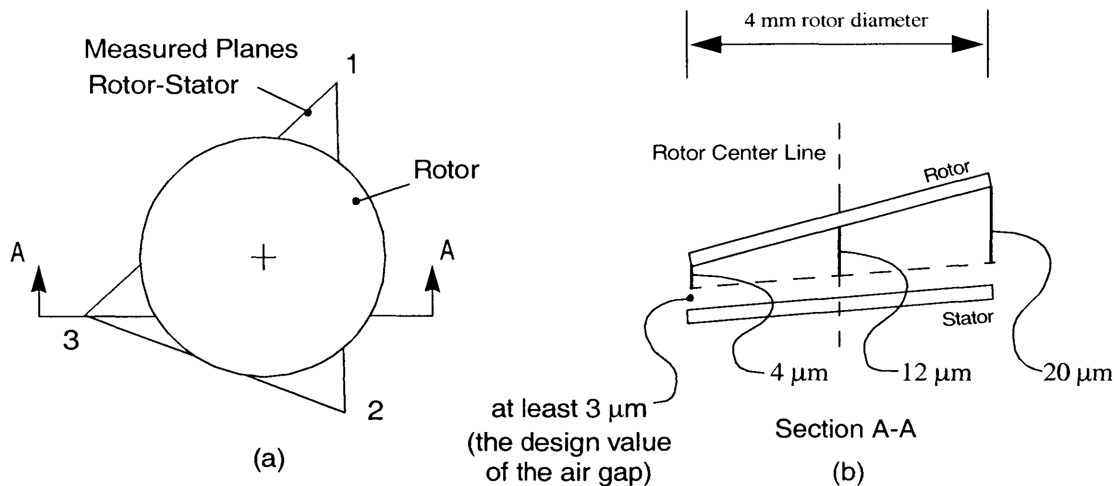

Figure 5.4: Illustration showing the differential slope of the stator plane and rotor plane: (a) shows a top view of the tilt measurement points, and (b) shows the associated variation of the air gap.

5.2.1 Increase in the Air Gap Due to Epoxy

The epoxy assembly process has increased the air gap by an unknown amount as described in Section 4.5, but a lower bound has been measured. The increase in the air gap results from the small amount of epoxy that seeped between the rotor and stator die during assembly. Figure 5.4 illustrates the method used to measure the minimum increase in air gap due to this epoxy at room temperature. The location of the gap-increasing epoxy can be seen in Figure 5.5, where it is referred to as the "die epoxy." To measure the increase in the air gap, the microscope is first focused on the surface of the rotor die at Point 1 in Figure 5.4, then the stage is moved and the PIFOC is used to measure the out-of-plane component of the vector between Point 1 and Point 2[†], and that between Point 1 and Point 3. The microscope is then refocused on the surface of the stator die, and the process is repeated. According to the measurements, neither surface is level when firmly installed in the ZIF socket, but only a 0.5 μm out-of-plane difference is measured between the Point 1-2 vector on the rotor surface and the Point 1-2 vector on the stator surface. However, a 17 μm difference is measured in the vertical component of the Point 1-3 vectors on the two surfaces. From this, consideration of three similar triangles yields a 20 μm increase in the air gap at the right edge of the rotor, a 12 μm increase in the air gap at the center of the rotor, and a 4 μm increase in the air gap at the left edge of the rotor. These are only minimum increases due to the epoxy because the measurement technique can only detect relative tilt between the die. The range of the PIFOC is not large enough to measure the absolute distance from the rotor die surface to the stator die surface. Furthermore, the thickness of the

†. It is known that the movement of the microscope x-y stage does not cause random motion out of the x-y plane.

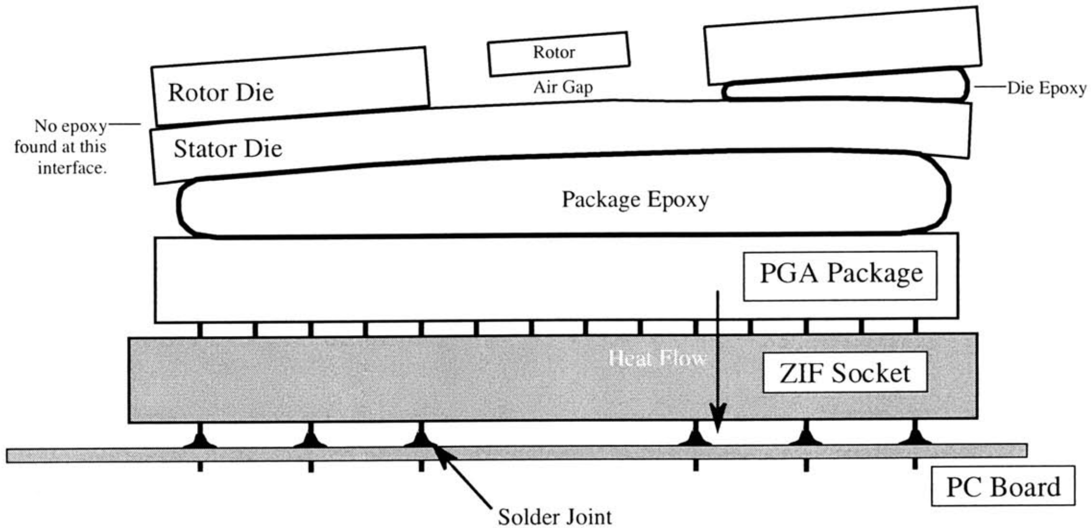

Figure 5.5: Cross section of the device mount. Note that since a thick layer of oxide covers the stator die, it is substantially curved. Thus the point of contact between the two die is unclear.

rotor wafer is not known precisely, therefore it cannot be accurately subtracted from such a measurement. However, epoxy is only observed between the die at the right edge of the rotor, and Point 3 represents a location where the rotor and stator bonding surfaces would be in contact in the absence of epoxy. Thus it is reasonable to assume that the air gap increase as measured by the tilt represents the only air gap increase due to the epoxy. Torque is inversely proportional to the air gap, so an effective air gap is calculated by performing an integral over the tilted plane of the rotor and equating the result to the inverse of the effective air gap. The resulting total effective air gap is calculated to be approximately 13 μm, 10 μm higher than design. The error in this measurement is conservatively estimated at ±2 μm because the absolute best error in a single PIFOC measurement in this situation is 0.5 μm.

5.2.2 Maintenance of Elevated Machine Temperature

Recall from Section 4.4 that the epoxy mentioned above connects Phase C to ground. This connection behaves like a 1.2 kΩ resistance, as determined by application of a DC voltage to only Phase C and measurement of the current through the ground lead of the package. No other phases are connected to ground, and Phase C is not connected to any other phases. During torque measurement, the current through Phase C is used to heat the entire motor rig in order to show a change in torque as a result of a changing rotor sheet resistance, which is a function of the rotor temperature.

A specific rotor temperature cannot be accurately produced, but the temperature can be precisely maintained. This is accomplished by using the PIFOC to observe the rise of the rotor surface

as the entire rotor assembly is heated. The motor is heated by Phase C in one of two ways. In one case, Phase C is connected to the op-amp electronics at reduced gain to provide a measured amount of heating; this case is denoted by an "AC" label in the column for peak heater voltage in Table 5.2. Alternatively, a DC voltage is applied to Phase C to provide a measured amount of heating while the other phases are excited normally; this case is denoted by the "DC" label in Table 5.2. Thus the device temperature is maintained by adjusting the voltage on Phase C such that the rise of the rotor surface is maintained.

Two temperatures are explored in the experiments described in this chapter. The highest temperature is estimated by touching the edge of the micromotor chip and noting that while the device cannot be touched comfortably for more than 5 seconds, it is not hot enough to boil a small drop of water [59]. This suggests that the maximum temperature is approximately 90 °C. At this temperature, the rotor is observed to rise 15 μm. The thickness of the package epoxy, the epoxy under the stator as illustrated in Figure 5.5, is estimated at 50 μm. According to its manufacturer Epoxy Technologies Incorporated, the H2OE epoxy has a coefficient of thermal expansion (CTE) equal to 31 ppm/°C below 150 °C. Therefore, the a 70 °C difference in temperature leads to only 0.1 μm of vertical rise and the observed rise cannot be due entirely to the epoxy.

Continuing down the cross section in Figure 5.5, the next possible source of the expansion is the PGA package and the pins connecting it to the ZIF socket. The pins consist of Ni-Au plated Kovar, an iron alloy that has a CTE of 5.3 ppm/°C. This alloy had been chosen by the manufacturer of the PGA package to closely match the CTE of the proprietary ceramic formulation that forms the bulk of the package. Because it is proprietary, the ceramic CTE could not be obtained, but it is estimated to be the same as that of Kovar for the purposes of this thesis. The total distance between the bottom of the package epoxy and the anchor point of the Kovar pins in the ZIF socket is 7 mm, so the total expansion over a temperature change of 70 °C is 2.6 μm.

Investigating further, the Kovar pins are anchored in the ZIF socket by brass clamping pins, which are themselves soldered to the PC board of the test jig described in Section 5.1.2. The distance between the anchor point of the Kovar pins and the solder joint of the brass pins into the PC board is 5 mm. Using the CTE of brass, 18 ppm/°C, a 70 °C temperature change leads to a rise of 5 μm. The total rise is now up to 8.9 μm.

Finally, the top of each solder joint protrudes 1 mm above the surface of the PC board. The CTE of the solder is 53 ppm/°C, just under that of lead. Thus the top of the solder joint will rise at least 3.7 μm. Since the edges are constrained by the PC board via, the rise will actually be slightly greater. Thus, by including the increase in length of each element in the chain from the solder joint up to the package epoxy, the vertical rise of the tethered motor due to a 70 °C increase in temperature is predicted to be greater than 13 μm, which is very close to the observed rise of 15 μm. The

difference is most likely due to the inability to properly account for expansion of every part of the actual structure, and not due to an expansion that is non-linear with temperature.

The preceding thermal analysis supports the notion that lower package temperatures, and therefore lower device temperatures, can be estimated very well using the observed rise of the tethered motor surface. This is done using similar triangles with a basis of zero rise at room temperature, 20 °C, and a 15 μm rise at 90 °C. For an observed rise between zero and 15 μm, the temperature is interpolated between 20 °C and 90 °C. In this thesis an observed rise of 4.5 μm is taken to indicate a temperature of 41 °C, as noted in Table 5.2.

The primary purpose of observing the rise of the rotor surface is to maintain a particular temperature during each experiment, in order to accurately to measure rotor rotation. Thus the thermal expansion is left to stabilize before in-plane motion measurements are made. Stabilization has been observed to take an hour or more, so fluctuations in temperature occur on a similar time scale and are not a concern during rotor deflection measurement as long as initial stabilization is accomplished. The rise of the rotor surface due to thermal expansion is monitored throughout each experiment in Table 5.2, and the voltage on the shorted phase is adjusted if the surface of the rotor moves vertically by more than 0.5 μm. If the surface is found to have risen by more than this during an experiment, the experiment is repeated.

5.2.3 Confirmation of Zero Air Gap Change versus Temperature

The air gap does not increase significantly as the epoxy between the rotor and stator is heated. This is predicted by the low CTE of the H2OE epoxy and the estimated maximum temperature of 90 °C. It has also been confirmed by comparing the measured rise of the rotor surface with a measurement of stator surface rise taken through the space adjacent to the tethers. The process proceeds in two steps, starting with a room temperature device. The ZEISS microscope is first focused on the rotor surface, and then a DC voltage is applied to Phase C. The rotor surface rises an amount that is measured with the PIFOC. Then the voltage is removed and the device is allowed to cool to room temperature, making sure that the rise of the rotor stabilizes at zero. Next the microscope is refocused down to the stator surface and the process is repeated using the exact same DC voltage on Phase C, with a check to make sure that the same power is supplied in the epoxy connection from Phase C to ground. The rise is again measured, and again, the voltage is removed to confirm that the device stabilizes at zero rise. The rise measurements from the rotor and stator yield the same results, confirming that the air gap length does not change when the device is heated, to within the accuracy of the measurement technique. The total estimated error in this measurement with the PIFOC is also estimated at 2 μm.

Table 5.2: Data collection experiment parameters, grouped into three sets. The torque curves for each set are plotted in Section 5.3.2.

Experiment Set	Stator Voltage (V)	Stator Excitation Frequency (kHz)	Torque Reversal Frequency (Hz)	Rotor Rotation Measurement Intervals	Phase C Peak Voltage (V)	Rotor Surface Rise from Heating (μm)	Estimated Rotor Temperature (°C)
3	60	300	100 - 2000	24	64 AC	15	90
	75	300	100 - 3000	30	64 AC	15	90
	90	300	100 - 2800	30	64 AC	15	90
1	75	100	100 - 3000	24	64 AC	15	90
	75	200	100 - 3000	24	59 AC	15	90
	75	300	100 - 3000	24	62 AC	15	90
	75	400	100 - 3000	24	60 AC	15	90
	75	500	100 - 3000	24	53 AC	15	90
2	75	100	100 - 3000	30	37 DC	4.5	41
	75	200	100 - 3000	30	37 DC	4.5	41
	75	300	100 - 3000	30	37 DC	4.5	41
	75	400	100 - 3000	30	37 DC	4.5	41
	75	500	100 - 3000	30	37 DC	4.5	41
	75	600	100 - 3000	30	33 DC	4.5	41
	75	700	100 - 3000	30	39 DC	4.5	41

5.2.4 Motion Measurement and Error Sources

For each combination of stator excitation frequency and voltage in the experiment schedule of Table 5.2, the reversal frequency f_r is swept from 100 Hz to 3 kHz. Figure 5.6 shows a plot of the response curve obtained by the microvision system for the 100 kHz experiment in experiment set 3. The figure also shows an overlay of the predicted response for a Duffing oscillator using the parameters given in the figure. The equation of motion for a Duffing oscillator and the method used to extract a value of torque from each experiment are each described in Section 5.3.

The data in Figure 5.6 provides a good example for a discussion of error sources in the motion measurement experiments. Some of these errors are evident in the low reversal frequency data of Figure 5.5. Error sources are either systematic, arising from the experimental technique, or they are random errors, arising from equipment uncertainty or statistical fluctuations [7]. Consider first the systematic errors in this experiment. Since the number of sample intervals is fixed within each measurement experiment, or each row of Table 5.2, the sampling rate decreases as f_r decreases, and it can become low enough to cause aliasing in the low frequency data [64] if higher harmonic motion is present, as it is for the lightly-damped tethered rotor. To avoid the problem in these experiments, the number of sample points is set high enough to keep the sampling rate above the Nyquist frequency of 2 times the natural frequency. Table 5.2 shows that the sampling rate, equal to the number of sample intervals times the reversal frequency, is always greater than or equal to 2.4 kHz for

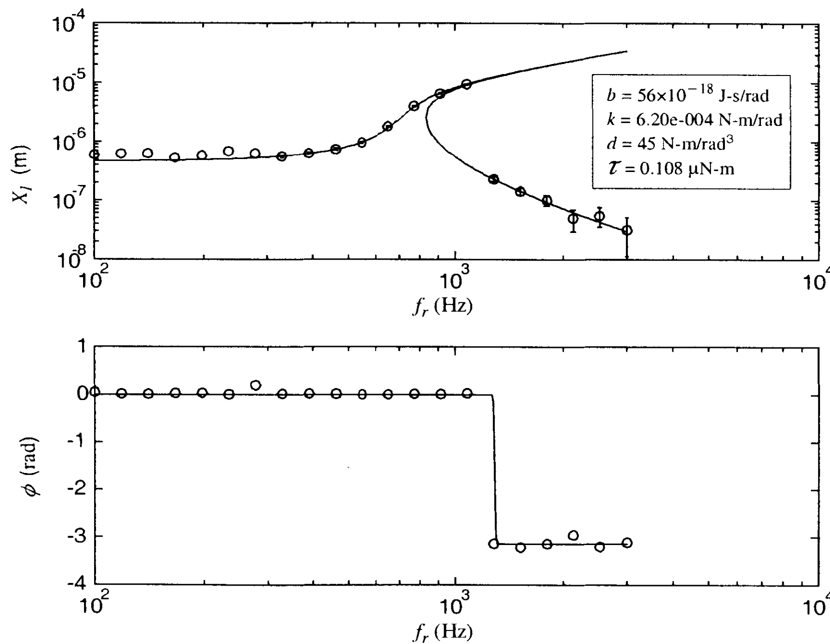

Figure 5.6: A plot of rotor perimeter tangential displacement versus reversal frequency, as measured by the microvision system. X_l is the fundamental fourier harmonic of the linear displacement in a direction tangential to the perimeter of the rotor.

the experiments in this thesis. This is greater than 2 times the natural frequency, or about 1.6 kHz, so aliasing is most likely not the cause of the observed scatter in the low frequency data of Figure 5.6.

Another candidate source of the low-frequency scatter comes from the forcing function. The torque is applied as a square-wave in time, so higher harmonics are not generally negligible. Since the device has a very high Q, these higher temporal torque harmonics can prematurely excite resonant motion at a low torque reversal frequency. Three of these higher harmonic resonances could be significant, with peaks appearing at 1/3, 1/5 and 1/7 the natural frequency of the tethered motor. This is not an aliasing problem, and it can be predicted. Notice the two very slight low-frequency peaks at approximately 253 Hz and 152 Hz in the data of Figure 5.6. These peaks correspond to approximately 1/3 and 1/5 the natural frequency of the tethered rotor. Thus, higher torque harmonics, resulting from the abrupt switching of the stator wave travel direction, may be the explanation for the observed low-frequency scatter in that data set.

There are other sources of systematic error that could contribute to the low-frequency scatter seen in Figure 5.6 and the remaining data included in Appendix F. First, there are external vibrations from which the tethered micromotor test rig cannot be totally isolated. The vibration isolation table is not perfect, so if there are modes of significant magnitude at frequencies above 2.5 kHz they could be aliased to the fundamental. Such aliasing would likely be more effective at particular frequencies since the modes would be due to such things as vibrating machinery near the test rig, and it would be hard to predict. In addition, it would most likely not be consistent from day to day. Second, micromotor TMA has only three tethers remaining. Although the tethers are very nearly symmetric around the rotor, lateral modes could be excited. These modes could either add or subtract from the motion fundamental reported by the vision system. Fortunately, sources of systematic error appear to be relatively minor and do not generally occur in the high frequency data that is used to fit torque.

Beyond systematic errors due to the measurement technique, statistical errors also affected the measurement of rotor deflection [7, 22]. Due to the accuracy of the microvision system, statistical errors were significant only in very high-frequency measurements, so error bars are only shown for high-frequency data in Figure 5.6. The last section noted that the microvision system is capable of measuring in-plane motion as small as 1 nm. Statistical error was quantified for the system configuration used in this thesis, showing that the highest level of accuracy could not be reproduced here. Statistical error was measured here by two means: First, the system was run as it would be during test, but the torque reversal stimulus was disconnected from the op-amp electronics. The system consistently measured 20 nm of random deflection due to steady background vibrations. Second, with the stimulus reconnected, the reversal frequency was increased until the predicted magnitude of

forced oscillation became much lower than 1 nm. This was repeated for several stator excitation frequencies. In each case, the measured very high-frequency motion was always seen to level off at an average magnitude of 20 nm. Thus, both approaches led to the same error estimate, and the statistical error was assumed to be 20 nm as reflected in the error bars on the data plots.

5.3 Data Analysis

In this section, the data collected as described in the previous sections is analyzed to extract a measurement of torque versus stator excitation frequency and stator voltage. First, the behavior of the rotor on its tethers is explained in terms of the equation of motion for a Duffing oscillator. Then the torque and spring stiffnesses are determined for each experiment by fitting the calculated response curves to the measured response curves. For each experiment, the best fit torque is plotted versus the stator voltage spatial fundamental magnitude or the stator excitation frequency, depending on the experiment set, to produce Figure 5.9 and Figure 5.10.

5.3.1 A Duffing Oscillator

The data in Figure 5.6 reveals that the tethered rotor behaves as a Duffing oscillator. The response curve of this oscillator can take two forms [44, 74] and can even display chaotic behavior. The form observed here is non-chaotic and described by the equation

$$J_r\ddot{\theta} + b\dot{\theta} + k\theta + d\theta^3 = \tau_f(t). \qquad 5.1$$

Here $\theta = {x(t)}/{r_m}$ where $x(t)$ is the measured tangential displacement of the rotor at radius r_m; and J_r is the moment of inertia of the rotor given by $J_r = \frac{1}{2}M_r r_T^2$, where M_r is the mass of the rotor and r_T is the radius of the tethered rotor disk. The effective viscous damping coefficient enters through b; k is the equivalent linear spring stiffness; d is the equivalent cubic spring stiffness, and τ_f is the forcing torque whose time functionality is set by the op-amp power electronics and the microvision system as described previously. The torque function is thus not a perfect sine-wave and is expressed as

$$\tau_f(t) = \tau(f_e, \hat{V}, T_r) \sum_{n=1}^{\infty} \frac{4}{n\pi}\cos(\omega_r t), \qquad 5.2$$

where $\omega_r = 2\pi f_r$. For each torque harmonic, several harmonics of motion are excited due to the nonlinearity of the differential equation. However these higher harmonics are small and will be neglected here [44]. A single harmonic analysis is used here, so only the fundamental component of Equation 5.2 is considered. The error in this approach is discussed in Section 5.2.4.

The predicted amplitude of the fundamental mode of oscillation $\Theta_1 = X_1/r_m$ and its phase ϕ relative to the drive signal is found by solving the following two equations [44, 74]:

$$\left(\left(k - J_r\omega_r^2 + \frac{3}{4}d\Theta_1^2\right)^2 + b^2\omega_r^2\right)\Theta_1^2 = \tau^2(f_e, \hat{V}, T_r) \qquad 5.3$$

and

$$\frac{b\omega_r}{k - J_r\omega_r^2 + \frac{3}{4}d\Theta_1^2} = \tan\phi\,. \qquad 5.4$$

Thus, the measured motion is predicted to be

$$x(t) = r_m\Theta_1\cos(\omega_r t - \phi)\,. \qquad 5.5$$

In addition, the rotor of TMA is not in contact with the stator and does not rotate at high speed, so the damping coefficient b is expected to be very small. This means that the phase ϕ is zero below the natural frequency and $-\pi$ above the natural frequency, with a sharp phase transition at the natural frequency. This is confirmed by all experimental data, which, like Figure 5.6, all show a sharp phase transition.

Figure 5.6 shows that the cubic term in Equation 5.1 shears the resonance peak toward higher forcing frequencies. This means that for solutions not far above the natural frequency, there are three real solutions for the amplitude in Equation 5.3. It also means that the natural frequency is difficult to determine from the data. The phase transition, which is usually used to find the natural frequency, actually occurs well above the natural frequency, wherever the resulting amplitude of the forced motion suddenly switches from the largest real solution to the smallest solution of Equation 5.3, as seen in Figure 5.6. It can be shown that all solutions on the underside of this sheared peak are unstable, so the rotor cannot oscillate with any of those amplitudes.

Starting at a low reversal frequency and increasing the frequency in small increments, the amplitude first follows the upper curve in Figure 5.6. If the frequency can be increased smoothly beyond the natural frequency, when the two additional real solutions of Equation 5.3 appear the rotation amplitude will continue to follow the largest of these. As the reversal frequency is increased further, the difference between the two real solutions becomes so small that any random disturbance can perturb the rotor to oscillate at the amplitude of the middle solution such that when the disturbance vanishes the amplitude quickly decreases to the lowest solution of Equation 5.3. At that time the phase abruptly switches from zero to $-\pi$. In a practical experiment, this behavior means that even for modest Q it is nearly impossible to determine the damping coefficient in the presence of a Duffing oscillator. As damping increases, the sheared resonance peak will become increasingly blunt, but it is difficult to distinguish the difference between measurements showing a

jump across a very narrow sheared peak, from measurements showing a drop off the end of a blunt sheared peak. However, it is still possible to distinguish the extreme cases since appreciable damping will cause the phase to gradually decrease toward $-\pi$ as the natural frequency is approached. Since this behavior is not seen in any of the data from the experiments conducted on TMA, the viscous damping can be assumed to be very small for all measurements in this thesis.

Nevertheless, when fitting the equation of motion to the data in Figure 5.6, error can be reduced by making an estimate of the damping coefficient. This has been investigated through additional experiments that were designed to produce very small rotor deflections, making the cubic term in Equation 5.2 negligible. Using the measured response curves, a Matlab™ function is used to fit a standard second order equation and find the Q of TMA. From this, the equivalent viscous damping coefficient [74] for tethered motor device TMA is calculated to be $b \cong 56 \times 10^{-18}$ J-s/rad and is enforced on all fits to the data from the experiments in Table 5.2, as reflected in the legend of Figure 5.6 and in the legends of the data included in Appendix F.

5.3.2 Curve Fit to Find Stiffness and Torque

To fit the equation of motion for the Duffing oscillator to the measured deflection curves, it was only necessary to know the mass of the rotor, since the geometry was known precisely. Without destroying the motor after testing, the mass had to be estimated. To obtain an excellent estimate of the mass of one rotor, the masses of several tethered rotors that had broken free from discarded die were measured. These masses were found to be tightly grouped around 13.1 ± 0.1 mg, so this number was used for all fits.

Knowing the mass, and hence the rotational inertia J_r, the values of the linear spring stiffness k, the cubic spring stiffness d, and the torque magnitude τ were then found to make the best visual fit of Equation 5.3 to each of the measured deflection curves listed in Appendix F. The fitted stiffnesses are plotted in Figure 5.7 and Figure 5.8. Fits were performed for each of the experiments listed in Table 5.2. Across all experiments, no attempt was made to force the same stiffnesses during the fitting procedure; the visual fit uniquely determines the two stiffnesses and the torque. As seen in the figures, the linear stiffness decreased by 22% when the temperature was doubled from 45 °C to 90 °C. As the temperature was decreased, the linear stiffness tended toward the predicted room temperature value of $3k_\theta/8 = 7.25 \times 10^{-4}$ N/rad. The stiffness calculated in Section 3.4.2 is modified for this comparison since only three out of eight tethers remain in device TMA. Excellent agreement was found between the two 90 °C experiments, the fitted linear stiffness terms varied by only 4%. For the cubic stiffness term, no dependence on temperature was measured; its value is steady at 45 N/rad^{-3} within the accuracy of the fit.

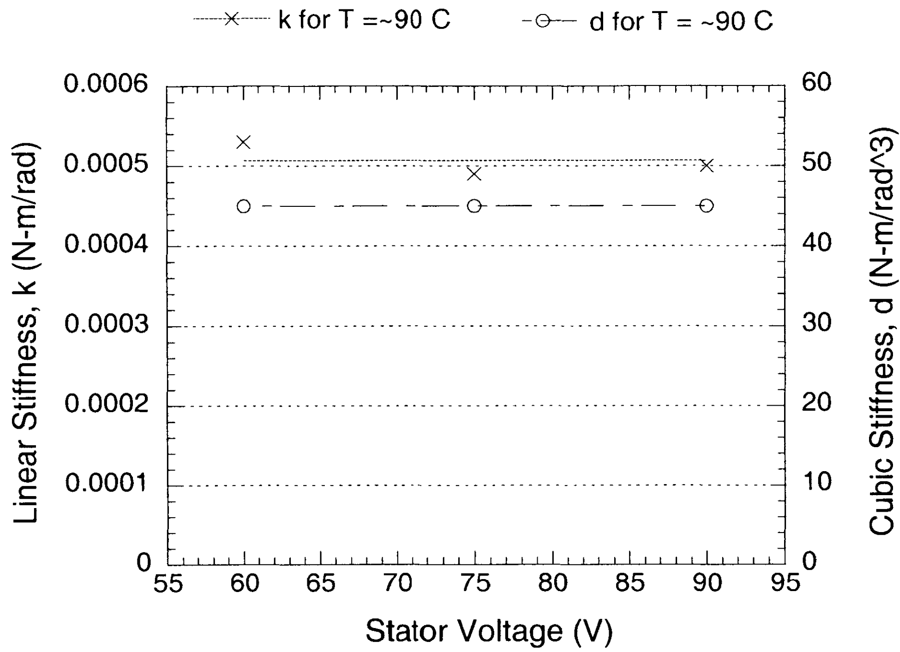

Figure 5.7: Fitted linear and cubic stiffnesses for experiment set 1.

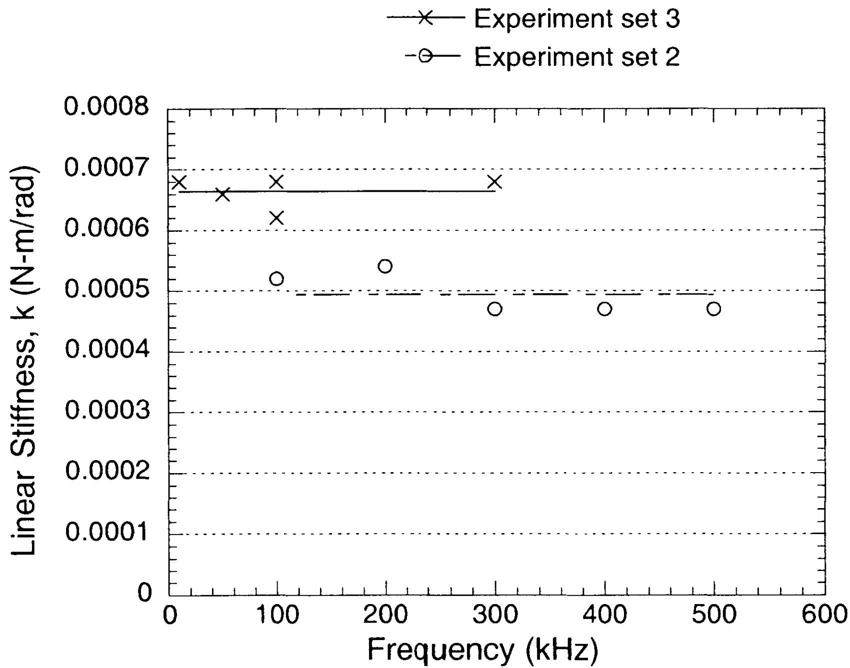

Figure 5.8: Fitted linear stiffnesses for experiment sets 2 and 3. The cubic stiffness is the same as in experiment set 1. Note the increase in stiffness as the tethered motor temperature decreases from 90 °C in experiment set 2, to 41 °C in experiment set 3.

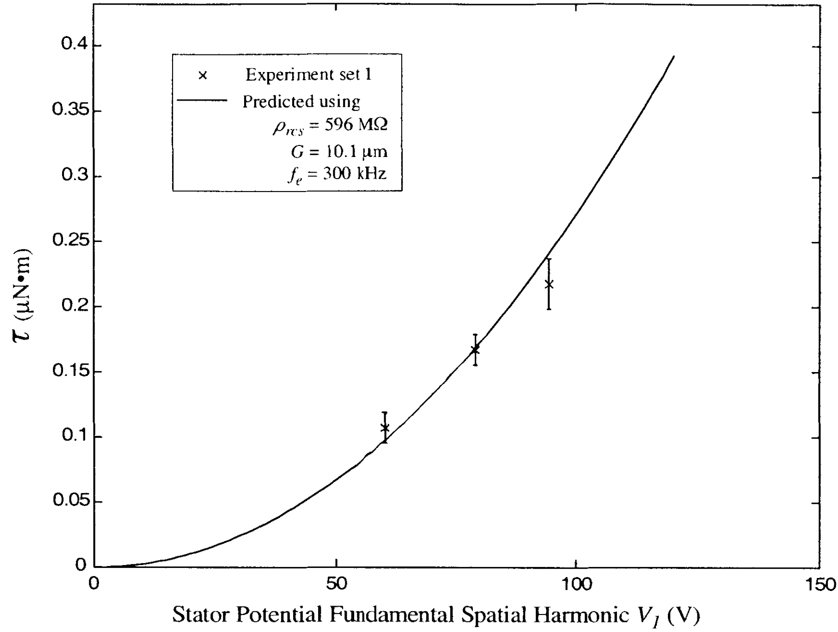

Figure 5.9: Plot of measured torque versus stator voltage, for stator excitation frequency equal to 300 kHz. Predicted torque is fit by the method of least squares. The fit assumes that Phase C does not contribute to torque.

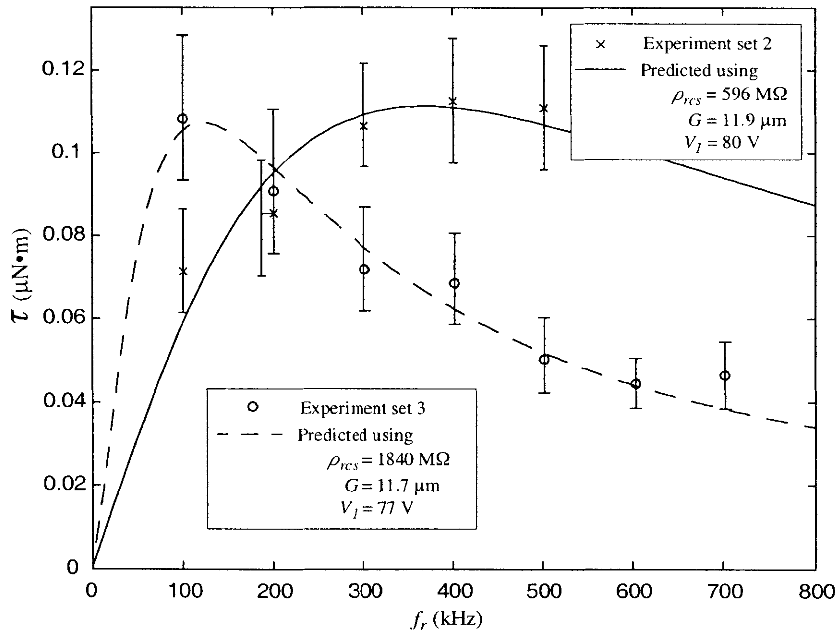

Figure 5.10: Plots of measured torque versus stator excitation frequency, for two rotor temperatures, with predicted torque curves fit by the method of least-squares. The fit to Set 2 assumes that Phase C does not contribute to the torque.

Next, extracted torque is compared to predictions from the models of Chapter 3. Torque is first analyzed as a function of the stator traveling potential wave spatial fundamental, at a single stator excitation frequency, using experiment set 1 in Table 5.2. To fit a prediction curve to this data, the sheet resistance is fixed at about 3 times the design value, for reasons that will become clear below, and the air gap is used as a fit parameter. Figure 5.9 plots torque versus the magnitude of the fundamental spatial voltage harmonic corresponding to the applied electrode voltages, confirming that the dependence is nearly quadratic as expected from Equation 3.1. No explanation has been found for the divergence of the data from prediction.

The fundamental voltage on the abscissa of Figure 5.9 does not include the voltage applied on Phase C. As noted above, epoxy has seeped between the rotor and stator die, connecting Phase C to ground, and Phase C is the only phase electrically affected in this way. The equivalent resistance of the current pathway starting at the branch point and travelling around the ring interconnect to the electrodes is 2.7 kΩ. This is more than twice the measured resistance of Phase C to ground. Because of the resultant voltage divider, it is unlikely that the electrodes of Phase C are able to charge fully, so the voltage of Phase C would be too low to contribute to torque. Thus, the stator potential fundamental on the horizontal axis of Figure 5.9 is calculated from the measured power electronic output voltages, but with Phase C assumed to be equal to zero. Additional support for this assumption comes from the excellent agreement of maximum torques between experiment sets 2 and 3. In experiment set 2, an AC voltage is applied to Phase C; AC voltages should contribute to torque. In experiment set 3, a DC voltage is applied to Phase C; DC voltages do not contribute to torque. Since the two torque results match, the AC voltage applied to Phase C in experiment set 2 does not appear to contribute to torque. Thus, it is concluded that the electrodes of Phase C are not active.

Next, torque is analyzed as a function of the stator excitation frequency using experiment sets 2 and 3, each carried out with a single stator voltage. The extracted torque is plotted in Figure 5.10. Due to the nature of the op-amp electronics, it is not possible to reproduce an exact set of electrode voltages and relative phase delays from one experiment to the next. For these electronics, both gain and the actual shape of the square-waves are functions of the stator excitation frequency. To account for variation in the applied stator voltage from one data point to the next, the voltage inputs to the stator are measured, the stator potential wave fundamental is calculated, and extracted torque is normalized based on the stator potential wave spatial fundamental. The fundamental corresponding to the peak extracted torque data point, in each of sets 2 and 3, is chosen as the reference. Then all other extracted torque numbers in each set are adjusted relative to this data point to obtain the normalized extracted torques. To perform the normalization, for each data point the magnitude of the fundamental stator potential spatial harmonic is calculated. Then each raw extracted torque

number is multiplied by the square of the ratio of the fundamental spatial harmonic for that data point, to the fundamental spatial harmonic for the reference data point. The normalized extracted torque is plotted in Figure 5.10.

Finally, a predicted torque curve is fit to the normalized extracted torque data for each experiment, producing the curves in Figure 5.10. Here both the rotor sheet resistance and rotor-stator air gap length are used as the fit parameters in a least-squares algorithm; their fitted values are shown in the figure. The curves are calculated using all temporal harmonics of the measured electrode voltages for the reference data point of that set. Thus some error is generated because the normalization method does not adequately account for them. From another point of view, the error arises because only one stator traveling wave can be used to calculate the predicted curve, while in actuality each data point was generated with a unique stator potential wave because of limitations of the power electronics. However, since the phase delays of the higher harmonics are not well balanced, they do not contribute substantially to torque and the error is small.

These results suggest that the air gap is nearly 12 μm, approximately 4 times its design value. This compares well with the air gap measurement reported in Section 5.2.1. Further, the rotor sheet resistance is found to be higher than its design value, and is found to vary with temperature. This result is discussed further below.

5.4 Summary and Conclusions

This chapter described the equipment and procedures used to measure the torque of the tethered motor. The first section reviewed the design and implementation of the electronics, the test platform, and the computer microvision system used to measure the deflection of the rotor. The next section described the use of the electronics and vision system to perform rotor deflection measurements, and used one set of deflection measurements to discuss possible sources of error. The very last section described the theory of the predicted rotor motion and the application of that theory to the measured rotor deflection in order to extract micromotor torque.

Two primary conclusions follow from the results of this chapter. First, if the larger air gap length is accepted based on the measurements reported in Section 5.2.1, then the models of Chapter 2 predict the behavior of the electric induction micromotor very well. The predicted torque curves are well within the estimated error of the measurements. Second, the design goals defined in Chapter 3 have not been met. The tethered motor should have produced a peak torque of approximately 28 μN-m at 300 V and 750 kHz, at room temperature. Instead it obtained a peak torque of 0.22 μN-m at 90 V and 300 kHz, at approximately 90 °C.

The larger air gap is one part of the failure to reach the design goals. For an otherwise perfect tethered motor operated at a stator voltage of only 75 V, having an air gap of 12 μm instead of the intended 3 μm, a peak torque of only 0.19 μN-m is predicted by the models. Beyond the larger air gap, an inoperable Phase C drops the predicted peak torque to 0.13 μN-m, which compares well to the measured 0.12 μN-m at this frequency and voltage. Thus, the failure to achieve the desired torque is accounted for by fabrication errors.

No good explanation has been found for the discrepancy between the 75 V data point of experiment set 1 and the 300 kHz data point of experiment set 2. Ideally, the torque should be the same for each of these experiments. As measured, the torque measured in experiment set 1 is 59% higher than the torque measured in experiment set 2. This error is most likely the result of poor data collection. A review of the plots of the displacement data contained in Appendix F shows that there are some unaccounted for sources of error in this data. Although the high frequency data, which is used to extract the torque, appears to have little error, there is a probability that error in this data is responsible for the discrepancy.

Finally, comparison of experiment sets 2 and 3 shows that the resistivity of the rotor conductor changes with temperature. Given the difficulty in designing and constructing high-voltage high-frequency power electronics with variable frequency capability that could compensate for resistivity changes, it is important to understand this phenomenon. First the two data points of rotor conductor sheet resistance are converted to resistivity and plotted versus $1/kT$ as shown in Figure 5.11. Then an exponential is fit based on a model of polysilicon resistivity summarized by [29] as indicated in the figure. The fitted activation energy of 0.24 eV corresponds to a Boron dopant concentration of approximately 10×10^{16} cm^{-3}, according to Figure 5.12 of [29]. The dose for the Boron implant of the rotor conductor in the tethered motor is 5.5×10^{12} cm^{-2}, which results in a dopant concentration of 11×10^{16} cm^{-3} if all implanted carriers are electrically active throughout the 0.51 μm thick rotor conductor. However, not all implanted dopant will become electrically active. Some is lost during the implant, and since Boron segregates into oxide, some diffuses into the rotor insulator and capping oxide during the 1000 °C anneal after implant. An implant efficiency of just over 90% is somewhat high, but reasonable, so the measured activation energy is also reasonable from this viewpoint. From Figure 5.11, the rotor conductor resistivity at room temperature is extrapolated to 1661 Ω-m, for a sheet resistance of 3256 MΩ, approximately 17 times higher than the design value.

Most of the difference between actual rotor sheet resistance and the design target can be explained by a comparison of actual tethered motor rotor process flow versus the ideal rotor process flow. The absence of a wafer bond means that the polysilicon in the tethered motor rotor did not undergo the planned anneal step at 1100 °C for 60 minutes. In contrast, the polysilicon in the rotor

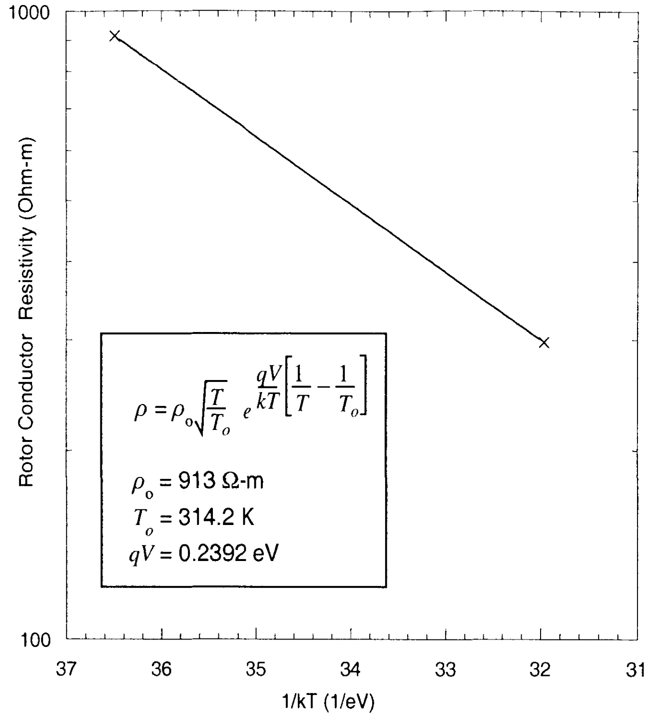

Figure 5.11: Variation in rotor conductor resistivity with rotor temperature, reduced from the torque measurements of experiment sets 2 and 3. See [29] for the origin of the resistivity equation.

conductor test structures described in Section 3.4.1 underwent two anneals in N_2 at 1100 °C. Ion implantation makes the polysilicon amorphous, and grain recrystallization takes place during the post-implant anneal at 1000 °C. For moderately-doped polysilicon, significant additional grain growth occurs during subsequent annealing at 1100 °C. The resistivity of moderately-doped polysilicon is inversely proportional to grain size [29]. Thus an order of magnitude smaller grain size, due to the lack of the 1100 °C anneal for the tethered motor, would account for the difference between the actual sheet resistance in the motor and the sheet resistance predicted using the rotor conductor test structures. Based on simulations with the software package SUPREME-III, for an as-deposited grain size near 50 nm, the grain size of moderately-doped polysilicon after an 1100 °C anneal is nearly 500 nm. Thus, because tethered motor TMA was not assembled with a fusion bond, the anneal at 1100 °C did not take place and the grains did not grow. Thus the resistivity of the tethered motor rotor should be approximately an order of magnitude higher than the design value, and in fact it is.

Chapter 6

Concluding Remarks

6.1 Summary

This thesis presented the analysis, design, fabrication, and testing of an axial gap electric induction micromotor. The micromotor developed in this thesis was successfully implemented in a micromotor-compressor described in [21] toward eventual use as an electric starter motor and generator in a micro gas-turbine generator and a stand-alone micromotor-compressor. In Chapter 2, electromechanical models were developed to predict the performance of the micromotor. The models included both analytical distributed-field models and lumped-parameter equivalent-circuit models derived from the distributed-field models. The distributed-field models concentrated on the air gap and rotor of the machine while the equivalent-circuit models included stator wiring and the associated parasitic resistance and capacitance. Both forms of the model were developed to be sufficiently general for the prediction of either motor performance or generator performance in an electric induction micromachine. In Chapter 3 the distributed-field models were used to optimize micromotor performance, measured in terms of torque output, and the equivalent-circuit models were combined with a circuit model for a power electronic drive to predict the total efficiency of the micromotor and drive electronics combined.

The development of all fabrication technology needed to build a tethered electric induction micromotor was completed as part of this thesis and reported in Chapter 4. Development of several crucial processes required relatively greater effort and was highlighted in this thesis. First, this thesis developed a reliable process for uniform thick buried oxide on silicon (TBOS). This is a damascene process enabling 10–20 μm of insulator to be recessed into the surface of a wafer so that wafer bow from residual stresses in the thick insulator may be reduced without reducing the ability to perform critical dimension photolithography anywhere on the surface of the wafer. Second, although a successful wafer bonding process in the presence of many thin films was not executed as part of this thesis, a considerable amount of bonding knowledge was gained. In place of wafer bonding, a method for aligned assembly on the die-level was created. Third, a process was developed to produce a polysilicon rotor conductor with a well-defined resistivity. Fourth, a specialized deep reac-

tive ion etch process was developed, using an inductively-coupled plasma etcher to define deep, high aspect ratio silicon tethers between the rotor and a rigid support that were used to transduce torque produced by the micromotor into rotational deflection. These tethers were very tall and very thin to be very compliant in the azimuthal direction, yet very stiff in the axial direction. Finally, the illustrations of the tethered motor and the summary of the process flows belied the actual complexity the entire fabrication process. The tethered motor process consisted of 13 masks and over 170 process steps; this thesis developed every non-standard unit process step in the flow.

In Chapter 5, the thesis presented measured torque data as a function of stator voltage and stator excitation frequency. Torque was extracted from deflection measurements that were made possible through the use of a specialized computer microvision system [22]. Electronics were developed to be integrated with the microvision system so that oscillatory motion was produced in the tethered motor. From the functional dependence of the measured amplitude of the oscillatory motion versus the oscillation frequency, the tethered motor was found to constitute a Duffing oscillator. Thus, the solution to Duffing's equation was used to extract the linear and cubic coefficients of stiffness of the bulk silicon spring, and to extract the torque produced by the electric induction micromotor. This method was used to measure the torque as function of both stator voltage and stator excitation frequency. Next, the electromechanical models developed in Chapter 2 were utilized to fit calculated torque curves to the measured torque data. Finally, the torque data was examined to determine how well the micromotor performed with respect to both the models of Chapter 2 and the design objectives of Chapter 3.

6.2 Conclusions

The work presented in this thesis proves that a powerful electrostatic induction motor can be built on the micro-scale using only materials that are compatible with CMOS processes, that its torque can be measured, and that the torque output rivals that of other micromotors.

The primary objectives of this thesis were to demonstrate that a micro-scale electric induction machine fabricated with CMOS processes could meet the needs of the micro gas-turbine generator, and that its analysis and design could be successfully executed based on the understanding embodied in the models of Chapter 2 and explored in Chapter 3.

In light of these goals, this thesis yields two summary conclusions. First, if the large air gap length is accepted based on the discussion in Section 5.2.1, then the models of Chapter 2 predict the behavior of the electric induction micromotor very well. The predicted torque curves are well within the estimated error of the measurements. Second, the design goals defined in Chapter 3 have not been met. At the full voltage of 300 V, the tethered motor should have produced a peak torque

of approximately 28 μN-m at 750 kHz, at room temperature. Instead, the tethered motor obtained a peak torque of 0.22 μN-m at 300 kHz, at approximately 90 °C.

The larger air gap is one part of the failure to reach the design goals. For an otherwise perfect tethered motor operated at a stator voltage of only 75 V, having an air gap of 12 μm instead of the intended 3 μm, a peak torque of only 0.19 μN-m is predicted by the models. Beyond the larger air gap, an inoperable Phase C drops the predicted peak torque to 0.13 μN-m, which compares well to the measured 0.12 μN-m at this frequency and voltage. Thus, the failure to achieve the desired torque is accounted for by fabrication errors.

No good explanation has been found for the discrepancy between the 75 V data point of experiment set 1 and the 300 kHz data point of experiment set 2. Ideally, the torque should be the same for each of these experiments. In actuality, the torque measured in experiment set 1 is 59% higher than the torque measured in experiment set 2. This error is most likely the result of poor data collection. A review of the plots of the displacement data contained in Appendix F shows that there are some unaccounted for sources of error in this data at low reversal frequencies. Although the high frequency data, which is used to extract the torque, appears to have no error beyond random noise, there is a probability that error in this data is responsible for the 59% discrepancy.

Finally, comparison of experiment sets 2 and 3 shows that the resistivity of the rotor conductor changes with temperature. Given the difficulty in designing and constructing high-voltage high-frequency power electronics with variable frequency capability that could compensate for resistivity changes, it is important to understand this phenomenon. First the two data points of rotor conductor sheet resistance are converted to resistivity and plotted versus $1/kT$ as shown in Figure 5.11. Then an exponential is fit based on a model of polysilicon resistivity summarized by [29] as indicated in the figure. The fitted activation energy of 0.24 eV corresponds to a Boron dopant concentration of approximately 10×10^{16} cm^{-3}, according to Figure 5.12 of [29]. The dose for the Boron implant of the rotor conductor in the tethered motor is 5.5×10^{12} cm^{-2}, which results in a dopant concentration of 11×10^{16} cm^{-3} if all implanted carriers are electrically active throughout the 0.51 μm thick rotor conductor. However, not all implanted dopant will become electrically active. Some is lost during the implant, and since Boron segregates into oxide some diffuses into the rotor insulator and capping oxide during the 1000 °C anneal after implant. An implant efficiency of just over 90% is somewhat high, but reasonable, so the measured activation energy is also reasonable. From this, the rotor conductor resistivity at room temperature is extrapolated to 1661 Ω-m, or 3256 MΩ, approximately 17 times higher than the design value.

Most of the difference between actual rotor sheet resistance and the design value can be explained by a comparison of actual tethered motor rotor process flow versus the ideal rotor process flow. The absence of a wafer bond means that the polysilicon in the tethered motor rotor did not

undergo the planned anneal step at 1100 °C for 60 minutes. In contrast, the polysilicon in the rotor conductor test structures described in Section 3.4.1 underwent two anneals in N_2 at 1100 °C. Ion implantation makes the polysilicon amorphous, and grain recrystallization takes place during the post-implant anneal at 1000 °C. For moderately-doped polysilicon, significant additional grain growth occurs during subsequent annealing at 1100 °C. The resistivity of moderately-doped polysilicon is inversely proportional to grain size [29]. Thus an order of magnitude difference in grain size, due to the lack of the 1100 °C anneal for the tethered motor, would account for the difference between the actual sheet resistance in the motor and the sheet resistance predicted using the rotor conductor test structures. Based on simulations with the software package SUPREME-III, for an as-deposited grain size near 50 nm, the grain size of moderately-doped polysilicon after an 1100 °C anneal is nearly 500 nm. Thus, because tethered motor TMA was not assembled with a fusion bond, the anneal at 1100 °C did not take place and the grains did not grow. Thus the resistivity of the tethered motor rotor should be approximately an order of magnitude higher than the design value, and in fact it is.

Finally, note that the temperature dependence of the moderately-doped polysilicon prohibits its use in the micro gas-turbine generator because of the high temperatures of that device. An alternative solution must be found.

Technical Points

From a fabrication point of view, the results of this thesis confirm that a proper wafer bonding solution is required to produce a properly functioning electric induction motor. Nearly all difficulties in achieving the objectives of this thesis stem from the inability to bond the rotor and stator wafers. In the absence of wafer bonding, epoxy is required to assemble the tethered motor. First, this causes great uncertainty in the air gap length because the epoxy is drawn between the rotor and stator dice by capillary action. Second, the epoxy has shorted out Phase C. Finally, the absence of the wafer-bonding anneal also has lead to an error in the fabrication process of the most important part of the electric induction machine, the rotor conductor, resulting in a rotor sheet resistance that is very different from that predicted by the rotor conductor development experiments. This has led to a need to heat the device to decrease the rotor sheet resistance and enable torque measurements.

The thesis also confirms that wafer bonding is not possible after multiple thin film depositions, or after these films are stripped, unless special surface preparation such as Chemical Mechanical Planarization/Polishing (CMP) is provided afterwords. Thin film deposition processes do not always produce films that are smooth enough to bond—a bondable thin film must generally have an rms roughness of no more than 10 Å, and when thin films are stripped in a wet or dry etching process, care must be taken to ensure complete removal. Just a few isolated remaining islands of a thin

film can completely prohibit wafer bonding. Therefore it is essential to develop a reliable optimized CMP process to planarize and polish the wafer surface to enable wafer bonding.

A reliable planarization scheme is especially critical for the TBOS process. In this case an optimized CMP serves three purposes. First, a good CMP process removes any stray pieces of field oxide; in the tethered motor these could be as large as the thickness of the thick buried oxide. Second, CMP polishes the surface of the field oxide so that newly deposited films are not seeded with a rough surface, causing the surface of the growing film to be rough\. Finally, CMP removes the 50 μm-wide lip around the rim of the silicon pit, making precise photolithography possible over the entire wafer surface.

The fabrication results described in Chapter 4 show that it is possible to reliably produce very high aspect ratio mechanical springs in single crystal silicon using an ICP etcher. The results reported in Chapter 5 also confirm that the small deflection bulk spring constants are very close to predictions by simple beam theory. However, Chapter 4 also points out that the etch obtained is sensitive to the condition of the etcher. Thus the etch recipe should be tested and possibly adjusted if significant time has passed since the last etch, or if the etcher is known to be in some non-equilibrium state.

Through the results of Chapter 5, some of the difficulties with the utilized high-frequency high-voltage power electronics are clearly apparent. First, higher temporal harmonics due to square-wave electrode excitation do not appear to affect the torque significantly for the data reported in this thesis because they do not appear to have the proper phase relation, but since this cannot be confirmed for all voltage and frequency combinations the higher temporal harmonics must be included in the analysis, making the analysis much more laborious and its interpretation less intuitive. Second, the op-amps in the power electronics are operated near the limits of their capabilities, therefore even the fundamental temporal harmonic of a generated waveform is imperfect. For both of these reasons, the use of a square-wave power-electronic drive makes data reduction a laborious process and therefore impedes data interpretation. On the other hand, in the next best topology, a series resonant topology that would produce near perfect sine waves, it is quite difficult to obtain a wide frequency range with a single set of electronics. Furthermore, the square-wave topology is more easily mated with the computer microvision system. Thus, the choice of a power electronic topology is a difficult compromise, and could be considered further.

Finally, although this thesis considers only an electric induction motor, the tethered motor concept in combination with computer microvision is sufficiently general to enable other motor types to be tested as well. In fact, at this time there is another effort underway to test the performance of a magnetic induction motor using the same approach. Micromagnetic technology has advanced significantly in recent years and may soon be a suitable technology for microturbomachinery applica-

tions like the micro gas-turbine generator. However, it is important to remember that the performance of micromagnetic technology will suffer in the presence of the extreme heat generated by the micro gas-turbine.

6.3 Recommendations for Future Work

In order to achieve the goals set forth for the electric induction motor, it is necessary to solve problems with the following matters: bonding, rotor conductor resistivity, and power electronics. First, and most strongly, it is recommended that much more research be conducted to develop an adequate wafer bonding solution for wafers that have had any thin films on the bonding surface at any time during processing. As stated above, nearly all difficulties in the production and interpretation of measurements reported in Chapter 5 stem from the inability to bond the rotor and stator wafers. A wafer bonding solution would have greatly reduced uncertainty in the measured torque data.

Second, although the temperature sensitivity of moderately-doped polysilicon happened to be an advantage for the tethered motor in this thesis (because the room temperature resistivity was much higher than expected), it causes problems in the micromotor-compressor and will be completely inadequate for the micro gas-turbine generator. It is possible to reduce the temperature coefficient of resistance (TCR) in moderately-doped polysilicon by doping with both Phosphorous and Boron, but it will be necessary to carefully control the implant dosage and account for segregation of Phosphorous to grain boundaries. This will be necessary if doped polysilicon is to be used in future devices. Conversely, perhaps another type of rotor conductor should be developed. Moderately-doped polysilicon was never intended for the high-temperature environment of the micro gas-turbine engine. As an alternative, it has been proposed that electron tunneling be employed to produce a rotor conductor whose resistivity is reliable and maintained even as the temperature is increased through 1000 K.

Third, available power electronics are simply not adequate to reach the objectives of this thesis. The frequency is limited to hundreds of kHz, and the voltage is limited to less than 100 V. In addition, the method of reversing the direction of the motor torque so that oscillatory rotor deflection could be measured complicates the interpretation of high reversal frequency data—and the interpretation of torque data—and causes inaccuracies in the low reversal frequency data. A better approach is needed to cause the rotor oscillation. One method that had been initiated as part of the research of this thesis, though not described in the thesis, involves oscillation of the DC voltage supplied to the power electronics. This approach is probably not possible with the op-amp electronics used in this thesis, but had been successfully tested using the series resonant topology. The approach was not used simply because the frequency range of the resonant power electronics could not be adequately extended.

Finally, in order to reach beyond the goals set out in Chapter 3, portions of the fabrication process beyond bonding and the rotor conductor will also need to be improved. First, by using more advanced photolithography equipment, much smaller electrodes with better alignment control could be obtained. According to the analysis in Section 3.2.5, this would increase the upper bound on stator periodicity and increase the maximum torque produced by the induction motor. However, as the inter-electrode gap is decreased, the stator rated voltage may also need to decrease to avoid breakdown. Second, according to Section 3.2.4, by replacing the rotor insulator with a thicker dielectric or one with a lower permittivity, greater maximum torque could likewise be obtained. And finally, Section 3.3.1 shows that a metallized stator would produce a much more efficient motor, with more predictable electrode voltages. Future versions of the electric induction motor should be fabricated using metal electrodes. Each suggestion for fabrication improvement cannot be considered alone; a change in any one unit process step will impact the entire fabrication process, as is true for the fabrication of any complex microelectromechanical system.

Appendix A

Consequences of the Inter-Electrode Gap

It may be possible to reduce the viscous drag in the air gap by etching deep trenches in the inter-electrode gap. It has been shown that the effectiveness of the trenches is increased if they are made as wide as possible. The trenches serve to increase the effective air gap length where fluid drag is concerned. However, an increase in the inter-electrode gap has a detrimental effect on the mechanical torque output from the electric induction machine in a manner similar to the dependence on active area shown in Figure A.1. The decrease in torque is related to the dependence of torque on active machine area but is tempered by the nature of the electric fields across the insulating inter-electrode gap.

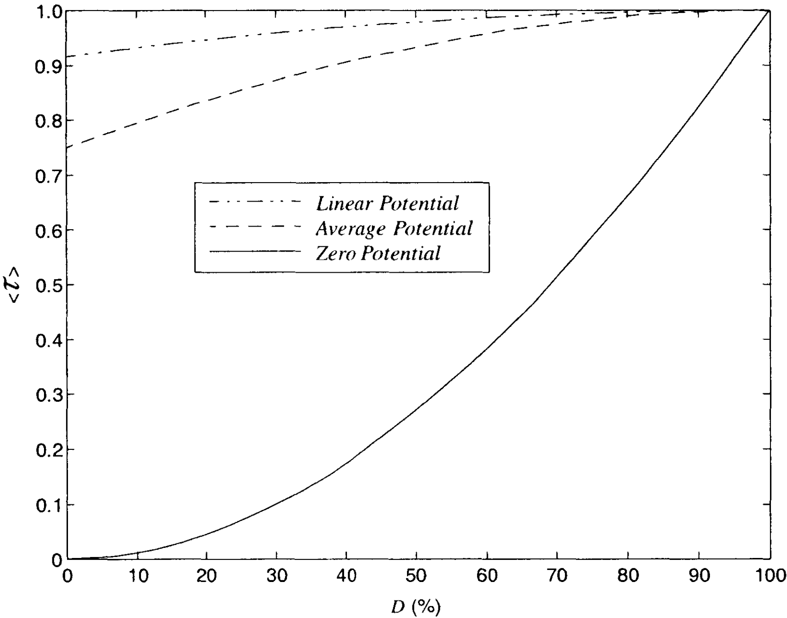

Figure A.1: Normalized maximum electromechanical torque plotted as a function of the stator electrode duty ratio D. The duty ratio is the ratio between the area of the electrodes and the area of the inter-electrode insulating gaps. Each curve is for a different assumed potential function across the inter-electrode insulating gap.

In the baseline design, the inter-electrode insulating gap is a constant width from the inner radius of the stator electrodes to the outer radius. This gap could be opened only as far as the inner radius allows. Yet wider gaps could be obtained at the outer radius where viscous drag is most severe. Therefore to obtain the results shown in Figure A.1, the gap is allowed to grow linearly with radius, and the fraction of the stator covered by electrodes is referred to as the duty ratio.

To simplify the analysis, the development of the 3D multiple-harmonic model begins by assuming a potential distribution between the stator electrodes. As the inter-electrode gap widens, the assumed potential takes on greater significance. To illustrate this, Figure A.1 shows results given three different assumptions: a time-harmonic spatially linear function, a time-harmonic spatially constant average, and a time-invariant spatially constant zero potential. Which case is applicable in the baseline design is not known exactly because it depends in part upon the cleanliness of the exposed insulator surface between the electrodes. However, it is clear that this issue requires further study since the baseline design effectively has a duty ratio of 50 at the inner radius and 75% at the outer radius.

Appendix B

The Micromotor-Compressor

The micromotor-compressor provides a design framework and near-term application goal for the electric induction micromotor. The motor-compressor is a complex device, composed of many sub-systems, intended to produce a compression ratio sufficient to pump compressed gases through a fuel cell for better efficiency. In so-doing, it will provide valuable data for use in the future design of the compressor within the micro gas-turbine generator. The integration of all motor-compressor sub-systems is quite involved and is therefore the subject of a separate Ph.D. thesis [21]. However a summary of several key points will serve to describe the motor-compressor in sufficient detail for the purposes of this thesis.

The motor-compressor consists of a centrifugal compressor that is driven at high speed by an electric induction motor while supported on gas bearings. The compressor performs work on a fluid at a rate that is proportional to the square of the tip speed of its blades, thus it is intended to operate at high rotational velocities. Naturally, the compressor itself is intended to be the primary beneficiary of power converted by the electric induction motor, but at the design speed of the motor-compressor the air gap dissipates a large fraction of the total energy converted by the induction micromotor. In addition, the gas bearings also dissipate considerable power. These include one journal bearing and two thrust bearings. The thrust bearings dissipate the most energy per area unit, given the small clearance needed in for efficient operation.

Preliminary coupled simulations were conducted in an attempt to optimize the electromechanical design of the motor-compressor [21]. The electromechanical models of Chapter 2 were coupled with fluid-mechanical models of the motor-compressor and several aspects of the design were varied in a search-mode optimization. The first bubble in Figure 3.10 shows design aspects that were affected in this preliminary consideration. Note in particular the distinction between motor radii and rotor radius. The former denotes the extent of the active, torque-producing surface of the electric induction machine, while the latter denotes the size of the rotating machinery. By making rotor radius larger and the outer motor radius smaller, it is possible to increase compressor tip speed while

maintaining (or even decreasing) motor velocity. In so doing, viscous losses in the micromotor air gap and thrust bearings are minimized and become a much smaller fraction of the total losses due to fluid friction, while compressor work is increased with the square of the tip speed. However in the baseline design of the motor-compressor, the power balance is only slightly positive.

The preliminary optimization clearly outlined a better design, however a great deal of effort had already been invested in modeling and fabrication of a first-generation bearing test rig. This decision prescribed the radii listed in Table 3.1. A decision was made to preserve this geometry and thus make use of any data resulting from the bearing rig. Therefore, the rotor disk radius was not optimized, and the motor radii were changed only slightly to accommodate a bearing seal. In addition, the electrode geometry was defined to include the maximum number of electrodes possible given a limit on the minimum line width able to be resolved in available photo lithography equipment, and thrust bearings were optimized. Thus, at that point, it was not possible to truly optimize the design, and as yet an attempt has not been made to fabricate the optimized design. So, even though the motor could produce up to 9 W in an optimized version, with several watts available to drive the compressor, the net power available to the compressor remains a fraction of a watt in the baseline design. Fortunately, the analysis, design, electromechanical optimization, and fabrication of an electric induction micromotor proves valuable even though the total system may not be optimized.

Appendix C

Additional Unit Process Development

This appendix is included to provide additional documentation about the process development that was required for many steps of the micromotor process flow, that necessary for the tethered motor as well as that necessary for any device which would incorporate the electric induction micromotor described in this thesis. Much of what is described here was borne out of equipment constraints and thus probably particular to the Microsystems Technology Laboratories.

C.1 Accelerated Development Approach

In order to deal with the extremely short time lines of the micro-engine project, a particular approach was used to fabricate lots of stator and rotor wafers. This approach has been dubbed the leader-follower approach and is not new, but it seems worthwhile to note that it was used here.

In this approach, each wafer lot was limited to 5 wafers, and several lots were processed in parallel, skewed by at least one process step each, and designated A, B, C etc. Processing of lot A was started first, followed by lot B, then C etc. In this way, lot A finds defects in the process flow first, so that they can be fixed in lot B. If A is not destroyed by the defects, then it goes on to find the next flaw in the flow. Care must be taken to be sure that the next flaw found is not related to the presence of the first flaw. Likewise lot B, now staring out with an advantage since it will not suffer from the first flaw found, goes forward and finds any flaw not discovered by lot A. The cycle continues through lot C and how ever many more are deemed necessary. This approach relies on the fact that while one lot is in a machine, there is usually plenty of time for the builder to multi task and put one or more of the other lots in other machines. In the experience of this thesis, three lots is about the maximum number that can be processed at once without a loss of productivity. In cases where more than one builder is available, the number can be increased.

C.2 Stator Unit Process Development

C.2.1 Silicon Pit Etches

If the stator surface were completely flat, the air gap would be entirely defined by one fairly deep timed high density plasma Si etch, two timed PECVD silicon dioxide depositions, and one timed LPCVD polysilicon deposition. We have been able to reliably reproduce silicon dioxide and polysilicon thicknesses to within less than 5%; so these steps seem robust. However, the Si pit is 6 mm wide, almost three orders of magnitude more than its depth of 10 μm; and this has been shown to lead to a severe bowl shape, or the inverse, in high density plasma etchers. In our experience to date, after solving numerous machine problems, we have been able to etch pits whose depths are uniform to an average of 1%; so it would seem that there is no problem here.

However, plasma chemistries that produce a flat bottom also produce tall narrow silicon spikes due to micro-masking in the pit; it is feared that these would cause device failure. At present, to find additional processing difficulties as soon as possible, we are continuing with the remaining process steps while investigating possible silicon pit solutions in parallel. These include alternate etchers, alternate chemistries in the same etcher, or post etch thermal oxidation of the spikes whereupon they might be selectively removed. Thus if the spike problem can be resolved, the air gap design tolerance of 6000 Å suggests that we will be able to define the air gap within specification.

Issues with Intermediary Etches

In general, intermediary etches are defined here as those etches that are outside the design specifications of standard etchers — deeper than shallow etches intended with standard high-density plasma etchers such as the AME P5000, but well below the intended etch depths for deep reactive-ion etchers such as the STS Time-Multiplexed ICP Deep-Reactive-Ion Etcher or the Alcatel 601E. The tethered motor process flow contains 4 intermediary etches: two in silicon and two in oxide. All four etches used the AME P5000.

These intermediary etches are problematic for two reasons. First, micro-masking or wafer defects lead to non-uniformities across the bottom of etched features. And second, the etches required a long period of time in the etcher, leading to overheating or reaction product buildup on the etcher walls.

A basic silicon pit etch that had been optimized for shallow etches was initially used for both the stator and rotor flows, but this etch exposed the problem with micro-masking and caused dishing of the etch surface. The dishing would have lead to a non-uniform air gap. Since the device is designed for a minimum safe air gap, much of the air gap would then have been larger than called for, causing a decrease in device performance.

Dishing was decreased by making the etch recipe more isotropic, simultaneously reducing a problem caused by micro-masking. By the end of the 10 or 12 µm silicon pit etch, micro-masking on the native silicon surface created pillars approximately 1-2 µm wide as shown in. The micro-masking defects were initially thought to be remnants of the resist of oxide mask used, but the problem could not be corrected by longer develop times for the resist mask or longer wet etches of the oxide hard mask in hydrofluoric acid. The pillars were often over 5 µm high and were shown to lead to raised features in the air gap of the motor. If the process flow did not include planarization in a later step, these raised would cross the air gap and cause rotor strike, giving rise to a short circuit or a large friction force or both.

Unfortunately, the issue was never completely solved. The aforementioned modifications to the etch recipe, detailed in Appendix E, made the etch more isotropic so that many fewer pillars appeared, but in their place were small pits. Figure C.1 shows that these pits were most likely the result of the pillars being undercut near the end of the etch. Since the thick insulators easily fill and planarize these pits, this might not have been such a bad situation. However, since some pillars were wider, they were not undercut enough to break free, and remained in the pit. This happened to be the case for the rotor wafers of one lot so a planarization was added to the rotor flow for that lot. This lot happened to be the only one to make it into devices.

Oxide etches in the tethered motor process flow also required recipe development. These included the ILD and tether hard mask etches. In short, it was desired to develop much faster etches that had greater selectivity to the resist mask, so that less time needed to be spent in the etcher and

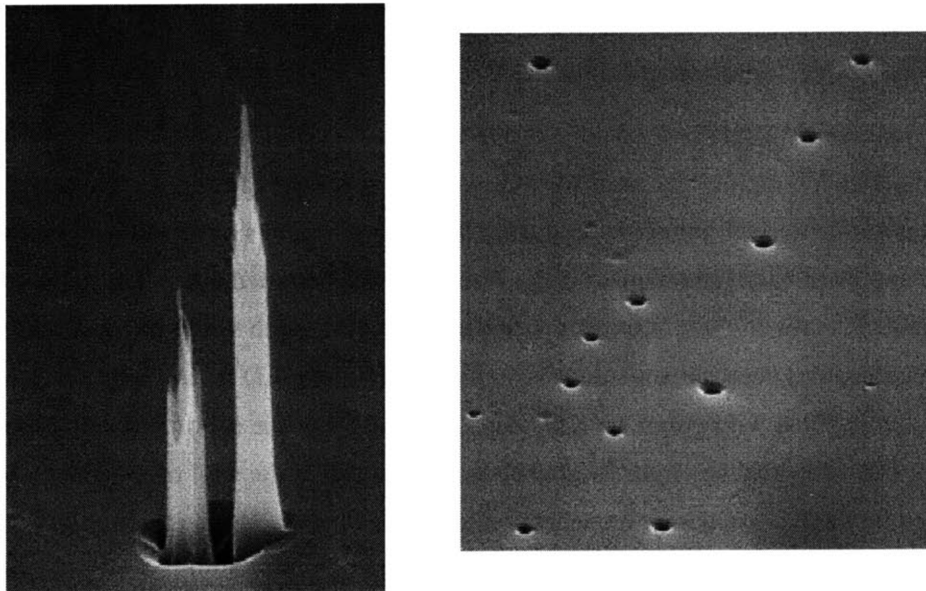

Figure C.1: (a) Silicon pillars that can remain after an intermediary etch. (b) Pits that remain when recipe is adjusted to decrease incidence of pillars.

thinner resist could be used, allowing finer features. Features to be etched ranged in size from 2 μm wide vias through the ILD to 20 μm wide halos through the tether hard mask. Recall that the ILD was 1 μm thick while the tether hard mask was 3 μm thick. Details of the etch recipe are listed in Appendix E. In summary, to the extent possible given available gases, Fluorine was removed from the etch chemistry. Fluorine ions are especially reactive with the hydrocarbon-based resist, so their removal decreased the etch rate of the resist. This improved the selectivity since the fluorine species did not contribute significantly to the ion-bombardment process which accomplishes the etch of the silicon dioxide.

Having said the above, these etches are not free of problems. Oxide etch of this depth required long process times. Etch rates of 35 Å/s were attained regularly, but even at this rate total etch times would be 5 min and 14 min for the ILD and tether hard mask, respectively. Thus if wafer cooling is not adequate, overheating will lead to a loss of selectivity, and perhaps burn the resist.

C.2.2 Electrode Etch

We encountered extreme electrode sidewall roughness which decreased the inter-electrode breakdown voltage and threatened to greatly limit power output. Fortunately the source of this problem was discovered to be an over-etch of the electrode layer that was necessitated by the highly anisotropic nature of the etch chemistry in use at the time. After this etch, small pillars of polysilicon remained between electrodes. These were cleared with a short, highly isotropic etch, which lead to the sidewall roughness. Electrode roughness was corrected through the use of a different etch chemistry that we have recently developed, see recipe E.3.2, and we believe that this issue has been resolved.

C.2.3 TEOS versus Silane-Based Oxide

The recessed stator flow had one side effect due to the initial choice of isolation material. Initially silane (SiH_4) PECVD oxide was used for the insulator layers of the stator. Since silane PECVD oxide does not migrate well into corners during deposition, regions of low density oxide were created on either side of each interconnect ring. These regions persisted even after a one-hour densification at 1100 °C. As one might expect, low density regions etch much more quickly than well-densified regions, thus deep narrow trenches were created in the ILD during the new etch-back steps and subsequently filled with polysilicon in Step 2 and Step 4 of the stator flow. In Step 2, this was not an issue since the trenches were located about 12 μm inside the wall of the silicon pit and were then covered by the ILD, making no connection to the electrodes. However, in Step 4 the electrode polysilicon filled the trenches formed during the ILD etch-back, and it turned out to be impossible to etch this material from the trenches. Thus the electrodes were shorted and the devices were not salvageable.

The solution for the next batch was to use TEOS (tetraethylorthosilicate, $Si(OCH_2CH_3)_4$ PECVD oxide as the ILD. This was expected to be a transparent solution since after densification TEOS has nearly the same properties as silane oxide. In addition, this is precisely the type of problem that TEOS PECVD oxide has historically been used to solve [TEOS paper from 99 report]. The second lot of recessed stator wafers showed no signs of accelerated etching.

C.2.4 Alignment Issues

The alignment and minimum feature size for via patterning and electrode patterning were designed with specific fabrication constraints in mind. The alignment tolerance is designed to be 2 μm, the minimum electrode width is 4 μm, and the smallest vias are close to 2.5 μm. Given the usual operating characteristics of the Karl Suess MA4 Contact Aligner in TRL, alignment was expected to be within 2 μm. It turned out that 1 μm was possible repeatedly. However, features on the wafer were changed by a larger margin than expected in comparison to their size on the mask, so this extra alignment accuracy was needed.

The minimum reproducible feature size, from mask to wafer was found to be about 1.5 μm for a 2 μm coat of OCG825 35 cs resist, the current ICL standard. Note that TRL uses OCG825 20 cs standard, which is less viscous and thus does not require a fast spin for the standard 1.1 μm coating. However, the low viscosity also limits the upper bound of thickness to about 1.6 μm. Features any smaller than this tend to show somewhat random variations in thickness and width. The minimum features included in the tethered motor mask set are 1.5 μm, these are only found in the verniers used to measure misalignment after patterning on the stator wafer and as a back-up to measure the rotor deflection. Note however, at this writing these verniers have actually not made into a functioning device. This is due to a mask error which was not corrected until the third lot of rotor wafers was started. The first lot was reduced to one wafer which was lost during the tether etch, and the second lot provided all tethered rotors which have been assembled into tethered motors.

Appendix D

Detailed Process Flow Descriptions

D.1 Complete Tethered Motor Stator Flow

1: Si double side polished prime, 10-20 Ω−cm — *x* wafers — Paul Tierney
2: Add alignment marks — ~2 μm deep — Z-ALIGN LF 4”
3: Piranha clean and 50:1 HF dip — Clean sink — pre-metal, ICL

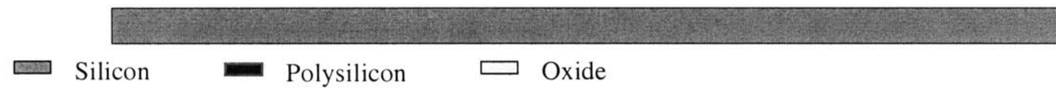

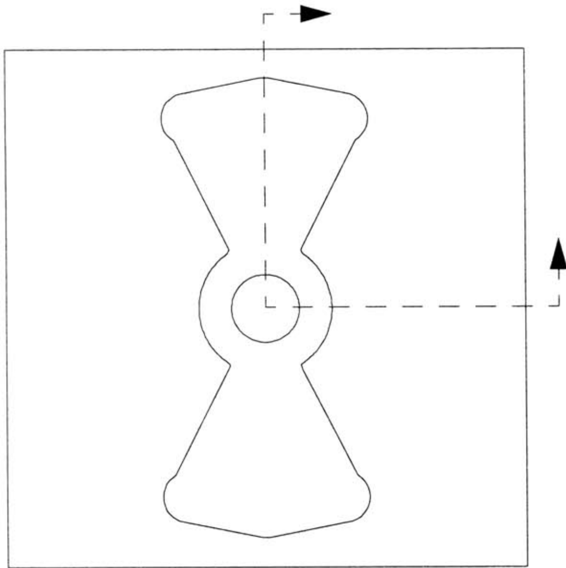

Mask: D1-STAT-PITS-DF

4: HMDS	25 min	HMDS, TRL
5: Thick positive resist coat	8 μm AZ P4612	coater, TRL
6: Prebake	60 s at 115 C	hotplate, TRL
7: Expose	25 s	ksaligner1, TRL
or	320 s	ksaligner2, TRL
8: Develop	2:30 min AZ 440 MIF	photo-wet-l
9: Postbake	5 min at 130 C	hotplate, TRL
10: Etch "gap pit," two options.		
10a: AME Etch	*rec NAGLE SI II*	
	⇒ ?? s for 12 μm	AME5000, ICL

- test etch rate on a monitor before use, nominal: 77.46 ± 3.52 Å/s

10b: STS Etch	*rec SF6_5*	
	⇒ ?? s for 12 μm	STS-1.TRL

- test etch rate on a monitor before use

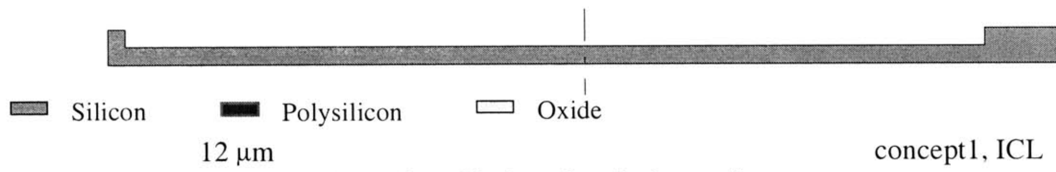

11: Dep PECVD "isolation ox"	12 μm	concept1, ICL

- include x LTO Monitors (bare Si), place monitors as: first in, middle in, last in if possible, keep these for future reference
- DO NOT DENSIFY

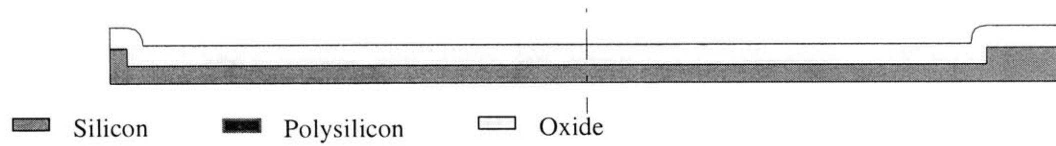

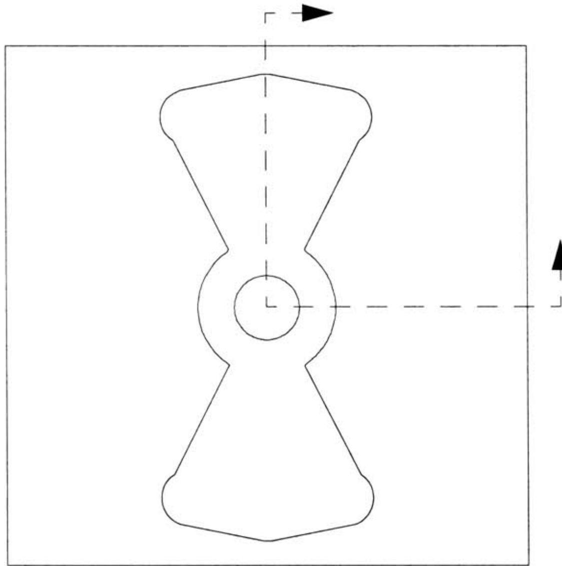

Mask: D2-STAT-CLEAROX-2-LF

Step	Parameters	Equipment
12: HMDS	25 min	HMDS, TRL
13: Thick positive resist coat	8 µm AZ P4612	coater, TRL
14: Prebake	60 s at 115 C	hotplate, TRL
15: Expose	25 s	ksaligner1, TRL
or	320 s	ksaligner2, TRL
16: Develop	2:30 min AZ 440 MIF	photo-wet-l
17: Postbake	5 min at 130 C	hotplate, TRL
18: Etch "isolation oxide"	7:1 BOE ⇒ approx. 40 min	oxide, ICL

• undensified Noveluus oxide etch rate: around 3500-3700 Å/min

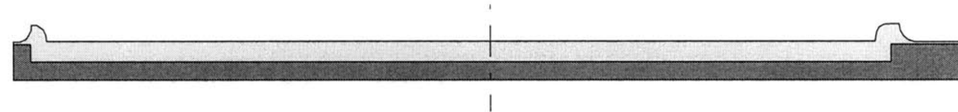

Silicon Polysilicon Oxide

Step		Parameters	Equipment
19: Piranha clean		10 min, clean sink	pre-metal, ICL
20: Dep PECVD "CMP stop"		2 µm	concept1, ICL
21: Densify		rec 190, 60 min, 1100 C	tubeB6, ICL
	or	rec 180, 60 min, 1100 C	tubeB5, ICL
	or	manual	tubeA2, B2, B3, TRL
22: CMP		table: 50 rpm quil: 30 rpm head: 3.0 psi back: 1.0 psi time: 12 min in smaller blocks	CMP, ICL
23: Post-CMP clean part I		piranha yellow dot containers	acid-hood, TRL
24: Post-CMP clean part II		standard rca in Novellus containers	rca, TRL

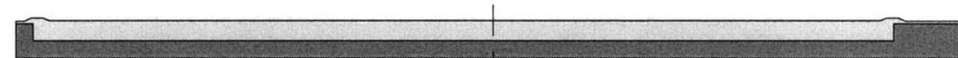

Silicon Polysilicon Oxide

Step		Recipe / Conditions	Equipment, Lab
25: Etch-back		until oxide recessed 2 μm, 7:1 BOE	oxide, ICL

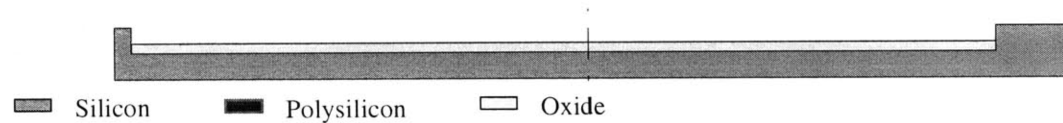

Step		Recipe / Conditions	Equipment, Lab
26: Measure “isolation ox” thickness in pit		rec Ox (n = 1.46) on Si	nanospec, TRL
	or	rec THICK OX BIG MAN	uv1280, ICL
27: Dep PECVD etch stop layer		2000 Å	concept1, ICL
28: Densify		rec 190, 60 min, 1100 C	tubeB6, ICL
	or	rec 180, 60 min, 1100 C	tubeB5, ICL
	or	manual	tubeA2, B2, B3, TRL
29: Dep Interconnect polySi		625 C, 10 000 Å	lpcvd, TRL
• include 3 Poly Monitors (1000 Å ox) for thickness measurement, place at load end of batch, middle of batch, and back of batch			
• the gas source for this tube is at the load			
30: Measure thickness		rec PolySi (n = 3.0) on 1000Å ox	nanospec, TRL
	or	rec”625 POLYSI”	uv1280, ICL
31: Implant “ring interconnects” in $POCl_3$ tube		rec 309	tubeA4, ICL
• include monitors from Step 29			
32: Clear $POCl_3$ oxide on all wafers		2+ min until solution beads on surface	oxide, ICL
33: Measure sheet R of “ring interconnects”		4-pt probe	prometrix, ICL
34: Measure thickness of monitors		rec PolySi (n = 3.0) on 1000Å ox	nanospec, TRL

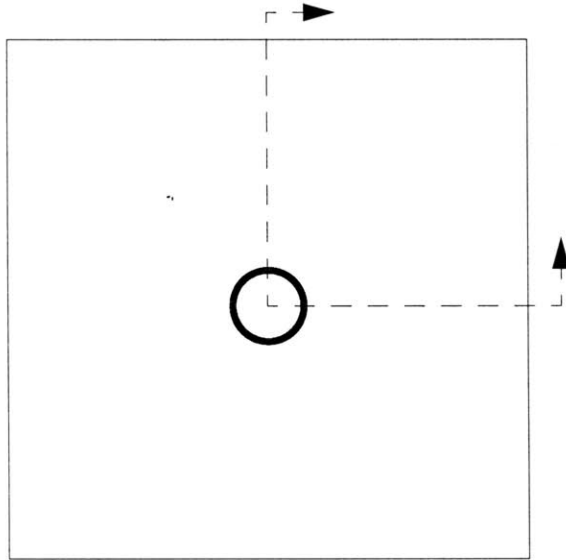

Mask: A-INTERCON-2

Step	Parameters	Equipment
35: HMDS	25 min	HMDS, TRL
36: Double thin resist	2 µm OCG825 35 cs	coater, TRL
37: Prekbake	1 min at 115 C	hotplate, TRL
38: Pattern	45 s	ksaligner2, TRL
39: Develop	1:30 min (1:1 OCG825)	phot-wet-l, TRL
40: Postbake	1 min at 130 C	hotplate, TRL
41: Etch pattern	rec NAGLE POLYSI	AME5000, ICL

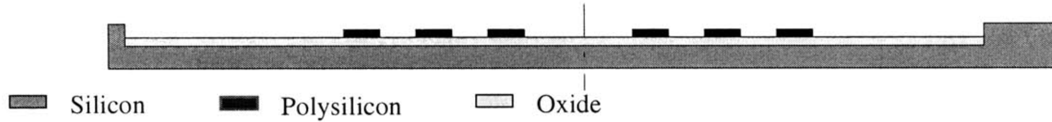

Step	Parameters	Equipment
42: Dep PECVD "ILD ox"	5 µm	concept1, ICL

- include 3 LTO Monitors (bare Si) in this and next two steps
- place monitors: first in, middle in, last in

Step		Parameters	Equipment
43: Densify		rec 190, 60 min, 1100 C	tubeB6, ICL
	or	rec 180, 60 min, 1100 C	tubeB5, ICL
	or	manual	tubeA2, B2, B3, TRL
44: Measure thickness of monitors		rec Ox (n = 1.46) on Si	nanospec, ICL
	or	rec THICK OX 5 PT	uv1280, ICL

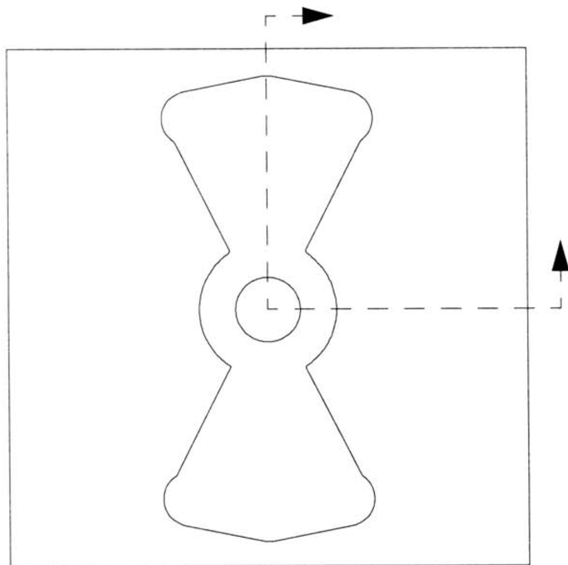

Mask: D2-STAT-CLEAROX-2-LF

Step	Parameters	Equipment
45: HMDS	25 min	HMDS, TRL
46: Thick positive resist coat	8 μm AZ P4612	coater, TRL
47: Prebake	60 s at 115 C	hotplate, TRL
48: Expose	25 s	ksaligner1, TRL
or	320 s	ksaligner2, TRL
49: Develop	2:30 min AZ 440 MIF	photo-wet-l
50: Postbake	5 min at 130 C	hotplate, TRL
51: Etch "isolation oxide"	3 μm in 7:1 BOE	oxide, ICL

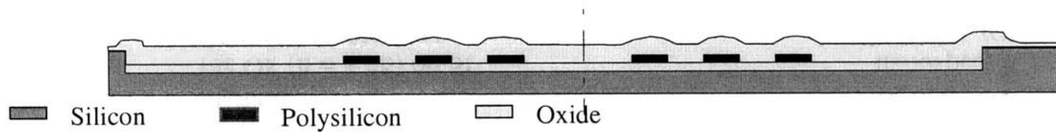

Step	Parameters	Equipment
52: CMP	table: 50 rpm quil: 30 rpm head: 3.0 psi back: 1.0 psi time: 12 min in smaller blocks	CMP, ICL
53: Post-CMP clean part I	piranha yellow dot containers	acid-hood, TRL
54: Post-CMP clean part II	standard rca in Novellus containers	rca, TRL
55: Etch back to 1 μm over interconnects	timed etch	oxide, ICL

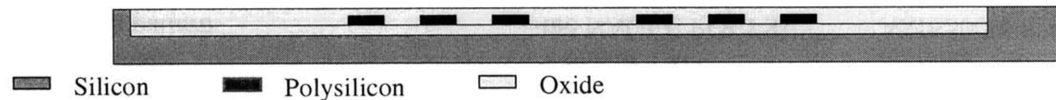

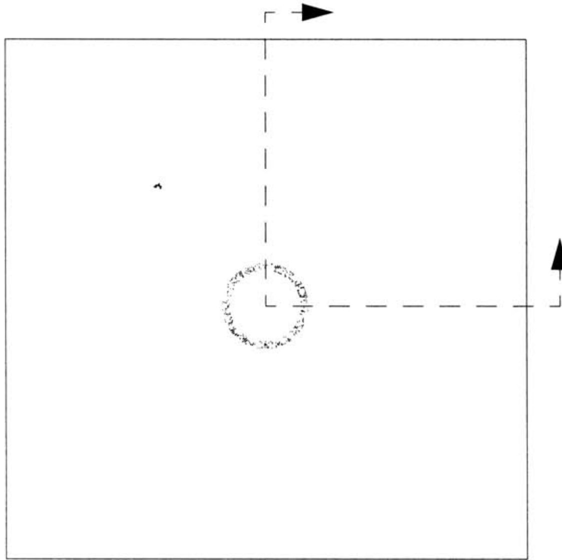

Mask: A-VIA-2

Step	Parameters	Equipment
56: HMDS	25 min	HMDS, TRL
57: Double thin resist	2 μm OCG825 35 cs	coater, TRL
58: Prekbake	1 min at 115 C	hotplate, TRL
59: Pattern	45 s	ksaligner2, TRL
60: Develop	1:30 min (1:1 OCG934)	phot-wet-l, TRL
61: Postbake	1 min at 130 C	hotplate, TRL
62: Etch pattern	rec NAGLE CHF3 590 s nominally, check rate	AME5000, ICL

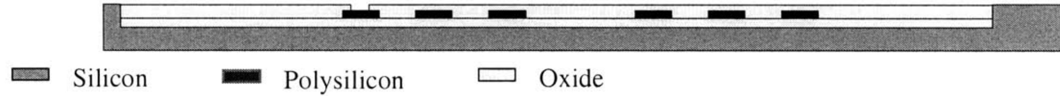

Step	Parameters	Equipment
63: Dep "Electrode polySi"625 C, 10 000 Å		lpcvd, TRL
• include 3 Poly Monitors (1000 Å ox) for thickness measurement • place at load end of batch, middle of batch, and back of batch		
64: Measure thickness on monitors	rec PolySi (n = 3.0) on 1000Å ox	nanospec, TRL
65: Implant "Electrode polySi" in $POCl_3$ tube	rec 309	tubeA4, TRL
• include monitors from Step 63		
66: Clear $POCl_3$ oxide on all wafers	2+ min until solution beads on surface	oxide, ICL
67: Measure sheet R of "Electrode polySi"	4-pt probe	prometrix, ICL
68: Measure thickness on monitors	rec PolySi (n = 3.0) on 1000Å ox	nanospec, TRL
69: Dep PECVD "bond ox"	2000 Å	concept1, ICL
• include 3 LTO Monitors (bare Si) in this and next two steps • place monitors: first in, middle in, last in		
70: Densify	rec 190, 60 min, 1100 C	tubeB6, ICL
or	rec 180, 60 min, 1100 C	tubeB5, ICL
or	manual	tubeA2, B2, B3, TRL
71: Measure thickness of monitors	rec Ox (n = 1.46) on Si	nanospec, ICL
72: CMP	table: 50 rpm quil: 30 rpm head: 3.0 psi	CMP, ICL

	back: 1.0 psi	
	time: 12 min in smaller blocks	
73: Post-CMP clean part I	piranha yellow dot containers	acid-hood, TRL
74: Post-CMP clean part II	standard rca in Novellus containers	rca, TRL

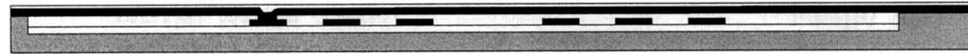

Silicon Polysilicon Oxide

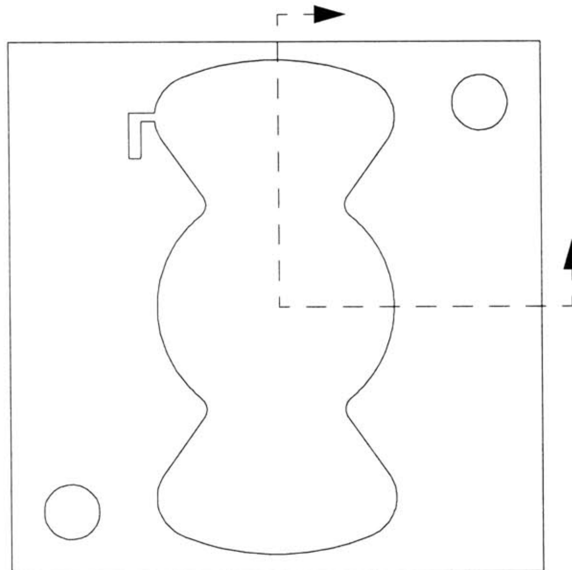

<u>Mask: A-BONDOX-CLEAR</u>

75: HMDS	25 min	HMDS, TRL
76: Double thin resist	2 μm OCG825 35 cs	coater, TRL
77: Prekbake	1 min at 115 C	hotplate, TRL
78: Pattern	45 s	ksaligner2, TRL
79: Develop	1:30 min (1:1 OCG934)	phot-wet-l, TRL
80: Postbake	1 min at 130 C	hotplate, TRL
81: Etch pattern	2 min, 7:1 BOE	oxide, ICL

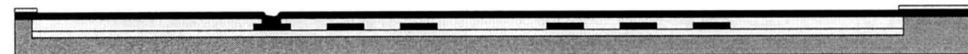

Silicon Polysilicon Oxide

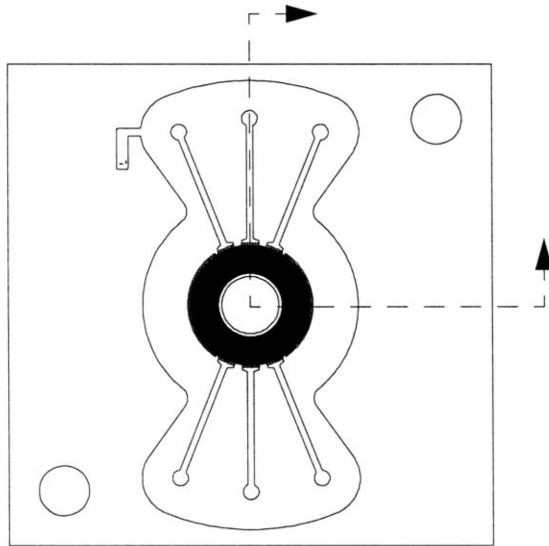

Mask: A-ELECTRODE-2

82: HMDS	25 min	HMDS, TRL
83: Double thin resist	2 μm OCG825 35 cs	coater, TRL
84: Prekbake	1 min at 115 C	hotplate, TRL
85: Pattern	45 s	ksaligner2, TRL
86: Develop	1:30 min (1:1 OCG934)	phot-wet-l, TRL
87: Postbake	1 min at 130 C	hotplate, TRL
88: Etch pattern	rec DPOLY-STD, 150 s	AME5000, ICL

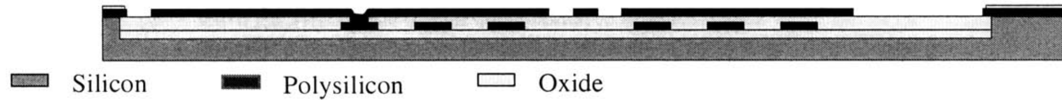

More steps added after this point to make fluid passages and define aft thrust bearings in the motor compressor [Luc's thesis].

D.2 Complete Tethered Rotor Flow

Step	Recipe	Machine
1: Si double side polished prime, 1-10 Ω–cm	10, 400 μm wafers (TTV 20 μm)	Si Quest
• even if not specified, where nec a handle wafer will be used to protect the double polished wafer		
2: Alignment marks	rec 10, 1-2 μm	etcher-1, ICL
• using etcher-1 will help keep backside from being damaged		
3: Piranha clean and 50:1 HF dip	Clean sink	pre-metal, ICL
4: Now process on "Bottom Side" of wafers		
5: Dep PECVD "pit mask ox"	rec 2.0 μm	concept1, ICL
• latest results: 1.82 μm at center 10/27/98		
• include at least 2 additional monitors for pit etch rate test in Step 22		
6: Densify hard mask	rec 190, 60 min, 1100 C	tubeB6, ICL
or	rec 180, 60 min, 1100 C	tubeB5, ICL
7: Measure "isolation ox A" thickness	rec Oxide on Si	uv1280, ICL
8: Now process on "Top Side" of wafers		

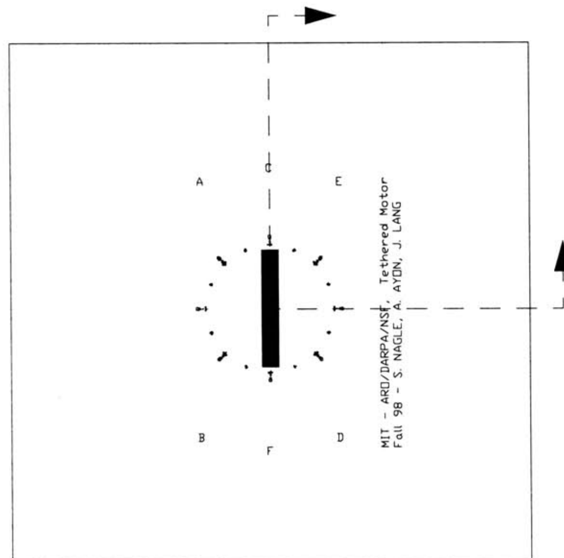

Mask: BT-MOIRE

Step	Recipe	Machine
9: HMDS	25 min	HMDS, ICL
10: Thick coat and prebake	rec 15	coater, ICL
11: Expose	40 s	ksaligner2, TRL
12: Develop and postbake	rec 24	developer, ICL
13: Produce "moire pattern"	rec $SF_6/O_2/Cl_2$	AME5000, ICL
or	rec 10, 400 s, 2 μm	etcher-1, ICL
or	rec NAGLE SI, 2 μm	AME5000, ICL

- although it is currently not possible to have all of these gases in one chamber in the AME5000, an $SF_6/O_2/CHF_3$ recipe is well documented to produce "black Si"
- SF_6 may be connected to chamber A via the Reif group lines (they and Joe Walsh have approved it)

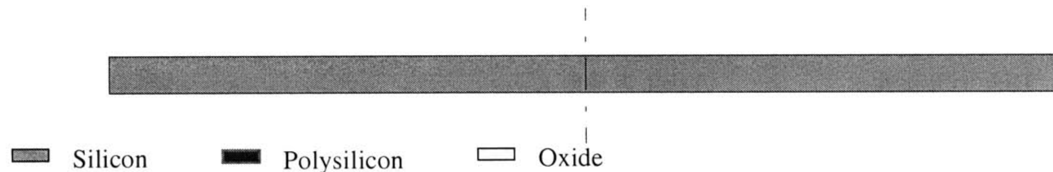

14: Now process on "Bottom Side" of wafers

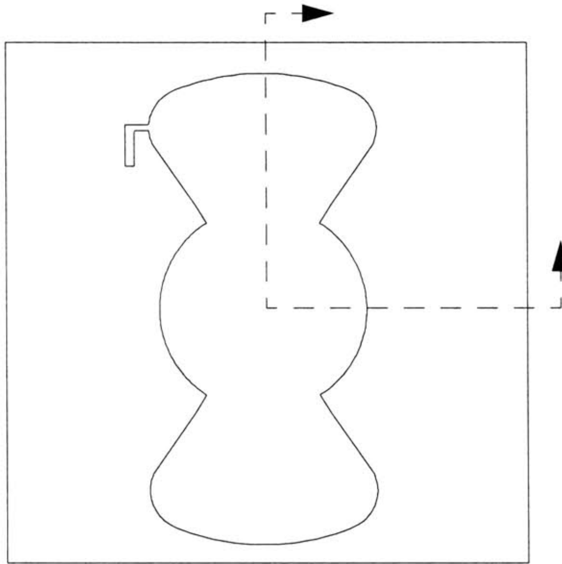

Mask: BB-ROTISO_PIT

Step	Recipe	Machine
15: HMDS	25 min	HMDS, ICL
16: Double coat and prebake	rec 15	coater, ICL
17: Expose	90 s	ksaligner2, TRL
18: Develop	rec 24	developer, ICL
19: Etch "pit mask ox"	20+ min, 7:1 BOE ⇒ or until clear	oxide, ICL
20: Clean wafers	strip sink piranha clean sink piranha 50:1 HF	pre-metal, ICL
21: Protect "Top Side"	AZ P4612	coater-prebake, TRL

22: Etch "gap pit"

22a: AME option

Step	Recipe	Machine
22a.i: Etch "gap pit"	rec NAGLE SI II ⇒ 00:07:56 for 13.5 μm	AME5000, ICL

- be sure machine has run with plasma for at least 15 min prior; etch rate has been shown to vary greatly as machine warms up
- test etch rate on a monitor before use, nominal: 212 ± 3.52 Å/s as of 11/98

22b: STS option

Step	Recipe	Machine
22b.i: Etch "gap pit"	rec MIT37 ⇒ 476 s for 13.5 μm	sts, TRL

- based on latest reports of 1.7 μm/min etch rate in this recipe

Step	Recipe	Machine
23: Clean wafers	strip sink piranha	pre-metal, ICL
24: Strip "pit mask ox" • until cleared	?? min, 7:1 BOE	oxide, ICL
25: Clean wafers	clean sink piranha and 50:1 HF	pre-metal, ICL

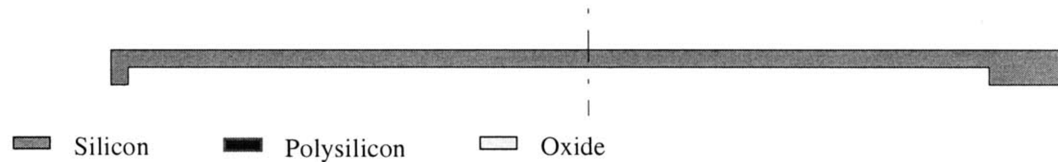

Silicon Polysilicon Oxide

Step	Recipe / Parameters	Equipment
26: Dep PECVD "isolation ox A"	rec nagle1	concept1, ICL
• set time per station based on results from 10 µm recipe • fill pits with oxide to level of native Si surface • place monitors as: first in, middle in, last in • use monitors for develop charac., etch the monitors before and/or along with device wafers, carry through Step 84		
27: Measure "isolation ox A" thickness	rec Thick SiO2 under GUEST1	uv1280, ICL

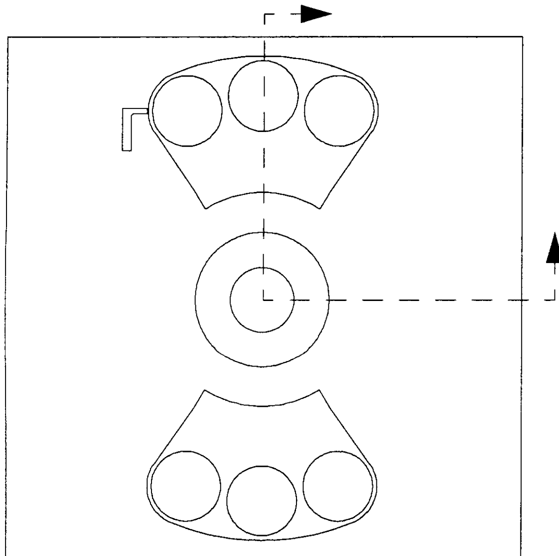

Mask: BB-ROTISO_CLEAR

Step	Recipe / Parameters	Equipment
28: HMDS	25 min	HMDS, ICL
29: Thick positive resist coat	8 µm AZ P4612 ~ 2.5 krpm on a good day	coater, TRL
30: Prebake	30 s	blue oven plate, TRL
31: Expose	60 s	ksaligner1, TRL
or	600 s	ksaligner2, TRL
• using vacuum - hold handle during alignment - hit vac before releasing • alignment and pattern transfer can then be extremely good		
32: Develop	~1:30 min, AZ 440 MIF	photo-wet-l, TRL
33: Postbake	5 min	blue oven plate, TRL
34: Wet etch "isolation ox"	7:1 BOE, 3600 Å/min	oxide, ICL
• from second dip on, make sure air bubbles do not cling in small holes		

Step	Recipe / Parameters	Equipment
35: Strip thick resist	strip sink piranha	pre-metal, ICL
36: Clean wafers	clean sink piranha + 15 s 50:1 HF	pre-metal, ICL
37: Dep PECVD "CMP stop A"	rec 3.0 µm	concept1, ICL
• place monitors as: first in, middle in, last in • keep these for future reference to this layer if needed		
38: Densify	rec 190, 60 min, 1100 C	tubeB6, ICL
or	rec 180, 60 min, 1100 C	tubeB5, ICL
39: Measure "CMP stop A" thickness	rec Oxide on Si	uv1280, ICL
40: CMP	table: 25 rpm quil: 15 rpm head: 4 psi back: 1 psi time: 20 min	CMP, ICL

Step	Recipe	Machine
41: Post-CMP clean part I	piranha yellow dot containers	acid-hood, TRL
42: Post-CMP clean part II	standard rca in Novellus containers	rca, TRL
43: Measure "CMP stop A" thickness	rec Oxide on Si	uv1280, ICL
		P10, ICL
44: Measure "Bottom Side" features		uv1280, ICL
		P10, ICL
45: Etch back and set gap	timed etch	oxide, ICL
• this step (with the addition of 1 μm next) will define the stator-rotor gap		P10, ICL
		uv1280, ICL
46: Repeat last two steps as necessary		
47: Clean wafers	clean sink piranha + 15 s 50:1 HF	pre-metal, ICL
48: Dep PECVD "isolation ox B"	rec 1.0 μm	concept1, ICL
• place monitors as: first in, middle in, last in		
• keep these for future reference to this layer if needed		
49: Dep PECVD "tether mask ox"	rec >3.0 μm	concept1, ICL
• latest results: 2.82 μm at center 10/27/98		
50: Densify	rec 190, 60 min, 1100 C	tubeB6, ICL
or	rec 180, 60 min, 1100 C	tubeB5, ICL
51: Measure "isolation ox B" and "tether mask ox"	rec Ox (n = 1.46) on Si	uv1280, ICL
• add results from B and A monitors and compare to total thickness measured on the device wafers		
52: Etch back if necessary	BOE etch "air gap" to 3 μm	oxide, ICL
53: Clean wafers if necessary	clean sink piranha + 15 s 50:1 HF	pre-metal, ICL

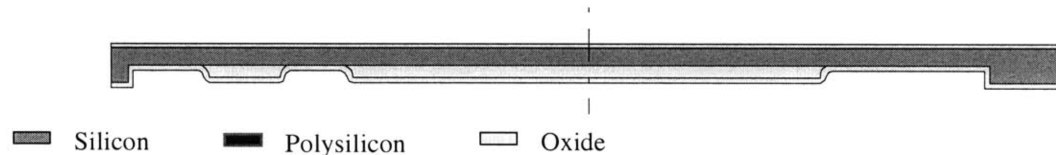

Step	Recipe	Machine
54: Add "rotor film monitors" to flow, called:	3 "Sigma Monitors"	
• include 3 "Sigma Monitors" (for conductivity) which have been prepared to the proper point using the flow "Flow Rotor Film v3"		
55: RCA clean all wafers	standard clean w/ Novellus containers	rca, TRL
56: Dep "rotor film"	rec 625 C, 5000 Å	lpcvd, TRL
• include up to 3 Poly Monitors (1000 Å ox) for thickness measurement, "delta monitors"		
• place "delta monitors" and "sigma monitors" at load end of batch, middle of batch, and back of batch		
• the gas source for this tube is at the load		

Step		Recipe	Equipment
57: Measure "rotor film" thickness		rec PolySi (n = 3.0) on 1000Å ox	nanospec, TRL
	or		uv1280, ICL
58: Clean wafers		clean sink piranha + 15 s 50:1 HF	pre-metal, ICL
59: Dep "implant shield"		rec 2400 Å	concept1, ICL
• place monitors: first in, last in			
60: Densify "implant shield"		rec 295, 30 min, 950 C	tubeB6, ICL
	or	rec 205, 30 min, 950 C	tubeB5, ICL
61: Out-source implant of "rotor film"		approx. 5.5e12, 180 keV	Ion Implant Services
62: Drive-in and anneal		rec 195, 25 min, 1000 C	tubeB6, ICL

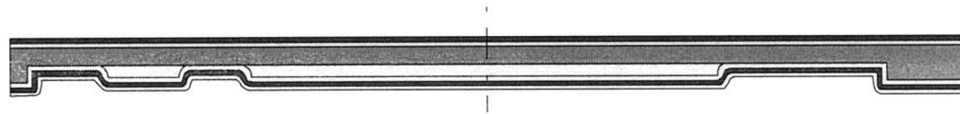

Silicon Polysilicon Oxide

Step	Recipe	Equipment
63: Split "rotor film monitors" from flow	3 Sigma Monitors	
• finish these monitors using the flow "Flow Rotor Film v3"		
64: Clear "implant shield" on all wafers	7:1 BOE, 3 min	oxide, ICL
• until water beads on poly and bottom side		

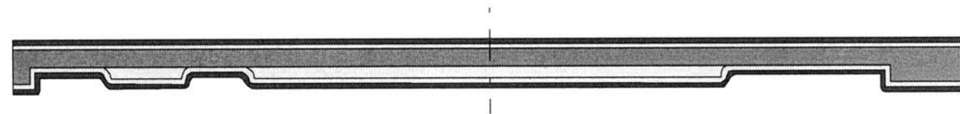

Silicon Polysilicon Oxide

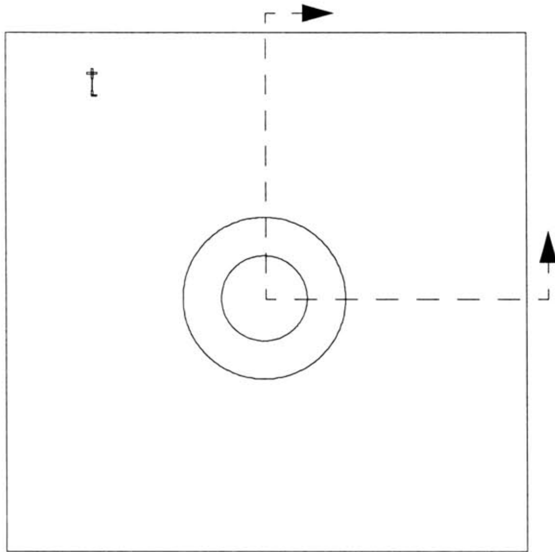

Mask: BB-ROTFILM or BB-ROTFILM_CAL

Step	Parameters	Equipment
65: HMDS	25 min	HMDS, ICL
66: Thick positive resist coat	8 μm AZ P4612 ~ 2.5 krpm on a good day	coater, TRL
67: Prebake	30 s	blue oven plate, TRL
68: Expose right half of wafer	90 s	ksaligner1, TRL
or	600 s	ksaligner2, TRL

- use mask **BB-ROTFILM**
- using vacuum - hold handle during alignment - hit vac before releasing
- alignment and pattern transfer can then be extremely good

Step	Parameters	Equipment
69: Expose left half of wafer	15 s	ksaligner1, TRL

- use mask **BB-ROTFILM_CAL**

Step	Parameters	Equipment
70: Clear expose alignment window	60 s	ksaligner1, TRL
71: Develop	~1:30 min, AZ 440 MIF	photo-wet-l, TRL
72: Postbake	5 min	blue oven plate, TRL

Step		Parameters	Equipment
73: Isotropic PolySi etch		rec “NAGLE SI ISO” ⇒ 42 s, 0.5 μm	AME5000, ICL
	or	modified recipe #10 ⇒ 35 s, 0.5 μm	etcher-1

- Rec #10 changes: 15 s descum, only etch gases: He: 70, SF6: 100 sccm, 25 s stab, etch: 200 W; overetch: 25% of etch time, 100 W
- careful with any additional over-etch, takes 500 A of oxide off the outer 15-20 mm of the wafer, center is fine
- try to make sure any stringers have cleared from side-walls

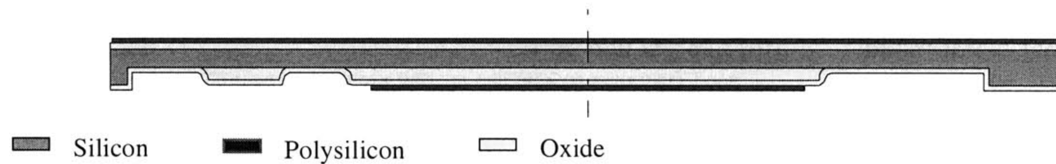

Step	Parameters	Equipment
74: Strip thick resist	strip sink piranha	pre-metal, ICL

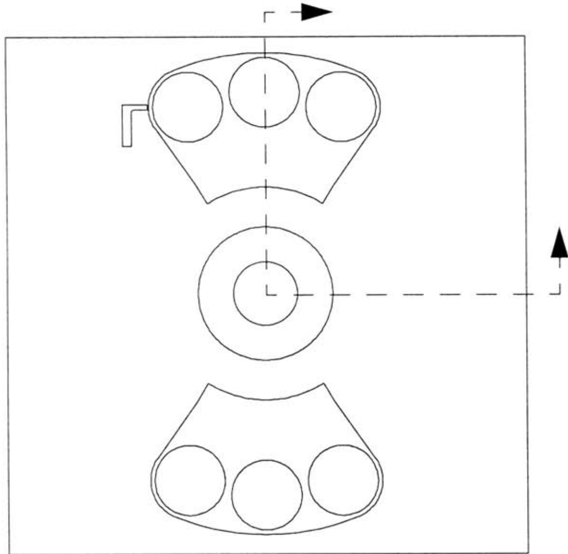

Mask: BB-ROTISO_CLEAR

Step	Parameters	Equipment
75: HMDS	25 min	HMDS, ICL
76: Thick positive resist coat	8 μm AZ P4612 ~ 2.5 krpm on a good day	coater, TRL
77: Prebake	30 s	blue oven plate, TRL
78: Expose	60 s	ksaligner1, TRL
or	600 s	ksaligner2, TRL

- using vacuum - hold handle during alignment - hit vac before releasing
- alignment and pattern transfer can then be extremely good

Step	Parameters	Equipment
79: Develop	1:30 min AZ 440 MIF	photo-wet-l, TRL
80: Postbake	5 min	blue oven plate, TRL
81: Wet etch "isolation ox B"	7:1 BOE, 10-15 min	oxide, ICL

- 500 Å over-etch included based on measured 1000 Å/min etch rate of densified Novellus oxide
- make sure the edges are cleared as well, the Novellus deposits extra oxide in 2-4 spots
- inspect for clear in bonding area and under the tether area

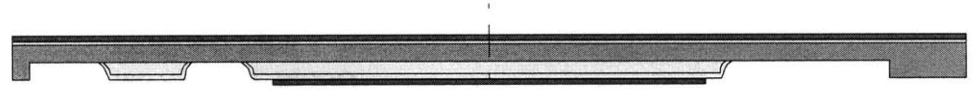

Silicon Polysilicon Oxide

Step	Parameters	Equipment
82: Strip thick resist	strip sink piranha	pre-metal, ICL
83: Now process on "Top Side" of wafers		
84: Isotropic PolySi etch	⇒ rec 10, 1.5 min	etcher-1, ICL
85: Clean wafers	clean sink piranha + 15 s 50:1 HF	pre-metal, ICL

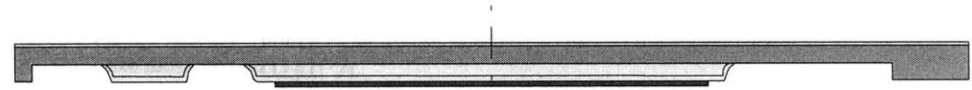

Silicon Polysilicon Oxide

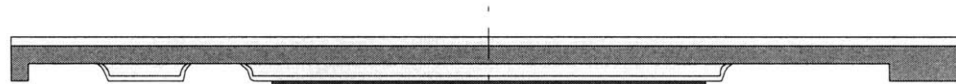

Silicon Polysilicon Oxide

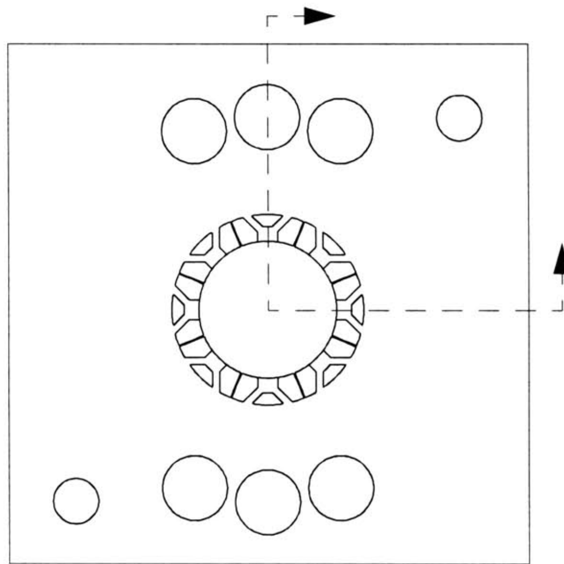

Mask: BT-TETHER

86: HMDS	25 min	HMDS, ICL
87: Double positive resist coat	rec 15	coater, ICL
	then rec 11	
88: Expose	⇒ 45 s	ksaligner2, TRL
89: Develop	2:30 min:s OCG934	photo-wet-l, TRL
90: Attach 400 um, Si handle wafer	1/4" ring, 3 vent holes	coater, TRL
91: Postbake	3 min on plate	blue oven, TRL
or		
	rec 43	developer, ICL
92: Etch "tether mask ox"	rec NAGLE CHF_3	AME5000, ICL
	⇒ 777 s, 2.8 μm	

• based on most recent etch rate (3/98); significant over-etch is allowed

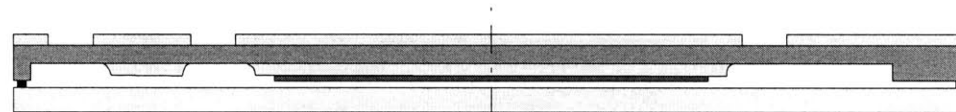

Silicon Polysilicon Oxide

93: Remove Si handle wafer		acetone, methanol	photo-wet-l, TRL
94: Clean wafers		strip sink piranha + 15 s 50:1 HF	pre-metal, ICL
	or	piranha in blue dot containers	acid-hood, TRL
95: Attach Quartz handle wafer		1/4" ring, 3 vent holes	coater, TRL
96: Etch tethers		rec TM02	sts, TRL
		⇒ nominal 5.25 h, 386.5 μm (through wafer)	

• first do 1 hour etch on tether mask montior wafer, on a quartz handle wafer, check oxide etch rate
• proceed in two steps: check rates after 1 hr of etch, then continue if things check-out

97: Remove remaining hard mask	rec NAGLE CHF_3	AME5000, ICL

		⇒ 60 s, ~1500 Å	
98: Remove handle wafer		acetone, methanol	photo-wet-l, TRL
99: Clean wafers		strip sink piranha + 15 s 50:1 HF	pre-metal, ICL
	or	piranha in blue dot containers	acid-hood, TRL
100: Inspect		Check dimensions, tethers	microscope, TRL
	or		microscope, ICL
101: RCA clean all wafers • bonding will be next		standard rca in Novellus containers	acid-hood, TRL

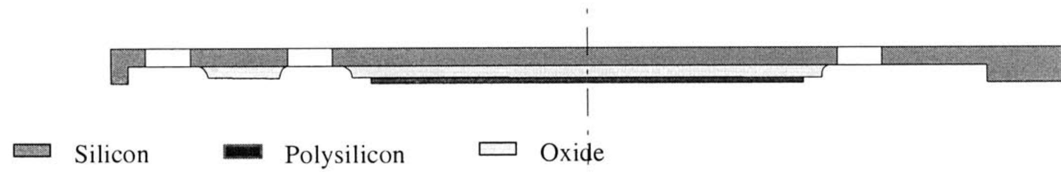

D.3 Complete Rotor Conductor Test Structure Flow

Step	Parameters	Equipment
1: Si single side polished prime, 10-20 Ω–cm	25 wafers	Paul Tierney
2: Piranha clean and 50:1 HF dip	Clean sink	pre-metal, ICL

Silicon Polysilicon Oxide

Step	Parameters	Equipment
3: Dep PECVD "rotor ox"	rec 1 μm	concept1, ICL

- include 3 LTO Monitors (bare Si) in this and next two steps
- place monitors: first in, middle, last in

Step	Parameters	Equipment
4: Densify "rotor ox"	rec 190, 60 min, 1100 C	tubeB6, ICL
5: Measure "rotor ox" monitor thickness	rec Ox on Si (n = 1.46)	nanospec, ICL

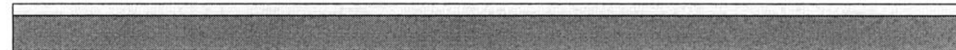

Silicon Polysilicon Oxide

Step	Parameters	Equipment
6: Optional CMP or no CMP of oxide		
6a: CMP included		
6a.i: CMP for bonding	rec "60 s, 3 psi"	cmp, ICL
6a.ii: Piranha clean	10 min	acid-hood, TRL
6a.iii: RCA clean		acid-hood, TRL
6a.iv: Measure "rotor ox" monitor thickness	rec Ox on Si (n = 1.46)	nanospec, ICL
6b: CMP not included		
6b.i: RCA clean		acid-hood, TRL

Step	Recipe	Machine
7: Dep LPCVD polySi: Coarse grain or Fine grain		
7a: Coarse grain poly		
• include 3 Poly Monitors (1000 Å ox) for thickness meaurement • place at load end of batch, middle of batch, and back of batch • the gas source for this tube is at the load		
7a.i: Dep Coarse grain poly	rec 625 C, 5000 Å	lpcvd, TRL
7a.ii: Measure thickness	rec PolySi on 1000A (n = 3.0)	nanospec, ICL
7b: Fine grain poly		
• include 3 LTO Monitors (bare Si) for refractive index meaurement • include 3 Poly Monitors (1000 Å ox) for thickness meaurement • place at load end of batch, middle of batch, and back of batch • the gas source for this tube is at the load		
8: Dep Fine grain poly	rec 585 C, 5000 Å	lpcvd, TRL
9: Measure refractive index		uv1280, ICL
10: Measure thickness	rec PolySi on 1000A (n = ?)	nanospec, ICL

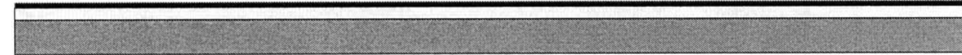

Silicon Polysilicon Oxide

Step	Recipe	Machine
11: Piranha clean and 50:1 HF dip	Clean sink	pre-metal, ICL
12: Dep PECVD "capping ox"	rec 2400 Å	concept1, ICL
• include 3 LTO Monitors (bare Si) in this and next two steps • place monitors: first in, middle, last in • include 5 bare Si for implant monitor		
13: Densify "capping ox"	rec 295, 20 min, 950 C	tubeB6, ICL
14: Measure thickness	rec Ox on Si (n = 1.46)	nanospec, ICL

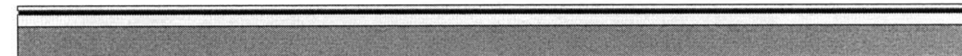

Silicon Polysilicon Oxide

15: Scribe wafers	backside	
16: Piranha clean and 50:1 HF dip	Clean sink	pre-metal, ICL
17: Outsource for ion implant	Reference value matrix	Ion Implant Services
18: Piranha clean and 50:1 HF dip	Clean sink	pre-metal, ICL
19: Drive-in and activation	rec 195, 25 min, 1000 C	tubeB6, ICL
20: Strip "capping ox"	3 min, 7:1 BOE	oxide, ICL

Silicon Polysilicon Oxide

21: Piranha clean and 50:1 HF dip	Clean sink	pre-metal, ICL
22: Dep PECVD "gap ox"	1000 Å	concept1, ICL
23: Densify "gap ox" [also first bond anneal mimic]	rec 190, 60 min, 1100 C	tubeB6, ICL

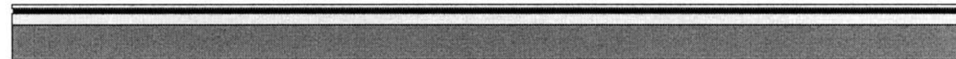

Silicon Polysilicon Oxide

24: Dep Aluminum • include 3 poly monitors for similar reflectivity	5000 Å	e-beam

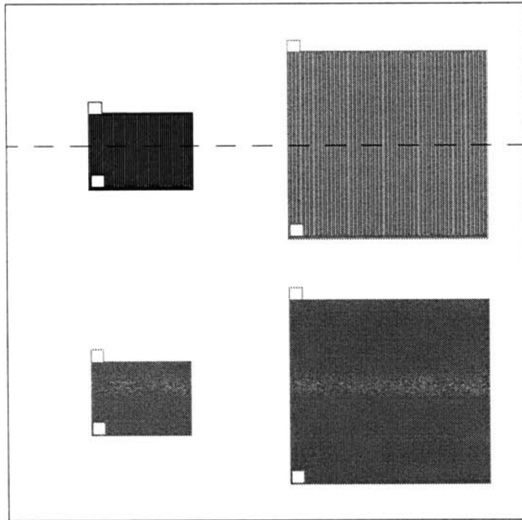

Mask: Cart-01 (10X reticle)

Step	Parameters	Equipment
25: HMDS		
26: Coat wafers, positive resist	rec 11, 115 C bake	coater, ICL
27: Clear-field expose wafers	F=244 E=0.18 (nom.)	stepper2, ICL
• do focus expo wafer F=[240:1:247] and E=[0.15:0.02:0.30]		
• develop and inspect focus expo wafer		
28: Develop wafers	prog 20, 130 C bake	developer, ICL
29: Inspect		microscope, ICL
• repeat steps as necessary for good develop		microscope, ICL
30: Etch Aluminum	rec 36, 43 s	etcher-3, ICL
31: Inspect		microscope, ICL
• strip all Al and re-dep if necessary		
32: Ash	1 min	asher, ICL
33: Sinter Aluminum	rec 710	TubeB8, ICL

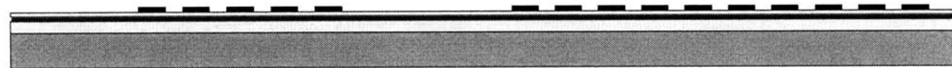

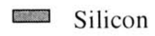 Silicon 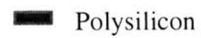 Polysilicon 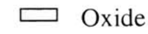 Oxide

Appendix E

Fabrication Recipes

E.1 Deposition Recipes

E.1.1 Electron Beam Aluminum Deposition

Temescal VES-2550

Parameter	Value
Rise Time	1:00 min
Soak Time	1:00 min
Pre-deposition Time	0:30 min
Set Point	0
Soak Power	19%
Pre-deposition Power	21%
Maximum Power	26%
Idle Power	0%
Tooling	34% with planetary
	61% with lift-off plate
Density	2.70
Acoustic Impedence	8.17

E.2 Lithography Recipes

E.2.1 Thin Resist: OCG825 20 cs 1.1 μm

Solitec Spinner

Step	Time	Parameter Value
Dispense		4 ml resist, no spin
Spread	6 s	500 rpm
Spin	30 s	2500 rpm
Pre-bake	1:00 min	115 °C hot plate
Expose	25 s	Machine: ks2
Develop	1:00 min	OCG 934 1:1
Post-bake	1:00 min	130 °C hot plate

E.2.2 Intermediary Resist: OCG825 35 cs 2.1 μm

Solitec Spinner

Step	Time	Parameter Value
Dispense		4 ml resist, no spin
Spread	6 s	500 rpm
Spin	30 s	1800 rpm
Pre-bake	1:00 min	115 °C hot plate
Expose	45 s	Machine: ks2
Develop	1:30 min	OCG 934 1:1
Post-bake	1:00 min	130 °C hot plate

E.2.3 Thick Resist: AZ P4620 8-9 μm

Solitec Spinner

Step	Time	Parameter Value
Dispense	until wafer covered	dispense or pipet on wafer
Spread	6 s	750 rpm
Spin	30 s	2500 rpm
Spin	30 s	2500 rpm
Pre-bake	1:00 min	115 °C hot plate
Expose	45 s	Machine: ks2
Develop	1:30 min	AZ 440 MIF
Post-bake	1:00 min	130 °C hot plate

E.2.4 Image Reversal Resist: AZ 5214 1 μm

Solitec Spinner

Step	Time	Parameter Value
Dispense		4 ml resist, no spin
Spread	6 s	500 rpm
Spin	30 s	1500 rpm
Pre-bake	30 min	90 °C oven
Pattern Expose	22 s	Machine: ks2
Post-exposure Bake	1:45 min	115 °C hot plate
Flood Expose	1:00 s	Machine: ks1
Develop	1:00 min	OCG 934 1:1
Post-bake	1:00 min	130 °C

E.3 Etch Recipes

E.3.1 Anisotropic Intermediary Silicon Etch

Applied Materials P5000

Parameter	Value
Cl_2 Flow	56 sccm
HBr Flow	7 sccm
Power	350 W
Field	50 Gauss
Pressure	15 mtorr

E.3.2 Anisotropic Polysilicon Etch

Applied Materials P5000

Parameter	Value
Cl_2 Flow	80 sccm
HBr Flow	20 sccm
NF_3 Flow	15 sccm
Power	350 W
Field	90 Gauss
Pressure	90 mtorr

E.3.3 Anisotropic Intermediary Oxide Etch

Applied Materials P5000

Parameter	Value
CHF_3 Flow	30 sccm
Power	400 W
Field	90 Gauss
Pressure	15 mtorr

E.3.4 Isotropic Intermediary Silicon Etch: sts1 recipe SF6_5

Surface Technolgy Systems Multiplexed ICP Deep RIE

Parameter	Value
SF_6 Flow	30 sccm
Coil Power	400 W
Platten Power	290 W
APC Angle	30°

E.3.5 Isotropic Polysilicon Etch

Applied Materials P5000

Parameter	Value
SF_6 Flow	30 sccm
Power	200 W
Field	50 Gauss
Pressure	30 mtorr

E.3.6 Deep Silicon Etches

MIT37

Surface Technolgy Systems Multiplexed ICP Deep RIE

Parameter	Passivation Step	Etch Step
SF_6 Flow (sccm)	0	140
C_4C_8 Flow (sccm)	95	0
Cycle Time (s)	11	15
Overlap Time (s)	0	0.5
Coil Power (W)	600	600
Platten Power (W)	0	120
APC Valve Angle	65°	65°

MIT59

Surface Technolgy Systems Multiplexed ICP Deep RIE

Parameter	Passivation Step	Etch Step
SF_6 Flow (sccm)	0	105
C_4C_8 Flow (sccm)	40	0
Cycle Time (s)	11	14
Overlap Time (s)	0	0.5
Coil Power (W)	600	750
Platten Power (W)	60	120
APC Valve Angle	65°	65°

MIT69

Surface Technolgy Systems Multiplexed ICP Deep RIE

Parameter	Passivation Step	Etch Step
SF_6 Flow (sccm)	0	105
C_4C_8 Flow (sccm)	40	0
Cycle Time (s)	11	14
Overlap Time (s)	0	0.5
Coil Power (W)	600	750
Platten Power (W)	60	100
APC Valve Angle	65°	65°

TM01

Surface Technolgy Systems Multiplexed ICP Deep RIE

Parameter	Passivation Step	Etch Step
SF_6 Flow (sccm)	0	85
C_4C_8 Flow (sccm)	40	0
Cycle Time (s)	11	14
Overlap Time (s)	0	0.5
Coil Power (W)	600	750
Platten Power (W)	60	120
APC Valve Angle	65°	65°

TM02

Surface Technolgy Systems Multiplexed ICP Deep RIE

Parameter	Passivation Step	Etch Step
SF_6 Flow (sccm)	0	105
C_4C_8 Flow (sccm)	60	0
Cycle Time (s)	11	14
Overlap Time (s)	0	0.5
Coil Power (W)	600	750
Platten Power (W)	60	120
APC Valve Angle	65°	65°

TM03

Surface Technolgy Systems Multiplexed ICP Deep RIE

Parameter	Passivation Step	Etch Step
SF_6 Flow (sccm)	0	105
C_4C_8 Flow (sccm)	60	0
Cycle Time (s)	11	14
Overlap Time (s)	0	0.5
Coil Power (W)	600	750
Platten Power (W)	60	100
APC Valve Angle	65°	65°

TM04

Surface Technolgy Systems Multiplexed ICP Deep RIE

Parameter	Passivation Step	Etch Step
SF_6 Flow (sccm)	0	105
C_4C_8 Flow (sccm)	80	0
Cycle Time (s)	11	14
Overlap Time (s)	0	0.5
Coil Power (W)	600	750
Platten Power (W)	60	120
APC Valve Angle	65°	65°

TM05

Surface Technolgy Systems Multiplexed ICP Deep RIE

Parameter	Passivation Step	Etch Step
SF_6 Flow (sccm)	0	105
C_4C_8 Flow (sccm)	60	0
Cycle Time (s)	11	14
Overlap Time (s)	0	0.5
Coil Power (W)	600	750
Platten Power (W)	60	130
APC Valve Angle	65°	65°

Appendix F

Measured Data

Raw data as meaured with the computer microvision system are included in this appendix. Each page contains one motion measurement dataset and the measured fundamental component of the stator voltage, at the output of the power electronics. The three curves drawn through the motion data correspond to the best fit plus a lower and upper bound based on the error bars on the measured motion.

F.1 Experiment Set 1

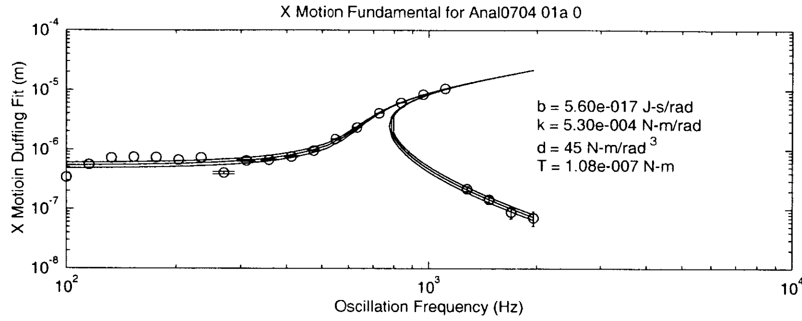

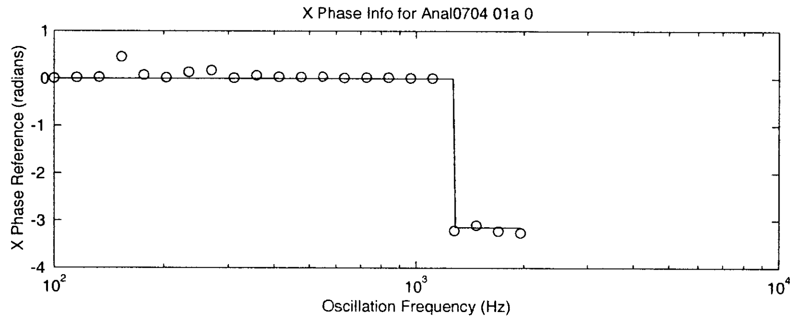

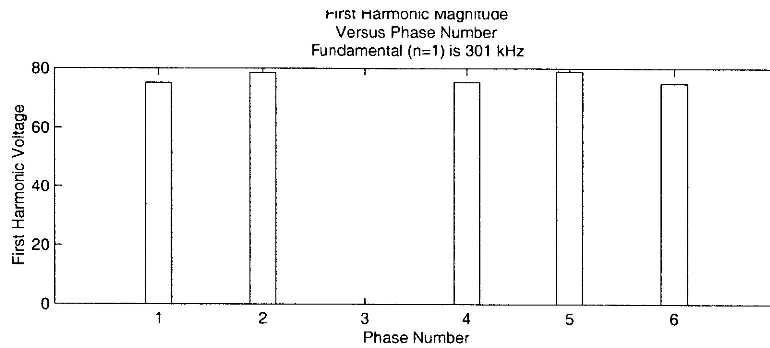

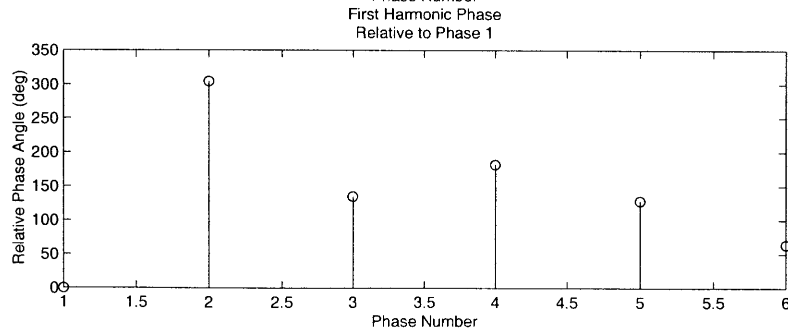

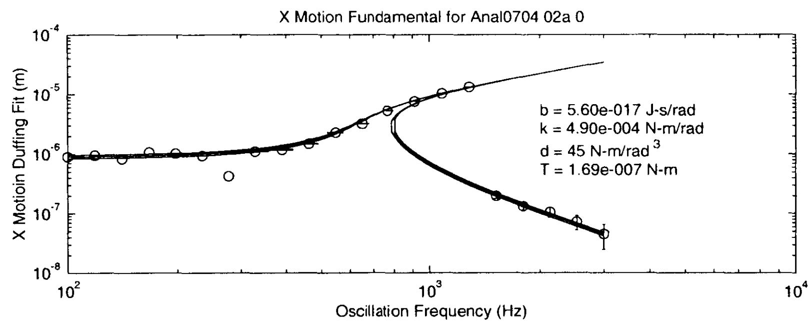
X Motion Fundamental for Anal0704 02a 0
X Motioin Duffing Fit (m)
Oscillation Frequency (Hz)
b = 5.60e-017 J-s/rad
k = 4.90e-004 N-m/rad
d = 45 N-m/rad^3
T = 1.69e-007 N-m

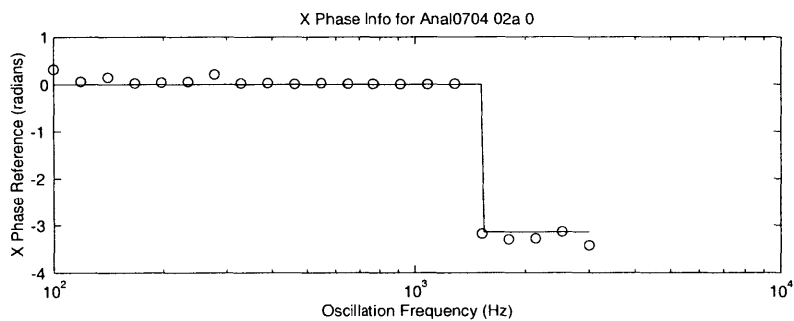
X Phase Info for Anal0704 02a 0
X Phase Reference (radians)
Oscillation Frequency (Hz)

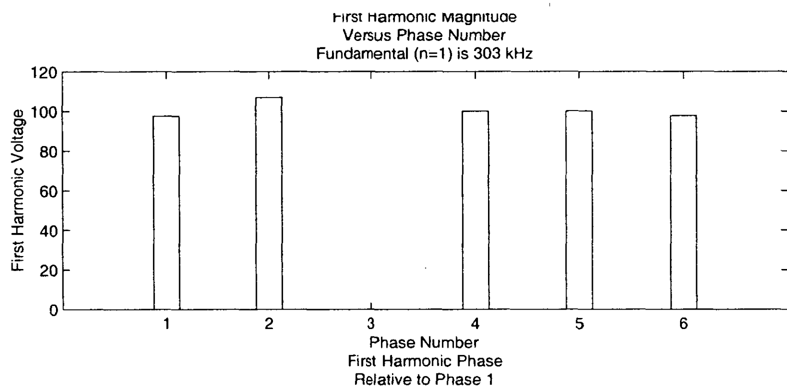
First Harmonic Magnitude
Versus Phase Number
Fundamental (n=1) is 303 kHz
First Harmonic Voltage
Phase Number

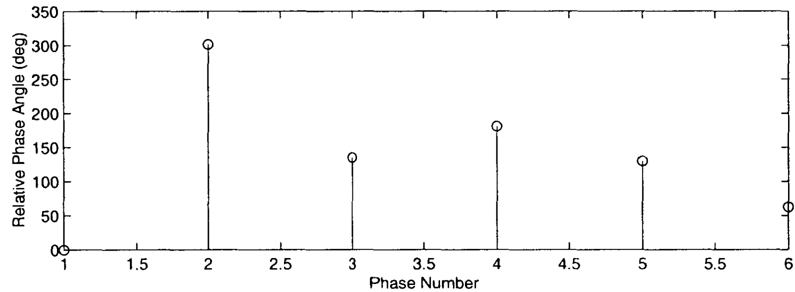
First Harmonic Phase
Relative to Phase 1
Relative Phase Angle (deg)
Phase Number

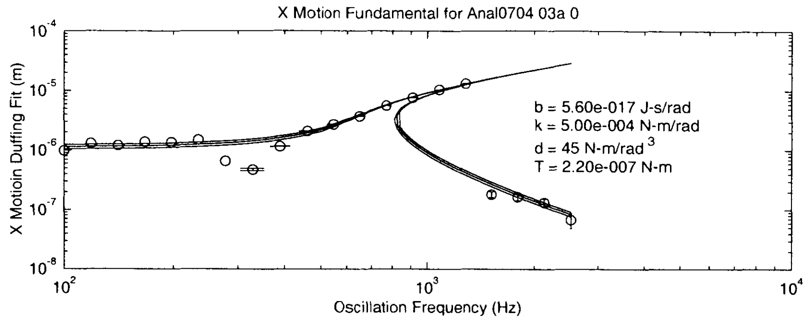
X Motion Fundamental for Anal0704 03a 0
X Motioin Duffing Fit (m)
Oscillation Frequency (Hz)
b = 5.60e-017 J-s/rad
k = 5.00e-004 N-m/rad
d = 45 N-m/rad^3
T = 2.20e-007 N-m

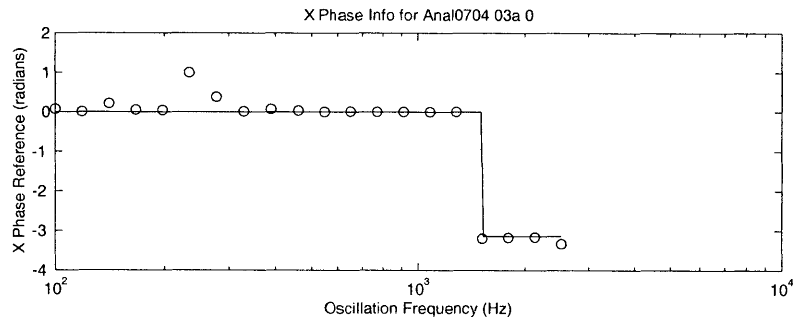
X Phase Info for Anal0704 03a 0
X Phase Reference (radians)
Oscillation Frequency (Hz)

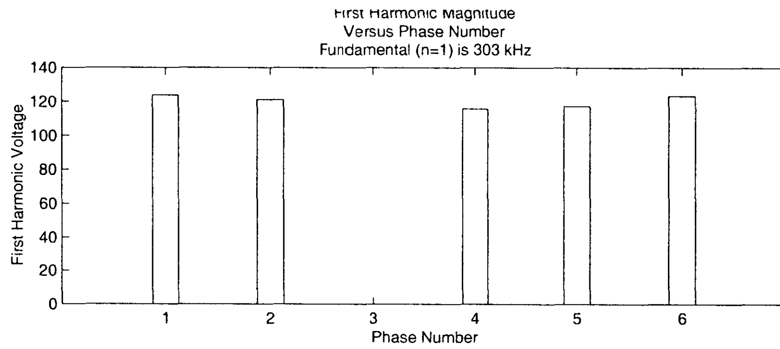
First Harmonic Magnitude
Versus Phase Number
Fundamental (n=1) is 303 kHz
First Harmonic Voltage
Phase Number

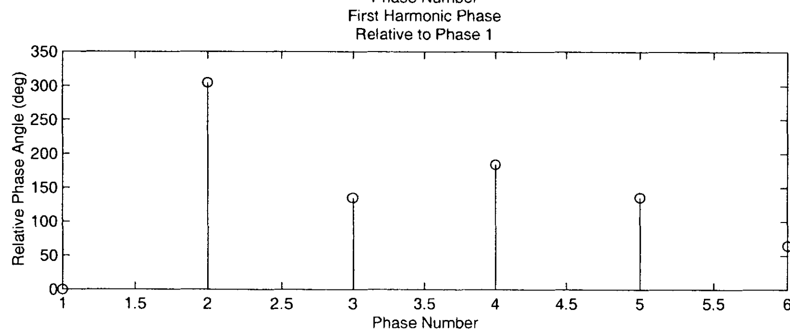
First Harmonic Phase
Relative to Phase 1
Relative Phase Angle (deg)
Phase Number

F.2 Experiment Set 2

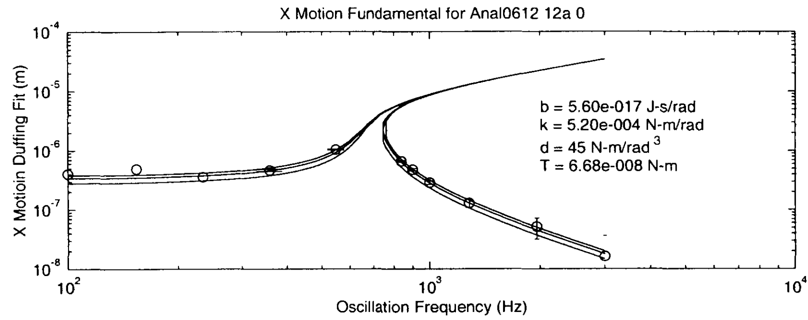

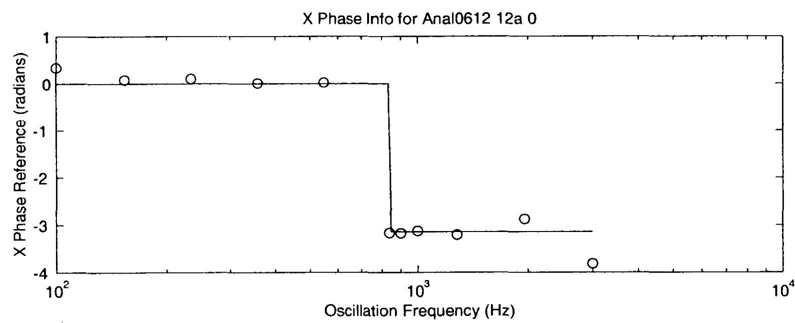

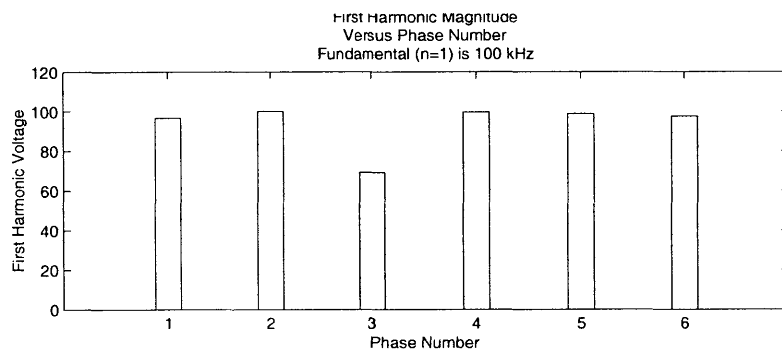

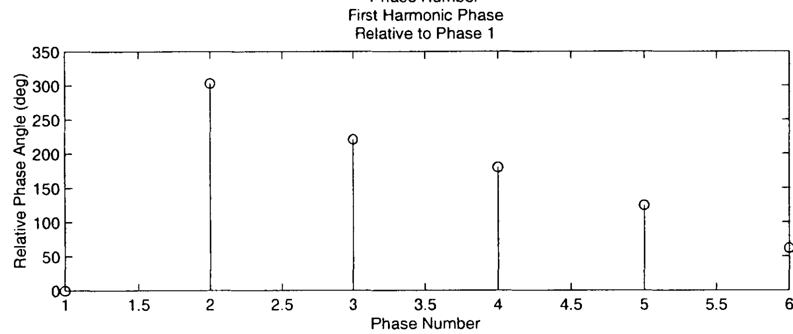

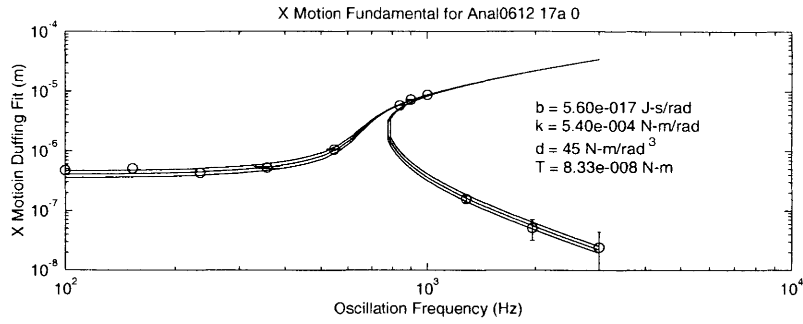
X Motion Fundamental for Anal0612 17a 0
X Motioin Duffing Fit (m)
Oscillation Frequency (Hz)
b = 5.60e-017 J-s/rad
k = 5.40e-004 N-m/rad
d = 45 N-m/rad 3
T = 8.33e-008 N-m

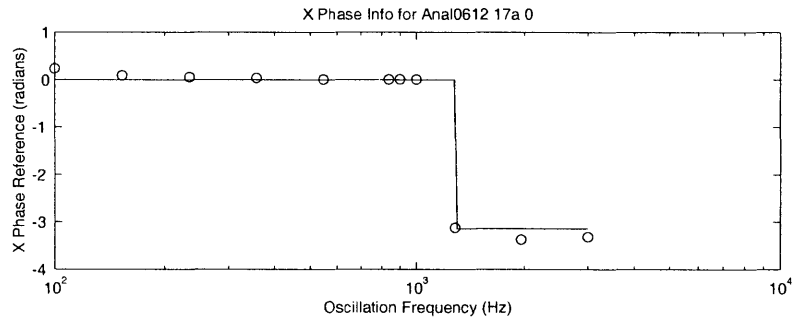
X Phase Info for Anal0612 17a 0
X Phase Reference (radians)
Oscillation Frequency (Hz)

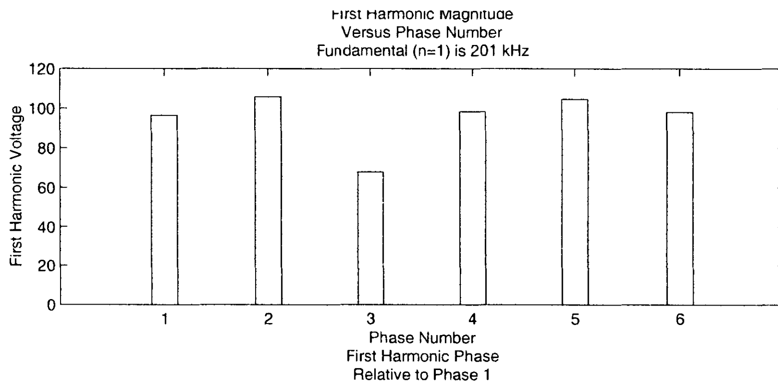
First Harmonic Magnitude
Versus Phase Number
Fundamental (n=1) is 201 kHz
First Harmonic Voltage
Phase Number

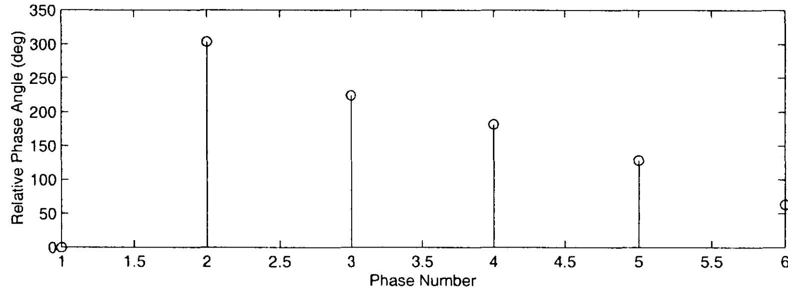
First Harmonic Phase
Relative to Phase 1
Relative Phase Angle (deg)
Phase Number

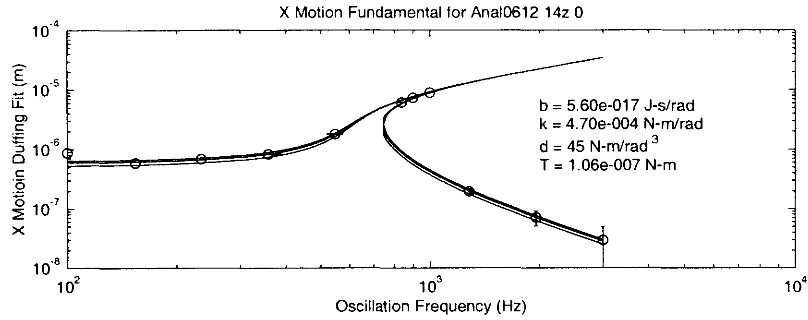
X Motion Fundamental for Anal0612 14z 0
X Motioin Duffing Fit (m)
b = 5.60e-017 J-s/rad
k = 4.70e-004 N-m/rad
d = 45 N-m/rad^3
T = 1.06e-007 N-m
Oscillation Frequency (Hz)

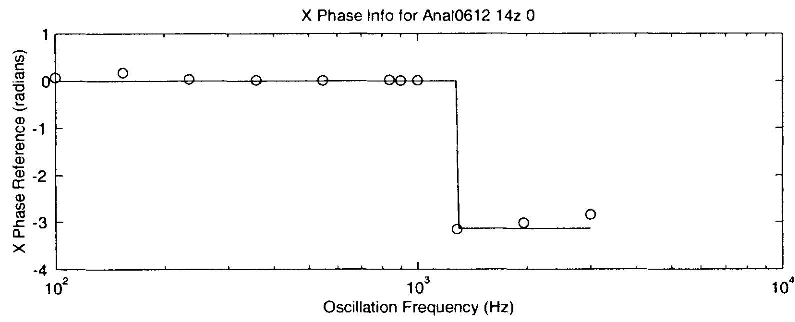
X Phase Info for Anal0612 14z 0
X Phase Reference (radians)
Oscillation Frequency (Hz)

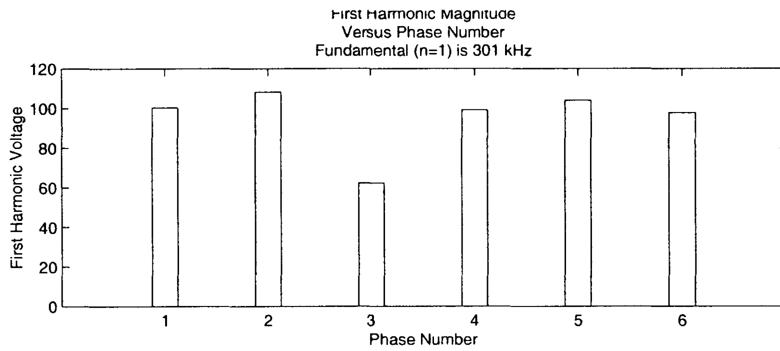
First Harmonic Magnitude
Versus Phase Number
Fundamental (n=1) is 301 kHz
First Harmonic Voltage
Phase Number

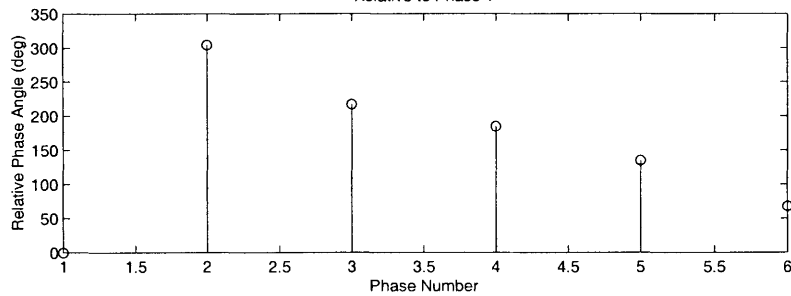
First Harmonic Phase
Relative to Phase 1
Relative Phase Angle (deg)
Phase Number

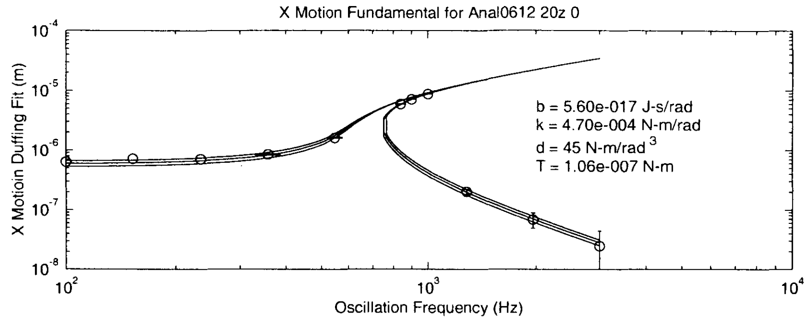
X Motion Fundamental for Anal0612 20z 0
X Motioin Duffing Fit (m)
b = 5.60e-017 J-s/rad
k = 4.70e-004 N-m/rad
d = 45 N-m/rad 3
T = 1.06e-007 N-m
Oscillation Frequency (Hz)

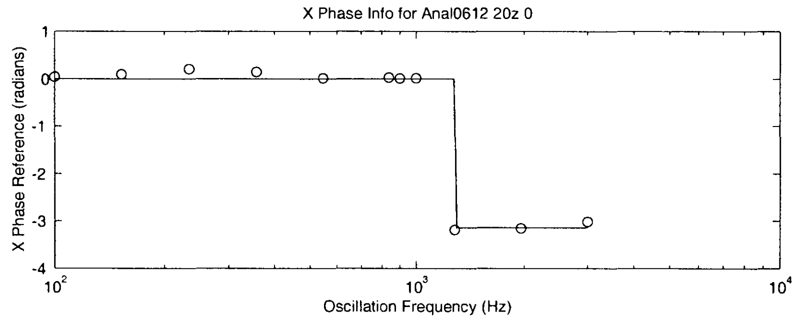
X Phase Info for Anal0612 20z 0
X Phase Reference (radians)
Oscillation Frequency (Hz)

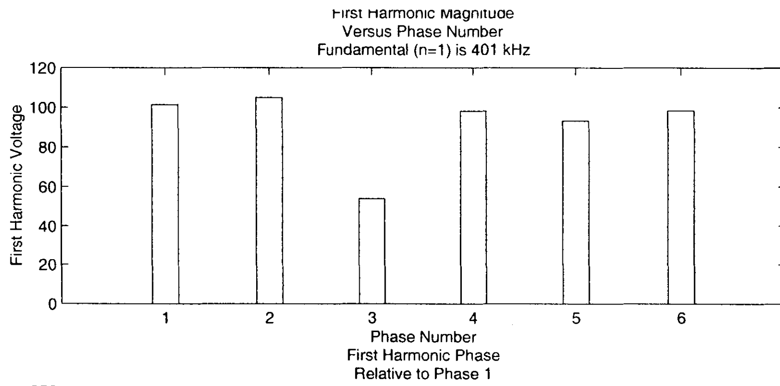
First Harmonic Magnitude
Versus Phase Number
Fundamental (n=1) is 401 kHz
First Harmonic Voltage
Phase Number

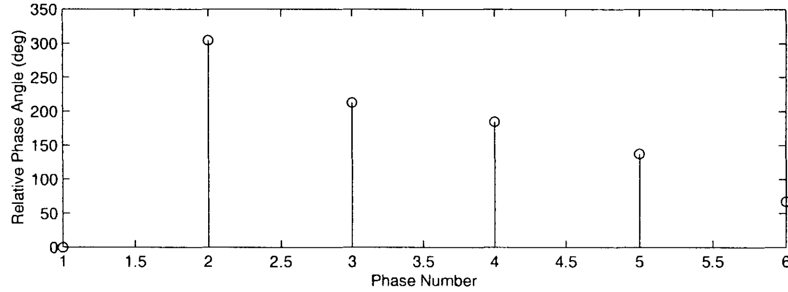
First Harmonic Phase
Relative to Phase 1
Relative Phase Angle (deg)
Phase Number

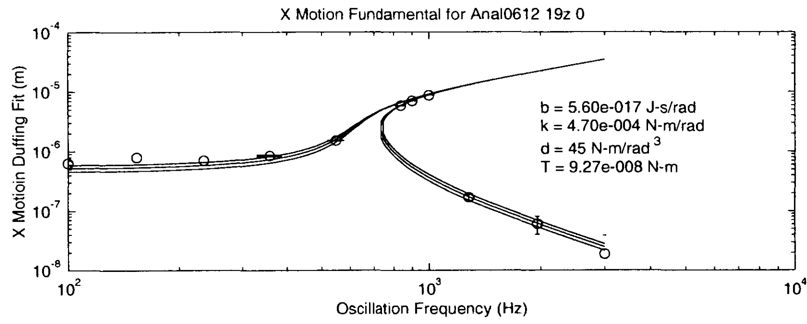
X Motion Fundamental for Anal0612 19z 0
X Motioin Duffing Fit (m)
Oscillation Frequency (Hz)
b = 5.60e-017 J-s/rad
k = 4.70e-004 N-m/rad
d = 45 N-m/rad 3
T = 9.27e-008 N-m

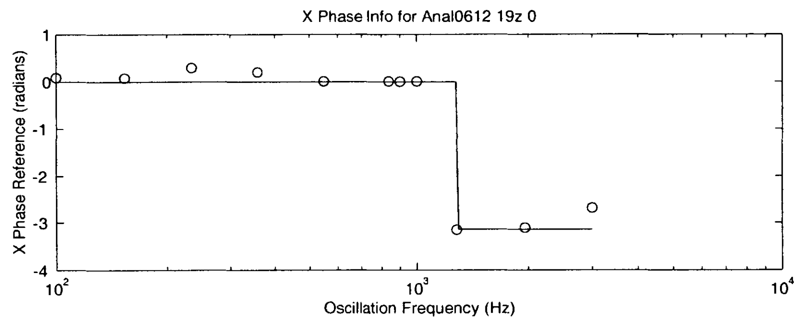
X Phase Info for Anal0612 19z 0
X Phase Reference (radians)
Oscillation Frequency (Hz)

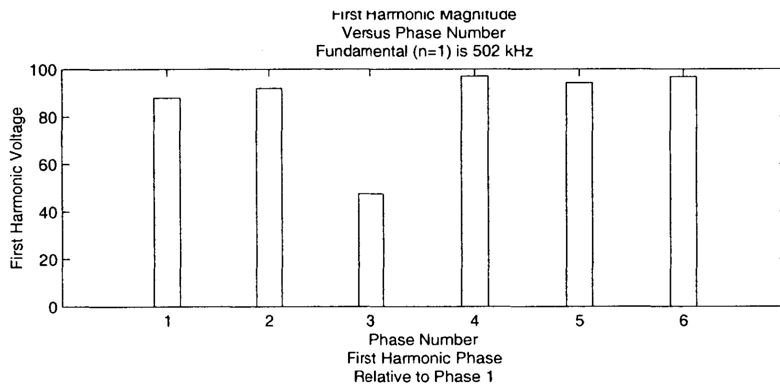
First Harmonic Magnitude
Versus Phase Number
Fundamental (n=1) is 502 kHz
First Harmonic Voltage
Phase Number

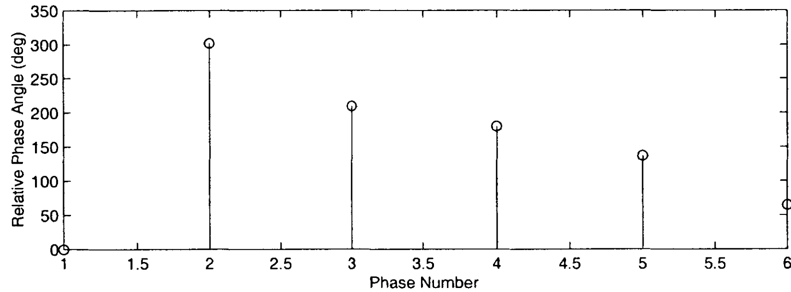
First Harmonic Phase
Relative to Phase 1
Relative Phase Angle (deg)
Phase Number

F.3 Experiment Set 3

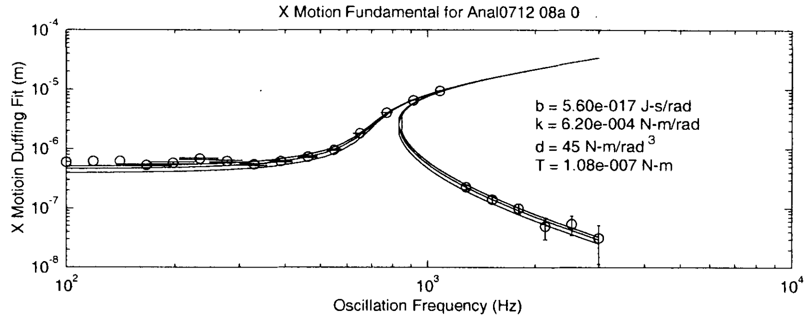

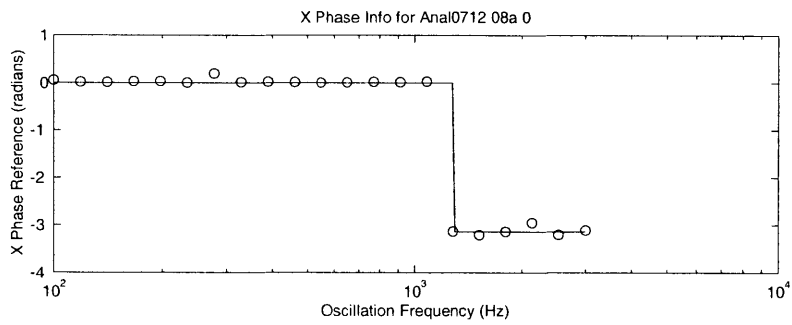

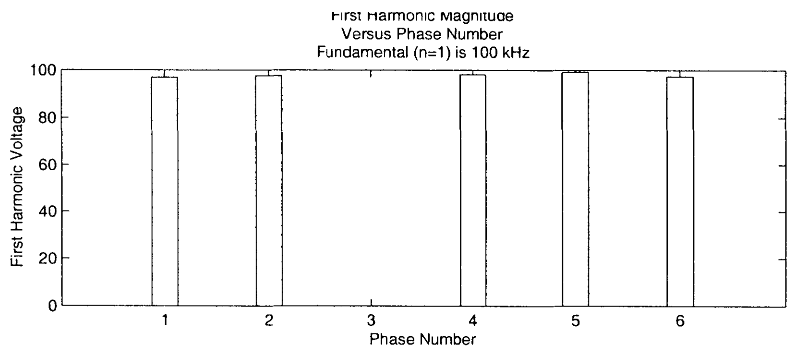

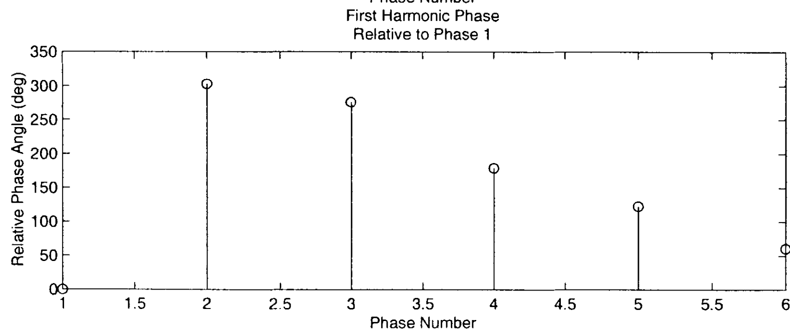

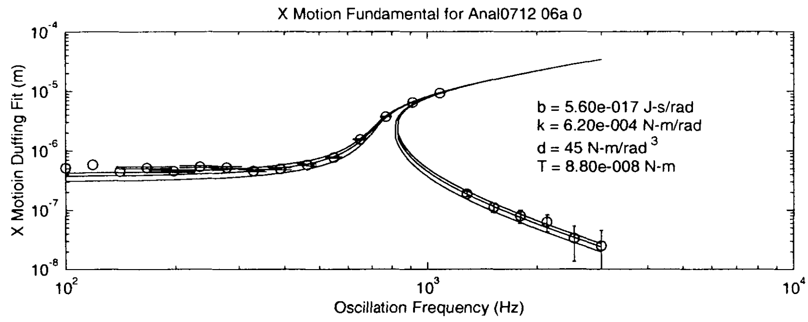
X Motion Fundamental for Anal0712 06a 0
X Motioin Duffing Fit (m)
Oscillation Frequency (Hz)
b = 5.60e-017 J-s/rad
k = 6.20e-004 N-m/rad
d = 45 N-m/rad 3
T = 8.80e-008 N-m

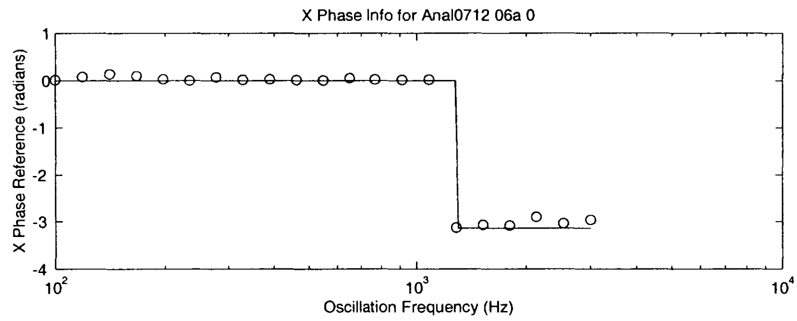
X Phase Info for Anal0712 06a 0
X Phase Reference (radians)
Oscillation Frequency (Hz)

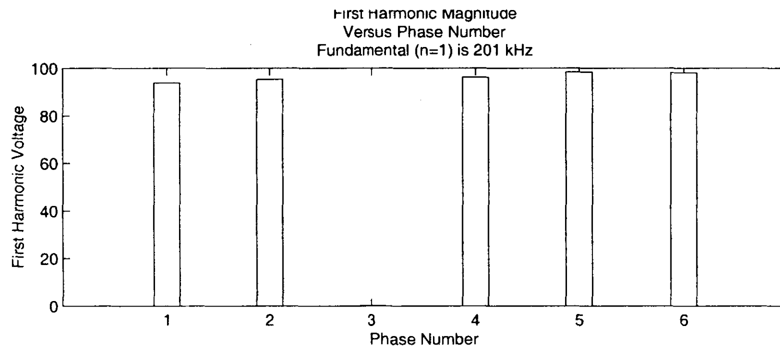
First Harmonic Magnitude
Versus Phase Number
Fundamental (n=1) is 201 kHz
First Harmonic Voltage
Phase Number

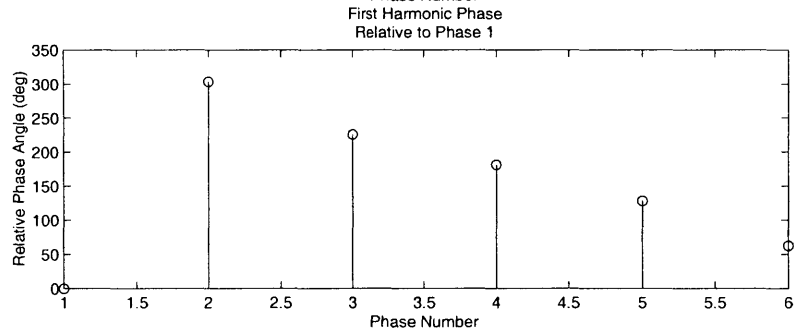
First Harmonic Phase
Relative to Phase 1
Relative Phase Angle (deg)
Phase Number

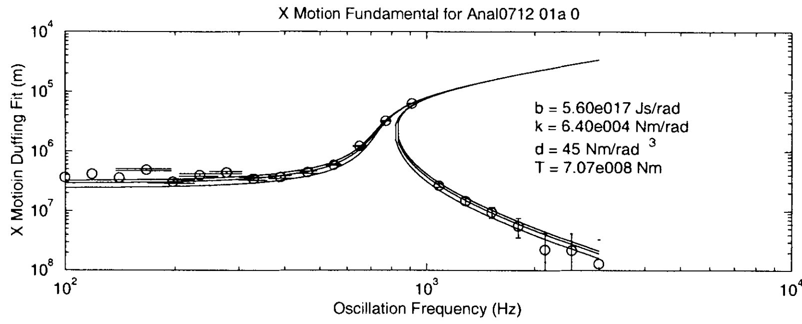
X Motion Fundamental for Anal0712 01a 0
X Motioin Duffing Fit (m)
Oscillation Frequency (Hz)
b = 5.60e017 Js/rad
k = 6.40e004 Nm/rad
d = 45 Nm/rad 3
T = 7.07e008 Nm

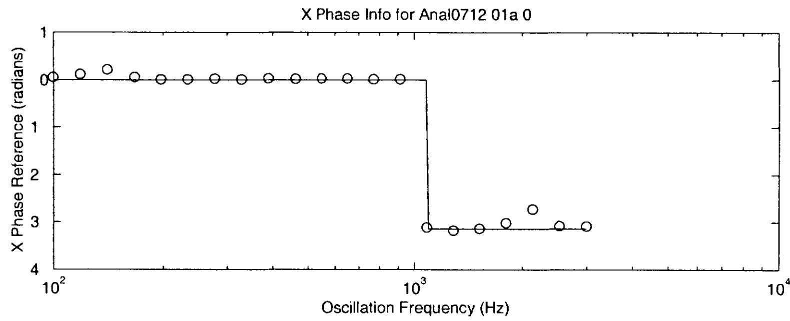
X Phase Info for Anal0712 01a 0
X Phase Reference (radians)
Oscillation Frequency (Hz)

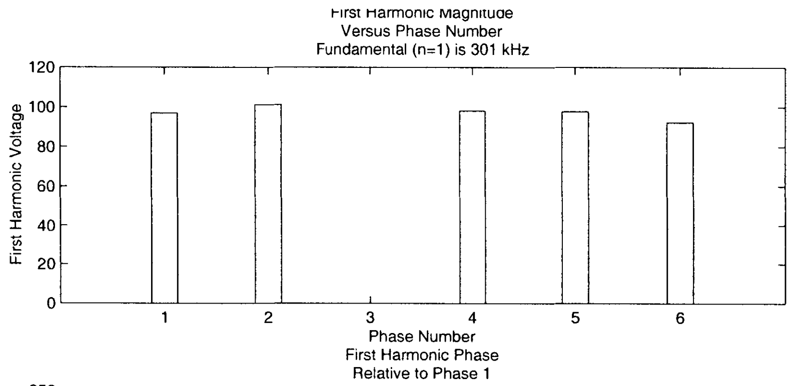
First Harmonic Magnitude
Versus Phase Number
Fundamental (n=1) is 301 kHz
First Harmonic Voltage
Phase Number

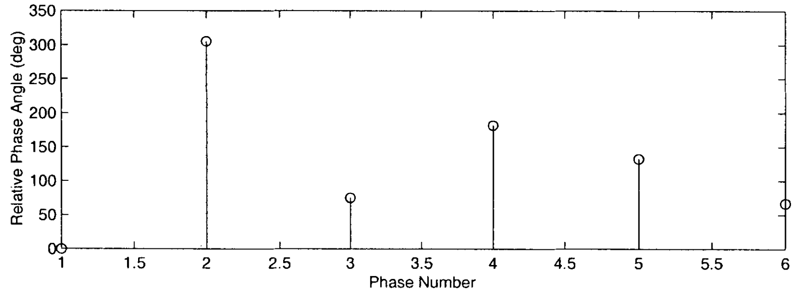
First Harmonic Phase
Relative to Phase 1
Relative Phase Angle (deg)
Phase Number

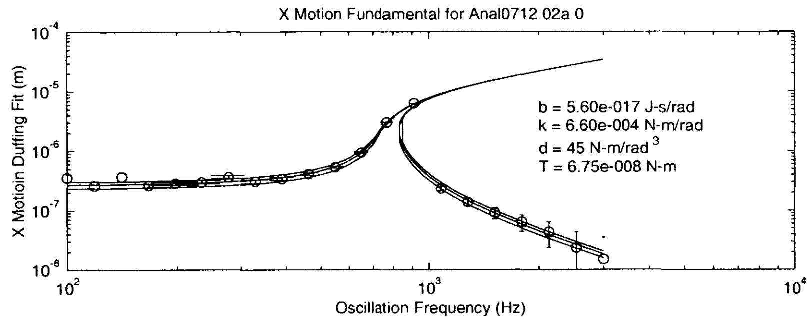
X Motion Fundamental for Anal0712 02a 0
X Motioin Duffing Fit (m)
Oscillation Frequency (Hz)
b = 5.60e-017 J-s/rad
k = 6.60e-004 N-m/rad
d = 45 N-m/rad 3
T = 6.75e-008 N-m

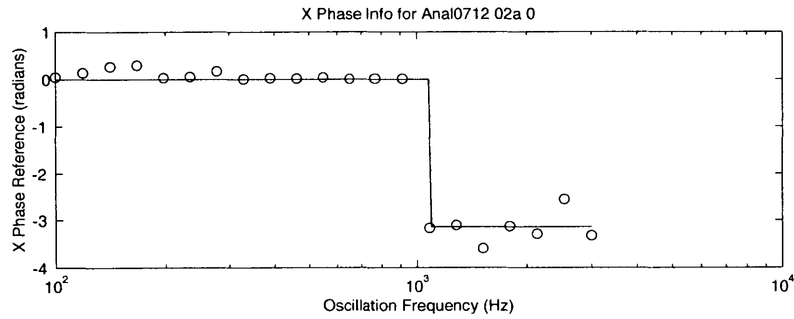
X Phase Info for Anal0712 02a 0
X Phase Reference (radians)
Oscillation Frequency (Hz)

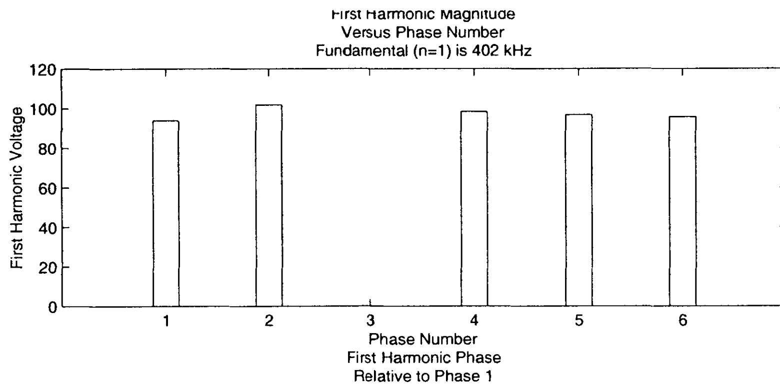
First Harmonic Magnitude
Versus Phase Number
Fundamental (n=1) is 402 kHz
First Harmonic Voltage
Phase Number

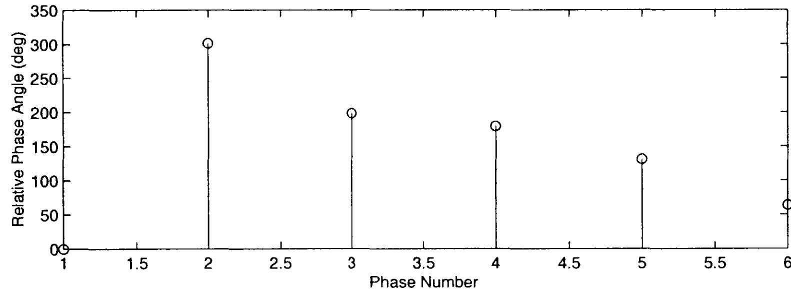
First Harmonic Phase
Relative to Phase 1
Relative Phase Angle (deg)
Phase Number

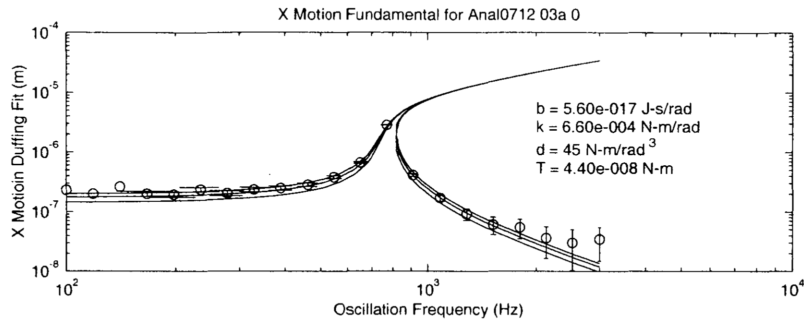
X Motion Fundamental for Anal0712 03a 0
X Motioin Duffing Fit (m)
b = 5.60e-017 J-s/rad
k = 6.60e-004 N-m/rad
d = 45 N-m/rad 3
T = 4.40e-008 N-m
Oscillation Frequency (Hz)

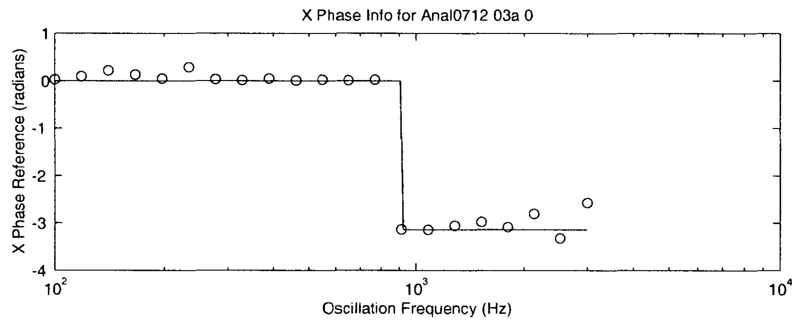
X Phase Info for Anal0712 03a 0
X Phase Reference (radians)
Oscillation Frequency (Hz)

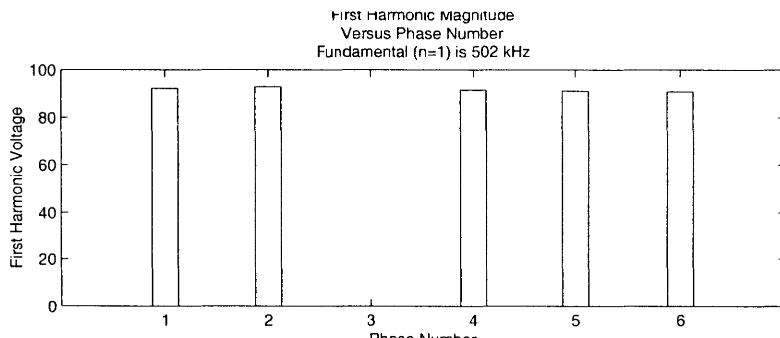
First Harmonic Magnitude
Versus Phase Number
Fundamental (n=1) is 502 kHz
First Harmonic Voltage
Phase Number

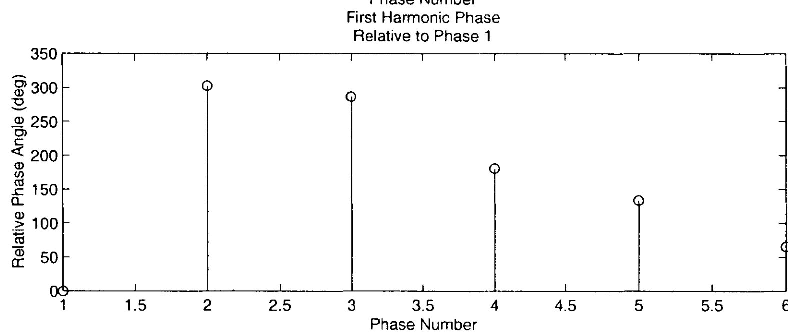
First Harmonic Phase
Relative to Phase 1
Relative Phase Angle (deg)
Phase Number

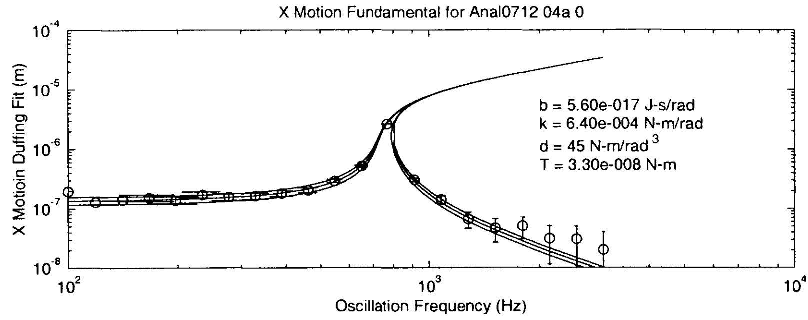
X Motion Fundamental for Anal0712 04a 0
X Motioin Duffing Fit (m)
b = 5.60e-017 J-s/rad
k = 6.40e-004 N-m/rad
d = 45 N-m/rad 3
T = 3.30e-008 N-m
Oscillation Frequency (Hz)

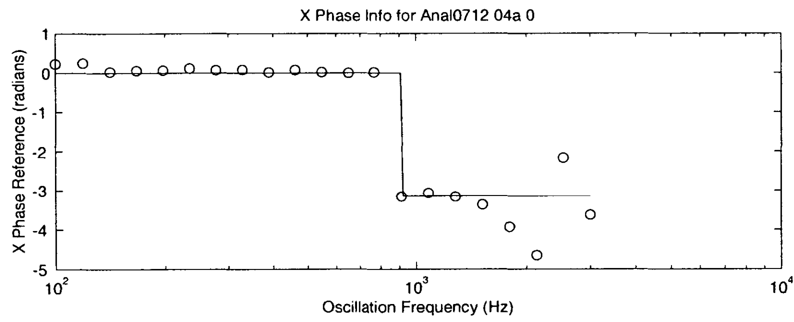
X Phase Info for Anal0712 04a 0
X Phase Reference (radians)
Oscillation Frequency (Hz)

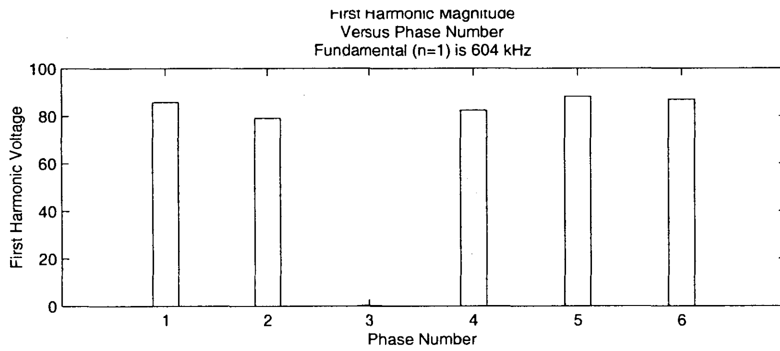
First Harmonic Magnitude
Versus Phase Number
Fundamental (n=1) is 604 kHz
First Harmonic Voltage
Phase Number

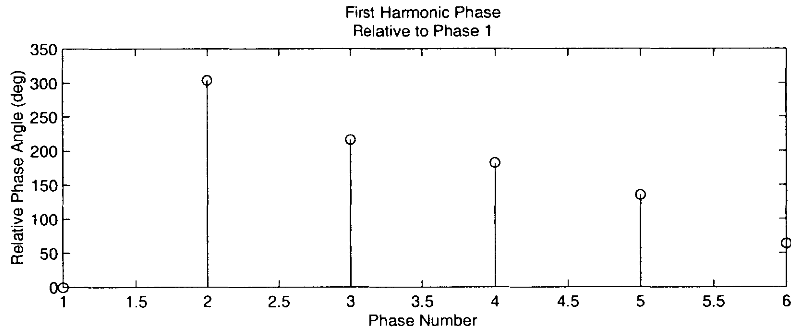
First Harmonic Phase
Relative to Phase 1
Relative Phase Angle (deg)
Phase Number

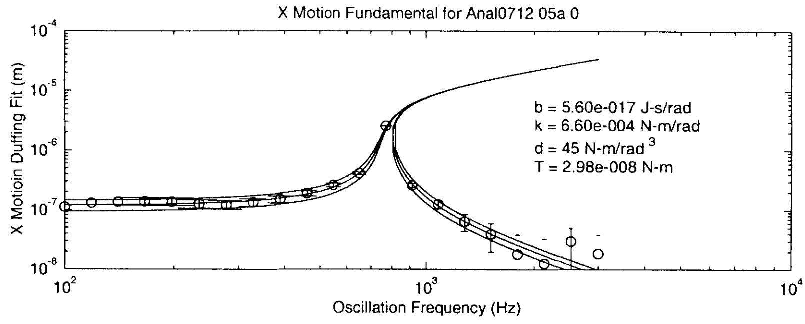
X Motion Fundamental for Anal0712 05a 0
X Motioin Duffing Fit (m)
b = 5.60e-017 J-s/rad
k = 6.60e-004 N-m/rad
d = 45 N-m/rad 3
T = 2.98e-008 N-m
Oscillation Frequency (Hz)

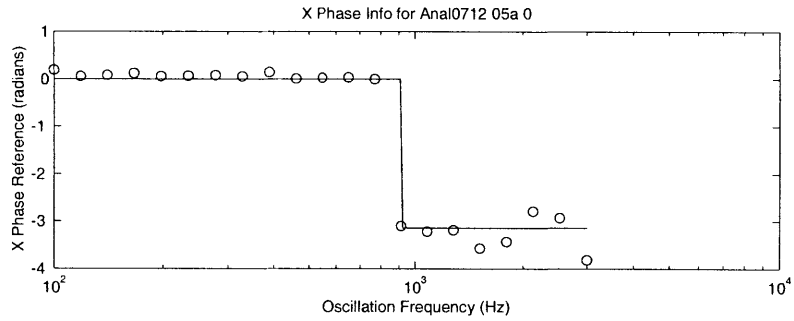
X Phase Info for Anal0712 05a 0
X Phase Reference (radians)
Oscillation Frequency (Hz)

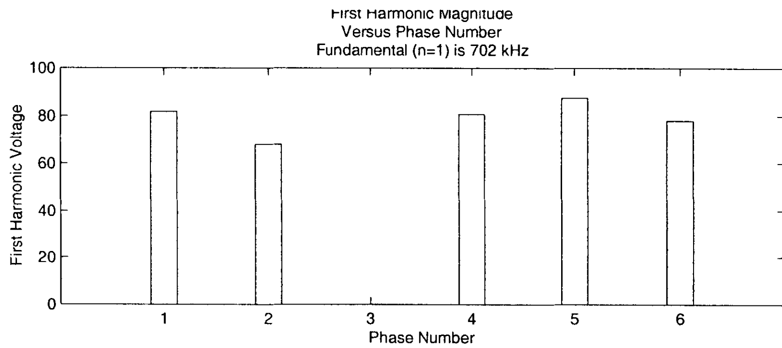
First Harmonic Magnitude
Versus Phase Number
Fundamental (n=1) is 702 kHz
First Harmonic Voltage
Phase Number

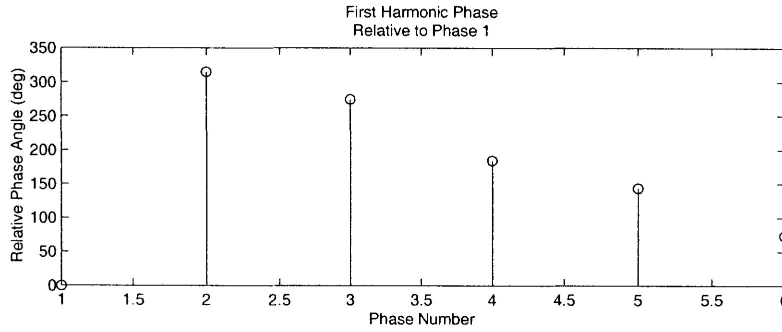
First Harmonic Phase
Relative to Phase 1
Relative Phase Angle (deg)
Phase Number

Bibliography

1) C. H. Ahn, Y. J. Kim, and M. G. Allen; "A planar variable reluctance magnetic micromotor with fully integrated stator and coils;" *Journal of Microelectromechanical Systems*, **2**(4), December 1993, 165-73.

2) R. Arno; "Über ein rotirendes elektrisches feld und dursh elektrostatische hysteresis bewirkte rotationen;" *Electrotechn Z*; **14**, 1863 17-18.

3) A. A. Ayon, R. Braff, C. C. Lin, H. H. Sawin, M. A. Schmidt; "Characterization of a time multiplexed inductively coupled plasma etcher;" *Journal of the Electrochemical Society*, **146**(1), 1999, 339-49.

4) S. F. Bart, "Modeling and design of electroquasistatic microactuators;" Ph.D. Thesis, Massachusetts Institute of Technology, Cambridge, MA; September, 1990.

5) S. F. Bart and J. H. Lang, "An analysis of electroquasistatic induction micromotors," *Sensors and Actuators*, **20**, November, 1989, 97-106.

6) W. Benecke and H-C. Petzold; "Linear and rotational magnetic micromotors fabricated using silicon technology;" Proceedings. IEEE Micro Electro Mechanical Systems. An Investigation of Micro Structures, Sensors, Actuators, Machines and Robots, 1992, 183-9.

7) P. R. Bevington and D. K. Robinson; Data Reduction and Error Analysis for the Physical Sciences; McGraw Hill, Boston, MA; 1992.

8) B. Bollée; "Electrostatic motors;" *Philips Technical Review*, **30**(6/7), 1969, 178-94.

9) J. M. Boyd and J. P. Ellul; "A one-step shallow trench global planarization process using chemical mechanical polishing;" *Journal of the Electrochemical Society*, **144**(5), 1838-41.

10) J. H. Calderwood and R. Mognaschi; "The spatial harmonic content of the field of an electrostatic induction motor;" *International Journal of Applied Electromagnetics in Materials*, **6**(3), November 1995, 197-205.

11) J. F. Charpentier, Y. Lefevre, E. Sarraute, and B. Trannoy; "Synthesis and modelling of an electrostatic induction motor;" *IEEE Transactions on Magnetics*, **31**(3), May 1995, 1404-7.

12) K-S. Chen, A. Ayon, and S. M. Spearing; "Controlling and testing the fracture strength of silicon on the mesoscale;" *Journal of the American Ceramic Society*, **83**(6), June 2000, 1476-84.

13) K-S. Chen; "Materials characterization and structural design of ceramic micro turbomachinery;" Ph.D. Thesis, MIT Department of Mechanical Engineering, February 1999.

14) S. D. Choi and D. A. Dunn; "A surface-charge induction motor;" Proceedings of the IEEE, **59**(5), May 1971, 737-48.

15) T. R. Christenson, T. J. Garino, and E. L. Venturini; "Deep X-ray lithography based fabrication of rare earth based permanent magnets and their applications to microactuators;" Proceedings of the Fifth International Symposium on Magnetic Materials, Processes, and Devices Applications to Storage and Microelectromechanical Systems (MEMS). Electrochem. Soc. 1999, 312-23.

16) E. R. Deustch; "Design, Experiment, and Analysis of Chemical Mechanical Polishing;" Internal Report, MIT 6.972 Semiconductor Manufacturing Course, May 1999.

17) V. R. Dhuler, M. Mehregany, and S. M. Phillips; "A comparative study of bearing designs and operational environments for harmonic side-drive micromotors;" *IEEE Transactions on Electron Devices*, **40**(1), November 1993, 1985-9.

18) A. H. Epstein and S. D. Senturia; "Macro Power from Micro Machinery;" *Science*; **276**, May 1997, 1211.

19) A. Epstein et al; "Power MEMS and Microengines;" Tranducers 97; 1997 International Conference on Solid-State Sensors and Actuators, Digest of Technical Papers; 2, 753-6, 1997.

20) J. A. Folta, C. E. Hunt, and S. N. Farrens; "Low-temperature wafer bonding of surfaces using a reactive sputtered oxide;" *Journal of the Electrochemical Society*, **141**(8), August 1994, 2157-60.

21) L. G. Frèchette; "Development of a microfabricated silicon motor-driven compressor system;" Ph.D. Thesis, MIT Department of Aeronautics and Astronautics, August 2000.

22) D. M. Freeman, A. J. Aranyosi, M. J. Gordon, S. S. Hong; "Multidimensional Motion Analysis of MEMS Using Computer Microvision;" Solid-State Sensor and Actuator Workshop. Transducer Research Foundation, Cleveland, OH; 1998, 150-5.

23) E. J. Garcia and J. J. Sniegowski JJ; "Surface micromachined microengine;" *Sensors & Actuators A*, **A48**(3), May 1995, 203-14.

24) H. Guckel, T. R. Christenson, K. J. Skrobis, T. S. Jung, J. Klein, K. V. Hartojo, and I. Widjaja; "A first functional current excited planar rotational magnetic micromotor;" Proceedings. IEEE. Micro Electro Mechanical Systems. An Investigation of Micro Structures, Sensors, Actuators, Machines and Systems, 1993, 7-11.

25) C. Gui, M. Elwenspoek, N. Tas, and J. G. E. Gardeniers; "The effect of surface rouhness on direct wafer bonding;" *Journal of Applied Physics*, **85**(10), May 1999, 7448-54.

26) C. Gui, M. Elwenspoek, J. G. E. Gardeniers, and P. V. Lambeck; "Present and future role of chemical mechanical polishing in wafer bonding;" *Journal of the Electrochemical Society*, **145**(6), June 1998, 2198-204.

27) J.-B. Huang, P.-S. Mao, Q.-Y. Tong and R.-Q. Zhang; "Study on Si electrostatic and electroquasistatic micromotors;" *Sensors and Actuators A*, **35**, November, 1993, 171-174.

28) S. C. Jacobsen, R. H. Price, J. E. Wood, T. H. Rytting, and M. Rafaelof; "The wobble motor: an electrostatic, planetary-armature, microactuator;" Proceedings: IEEE Micro Electro Mechanical Systems. An Investigation of Micro Structures, Sensors, Actuators, Machines and Robots, 1989, 17-24.

29) T. Kamins; Polycrystalline silicon for integrated circuits and displays; 2nd Ed, Kluwer Academic Pulishers, Boston, MA, 1998.

30) F. B. Kaufman, S. A. Cohen, and M. A Jaso; "Characterization of defects produced in TEOS thin films due to chemical-mechanical polishing (CMP);" Ultraclean Semiconductor Processing Technology and Surface Chemical Cleaning and Passivation. Symposium. Mater. Res. Soc. 1995, 85-95.

31) P. T. Krein and J. M. Crowley; "Harmonic effects in electrostatic induction motors;" *Electric Machines and Power Systems*, **10**(5-6), 1985, 479-97.

32) C. Kooy; "Torque on a resistive rotor in a quasi electrostatic rotating field;" *Applied Scientific Research*, **20**(2-3), February 1969, 161-72.

33) L. K. Lagorce, O. Brand, and M. G. Allen; "Magnetic microactuators based on polymer magnets;" *Journal of Microelectromechanical Systems*, **8**(1), March 1999, 2-9.

34) A. P. Lee, P. B. Ljung, and A. P. Pisano; "Polysilicon Micro Vibromotor;" Proceedings, IEEE Micro Electro Mechanical Systems, An Investigation of Micro Structures, Sensors, Actuators, Machines and Robots, IEEE, 1992, 177-82.

35) C. C. Lin, R. Ghodssi, A. A. Ayon, D. Z. Chen, S. Jacobsen, K. S. Breuer, A. H. Epstein, M. A. Schmidt, "Fabrication and Characterization of a Micro Turbine/Bearing Rig;" MEMS '99, Orlando FL, Jan. 1999.

36) C. C. Lin; "Development of a Microfabricated Turbine-Drive Air Bearing Rig;" Ph.D. Thesis, MIT Department of Mechanical Engineering, June 1999.

37) K. Ljungberg, Y. Bäcklund, A. Söderbärg, M. Bergh, M. O. Andersson, and S. Bengtsson; "The effects of HF cleaning prior to silicon wafer bonding;" *Journal of the Electrochemical Society*, **142**(4), April 1995, 1297-1303.

38) K. Ljungberg, A. Söderbärg, and U. Jansson; "Improved direct bonding of Si and SiO/sub 2/ surfaces by cleaning in H_2SO_4:H_2O_2:HF;" *Applied Physics Letters*, **67**(5), July 1995, 650-2.

39) T. Lobor; "A Microfabricated Electrostatic Motor Design and Process;" Master of Science Thesis, Massachusetts Institute of Technology, Cambridge, MA; February, 1988.

40) K. Lohner, K-S. Chen, A. A. Ayon, and S. M. Spearing; "Microfabricated silicon carbide microengine structures;" Materials Science of Microelectromechanical Systems (MEMS) Devices. Symposium. Mater. Res. Soc. 1999, 85-90.

41) C. G. Magnella, T. Ingwersen, and E. Fleck; "A comparison of planarization properties of TEOS and SiH_4 PECVD oxides;" 1988 Proceedings. Fifth International IEEE VLSI Multilevel Interconnection Conference, 1988, 366-73.

42) T. Martini, S. Hopfe, S. Mack, and U. Gosele; "Wafer bonding across surface steps in the nanometer range;" *Sensors & Actuators A*, **A75**(1), May 1999, 17-23.

43) B. Makin and B. J. Coles; "Novel Electrostatic Micromotors;" *Proceedings of the Sixth International Conference on Electrical Machines and Drives*, (Conf. Publ. No. 376), IEE, 1993, 1-3.

44) N. W. McLachlan; Ordinary Non-Linear Differential Equations in Engineering and Physical Sciences; 2nd Edition; Oxford University Press, London; 1956.

45) J. M. Meek and J. D. Craggs, editors; Electrical Breakdown of Gases; John Wiley and Sons, Inc; Chichester, 1978.

46) A. Mehra, A. A. Ayon, I. A. Waitz, M. A. Schmidt; "Microfabrication of High Temperature Silicon Devices Using Wafer Bonding and Deep Reactive Ion Etching;" *Journal of Microelectromechanical Systems*, **8**(2), June 1999, 152-60.

47) A. Mehra; "Development of a High Power Density Combustion System for a Silicon Micro Gas Turbine Engine;" Ph.D. Thesis, MIT Department of Aeronautics and Astronautics, February 2000.

48) M. Mehregany; "Microfabricated Silicon Electric Mechanisms;" Ph.D. Thesis; Massachusetts Institute of Technology, Cambridge, MA; May, 1990.

49) J. Melcher; Continuum Electromechanics; MIT Press, Cambridge, MA; 1981.

50) J. R. Melcher; "Traveling-Wave Induced Electroconvection;" *Phys. Fluids*, **9**(8), August 1966, 1548-55.

51) E. R. Mognaschi and J. H. Calderwood; ""A dielectric induction motor employing a rotating electric field;" Conference Record of the 1991 IEEE Industry Applications Society Annual Meeting, vol.1. New York, NY, 1991, 562-4.

52) E. R. Mognaschi ER and J. H. Calderwood JH; "Asynchronous dielectric induction motor;" IEE Proceedings-A-Science Measurement & Technology, **137**(6), November 1990, 331-8.

53) R. M. Moroney, R. M. White, and R. T. Howe; "Ultrasonic micromotors: physics and applications;" Proceedings. IEEE Micro Electro Mechanical Systems. An Investigation of Micro Structures, Sensors, Actuators, Machines and Robots, 1990, 182-7.

54) P. Muralt, M. Kohli, T. Maeder, A. Kholkin, K. Brooks, N. Setter, and R. Luthier; "Fabrication and characterization of PZT thin-film vibrators for micromotors;" *Sensors & Actuators A*, **A48**(2), May 1995, 157-65.

55) S. F. Nagle and J. H. Lang; "A Micro-Scale Electric-Induction Machine for a Micro Gas-Turbine Generator;" Proceedings of the 27th Meeting of the Electrostatics Society of America, Boston, MA; June 1999, 57-66.

56) M. Ohring; The Materials Science of Thin Films; Academic Press, Boston, MA, 1992.

57) D. J. Orr; "Macro-scale investigation of high speed gas bearings for MEMS devices;" Ph.D. Thesis, MIT Department of Aeronautics and Astronautics, February 2000.

58) F. Paschen; "Ueber die zum funkenübergang in luft, wasserstoff und kohlensäure bei verschiedenen drucken erforderliche potentialdifferenz;" *Annal der Physik*; **37**, 1889, 69-96.

59) R. A. Pease; Troubleshooting Analog Circuits; Butterworth-Heineman, Newton, MA; 1993, p 83 of the paperback.

60) E. Peikos; "Numerical simulation of gas-lubricated journal bearings for microfabricated machines;" Ph.D. Thesis, MIT Department of Aeronautics and Astronautics, February 2000.

61) J. M. Perchard, H. E. Smith, R. O'Connor, J. Olsen, and K. Law; "Characterization of a multiple-step in-situ plasma enhanced chemical vapor deposition (PECVD) tetraethylorthosilicate (TEOS) planarization scheme for submicron manufacturing;" Proceedings of SPIE - the International Society for Optical Engineering, **1188**, 1990, 75-85.

62) K. E. Petersen and C. R. Guarnier; "Young's modulus measurements of thin films using micromechanics;" *Journal of Applied Physics*, **50**(11), pt.1, Nov. 1979, 6761-6.

63) G-A. Racine, R. Luthier, P. Luginbuhl, K. Brooks, N. Setter, N. F. De Rooij; "Hybrid ultrasonic elastic force motors micromachined in silicon;" *Integrated Ferroelectrics*, **8**(1-2), 1995, 25-34.

64) W. McC. Seibert; Circuits, Signals, and Systems; MIT Press, Cambridge, MA; 1986.

65) O. M. Stuetzer; "Magnetohydrodynamics and Electrohydrodynamics;" *Phys. Fluids*, **5**(3), May 1962, 534-44.

66) Y-C. Tai, "IC-Processed Polysilicon Micromechanics: Technology, Material, and Devices;" Ph. D. Thesis, University of California; Berkeley, 1989.

67) Y.-C. Tai and R. S. Muller; "IC-Processed Electrostatic Synchronous Micromotors;" *Sensors and Actuators*, **20**, 1989, 49-55.

68) F. Tardif, I. Mansart, T. Lardin, O. Demolliens, M. Fayolle, Y. Gobile, J. Palleau, J. Torres; "Cleaning after silicon oxide CMP;" European Workshop. Materials for Advanced Metallization, MAM'97 Abstracts Booklet, **221**, 74-7.

69) L. Tavrow; "A LOCOS-Based Microfabricated Radial-Gap Electric Motor;" Ph.D. Thesis, Massachusetts Institute of Technology; February, 1991.

70) S. Timoshenko and S. Woinowsky-Kreiger; Theory of Plates and Shells; McGraw-Hill Book Company, New York, NY, 1959.

71) W. Trimmer and R. Jebens; "Harmonic Electrostatic Motors;" *Sensors and Actuators*, **20**, 1989, 17-24.

72) W. Trimmer and R. Jebens; "An operational harmonic electrostatic motor;" Proceedings: IEEE Micro Electro Mechanical Systems. An Investigation of Micro Structures, Sensors, Actuators, Machines and Robots, 1989, 13-16.

73) J. Ubbink; "Optimization of the Rotor Surface Resistance of the Asynchronous Electrostatic Motor;" *Applied Scientific Research*, **22**(6), Oct. 1970, 442-8.

74) W. Weaver, Jr; S. P. Tmioshenko; D. H. Young; Vibration Problems in Engineering; 5th Edition, John Wiley & Sons, New York, NY; 1990.

75) H. Woodson and J. Melcher; Electromechanical Dynamics, Parts I and II; Robert E. Kreiger, Malabar, FL; 1968.

76) Private communication, Alar Toomre of the MIT Mathematics Department, 1996.